

NUMERICAL AND EXPERIMENTAL ANALYSIS OF FLAPPING WING
MOTION

A THESIS SUBMITTED TO
THE GRADUATE SCHOOL OF NATURAL AND APPLIED SCIENCES
OF
MIDDLE EAST TECHNICAL UNIVERSITY

BY

EBRU SARIGÖL

IN PARTIAL FULFILLMENT OF THE REQUIREMENTS
FOR
THE DEGREE OF DOCTOR OF PHILOSOPHY
IN
AEROSPACE ENGINEERING

JULY 2007

**NUMERICAL AND EXPERIMENTAL ANALYSIS OF FLAPPING
WING MOTION**

Submitted by **EBRU SARIGÖL** in partial fulfillment of the requirements
for the degree of **Doctor of Philosophy in Aerospace Engineering,**
Middle East Technical University by,

Prof. Dr. Canan Özgen
Dean, Graduate School of **Natural and Applied
Sciences** _____

Prof. Dr. İsmail Hakkı Tuncer
Head of Department, **Aerospace Engineering** _____

Prof. Dr. Nafiz Alemdaroğlu
Supervisor, **Aerospace Engineering, METU** _____

Examining Committee Members:

Prof. Dr. Kahraman Albayrak
Mechanical Engineering Dept., METU _____

Prof. Dr. Nafiz Alemdaroğlu
Aerospace Engineering Dept., METU _____

Prof. Dr. Mehmet Ş. Kavsaoglu
Aeronautical Engineering Dept., İTÜ _____

Prof. Dr. Yusuf Özyörük
Aerospace Engineering Dept., METU _____

Assist. Prof. Dr. Serkan Özgen
Aerospace Engineering Dept., METU _____

Date: _____23.07.2007_____

I hereby declare that all information in this document has been obtained and presented in accordance with academic rules and ethical conduct. I also declare that, as required by these rules and conduct, I have fully cited and referenced all material and results that are not original to this work.

Name, Last Name :Ebru Sarigöl

Signature :

ABSTRACT

NUMERICAL AND EXPERIMENTAL ANALYSIS OF FLAPPING WING MOTION

Sarıgöl, Ebru

Ph.D., Department of Aerospace Engineering

Supervisor: Prof. Dr. Nafiz Alemdaroğlu

July 2007, 241 pages

The aerodynamics of two-dimensional and three-dimensional flapping motion in hover is analyzed in incompressible, laminar flow at low Reynolds number regime. The aim of this study is to understand the physics and the underlying mechanisms of the flapping motion using both numerical tools (Direct Numerical Simulation) and experimental tools (Particle Image Velocimetry PIV technique). Numerical analyses cover both two-dimensional and three-dimensional configurations for different parameters using two different flow solvers. The obtained results are then.

analyzed in terms of aerodynamic force coefficients and vortex dynamics. Both symmetric and cambered airfoil sections are investigated at different starting angle of attacks. Both numerical and experimental simulations are carried out at Reynolds number 1000. The experimental analysis is carried out using Particle Image Velocimetry (PIV) technique in parallel with the numerical tools. Experimental measurements are taken for both two-dimensional and three-dimensional wing configurations using stereoscopic PIV technique.

Keywords: flapping motion, hover, low Reynolds number, DNS, vortex, unsteady aerodynamics, PIV

ÖZ

ÇIRPAN KANAT HAREKETİNİN SAYISAL VE DENEYSEL İNCELENMESİ

Sarıgöl, Ebru

Doktora, Havacılık ve Uzay Mühendisliği Bölümü

Tez Yöneticisi Prof. Dr. Nafiz Alemdaroğlu

Temmuz 2007, 241 sayfa

Sıkıştırılmaz, ve laminer akış şartlarındaki düşük Reynolds sayısında iki ve üç boyutlu kanat modelleri için havada asılı kalma konumunda çirpan kanat hareketinin aerodinamiği incelenmiştir. Bu çalışmanın amacı, çirpan kanat hareketinin fiziğini ve altında yer alan aerodinamik mekanizmaların direk sayısal simülasyon ve deneysel araçlarla incelenmesidir. İki ve üç boyutlu sayısal çalışmalar iki farklı akış çözücüsü kullanılarak değişik parametrelerin incelenmesini kapsamaktadır. Elde edilen sonuçlar aerodinamik kuvvetler ve girdap dinamiği açılarından incelenmiştir.

Çalıřmada, deęiřik bařlangıç hücüm aıları için hem simetrik hem de kamburlu kanat kesitleri kullanılmıřtır. Sayısal ve deneysel alıřmalar Reynolds sayısı 1000 için yapılmıřtır. Deneysel analizler için Paracıklı Hız Görüntüleme (PIV) teknięi kullanılmıřtır.

Anahtar Kelimeler: ırpan kanat hareketi, havada asılı kalma, düşük Reynolds sayısı, DNS, girdap, zamana baęlı aerodinamik, PIV

To whom I love

ACKNOWLEDGEMENTS

I would like to express my sincere thanks to my supervisor, Prof. Dr. Nafiz Alemdarođlu for his guidance, advice and insight throughout this study.

I would like to thank to Assoc. Prof. Dr. Serkan Özgen for his guidance, encouragement and friendship during this study. His valuable comments and kind support motivated a lot. I would like to extend my appreciation to my jury members Prof. Dr. Mehmet Ş. Kavsaoglu, Prof. Dr. Kahraman Albayrak and Prof. Dr. Yusuf Özyörük for their suggestions and contributions.

I would like to express my thanks to my family for their endless support and love throughout my life.

I would like to thank to Yüksel Ortakaya, my precious love for giving me insight about not only the academical work but the life itself as well. I would not make it this far without his love and support. This thesis is dedicated to him.

I want to express my special thanks to Kadriye Tiryaki, my best friend for always believing in me and supporting me in any case. Her never ending encouragement made it possible to endure during the hard times.

I want to thank to my colleagues, H. Özgür Demir, Mustafa Kaya and Evrim Dizemen for their support and friendship.

I would like to thank to Mrs. Nilgün Kaplan and Ms. Figen Kılıç for their love, support and motivation. I also would like to thank to Mr. Murat Ceylan for his kind and endless assistance throughout the experimental part of the study and motivation during the writing of this thesis.

TABLE OF CONTENTS

PLAGIARISM	iii
ABSTRACT	iv
ÖZ	vi
DEDICATION	viii
ACKNOWLEDGEMENTS	ix
TABLE OF CONTENTS	xi
LIST OF TABLES	xv
LIST OF FIGURES	xvi
LIST OF SYMBOLS	xxx
CHAPTER	
1 INTRODUCTION	1
1.1 Background	1
1.2 Objective and Outline of the Present Study	6
2 THEORY OF FLAPPING WING MOTION MECHANISM	10
2.1 Flapping Motion	10
2.1.1 Hovering	19
2.1.2 Clap and Fling Mechanism	22

3	LITERATURE SURVEY.....	24
3.1	Review of Numerical Studies	25
3.2	Review of Experimental Studies	32
3.3	Review of Numerical and Experimental Studies	42
4	EXPERIMENTAL SETUP.....	45
4.1	Experimental Setup.....	45
4.2	Particle Image Velocimetry (PIV) Technique	50
4.2.1	Seeding of Flow Field	51
4.2.2	Illumination	56
4.2.3	Cameras	60
4.2.4	Synchronization.....	63
4.2.5	Correlation	64
4.2.6	Validation and further analysis	70
4.3	Vortex Identification Techniques.....	76
4.3.1	Scalar Methods	78
4.3.2	Second Invariant of Velocity Gradient, Q Criterion	80
4.3.3	Two Negative Eigenvalues of $(S^2 + \Omega^2)$, λ_2 Criterion.....	82
5	TWO-DIMENSIONAL NUMERICAL ANALYSIS OF FLAPPING MOTION.....	87
5.1	Definition of Geometry and Flapping Motion in Numerical Analysis	87
5.2	Solver Description, STAR-CD	90
5.2.1	Computational Domain	91
5.2.2	Numerical Parametric Study	96
5.2.2.1	Effect of Thickness on Flapping Motion	96

5.2.2.2	Effect of Camber on Flapping Motion.....	113
5.2.2.3	Analysis of Different Cambered Profiles	130
5.2.2.4	Effect of Leading Edge Radius on Flapping Motion.....	137
5.3	Solver Description, Fluent.....	141
5.3.1	Parallel Implementation.....	142
5.3.2	Speedup and Efficiency.....	143
5.3.3	Computational Domain	145
5.3.4	Comparison of Results of STAR-CD and FLUENT	146
6	TWO-DIMENSIONAL EXPERIMENTAL ANALYSIS OF FLAPPING MOTION.....	151
6.1	Experimental Results	152
6.2	Comparison of Experimental and Numerical Results.....	161
7	THREE-DIMENSIONAL NUMERICAL ANALYSIS OF FLAPPING MOTION.....	175
7.1	Numerical Analysis.....	175
7.2	Comparison of Two-Dimensional and Three-Dimensional Numerical Solutions	193
8	THREE-DIMENSIONAL EXPERIMENTAL ANALYSIS OF FLAPPING MOTION.....	198
8.1	Experimental Analysis.....	198
8.2	Three-dimensional Experimental Results.....	204
8.3	Comparison of Experimental Results to Numerical Computations.....	208

9 CONCLUSION	216
9.1 General Conclusions	217
9.2 Future Work	224
REFERENCES	226
CURRICULUM VITAE	238

LIST OF TABLES

TABLES

Table 4.1 Specifications of seeding particle	56
Table 4.2 Comparison of experimental and numerical periods for Re=1000	62
Table 5.1 Two-dimensional solution domain details for different airfoil profiles	92
Table 5.2 Average lift and drag coefficients over [5T 6T].....	130
Table 5.3 Leading edge radii values of different airfoil profiles	138

LIST OF FIGURES

FIGURES

Figure 1.1 Comparison of flight regime of Micro Air Vehicles to existing flight regimes (from Ref. [2]).....	3
Figure 2.1 Cartoon representation of delayed stall mechanism (adopted from Ref. [7])	12
Figure 2.2 Rotational lift for a rotating ball and a rotating wing (from Ref. [7])	14
Figure 2.3 Cartoon representation of wake capture mechanism. (V and W indicate the velocity of the wing and of the fluid wake relative to an inertial frame, respectively. Resultant velocity of the wing relative to the fluid is given by $V_{tot} = V - W$.) (From Ref. [7])	16
Figure 2.4 Schematic representation of downstroke phase (from Ref. [8])	17
Figure 2.5 Schematic representation of upstroke phase (from Ref. [8])	18
Figure 2.6 Symmetrical hovering of a hummingbird (from Ref. [1]).....	20
Figure 2.7 The wing tip path of a hummingbird viewed from side, illustrating a horizontal stroke plane (from Ref. [9])	21
Figure 2.8 The schematic representation of two hovering styles: normal hovering using a horizontal stroke plane (left) and hovering using an inclined stroke plane (right) (from Ref. [5])	22

Figure 2.9 Clap-Fling mechanisms: wings approaching each other to clap (A–C) and flinging apart (D–F). Black lines show flow lines, and dark blue arrows show induced velocity. Light blue arrows show net forces acting on the airfoil (from Ref. [5]).	23
Figure 3.1 A two-dimensional view of the wingtip path for a bumblebee <i>Bombus terrestris</i> at different flight speeds. Resultant aerodynamic forces are shown for representative downstrokes and upstrokes. The anatomical lower wing surface is marked by a triangle at the leading edge. Wing beat frequency and stroke amplitude did not vary significantly with speed, and values of the advance ratio J are calculated using their means (from Ref. [12]).	26
Figure 3.2 Picture of male <i>Drosophila melanogaster</i> (from Ref. [48])	34
Figure 3.3 An adult <i>Manduca sexta</i> (from Ref. [52])	35
Figure 3.14 Rock piegon in flight (from Ref. [56])	37
Figure 3.5 Hummingbird Hawkmoth (<i>macroglossum stellatarum</i>) (from Ref. [63])	38
Figure 3.6 Rufous Hummingbird (<i>Selasphorus rufus</i>) (from Ref. [65])	39
Figure 4.1 Experimental setup with water tank.	46
Figure 4.2 Upper mechanism for translational and rotational motions of the experimental setup.	47
Figure 4.3 Translational and rotational mechanisms of the upper mechanism.	48
Figure 4.4 GUI for the motion control program of the mechanism.	50
Figure 4.5The experimental visualization with and without mirror in the water tank.	59
Figure 4.6 Water tank with the whole experimental setup.	59
Figure 4.7 Numerical processing flowchart in Flow Manager Software.	65

Figure 4.8 Flow diagram of adaptive processing in Flow Manager Software.	66
Figure 4.9 Overlapping of interrogation areas.....	67
Figure 4.10 Deformation options in PIV.	67
Figure 4.11 .Window options in adaptive correlation procedure in Flow Manager software.....	68
Figure 4.12 Velocity vector located at the center of the interrogation window (second order interpolation)	70
Figure 4.13 Example of validation settings for PIV analysis using adaptive correlation methodology.....	72
Figure 4.14 (a)- (c) Comparison of non-dimensional desired x-position, velocity and angle of attack distributions to actually observed values data at $\alpha=45^\circ$, $Re=1000$, $x_v= x_a=2c$	73-74
Figure 4.15 Experimental setup (a) front view, (b) side view.....	75
Figure 4.16 Airfoil made of transparent acrylic in the water tank.	76
Figure 5.1 Kinematics of flapping motion.	88
Figure 5.2 Definition of flapping motion.	89
Figure 5.3 (a)-(b) Two-dimensional grid domain for NACA 0012.	93
Figure 5.4 Boundary Conditions. (a) Symmetry planes for both sides of the discs, (b) Pressure Boundary for the far field, (c) Wall boundary. ..	93
Figure 5.5 Grid dependence study for two dimensional flapping motion analyses.....	95
Figure 5.6 Computational mesh for NACA 0010 (1 st column), NACA 0012 (2 nd column) and NACA 0015 (3 rd column) (a) full mesh, (b) closer view around the profile.	97
Figure 5.7 Lift coefficient distribution with respect to time for $\alpha=30^\circ$, $x_v=2c$, $Re=1000$ with rotation axis at $\frac{1}{4}c$ for one period.....	99

Figure 5.8 Drag coefficient distribution with respect to time for $\alpha=30^\circ$, $x_v=2c$, $Re=1000$ with rotation axis at $\frac{1}{4}c$ for one period.....	99
Figure 5.9 Non-dimensional vorticity contours of NACA 0010 (1 st column), NACA 0012 (2 nd column) and NACA 0015 (3 rd column) during the first half downstroke for $\alpha=45^\circ$, $x_v=2c$, $Re=1000$	102
Figure 5.10 Non-dimensional Q (second invariant of velocity gradient) contours of NACA 0010 (1 st column), NACA 0012 (2 nd column) and NACA 0015 (3 rd column) during the first half downstroke for $\alpha=45^\circ$, $x_v=2c$, $Re=1000$	103
Figure 5.11 Non-dimensional λ_2 (second negative eigenvalue of $(S^2+\Omega^2)$) contours NACA 0010 (1 st column), NACA 0012 (2 nd column) and NACA 0015 (3 rd column) during the first half downstroke for $\alpha=45^\circ$, $x_v=2c$, $Re=1000$	104
Figure 5.12 Lift coefficient variations with respect to time for $\alpha=45^\circ$, $x_v=2c$, $Re=1000$ with rotation axis at $\frac{1}{4}c$ for one period.	105
Figure 5.13 Drag coefficient variations with respect to time for $\alpha=45^\circ$, $x_v=2c$, $Re=1000$ with rotation axis at $\frac{1}{4}c$ for one period.	106
Figure 5.14 Lift coefficient variations with respect to time for $\alpha=60^\circ$, $x_v=2c$, $Re=1000$ with rotation axis at $\frac{1}{4}c$ for one period.	106
Figure 5.15 Drag coefficient variations with respect to time for $\alpha=60^\circ$, $x_v=2c$, $Re=1000$ with rotation axis at $\frac{1}{4}c$ for one period.	107
Figure 5.16 Lift to drag ratio variation over one period at $\alpha=30^\circ$, $x_v=2c$, $Re=1000$	108
Figure 5.17 Lift to drag ratio variation over one period at $\alpha=45^\circ$, $x_v=2c$, $Re=1000$	109
Figure 5.18 Lift to drag ratio variation over one period at $\alpha=60^\circ$, $x_v=2c$, $Re=1000$	110

Figure 5.19 Pressure contours of NACA 0010 (1 st column), NACA 0012 (2 nd column) and NACA 0015 (3 rd column) for $\alpha=45^\circ$, $x_v=2c$, $Re=1000$. .	111
Figure 5.19 (Continued) Pressure contours of NACA 0010 (1 st column), NACA 0012 (2 nd column) and NACA 0015 (3 rd column) for $\alpha=45^\circ$, $x_v=2c$, $Re=1000$	112
Figure 5.20 NACA 6412 airfoil profile.	114
Figure 5.21 Computational mesh for NACA 6412.	114
Figure 5.22 Comparison of drag coefficients of NACA 6412 and NACA 0012 for $Re = 1000$ at $\alpha = 30^\circ$	115
Figure 5.23 Comparison of lift coefficients of NACA 6412 and NACA 0012 for $Re = 1000$ at $\alpha = 30^\circ$	116
Figure 5.24 Comparison of drag coefficients of NACA 6412 and NACA 0012 for $Re = 1000$ at $\alpha = 45^\circ$	116
Figure 5.25 Comparison of lift coefficients of NACA 6412 and NACA 0012 for $Re = 1000$ at $\alpha = 45^\circ$	117
Figure 5.26 Comparison of drag coefficients of NACA 6412 and NACA 0012 for $Re = 1000$ at $\alpha = 60^\circ$	117
Figure 5.27 Comparison of lift coefficients of NACA 6412 and NACA 0012 for $Re = 1000$ at $\alpha = 60^\circ$	118
Figure 5.28 Identification of vortex regions of NACA 6412 by non-dimensional vorticity (1 st column), second invariant of velocity gradient, Q criteria (2 nd column) and, λ_2 contours, second negative eigenvalue of $(S^2+\Omega^2)$ (3 rd column) during the first half period for $\alpha=45^\circ$, $x_v=2c$, $Re=1000$	119
Figure 5.28 (Continued) Identification of vortex regions of NACA 6412 by non-dimensional vorticity (1 st column), second invariant of velocity gradient, Q criteria (2 nd column) and, λ_2 contours, second negative	

eigenvalue of $(S^2+\Omega^2)$ (3^{rd} column) during the first half period for $\alpha=45^\circ$, $x_v=2c$, $Re=1000$	120
Figure 5.29 Comparison of vortex regions of NACA 0012 (left) and NACA 6412 (right) by non-dimensional vorticity contours, second invariant of velocity gradient tensor, Q contours and second negative eigenvalue of $(S^2+\Omega^2)$, λ_2 contours at the end of the first half downstroke ($t^*=0.25$) for $\alpha=45^\circ$, $x_v=2c$, $Re=1000$	123
Figure 5.30 Comparison of vortex regions of NACA 0012 (left) and NACA 6412 (right) by non-dimensional vorticity contours at different angles of attack at the end of the first half downstroke ($t^*=0.25$).	124
Figure 5.31 Lift coefficient variation versus Reynolds number comparison for NACA 6412 at $\alpha=30^\circ$	125
Figure 5.32 Power density spectrum analysis for Reynolds number at $\alpha=30^\circ$	125
Figure 5.33 Lift coefficient variation versus Reynolds number comparison for NACA 6412 at $\alpha=45^\circ$	126
Figure 5.34 Power density spectrum analysis for Reynolds number at $\alpha=45^\circ$	126
Figure 5.35 Lift coefficient variation versus Reynolds number comparison for NACA 6412 at $\alpha=60^\circ$	127
Figure 5.36 Power density spectrum analysis for Reynolds number at $\alpha=60^\circ$	127
Figure 5.37 Power density spectrum analysis for angle of attack at $Re=1000$	128
Figure 5.38 Power density spectrum analysis for angle of attack at $Re=2000$	128

Figure 5.39 Comparison of drag coefficient distributions of different airfoil sections at $Re = 1000$, $\alpha = 30^\circ$.	132
Figure 5.40 Comparison of lift coefficient distributions of different airfoil sections at $Re = 1000$, $\alpha = 30^\circ$.	132
Figure 5.41 Comparison of drag coefficient distributions of different airfoil sections at $Re = 1000$, $\alpha = 45^\circ$.	133
Figure 5.42 Comparison of lift coefficient distributions of different airfoil sections at $Re = 1000$, $\alpha = 45^\circ$.	132
Figure 5.43 Comparison of drag coefficient distributions of different airfoil sections at $Re = 1000$, $\alpha = 60^\circ$.	134
Figure 5.44 Comparison of lift coefficient distributions of different airfoil sections at $Re = 1000$, $\alpha = 60^\circ$.	135
Figure 5.45 Comparison of lift-to-drag ratio variations of different airfoil sections at $Re = 1000$, $\alpha = 30^\circ$ in one period.	136
Figure 5.46 Comparison of lift-to-drag ratio variations of different airfoil sections at $Re = 1000$, $\alpha = 45^\circ$ in one period.	136
Figure 5.47 Comparison of lift-to-drag ratio variations of different airfoil sections at $Re = 1000$, $\alpha = 60^\circ$ in one period.	137
Figure 5.48 Comparison of lift coefficient variations in one period for different airfoil profiles at $Re = 1000$, $\alpha = 45^\circ$.	139
Figure 5.49 Comparison of drag coefficient variations in one period for different airfoil profiles at $Re = 1000$, $\alpha = 45^\circ$.	139
Figure 5.50 Comparison of vortex regions by non-dimensional vorticity contours during the first rotational phase at $Re = 1000$, $\alpha = 45^\circ$ (NACA 63-215 airfoil at the 1 st row, NACA 64(2)015 airfoil at the 2 nd row, Göttingen GOE 122 airfoil at the 3 rd row and NACA 63218 airfoil at the 4 th row).	140

Figure 5.51 Speedup plot for two-dimensional results.....	144
Figure 5.52 Efficiency plot of two-dimensional results... ..	145
Figure 5.53 Computational domain in Fluent simulations.	146
Figure 5.54 Comparison of lift (left) and drag (right) coefficient distributions calculated by Fluent and STAR-CD at $\alpha=45^\circ$, $x_v=2c$, Re=1000 with rotation axis at $1/4c$ for 6th and 7 th period.	147
Figure 5.55 Comparison of STAR-CD (left) and Fluent (right) solutions in terms of non-dimensional vorticity contours at Re =1000 and $\alpha=45^\circ$ during the first half period.	148
Figure 5.56 Comparison of STAR-CD (left) and Fluent (right) solutions in terms of non-dimensional second invariant of velocity gradient, Q contours at Re =1000 and $\alpha=45^\circ$ during the first half period.	149
Figure 5.57 Comparison of STAR-CD (left) and Fluent (right) solutions in terms of non-dimensional λ_2 contours, second negative eigenvalue of $(S^2+\Omega^2)$ at Re =1000 and $\alpha=45^\circ$ during the first half period.	150
Figure 6.1 Procedure for obtaining the velocity vectors from PIV measurements.	153
Figure 6.2 PIV image of the airfoil obtained by merging the images of the cameras.	154
Figure 6.3 Procedure for obtaining the velocity vectors from merged images.	155
Figure 6.4 Comparison of second invariant of velocity gradient, Q contours at $t^*=0.20$ at the overlapping region.	156
Figure 6.5 Schematic representations of vortex regions shown with the airfoil.	157

Figure 6.6 Identification of vortices according to their locations on both experimental and numerical non-dimensional vorticity contours at the beginning of the second downstroke phase ($t^*=0.77$)	158
Figure 6.7 Identification of vortex regions by non-dimensional vorticity, $ \omega $ and second invariant of velocity gradient, Q contours at $t^*=0.10$ (first half of downstroke).....	159
Figure 6.8 Identification of vortex regions by non-dimensional vorticity, $ \omega $ and second invariant of velocity gradient, Q contours at $t^*=0.15$ (first half of downstroke)	159
Figure 6.9 Identification of vortex regions by non-dimensional vorticity, $ \omega $ and second invariant of velocity gradient, Q contours at $t^*=0.20$ (first half of downstroke)	160
Figure 6.10 Identification of vortex regions by non-dimensional vorticity, $ \omega $ and second invariant of velocity gradient, Q contours at $t^*=0.23$ (first half of downstroke)	161
Figure 6.11 Identification of vortex regions by non-dimensional vorticity, $ \omega $ and second invariant of velocity gradient, Q contours at $t^*=0.25$ (end of first half of downstroke)	161
Figure 6.12 Comparison of experimental (left) and numerical (right) non-dimensional vorticity contours at the first quarter period at $\alpha=45^\circ$, $Re = 1000$	163
Figure 6.12 (continued) Comparison of experimental (left) and numerical (right) non-dimensional vorticity contours at the second quarter period at $\alpha=45^\circ$, $Re = 1000$	164

Figure 6.12 (continued) Comparison of experimental (left) and numerical (right) non-dimensional vorticity contours at the third quarter period at $\alpha=45^\circ$, $Re = 1000$	165
Figure 6.12 (continued) Comparison of experimental (left) and numerical (right) non-dimensional vorticity contours at the fourth quarter period at $\alpha=45^\circ$, $Re = 1000$	166
Figure 6.13 Comparison of experimental (left) and numerical (right) non-dimensional Q contours, second invariant of velocity gradient tensor, at the first quarter period at $\alpha=45^\circ$ $Re = 1000$	167
Figure 6.13 (continued) Comparison of experimental (left) and numerical (right) non-dimensional Q contours, second invariant of velocity gradient tensor, at the second quarter period at $\alpha=45^\circ$, $Re = 1000$	168
Figure 6.13 (continued) Comparison of experimental (left) and numerical (right) non-dimensional Q contours, second invariant of velocity gradient tensor, at the third quarter period at $\alpha=45^\circ$, $Re = 1000$	169
Figure 6.13 (continued) Comparison of experimental (left) and numerical (right) non-dimensional Q contours, second invariant of velocity gradient tensor, at the fourth quarter period at $\alpha=45^\circ$, $Re = 1000$	170
Figure 6.14 Comparison of experimental (left) and numerical (right) non-dimensional λ_2 contours, second negative eigenvalue of $(S^2+\Omega^2)$, at the first quarter period at $\alpha=45^\circ$, $Re = 1000$	171
Figure 6.14 (continued) Comparison of experimental (left) and numerical (right) non-dimensional λ_2 contours, second negative eigenvalue of $(S^2+\Omega^2)$, at the second quarter period at $\alpha=45^\circ$, $Re = 1000$	172
Figure 6.14 (continued) Comparison of experimental (left) and numerical (right) non-dimensional λ_2 contours, second negative eigenvalue of $(S^2+\Omega^2)$, at the third quarter period at $\alpha=45^\circ$, $Re = 1000$	173

Figure 6.14 (continued) Comparison of experimental (left) and numerical (right) non-dimensional λ_2 contours, second negative eigenvalue of $(S^2+\Omega^2)$, at the fourth quarter period at $\alpha=45^\circ$, $Re = 1000$	174
Figure 7.1 Three-dimensional computational mesh. ...	177
Figure 7.2 Boundary conditions: (a) symmetry plane and the wing, (b) pressure outlet at the far field.	177
Figure 7.3 CPU time comparisons for three-dimensional solutions	178
Figure 7.4 Efficiency plot for three-dimensional solutions. ...	178
Figure 7.5 Iso-contours, $Q=8$ at $\alpha=45^\circ$, $Re = 1000$ during the first half downstroke.....	180
Figure 7.5 (continued) Iso-contours, $Q=8$ at $\alpha=45^\circ$, $Re = 1000$ during the first half upstroke.	181
Figure 7.5 (continued) Iso-contours, $Q=8$ at $\alpha=45^\circ$, $Re = 1000$ during the second half upstroke.....	182
Figure 7.5 (continued) Iso-contours, $Q=8$ at $\alpha=45^\circ$, $Re = 1000$ during the second half downstroke.....	183
Figure 7.6 Stream ribbons during the first quarter period (first downstroke) at $\alpha=45^\circ$, $Re = 1000$	185
Figure 7.7 Stream ribbons at the tip of the wing when $t^*=0.1$ (during first downstroke) at $\alpha=45^\circ$, $Re = 1000$	186
Figure 7.8 Pressure coefficient contours with vortex core lines at the end of the first quarter period ($t^*=0.25$).....	186
Figure 7.9 Pressure coefficient contours with vortex core lines at the end of the third quarter period ($t^*=0.75$).	187
Figure 7.10 Stream ribbons (colored) and vortex core lines (black) at the end of the first half downstroke ($t^*=0.25$) for $\alpha=45^\circ$, $Re = 1000$	187

Figure 7.11 Stream ribbons (colored) and vortex core lines (black) at the end of the second half upstroke ($t^*=0.75$).for $\alpha=45^\circ$, $Re = 1000$ (left view).....	188
Figure 7.12 Stream ribbons (colored) and vortex core lines (black) at the end of the second half upstroke ($t^*=0.75$).for $\alpha=45^\circ$, $Re = 1000$ (right view).....	188
Figure 7.13 Spanwise evolution of vortex regions during the first rotational phase for $\alpha=45^\circ$, $Re = 1000$	191
Figure 7.13 (Continued) Spanwise evolution of vortex regions during the first rotational phase for $\alpha=45^\circ$, $Re = 1000$	192
Figure 7.14 Comparison of drag coefficient distribution for two and three-dimensional numerical solutions.....	194
Figure 7.15 Comparison of lift coefficient distribution for two and three-dimensional numerical solutions.....	194
Figure 7.16 Comparison of vortex structures for two-dimensional (top) and three-dimensional solutions (bottom) at the midspan in terms of non-dimensional Q criteria, for $\alpha=45^\circ$, $Re = 1000$ during the first quarter period.....	196
Figure 7.16 (Continued) Comparison of vortex structures for two-dimensional (top) and three-dimensional solutions (bottom) at the midspan in terms of non-dimensional Q criteria, for $\alpha=45^\circ$, $Re = 1000$ during the second quarter period.....	197
Figure 8.1 Spanwise locations for 3D measurements.....	199
Figure 8.2 Calibration images of Camera 1 (left) and Camera 2 (right) for 3D visualizations.....	200
Figure 8.3 Sample PIV images of Camera 1 (left) and Camera 2 (right) for 3D measurements.....	201

Figure 8.4 Velocity vectors obtained via adaptive correlation.....	202
Figure 8.5 3D velocity vectors after applying moving average filter.....	202
Figure 8.6 Laser sheet visualization of hovering motion during the first quarter period at $\alpha=45^\circ$, $Re = 1000$	203
Figure 8.7 Laser sheet visualization of hovering motion during the second quarter period at $\alpha=45^\circ$, $Re = 1000$	203
Figure 8.8 Vortex regions identified by Q criteria during the first downstroke at different spanwise locations: $z/b= 0.5$ (first column), $z/b=0.73$ (2 nd column), $z/b=0.93$ (third column) and $z/b=1.03$ (fourth column).....	205
Figure 8.8 (continued) Vortex regions identified by Q criteria during first downstroke and upstroke at different spanwise locations: $z/b= 0.5$ (first column), $z/b=0.73$ (2 nd column), $z/b=0.93$ (third column) and $z/b=1.03$ (fourth column).....	206
Figure 8.8 (continued) Vortex regions identified by Q criteria during first upstroke at different spanwise locations: $z/b= 0.5$ (first column), $z/b=0.73$ (2 nd column), $z/b=0.93$ (third column) and $z/b=1.03$ (fourth column).....	207
Figure 8.9 Comparison of experimental (left) and numerical (right) results for the first quarter period at $z/b= 0.5$ spanwise location.....	209
Figure 8.9 (continued) Comparison of experimental (left) and numerical (right) results for the second quarter period at $z/b= 0.5$ spanwise location.....	210
Figure 8.10 Comparison of experimental (left) and numerical (right) results for the first half period at $z/b= 0.93$ spanwise location.....	213

Figure 8.10 (continued) Comparison of experimental (left) and numerical (right) results using the second invariant of velocity gradient tensor, Q criteria for the first half period at $z/b= 0.93$ spanwise location.....214

Figure 8.10 (continued) Comparison of experimental (left) and numerical (right) results for the first half period at $z/b= 0.93$ spanwise location.....215

LIST OF SYMBOLS

b	span
c	chord
C_D	drag coefficient
C_L	lift coefficient
dt	time step
p	pressure
Q	second invariant of velocity gradient
Re	Reynolds number
t	time
t_a	time corresponding to the x_a location, where the angle of attack changes
t_v	time corresponding to the x_v location where the velocity changes
T	period
u_i	absolute fluid velocity component in direction x_i
V	velocity of the flapping motion
V_0	maximum velocity during the flapping motion
V_P	velocity input to the Testpoint program for the photo timing

x_a	x position at the beginning of angle of attack change
x_i	Cartesian coordinate ($i=1, 2, 3$)
x_v	x position at the end of constant velocity region
$x_{T/4}$	maximum x location, half-amplitude
α	angle of attack
λ	eigenvalue
μ	dynamic viscosity
ρ	density
ν	kinematic viscosity
ω	vorticity
Ω_{ij}	rate of rotation tensor
S_{ij}	rate of deformation tensor
τ_{ij}	stress tensor components

CHAPTER I

INTRODUCTION

1.1 Background

During the last fifty years, advances in aerodynamic theory have enabled the design and development of a number of advanced flight vehicles. Most of the studies were directed to high speed flows and large scale vehicles. Due to the emphasis on the faster and bigger flight vehicles, the 'smaller and slower' flight regime has not been adequately addressed. The interest in small, slow-flying vehicles has been given a boost in recent years as many government and industrial "Micro Aerial Vehicle" (MAV) projects have begun. Government's interest is primarily for military purposes: to take advantage of such vehicles: swarms of inexpensive attack/reconnaissance vehicles, their ease of transport to the battlefield even in a soldier's backpack. As noted by Ames [1], industrial attention on MAV's is due to their safety and accessibility considerations: these vehicles can be used in areas such as contaminated and toxic areas, where entrance of humans is strictly prohibited.

According to definition employed by DARPA (Defense Advanced Research Project Agency, USA) an air vehicle whose size is less than 15 cm (about 6 inches) in length, width or height is called a Micro Air Vehicle. McMichael et al. [2] states that the limitation on the size may seem arbitrary but it is derived from both physical and technological considerations.

The form of Micro Air Vehicles is still an emerging research area. Various numbers of proposed designs have been built and tested, including flying wings, lifting bodies, conventional platforms, rotary wing platforms and flapping wing platforms. Among these platforms, flapping wings hold several distinct advantages over conventional platforms in the low Reynolds number regime. Most important advantage lies in the flapping wings' ability to achieve very high unsteady lift but also include advantages in the synergies inherent in combined lift and thrust mechanisms and in their ability to hover [1].

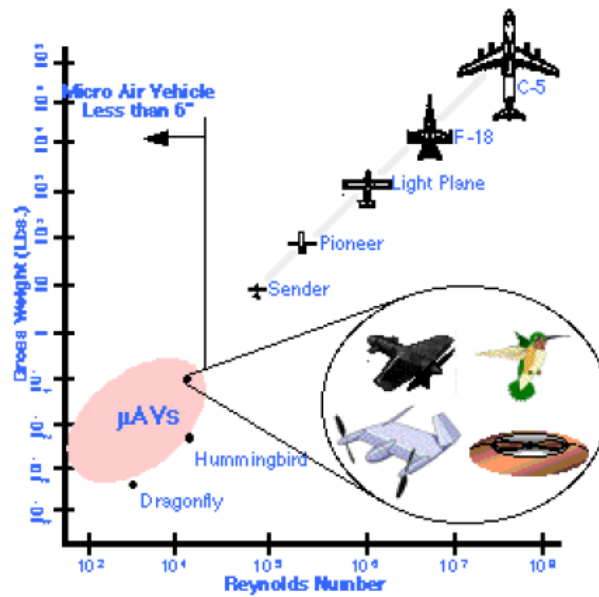


Figure 1.1 Comparison of flight regime of Micro Air Vehicles to existing flight regimes (from Ref. [2])

The flight regime of a conventional aircraft is more different than that of a small-scale air vehicle. Noting that common wind and gust profile around the ground can be order of 8 -11 m/s, precisely within the range of likely cruise speeds of MAV's they require enhanced maneuverability. But when the conventional aircrafts encounter extreme gust situations, the results are catastrophic. The ability of flapping wings' to achieve high lift coefficients quickly make them as ideal candidates for vehicles that require quick response to drastic changes in the relative wind [1].

The enhanced maneuverability of a flapping wing vehicle is a result of the same capability that enhances its gust response; maneuverability is simply enhanced gust response without the gust. The ability of small birds and

insects to quickly change direction and to achieve extremely high accelerations and decelerations has been observed in nature for thousands of years. Furthermore, flapping wings enable the “bounding” flight pattern seen in small birds. This type of flight is characterized by a short burst of flapping used to produce lift and thrust and push the bird forward and upward. The wings are then folded against the body and the bird continues in a low-drag, ballistic flight pattern until it reaches some minimum height and the cycle repeats. This type of flight could be a viable alternative to standard cruise flight pattern of conventional aircraft because it enables the bird (or MAV) to cover a large distance in a relatively short period of time with minimum energy expenditure. The ability to maintain a specific position in the air holds innumerable advantages over the more common loitering flight pattern used to maintain a position in a general area. While conventional planforms can be made to hover if given large prop/rotors, the power requirements are relatively high and the unstable nature of the “prop hanger” flight mode makes sustained hover difficult. Flapping wing flight vehicles are less restricted in this respect and MAV designs based around flapping wings are more conducive to sustained hover capability.

Flapping flight is more complicated than flight with fixed wings. For fixed wings the forward flight relative to the air causes the wings to produce lift. However, in biological flight the wings not only move forward relative to the air, but they also flap up and down, plunge, and sweep. Shyy et al. [3] note that, to attain the appropriate effective angle of incidence throughout the entire wing-stroke, the wings must constantly twist. In general the downstroke is the most valuable part of the flapping-

cycle, where the wings are fully extended, producing both lift and thrust at the same time. During the upstroke the wings are partly flexed (the outer part of the wing is folded towards the body of the bird) to reduce the moment of inertia and drag of the wings (i.e. to mitigate the negative effects of the upstroke). While flapping, birds systematically twist their wings to produce an aerodynamic effect similar to that produced by the ailerons on the wings of conventional airplanes. Specifically, one wing is twisted downward (pronated), thus reducing the angle of attack and the corresponding lift, while the other wing is twisted upward (supinated) to increase the angle of attack and therefore the lift. With different degrees of twisting between wings, the resulting force also enables a bird to roll. In order for a bird to be able to deform and twist its wings, an adaptation in the skeletal and muscular systems is required. The key features that seem desirable are: modification and reversal of camber between upstroke and downstroke, twisting, area expansion and contraction, and transverse bending. To perform these functions, birds have a bone structure in their wings somewhat similar to the one in a human arm, and muscles, which change the relative positions of these bones. However, birds have more stringent muscle and bone movement during flight.

The main aim of the studies in flapping motion is to investigate the physics and underlying mechanisms of flapping wings and therefore to have an idea about the generation of aerodynamic forces. The physics of the flapping motion can be extracted from the simplified configurations and the relevant information can be supported by numerical models. The aim of this study is to explore the aerodynamic mechanisms and vortex dynamics underlying the flapping motion by using numerical methods

such as direct numerical simulation tools and experimental techniques by using the Particle Image Velocimetry (PIV) technique.

1.2 Objective and Outline of the Present Study

This thesis is aimed at identifying and understanding the underlying aerodynamic mechanisms in flapping motion that are responsible for the generation of aerodynamic forces. In a recent study conducted by Kurtuluş [4] in the Aerospace Engineering Department of METU, hovering flapping motion was analyzed for a symmetrical two-dimensional airfoil. The present work is based on this recent study and is extended to the analysis of different airfoil profiles with different thickness and camber distribution. An experimental setup is built in the Aerospace Engineering Department of METU, for the experimental visualization of flow fields using the Particle Image Velocimetry (PIV) technique which is similar to the one used in the thesis study of Kurtuluş [4] in ENSMA, Poitiers, France. The numerical studies are extended to cover the three-dimensional analysis of flapping motion in hover and the experimental work is pushed to the visualization process of a three-dimensional wing geometry. Numerical and experimental results are thereafter compared with each other qualitatively and the flow fields are investigated for vortex regions.

The present study is organized in 9 chapters. Chapter 1 reviews the background of flapping motion and the importance of the phenomena for

the application of Micro air Vehicles, presenting the scope and the outline of the present study are also given in this chapter.

The second chapter describes the novel definitions and the related aerodynamic parameters of flapping motion. The third chapter, Chapter 3 reviews the previous studies conducted by several researchers.

The experimental setup and the experimental procedure used in the study are described in Chapter 4. The experimental analysis is conducted using Particle Image Velocimetry technique and the principles of this technique are given in this chapter. Since the most important phenomena of flapping motion is vortex formation and evolution, the methods that are used for the identification of vortices which thereafter used to compare the experimental and numerical work are also described in this chapter.

In Chapter 5, two-dimensional numerical simulation of flapping motion analysis is presented. The numerical simulations are carried out using commercially available finite-volume flow solvers, STAR-CD and Fluent. Different parameters are concerned during the simulation of two-dimensional flapping motion but the study concerns about the physical parameters instead of kinematical ones. Effect of profile thickness is studied on symmetrical NACA airfoils having different maximum thickness values. The parametric study is then extended to cambered profiles and the effect of camber is studied comparing the symmetric profile NACA 0012 and NACA 6412 profile both having the same maximum thickness value. NACA 6412 profile combines the symmetrical 0012 cross-section with a mean camber line having maximum 6%

thickness at the 40 % chord location. The study on the camber effect is then extended to cover the profiles Eppler and Göttingen airfoils. The aerodynamic force coefficient variations are compared with each other. The vortex regions of these profiles are investigated at specified set angle of attack.

Chapter 6 presents the two-dimensional experimental investigation of flapping motion carried out for the cambered airfoil profile, NACA 6412. The experiments are carried out for a Reynolds number of 1000 and for the set angle of 45° . The experimental results are then compared to those obtained from the numerical solutions of the two-dimensional flapping motion.

In Chapter 7, the three-dimensional numerical investigation of flapping motion is presented. The numerical simulations are performed on the finite wing configuration of NACA 6412 having a wingtip based on the revolving of mean camber line of the two-dimensional cross-section. The Reynolds number is taken as 1000 and the set angle of attack equals to 45. The wing is rectangular and there is no taper. The simulations are performed assuming that the wing is attached to a symmetry plane at the root section and the aspect ratio of the half wing is taken as 5. Three-dimensional numerical simulations are done using the finite volume flow solver, Fluent in a parallel environment. The results are compared to two-dimensional solutions again obtained using Fluent.

The results for the three-dimensional experimental investigation of flapping motion are presented in Chapter 8. The experimental

measurements are done four different spanwise locations and the spanwise evolution of vortex regions is analyzed. The experimental results are compared to three-dimensional numerical solutions as well as two-dimensional solutions.

The last chapter, Chapter 9 is dedicated to conclusions of the study. Some ideas for the future studies are also given in this last chapter.

CHAPTER II

THEORY OF FLAPPING WING MOTION MECHANISM

This chapter gives a brief review of the flapping wing motion and tries to describe the aerodynamic mechanisms for the generation of lift and drag during flapping motion in the light of the previous work available in the literature.

2.1 Flapping Motion

The wing stroke of an insect is divided into four phases: two translational phases (upstroke and downstroke), when the wing sweeps through the air with a high angle of attack, and two rotational phases (pronation and supination), when the wing rapidly rotates and reverses its direction of motion.

Previous studies have revealed that there are three main aerodynamic mechanisms responsible for the generation of lift:

- delayed stall,
- rotational circulation (Kramer effect) and
- wake capture.

Moreover, Sane [5] stated the importance and interaction of another unsteady mechanism, called the Wagner effect. Below, these mechanisms will be described briefly .

As stated by Walker [6], when a wing is started impulsively from rest, the circulation around it does not immediately attain its steady state value but instead it rises slowly. Sane [5] explains this delay in reaching the steady state value as the combination of two reasons. First, there is a finite time in the establishment of the Kutta condition. The second, is the generation and shedding of vortices at the trailing edge. Thereafter, the shed vorticity eventually rolls up in the form of a starting vortex during this process. This shedding of vorticity also counteracts the growth of circulation bound to the wing. After the starting vortex has moved sufficiently away from the trailing edge, the wing attains its maximum steady state circulation. This sluggishness in the development of circulation was first proposed by Wagner in 1925 and is often referred as the Wagner effect.

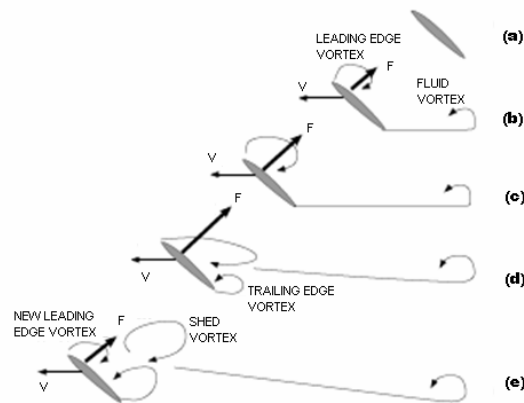


Figure 2.1 Cartoon representation of delayed stall mechanism (adopted from Ref. [7])

The **delayed stall** appears on the onset of the flapping wing definitions of motion of the wing. With reference to Schenato's Ph.D. dissertation, [7] and Figure 2.1, the mechanism is explained as follows: As the wing starts moving, a small vortex appears behind the leading edge, and an asymmetric, opposite swirl appears in the fluid close to the original resting position of the wing (see Figure 2.1 (b)). The presence of two vortices moving in opposite directions but with identical strength is the equivalent principle of conservation of momentum for fluids. The vortex above the wing creates a lower pressure on its leeward surface, thus producing a net aerodynamic force perpendicular to the wing surface. As the wing moves, the vortex behind the leading edge increases along with the aerodynamic force (Figure 2.1(c)). However, after a certain distance, a new vortex starts to appear behind the trailing edge to keep the total fluid momentum constant (Figure 2.1(d)). This vortex has a rotation opposite to that of the

leading edge vortex and in turn decreases the force production. Moreover, the vortex on the leading edge keeps on increasing till it reaches a critical size at which point it detaches from the wing and is shed into the fluid, thus decreasing even further the force production (Figure 2.1(e)). As soon as the leading edge vortex detaches, a new vortex starts to appear behind the leading edge and this process of the vortex building up and detaching repeats itself periodically.

Moreover, Schenato [7] also states that the vortex shedding process appears after the wing has traversed a distance of a few chord lengths; therefore the increased aerodynamic force production can be captured only at the very beginning of the wing movement. Insect wings move only few wing chord lengths when they flap, and thus are able to capture this enhanced force production.

Another very important characteristic of flapping flight is that the wings do not translate but rather rotate about their wing hinges. This means that the velocity of the wing with respect to the fluid is not constant along the wing longitudinal axis, but instead depends on the distance from the wing base. This creates a gradient of translational velocity along the wing axis. Ellington *et al.* [reference] observed the presence of a base-to-tip axial flow entrained by the leading edge vortex, and argued that this property helps the stability of the leading edge vortex. In contrast to the fixed winged vehicles for which large angle of attacks give rise to turbulence, the leading edge vortex is stable for angles of attack up to 90 degrees. The aerodynamic force generated is an increasing function of the angle of attack. The last important difference of delayed stall relative to fixed-wing

vehicles is that the aerodynamic force is almost perpendicular to the wing profile rather than perpendicular to the wing velocity.

The **rotational lift** mechanism is the result of a combination of the translational and rotational motions of the wing as stated by Schenato [7]. This mechanism is analogous to the one that allows a ball to curve when it is thrown with some spin, as commonly observed in baseball or tennis. In fact, an aerodynamic force perpendicular to the translational velocity appears if the ball has a back-spin as shown in Figure 2.2. The magnitude of the aerodynamic force generated by the rotational lift is approximately proportional to the product of the angular velocity and the translational velocity. It should be noted that the rotational lift is perpendicular to the velocity in a rotating ball whereas it is perpendicular to the surface of a rotating wing. Rotational lift is present in flapping flight at the end of each half-stroke when the wing is about to invert its direction of motion.

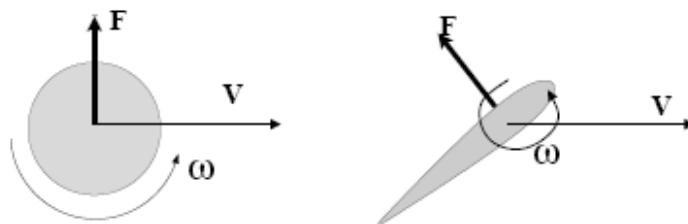


Figure 2.2 Rotational lift for a rotating ball and a rotating wing (from Ref. [7])

Another mechanism observed near the end of every stroke, is the substantial pronation and supination about the spanwise axis of insect wings, which allows them to maintain a positive angle of attack and generate lift during both forward and reverse strokes. The latter is explained by Sane [5] as follows: When a flapping wing rotates about a spanwise axis while translating, flow around the wing deviates from the Kutta condition and the stagnation region moves away from the trailing edge. Due to this reason, a sharp, dynamic gradient at the trailing edge occurs which leads to shear. To re-establish the Kutta condition, additional circulation must be generated around the wing because the fluid tends to resist the shear due to viscosity. Namely, the wing generates a rotational circulation in the fluid in order to counteract the effects of rotation. Note that the re-establishment of Kutta condition is not instantaneous, but do happen in a finite time. If, in this time interval, the wing continues to rotate rapidly, then the Kutta condition may never be actually observed at any instant during the rotation but the tendency of the fluid for the establishment of the Kutta condition may dictate the generation of circulation. Extra circulation proportional to the angular velocity of rotation will continue until the establishment of smooth, tangential flow at the trailing edge. This effect is also called the 'Kramer effect', after M. Kramer who first described it.

The last mechanism to generate lift in flapping motion is the so called **wake capturing mechanism**. It is present at the beginning of each half-stroke after the wing has inverted its motion and started to move. The wake capture, as explained by Schenato [7], appears when the wing interacts with the effects of the previous strokes prevailing in the ambient

fluid. The fluid behind the wing is dragged along with the motion of the wing, as shown in Figure 2.3. As the wing slows down and inverts its direction of motion, it hits the fluid behind which is still moving because of its imparted momentum. Therefore, the velocity of the wing relative to the fluid (which corresponds to $V - W$ using the notation of Figure 2.3) is larger than the velocity of the wing alone, and therefore results in the generation of a larger force. This is a simplified explanation of wake capture phenomenon.

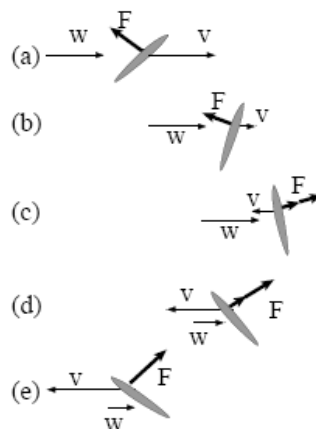


Figure 2.3 Cartoon representation of wake capture mechanism. (V and W indicate the velocity of the wing and of the fluid wake relative to an inertial frame, respectively. Resultant velocity of the wing relative to the fluid is given by $V_{\text{tot}} = V - W$.) (From Ref. [7])

As stated in literature, delayed stall is the main mechanism that accounts for the majority of the aerodynamic force production and that the

rotational lift and wake capture are present only for very short periods of the stroke when the wing rotates and changes direction of motion. Although these two mechanisms contribute only marginally to the mean lift, they play an important role in flight control since they can affect the distribution of forces.

These three lift generation mechanisms described above have also been investigated by other researchers like Hall [8]. Data collected from a robofly allowed the calculation of the total force vector with its direction designated as red arrows and its magnitude with blue arrows as shown in Figure 2.4.

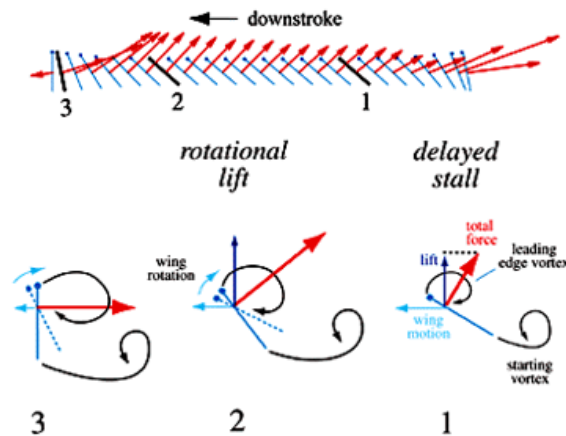


Figure 2.4 Schematic representation of downstroke phase (from Ref. [8])

As shown in Figure 2.4 , as a fly moves from right to left during the downstroke phase, blue arrows indicate the direction of wing movement and red arrows indicate the direction and magnitude of the forces generated in the stroke plane. During this phase, the insect uses two mechanisms for lift generation. Delayed stall **(1)** causes the formation of a leading-edge vortex that reduces the pressure over the leeward side of the wing surface. Rotational lift **(2)** is created when the insect rotates the angle of its wings (*dotted line*), creating a vortex similar to that of putting "backspin" on a tennis ball. At its completion **(3)**, the maneuver also results in a powerful force propelling the insect forward.

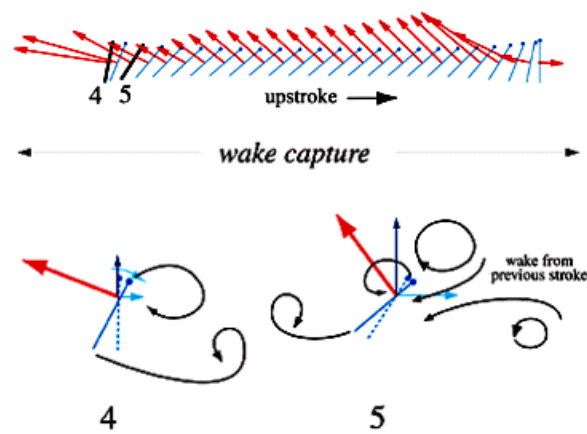


Figure 2.5 Schematic representation of upstroke phase (from Ref. [8])

During upstroke, shown in Figure 2.5, as the insect drives its wing upwards, it uses the so called wake capture mechanism to generate lift.

This gives the insect an extra added lift by recapturing the energy lost in the wake. As the wing moves through the air, it leaves vortices behind it (4). If the insect rotates its wing (*dotted line*), the wing can intersect its own wake and capture some of its energy in the form of lift (5).

The purpose of the present work conducted in this thesis is to demonstrate some of these lift generation mechanisms by numerical and experimental techniques. It is intended that the leading and trailing edge vortices will be put into evidence by using the Direct Numerical Simulation (DNS) tool and the Particle Image Velocimetry (PIV) technique to picture the total flow field with the shed vortices while simulating the planar wing motion for down and up strokes. The evolution and merger of these vortices during different phases of the flapping motion will then be compared and an explanation will be brought to the lift generation mechanism in the light of the previous discussions.

2.1.1 Hovering

Hovering is a particular mode of flight where the body is fixed in space with zero free stream velocity, as is defined in Ames's work [1]. The motion of fluid is present due to the motion of the wings. The main effect in hover is the generation of vertical force balancing the weight. The ability to hover depends on the size of a bird or insect, moment of inertia of the wings, degrees of freedom in the movement of the wings and the wing shape. Therefore, hovering is mainly performed by small birds, like hummingbirds and insects. There are two types of hovering motion:

symmetrical hovering described by Weis-Fogh and asymmetrical hovering described by Norberg.

Symmetrical hovering which is also called the normal or true hovering is performed by insects and hummingbirds. Ames [1] states that these animals hover with fully extended wings during the entire wing beat cycle. Generation of lift occurs during the entire wing stroke, except at the reversal points. The wings are rotated and twisted during the backstroke so that the leading edge of the wing remains the leading edge throughout the cycle, but the upper surface of the wing (lee ward side) during the forward stroke becomes the lower surface (wind ward side) during the backward stroke. While hovering, the body axis is inclined towards the horizontal plane and the wing movements describe a figure of a lying eight in the vertical plane.

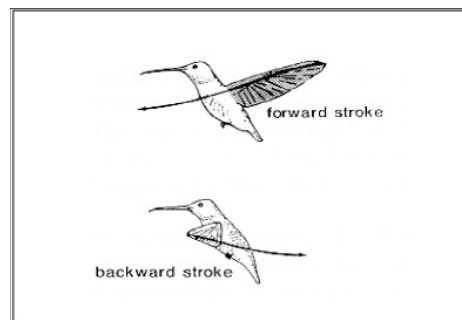


Figure 2.6 Symmetrical hovering of a hummingbird (from Ref. [1])

Ellington [9] notes that the amplitude of wing rotation during pronation and supination is large, enabling the wings to operate at an angle of attack favorable for lift on both morphological downstroke and upstroke [9].

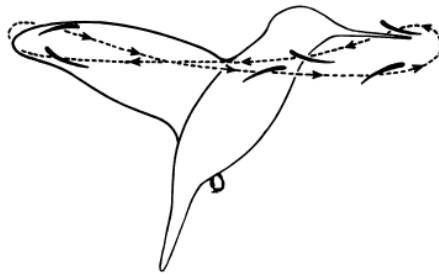


Figure 2.7 The wing tip path of a hummingbird viewed from side, illustrating a horizontal stroke plane (from Ref. [9])

Symmetrical hovering is used by birds which are not able to rotate their wings. To avoid large drag forces and negative lift forces, these birds flex their wings during the upstroke as Ames notes [1]. Also the tip feathers are rotated to let the air through during the upstroke which means that the lift is produced to balance the weight of the animal is mostly generated during the downstroke. To compensate for the absence of lift during the upstroke, the wings have to reach a higher lift coefficient that is attainable in the steady state.

Hovering of birds and bats are investigated by Ellington [9]. They partially flex their wings during the upstroke, however, and the individual

primaries (tip feathers) are also rotated to a negligible angle of attack. Any lift on the upstroke of an inclined stroke plane would produce a large horizontal thrust component, and this is probably the explanation for insignificant upstroke lift. The mean force generated during the downstroke is primarily responsible for mass support.

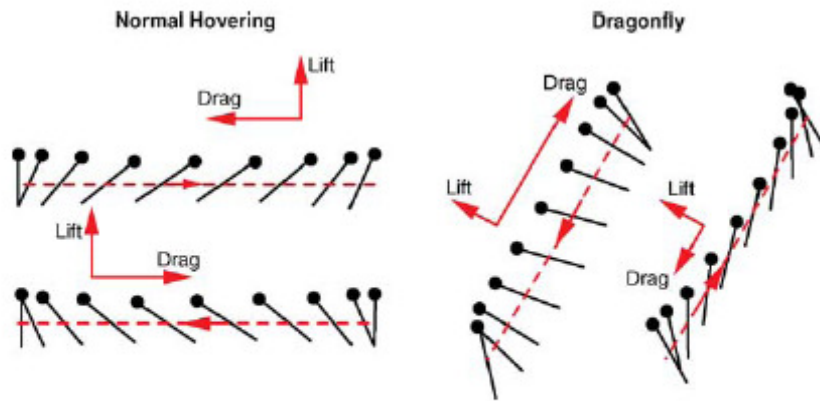


Figure 2.8 The schematic representation of two hovering styles: normal hovering using a horizontal stroke plane (left) and hovering using an inclined stroke plane (right) (from Ref. [5])

2.1.2 Clap and fling mechanism

The “clap and fling” mechanism” was explained by Weis-Fogh and Lighthill. Also, from a series of experiments using simplified mechanical models, explanation of the “clap and fling” mechanism for the generation of large lift coefficients by insects in hovering flight are suggested by Maxworthy [10]. Vortex motion and in particular the motion of vortex pairs and rings are a central concern in any description of the dynamics of hovering flight

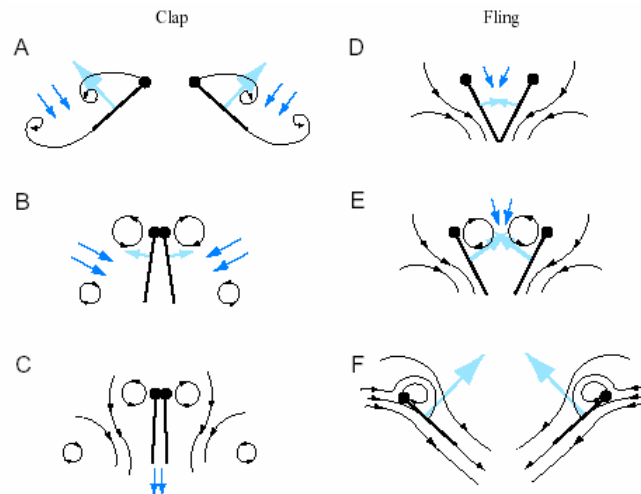


Figure 2.9 Clap-Fling mechanisms: wings approaching each other to clap (A–C) and flinging apart (D–F). Black lines show flow lines, and dark blue arrows show induced velocity. Light blue arrows show net forces acting on the airfoil (from Ref. [5]).

CHAPTER III

LITERATURE SURVEY

Flapping motion has been studied by many researchers. These studies cover a very wide range of parameters investigating the flapping motion of real birds and insects realized by using the numerical approaches and the experimental techniques as well as simplified generic configurations of wings simulating simplified flapping motion in hover. In literature flapping motion is investigated by using either the experimental techniques or the numerical methods and the results of these methods are compared with each other. This chapter is devoted to a brief review of all the previous work done in literature and to determine the gaps where the present numerical and experimental study could make a contribution.

3.1 Review of Numerical Studies

Aono and Liu [11] conducted a multi-block and overset grid-based computational fluid dynamics (CFD) study for the unsteady flows about a realistic body-wing model and the force-generation in the flapping flight of the hawkmoth hovering, based on the real flight data of a hawkmoth. The computed results demonstrated the presence of interaction among the leading-edge vortex (LEV), the trailing-edge vortex (TEV) and the wing tip vortex (TV), and hence quantified the roles of these vortices in aerodynamic force-generation.

The wing motion in free flight has been described for insects ranging from 1 mm to 100 mm wingspan. In the work conducted by Ellington [12], it is stated that in order to support the body weight, the wings typically produce 2–3 times more lift than can be accounted for by any conventional aerodynamics. It is also stated that to support a given mass, larger machines need less power, but smaller ones operating at higher frequencies will reach faster speeds.

Wang [13] gave a brief history of research in insect flight and discussed recent findings in unsteady aerodynamics of flapping flight at intermediate range of Reynolds numbers (10 – 10^4). He examined the unsteady mechanisms in uniform and accelerated motions, during forward and hovering flight, as well as passive flight of free-falling objects.

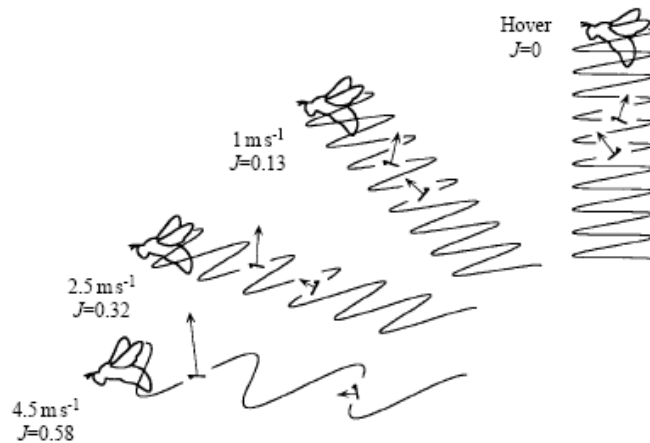


Figure 3.1 A two-dimensional view of the wingtip path for a bumblebee *Bombus terrestris* at different flight speeds. Resultant aerodynamic forces are shown for representative downstrokes and upstrokes. The anatomical lower wing surface is marked by a triangle at the leading edge. Wing beat frequency and stroke amplitude did not vary significantly with speed, and values of the advance ratio J are calculated using their means (from Ref. [12]).

Wang [14-15] solved the Navier-Stokes equations in elliptical coordinates for an elliptical wing in order to quantify the vortex dynamics that is essential for hovering and to identify a minimum two dimensional model that produces sufficient lift. The majority of insects, including dragonflies, hawkmoths, and fruit flies, employ a superposition of heaving and pitching motion to hover, sometimes referred to as a figure-eight motion. The vortex dynamics further elucidates the role of the phase relation between the wing translation and rotation in lift generation and explains why the instantaneous forces can reach a periodic state after only a few strokes. Wang [16] also implemented and tested the computational tool to

resolve the time-dependent vorticity and forces in unsteady viscous flows around a moving wing.

Streitlien and Triantafyllou [17] presented a numerical model under the assumption of two-dimensional ideal flow comparing exact average thrust and mean-flow momentum flux in the wake, and allowed two simple models for the wake, based on the linear foil theory and the Karman vortex street.

In 2002, Taylor and Thomas [18] analyzed the stability of flapping flight which has never been properly analyzed. Stability is essential to flying and is usually assumed to be problematic in flapping flight. Contrary to expectations, they have found that there is nothing inherently destabilizing about flapping: beating the wings faster simply amplifies any existing stability or instability, and flapping can even enhance stability compared to gliding at the same airspeed. This suggests that aerodynamic stability may not have been a particular hurdle in the evolution of flapping flight.

Hovering animals, like hovering helicopters, are predicted to possess neutral static stability. Flapping animals, like fixed wing aircraft, are predicted to be stable in forward flight if the mean flight force acts above and/or behind the centre of gravity. In this case, the downstroke will always be stabilizing [18].

Experiments were performed on an oscillating foil to assess its performance in producing large forces for propulsion and effective maneuvering by Read et al. [19]. Propulsive and maneuvering tests on an oscillating NACA 0012 foil provided systematic data on the thrust and side force production in harmonically flapping foils.

Watts et al. [20] modeled the wing mechanics of bat flight in level flight. They investigated the wing in a series of chordwise segments and calculated the magnitude of segmental aerodynamic forces assuming an elliptical, spanwise distribution of circulation at the middle of the downstroke. They have found that there was an order of magnitude difference between the lift coefficient and the thrust coefficient.

Wang and Sun [21] studied the aerodynamics and forewing–hindwing interaction of a model dragonfly in forward flight using the method of numerically solving the Navier–Stokes equations. Available morphological and stroke-kinematic parameters of dragonfly (*Aeshna juncea*) were used for the model dragonfly.

Zuo et al. [22] conducted a computational fluid dynamics (CFD) analysis to study the unsteady aerodynamics of a virtual flying bumblebee during hovering flight. Sun and Tang [23] conducted a computational fluid-dynamic analysis to study the unsteady aerodynamics of a model fruit fly wing. In both of these studies the solution of Navier-Stokes equations provided the velocity and pressure fields, from which the aerodynamic forces and vorticity wake structure were obtained. Insights into the

unsteady aerodynamic force generation process were gained from the force and flow-structure information.

Miller and Peskin [24], [25] used the immersed boundary method to solve the two-dimensional Navier–Stokes equations for two immersed wings performing an idealized ‘clap and fling’ stroke and a ‘fling’ half-stroke. Lift coefficients were calculated as functions of time per wing for a range of Reynolds numbers (Re) between 8 and 128. The instantaneous streamlines around each wing throughout the stroke cycle were calculated and related to the changes in lift and to the relative strengths and positions of the leading and trailing edge vortices. They showed that the lift generated by each wing during the ‘clap and fling’ of two wings when compared to the average lift produced by one wing with the same motion falls into two distinct patterns. Their results suggested that the Weis-Fogh mechanism of lift generation had greater benefit to insects flying at lower Re . Drag coefficients produced during fling are also substantially higher for the two-winged case than the one-winged case, particularly at lower Re .

Lewin and Haj-Hari [26] presented a numerical model for the two-dimensional flow around an airfoil undergoing a prescribed heaving motion in a viscous flow. The flow characteristics and the power coefficients were found for both periodic and aperiodic solutions. Additionally, some flows are asymmetric in that the upstroke is not a mirror image of the downstroke. The importance of viscous effects for low-Reynolds-number flapping flight were also discussed.

Smith et al. [27] contributed to the research of flapping wing aerodynamics and to the problem of lacking of an adequate method accomodating large-scale trailing edge vortices. The advantages of unsteady panel methods are introduced and illustrated by modelling the flapping wings of a tehered sphingid moth. The results are compared to those obtained from quasi-steady method.

Ramamurti and Sandberg [28]-[30] presented the numerical solution of three-dimensional flow past a three-dimensional *Drosophila* wing undergoing flapping motion by finite element method. The computed thrust and drag forces were compared to the results obtained from previous experimental studies. Grid independence study was also conducted to validate the computational results, and a grid-independent solution was obtained. The same solver was used to solve the viscous flow past a NACA 0012 airfoil at various pitching frequencies. They investigated the thrust generating mechanism of a flapping foil undergoing pitching and pitching and heaving motions at very low Reynolds number.

Sun and Tang [31] studied the lift and power requirements for hovering flight in *Drosophila virilis* using the computational fluid dynamics method. They solved the flow field numerically to obtain the velocity and pressure fields, and calculated the aerodynamic forces and moments. On the basis of the aerodynamic forces and moments and the inertial torques, the lift and power requirements for hovering flight were obtained.

Sun and Wu [32] carried out a CFD study on a modeled wing motion of a fruit fly in a forward flapping motion to obtain the aerodynamic force generation and power requirements.

Bozkurttaş et al. [33] conducted a numerical study in which a DNS/LES solver has been developed that is capable of simulating flapping flows in all their complexity. They tried to resolve the vortical features in the flow, which primarily determined the thrust and efficiency of the flapping foils.

Wu and Sun [34] solved the Navier-Stokes equations to obtain the unsteady aerodynamic forces on a flapping wing at a Reynolds number of 200. They have showed that the forces were dependent on dimensionless parameters such as; Reynolds number, stroke amplitude, mid-stroke angle, non-dimensional duration of wing rotation and rotation timing. One of the main conclusions from this study was that the large coefficients were due to the delayed stall mechanism.

Insect wing motion is inherently three-dimensional, and involves significant deformation of the elastic wing structure from the anchor at the insect thorax to the wing tip. Eldredge [35] described a viscous vortex particle method for the direct numerical simulation of the flow produced by an arbitrarily moving two-dimensional body. By applying this method he investigated a pitching and plunging elliptical wing at Reynolds number of 550.

Sun and Yu [36] conducted a CFD study to solve the Navier-Stokes equations using the method of moving overset grids to obtain the solution

of a hovering flight of a tiny insect, *Encarsia formosa*, at Reynolds number of 15. They found that the fling produced a large lift peak at the beginning of the downstroke whereas the clap produced a large lift peak near the end of the subsequent upstroke. The calculated mean lift was enough to support the weight of the insect.

The influence of different wing kinematic models on the aerodynamic performance of a hovering insect was investigated by means of two-dimensional time dependent Navier-Stokes simulations by Bos et al [37]. To simulate the flow around moving wings with predefined motions, a commercial CFD solver Fluent v6.1.22 was used. They considered a harmonic model, a Robofly model and two more realistic fruit fly models, all dynamically scaled at $Re = 110$. They had studied the vortex dynamics in detail as well as the resulting lift and drag forces.

Kaya [38] and Kaya and Tuncer [39]-[40] studied the thrust generation and path optimization of flapping foils in pitch and plunge. The numerical study that has been conducted covers the viscous unsteady solutions of Navier-Stokes equations in parallel.

3.2 Review of Experimental Studies

Experimental studies involve different approaches to explain the mechanisms of flapping motion. Ellington [9] examined the aerodynamics of hovering insect flight in a series of papers to evaluate the quasi-steady

and unsteady aerodynamic mechanisms. The second and third papers of the series presented complete data sets for variety of insects to be used in the following studies [41]-[42]. In the fourth paper, Ellington [43] combined theoretical considerations and available experimental studies on the aerodynamic mechanisms of lift generation in hovering animal flight. In the fifth paper of the series, Ellington [44] presented a full derivation of the vortex theory of hovering flight outlined in previous reports. The theory related the lift produced by flapping wings to the induced velocity as well as to the power of the wake. The last paper of Ellington [45] investigated the lift and power requirements for hovering insect flight that were estimated by combining the morphological and kinematical data from papers II and III with the aerodynamic analyses of papers IV and V.

Many researchers studied the aerodynamic forces and wing kinematics of flapping motion on robot fliers. Dickinson et al. [46] performed an experimental study to measure the aerodynamic forces on a robot fly at low Reynolds number regime covering a range of Reynolds number from 8 to 500. The experiments were conducted in a tank filled with mineral oil to match the experimental Reynolds number to that of a typical *Drosophila*, $Re=136$. They tried to explain the aerodynamic mechanisms that lie behind the motion of the robot wings.

Lehmann et al. [47] employed a dynamically scaled mechanical model of the small fruit fly *Drosophila melanogaster* (Reynolds number 100–200) to investigate the force enhancement due to contralateral wing interactions during stroke reversal (the ‘clap-and-fling’). Moreover, Digital Particle Image Velocimetry (DPIV) technique was used during clap-and-fling and

showed that the most obvious effect of the bilateral ‘image’ wing on flow occurs during the early phase of the fling, due to a strong fluid influx between the wings as they separated.

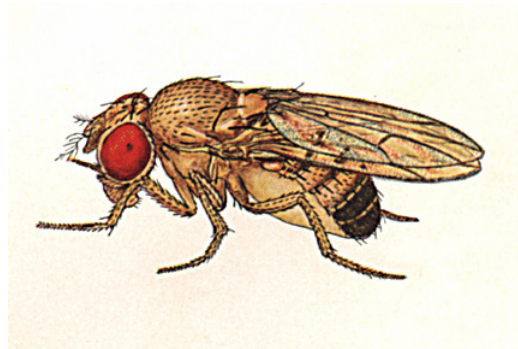


Figure 3.2 Picture of male *Drosophila melanogaster* (from Ref. [48])

Fry et al. [49] used 3D infrared high-speed video to capture the continuous wing and body kinematics of free-flying fruit flies, *Drosophila melanogaster*, during hover and slow forward flight. The wing kinematics are then replayed on a dynamically scaled robot model to measure the aerodynamic forces produced by the wings and the instantaneous forces, torques and power for a detailed analysis of hovering aerodynamics were estimated directly. The time-resolved aerodynamic forces were compared to a multi-component quasi-steady model, which predicted the time course and magnitude of measured forces with reasonable accuracy.

Dickson and Dickinson [50] used a dynamically scaled robot model of the fruit fly *Drosophila melanogaster* to investigate the forces produced by a wing revolving at constant angular velocity while simultaneously translating at velocities appropriate for forward flight. The amplitude and offset of the relationships of lift and drag coefficients are not constant, but depend upon the velocity profile experienced by the wing. A modified quasi-steady model that can account for the varying magnitudes of the lift and drag coefficients was developed which may also resolve the discrepancies in past measurements of wing performance based on translational and revolving motion.



Figure 3.3 An adult *Manduca sexta* (from Ref. [52])

Bomphrey et al. [51] presented the first Digital Particle Image Velocimetry (DPIV) analysis of the flow field around the flapping wings of an insect (the tobacco hawkmoth *Manduca sexta*). Detailed DPIV measurements showed that towards the end of the downstroke, the LEV structure is

consistent with that recently reported in free-flying butterflies and dragonflies: the LEV was continuous across the thorax and ran along each wing to the wingtip, where it inflected to form the wingtip trailing vortices.

Birch and Dickinson [53] used two-dimensional DPIV to visualize flow patterns around the flapping wing of a dynamically scaled robot for a series of reciprocating strokes starting from rest and the pattern of fluid motion was directly compared with the time history of force production.

Hedrick et al. [54] used a combination of high-speed 3-D kinematics and three-axis accelerometer recordings obtained from cockatiels flying in a low-turbulence wind tunnel in a broad range of flight speeds (1–13 m/s). The goals were to investigate the variation in instantaneous aerodynamic force production during the wing beat cycle of birds flying across a range of steady speeds, testing two predictions regarding aerodynamic force generation in upstroke and the commonly held assumption that all of the kinetic energy imparted to the wings of a bird in flapping flight is recovered as useful aerodynamic work.

Usherwood et al. [55] presented a novel experimental approach for determining the contributions of the wings and tails of pigeons in slow flight to weight support, and their aerodynamic power requirements. With simple kinematic measurements of orientation and velocity, the aerodynamic power requirements associated with aerodynamic forces on wings and tails could be calculated.



Figure 3.4 Rock pigeon in flight (from Ref. [56])

Hover et al. [57] used a NACA 0014 airfoil in a water tank to measure the forces and the torques acting on the airfoil at a Reynolds number of 30 000. The thrust and efficiency of harmonically heaving and pitching foil was studied for four different airfoil profiles concluding that the cosine angle of attack achieved a significant improvement over the other three cases resulting in high thrust values with reasonable efficiency.

Dickinson and Götz [58] tried to fill the deficit due to sparse data in low Reynolds number regime by quantifying the time-dependence of aerodynamic forces for a simple motion. The study covered the measurement of lift and drags on a two-dimensional model as well as simultaneous flow visualization aimed at the characterization of time-dependency of the forces produced by impulsively started wings and thereby expanded the knowledge of unsteady mechanisms that might be employed by insects during flight.

Recent work on flapping hawkmoth models conducted by Usherwood et al. [59]-[60] demonstrated the importance of a spiral 'leading-edge vortex' created by dynamic stall, and maintained by some aspect of spanwise flow, for creating the lift required during flight. They also investigated high force coefficients, similar to those observed for revolving model hawkmoth wings in the accompanying paper (for which steady leading-edge vortices are directly observed), are apparent for revolving model (mayfly, bumblebee and quail) and real (quail) animal wings for Reynolds numbers (Re) ranging from 1100 to 26 000. Results for bumblebee and hawkmoth wings agreed with those published previously for *Drosophila* ($Re \sim 200$).



Figure 3.5 Hummingbird Hawkmoth (*macroglossum stellatarum*) (from Ref. [63])

Willmott and Ellington [61] used a high-speed videography to record the sequences of individual hawkmoths in free flight over a range of speeds from hovering to 5 m/s. The following paper published by Willmott and Ellington [62] addressed the calculation of mean lift coefficients for hawkmoth flight at a range of speeds in order to investigate the aerodynamic significance of kinematic variation which accompanies changes in forward velocity.

Warrick et al. [64] used DPIV to visualize the flow field around the wake of a hovering hummingbird, *Selasphorus rufus*. The results showed that the forces were asymmetric: hummingbirds produce 75% of their weight support during the downstroke and only 25% during the upstroke. The wake of hummingbird wings also reveals evidence of leading-edge vortices created during the downstroke, indicating that they may operate at Reynolds numbers sufficiently low to exploit a key mechanism typical of insect hovering.



Figure 3.6 Rufous Hummingbird (*Selasphorus rufus*) (from Ref. [65])

Dickinson et al. [66] investigated the temporal control of a fast wing rotation in flies, the *ventral flip*, which occurs during the transition from downstroke to upstroke. The results they have obtained raised issues at both aerodynamic and neurobiological levels to answer the questions of the responsibility of flight musculature for steering movements independently control flip timing and wing beat amplitude and the interaction of these behaviors in the production of aerodynamic forces.

Birch et al. [67] studied the flow structure around the wing while the wing translated at 45° angle of attack with the use of a dynamically scaled robot and DPIV, they have quantified both the forces and fluid motion around an insect wing flapping at $Re=120$ and $Re=1400$. The results suggest that the transport of vorticity from the leading edge to the wake that permits prolonged vortex attachment takes different forms at different Re .

Sane and Dickinson [68] used a dynamically scaled model insect to measure the rotational forces produced by a flapping insect wing. They tried to characterize the effects of wing rotation on aerodynamic force generation under conditions that are appropriate for analysis of insect flight.

Birch and Dickinson [69] investigated the spanwise flow and the attachment of leading edge vortex in insect wings. The flow structure that is largely responsible for the good performance of insect wings has recently been identified as a leading-edge vortex. But because such vortices become detached from a wing in two-dimensional flow, an

unknown mechanism must keep them attached to (three-dimensional) flapping wings.

A three dimensional flow visualization of a hovering hawkmoth was studied in detail by Van den Berg and Ellington [70]-[71]. They studied the flow pattern of the three-dimensional flow field and the vortex wake on a dynamically scaled robot insect, “the flapper” that accurately mimicked the wing movements of a real hovering hawkmoth. Visualization of the flow field had been done by smoke release from the leading edge of the flapper wing and they confirmed the existence of a small, strong and stable leading-edge vortex, increasing in size from wing base to wing tip. They showed that the leading-edge vortex had a strong axial flow velocity which stabilized it and reduced its diameter.

Combes and Daniel [72] used an experimental approach to examine the relative contributions of inertial-elastic and fluid-dynamic forces to passive wing bending. They attached fresh *Manduca sexta* wings to a motor and flapped them around the dorsal-ventral axis of the wing hinge at a realistic wing-beat frequency and stroke amplitude, mimicking the large amplitude motions of freely flying moths.

Lu et al. [73] presented the physical images revealing the internal flow structures and their evolutions of dragonfly hovering based on the dye flow visualization conducted on an electromechanical model in water tunnel. From the qualitative information derived from the images, they found that spanwise flow was conspicuous regardless of the large aspect ratio of the wing.

3.3 Review of Numerical and Experimental Studies

Liu [74] proposed a new paradigm, *simulation-based biological fluid dynamics*, by directly solving the full Navier-Stokes equations through computer simulations. The paradigm is an integrated computational system, involving a morphological modeling subsystem, a kinematic modeling subsystem, a CFD modeling subsystem, and a post-processing subsystem for visualization. The method is tested on a realistic moth's model and address an overall understanding of the complicated vortex structures around a 3D flapping wing during the complete cycle of translational and rotational motions, as well as the corresponding time course of instantaneous force-production.

Sane [75] aimed to estimate the magnitude of gross flows around an insect body using the near-field approach and discuss their biological importance. In the first part of the work, she presented a derivation of induced airflow using helicopter (or rotor) theory and a blade element momentum approach modified for application to hovering insects. This model was used to predict the magnitude of mean self-generated air flow in flying insects. In the second paper, Sane and Jacobson [76] tested some of the theoretical predictions *via* systematic measurements of the magnitude of self-generated airflow along the insect body using hot-wire anemometry and showed that in addition to the mean induced flow predicted by the theory outlined here, there were additional higher frequency components due to flapping wing motion.

Wang et al. [77] compared computational, experimental and quasi-steady forces in a generic hovering wing undergoing sinusoidal motion along a horizontal stroke plane using Digital Particle Image Velocimetry (DPIV) technique. They investigated unsteady effects and compared two-dimensional computations and three-dimensional experiments in several qualitatively different kinematic patterns. They noted that the steady state two-dimensional forces underpredicted the three-dimensional forces whereas the transient two-dimensional forces were much closer to the actual three-dimensional forces.

Kurtuluş [4] studied the hovering flapping motion on a symmetrical airfoil both numerically and experimentally. The numerical laminar flow field is solved using a commercial flow solver, STAR-CD and the results were compared to experiments obtained from Particle Image Velocimetry technique.

The present work is an extension of the work done by Kurtuluş [4]. The experimental investigations are done with a 3 dimensional stereoscopic Particle Image Velocimetry (PIV) technique to look into the spanwise 3 Dimensionality effects of the Leading Edge (LEV) and Trailing Edge Vortices (TEV) created during flapping motion in hover. For present experiments an experimental set-up similar to that of Kurtuluş [4] was constructed comprising of a large tank filled with water and a two dimensional and a three dimensional wing model translated inside the tank with a prescribed flapping motion. The wing models were manufactured from transparent acrylic such that the laser plane cutting the wing could also illuminate the forward field of the wing as well as its

wake plane. For two dimensional measurements the measurements are realized at the mid plane of the two dimensional wing model supported by end plates. For three dimensional wing measurements the wing had no end plates and the aspect ratio of the wing was 5. The wing was supported by only one end plate and the other tip of the wing was free without end plates. This way it was possible to investigate the spanwise variation of the vortical flow structure over the wing's leeward and the windward sides.

For numerical investigations Direct Numerical Simulation technique is used to visualize the complete flow field. Time dependent Navier Stokes equations are solved for laminar flow therefore no turbulence modeling was required. Commercial flow solvers, "Star CD" and "Fluent" were used to solve the 2D and 3D flow fields respectively using the parallel solving capability of the later solver. Various parameters such as the thickness and the camber of the profiles are investigated. A prescribed flapping motion was imposed on the wing and the resulting flow field in terms of the Leading Edge (LEV) and the Trailing Edge (TEV) vortices and the rotational vortices are investigated.

The results of numerical calculations and experimental measurements are compared to each other in terms of the flow field topology and similarities and any discrepancies between them are explained with reference to the physics of the problem.

CHAPTER IV

EXPERIMENTAL SETUP

This chapter will describe the experimental setup in detail and the experimental procedures followed during the experiments.

4.1 Experimental Setup

The experimental set-up built at Aerospace Engineering Department of Middle East Technical University is very similar to the set-up established at Ecole Nationale Supérieure de Mécanique et d'Aérotechnique at Poitiers France, within the scope of the joint PhD thesis of Kurtuluş [4]. Experiments are carried out in a 1m x 1m x 1.5m water tank made of altuglass. The tank is filled with water. The water inside the tank is still and the wing model is translated by a translational mechanism placed above the tank. The wing model is placed between two plexi-glass end-plates each of which is 90 cm long and 50 cm wide and the distance between the plates is 50 cm which is also the total span of the 2D wing.

The chord length of the 2D wing is 6 cm and is placed between these two end-plates for two-dimensional flow measurements. The model and the endplates assembly are translated together by an accurate translational mechanism placed above the tank. The model is set to rotate about its center of rotation point which is placed at $1/4c$. The whole experimental setup is shown in Figure 4.1.

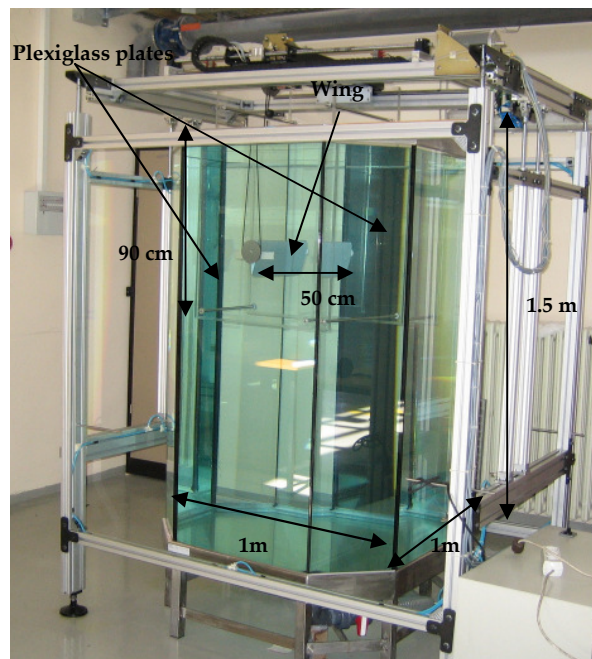


Figure 4.1 Experimental setup with water tank.

The experimental setup has two step motors. The first one drives a power screw to give the translational motion to the wing and end plates assembly. The second step motor is used for the rotation of the wing at the end of the down and up strokes. The resolutions of the step motors basically determine the translational and the rotational accuracies achieved during the experiments. There is ± 0.5 degree error in the calculation and setting of the angles and the program is accurate to second digit after the decimal point.

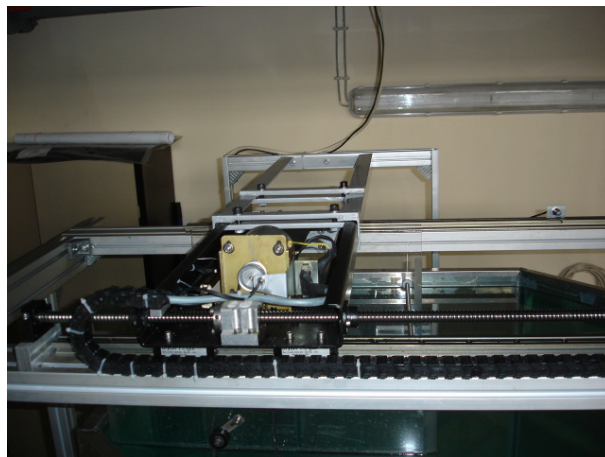


Figure 4.2 Upper mechanism for translational and rotational motions of the experimental setup

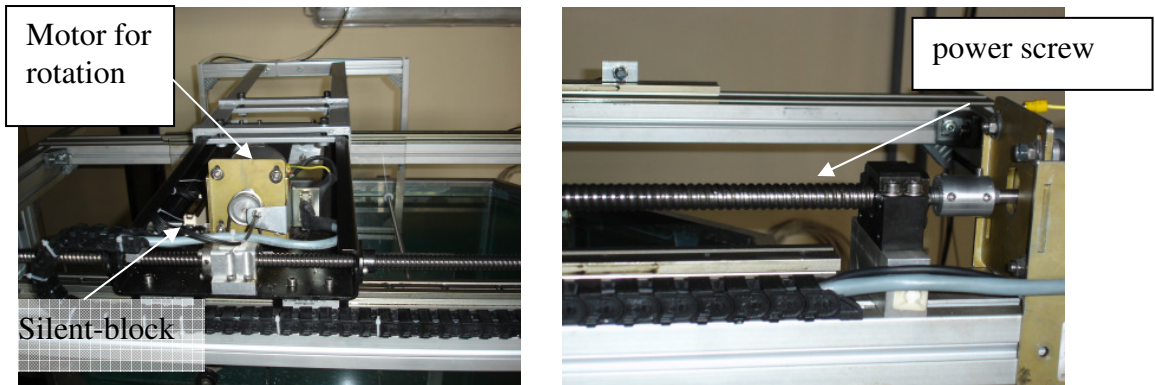


Figure 4.3 Translational and rotational mechanisms of the upper mechanism

The maximum linear speed in translational motion is 4 cm/s. The power screw moves 4 mm at each revolution of the main step motor. The step motors have 200 steps per revolution. These two step motors are controlled for velocity in open-loop PC. The flapping motion for the experiments is implemented exactly the same way as was done in the numerical studies. The velocity and the angle of attack of the profile are calculated at each 100 ms interval and the results are sent to the upper mechanism. The clock of the program is independent from the operating system.

The motion control program has two options; it can be run either manually or interactively. During the experiments, interactive version of the motion control program is used. Before performing any of the experiments a complete calibration of the experimental system is realized for positional and angle of attack accuracy. Thereafter, the profile is

positioned at the middle of the water tank just as in the numerical simulations. The user is asked to enter the linear speed, starting angle of attack, the positions for constant velocity and angles of attack. The interface also shows the values for the current positions, velocities and angles of attack in real time. Moreover, the variation of velocity and angle of attack with respect to time can also be observed during the experiments. The program also sends a 5V signal to the Flow Manager Hub for triggering the laser source and the stereo cameras of the DANTEC PIV system. The snapshot check points can be manually input at most for 10 different locations. When the “camera-start” button of the interface program (Figure 4.4) is activated the program displays the instantaneous position, velocity and the angle of attack of the model and writes these data into an excel data file. The interface of the control program is given in Figure 4.4.

In the experiments, a cambered airfoil profile, NACA 6412 is used. The chord length and the wing span are 6 cm and 48.5 cm respectively for the two-dimensional studies but for three-dimensional experiments the span is $b = 30$ cm. The wing is translated and rotated according to the motion kinematics scheme as used in the numerical simulations. The center of rotations for the 2D and 3D models are both located at the quarter chord. For two-dimensional experiments, the experiments are realized at the mid-span of the wing, sufficiently away from the effects of the end plates..

As noted before, hovering is a special case of flapping motion where the free stream velocity is zero. Before conducting the experiments the wing is set in motion for a duration of at least 10 periods in order to achieve the

periodicity of the flow. The Reynolds number based on the chord length and the maximum translational speed is 1000.

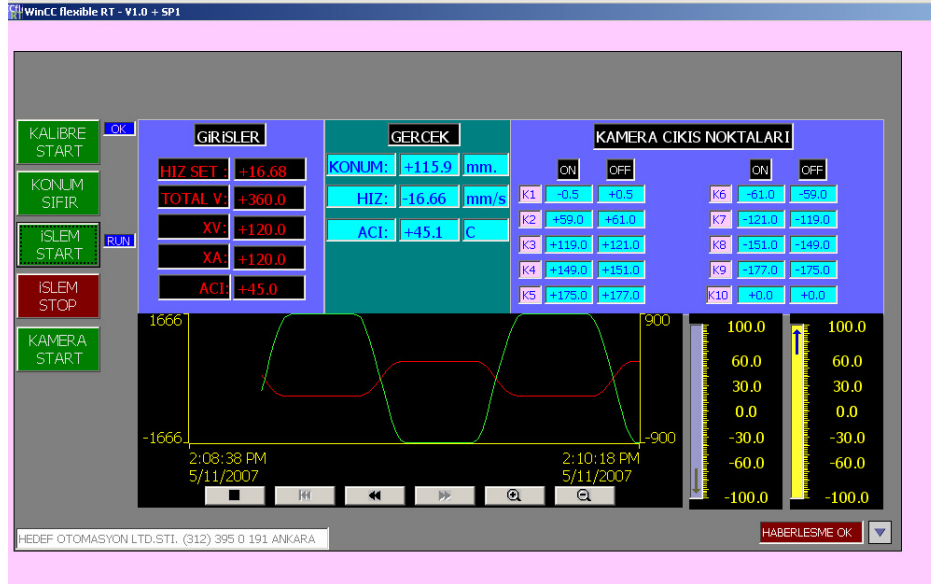


Figure 4.4 GUI for the motion control program of the mechanism

4.2 Particle Image Velocimetry (PIV) Technique

Particle Image Velocimetry (PIV) is a well known and advanced flow field measurement technique used to obtain the instantaneous velocity field based on the simple equation:

$$speed = \frac{distance}{time} \quad (4.1)$$

Main topics of PIV can be stated as follows:

- Seeding of flow field
- Illumination by a laser sheet
- Cameras to picture the flow field
- Synchronization of cameras with the laser pulses
- Correlation technique to analyze the position of seed from two successive images
- Validation and further analysis

These topics will now be explained in detail in the following sections.

4.2.1 Seeding of Flow Field

In PIV technique, the property actually measured is the distance traveled by particles suspended in the flow within a known time interval. These particles often called as “seeds” are already present in the flow or if not sufficient in number and in size are added externally to the flow. The seeding particles must be chosen carefully such that their size should not be very large, they should follow exactly the flow, and they should be suspended in the fluid. Moreover, they should have good light reflecting and scattering characteristics. In PIV measurements these particles are illuminated by a thin laser sheet and the light reflected from these light

scattering seeds are pictured in two successive images in order to detect their displacements during the time elapsed between the successive images. In this respect these seeding particles can be considered to be the actual velocity probes, and thus seeding considerations are important in PIV technique.

The seeding particles should be small enough to follow the flow accurately and large enough to scatter the light to be detected by the cameras. Moreover, the seeding particles should have the same density as the fluid, namely they should be neutrally buoyant in the fluid.

Particles whose motion is a representative of fluid continuum should have the following properties [80]:

- *Able to follow the flow.*
- *Good light scatterers*
- *Conveniently generated.*
- *Cheap.*
- *Non-toxic, non-corrosive, non-abrasive.*
- *Non-volatile, or slow to evaporate.*
- *Chemically inactive.*
- *Clean.*

In general the motion of seed particles suspended in a fluid is affected by the shape and the size of the particles, the relative densities of the particles and the fluid, the concentration of the particles in the fluid and the body forces.

The shape of the seeding particles affect the drag exerted on the particle by the surrounding fluid, and the size of the particles along with their relative density with respect to the density of the fluid in which they are suspended influence their response to velocity changes of the surrounding fluid.

Body forces, such as gravity, can normally be neglected, except in very slow moving flows, where buoyancy of the seeding particles may be an issue. The analysis of real particles' motion is rather complicated. Therefore for convenience real particles are assumed to be of spherical shape in an infinite fluid medium. It is assumed, that the results of these analysis apply qualitatively for real particles of irregular shape. This assumption is good for liquid particles and fair for mono disperse solid particles, but poor for other solid particles, such as agglomerates.

Basset [81] derived the equation of motion for a spherical particle relative to an infinite, stagnant fluid in 1888, and in 1959 Hinze [82] expanded this analysis to a moving fluid, considering the instantaneous velocity $V \equiv U_p - U_f$, of the particle relative to the fluid.

$$\begin{aligned}
 \underbrace{\frac{\pi}{6} d_p^3 \rho_p \frac{d\hat{U}_p}{dt}}_{\text{Accelerating force}} = & \underbrace{-3\pi\mu d_p \hat{V}}_{\text{Stokes viscous drag}} + \underbrace{\frac{\pi}{6} d_p^3 \rho_f \frac{d\hat{U}_f}{dt}}_{\text{Pressure gradient force on fluid}} \\
 & - \underbrace{\frac{\pi}{12} d_p^3 \rho_f \frac{d\hat{V}_p}{dt}}_{\text{Fluid resistance to accelerating sphere}} - \underbrace{\frac{3}{2} d_p^2 \sqrt{\pi\mu\rho_f} \int_{t_p}^t \frac{d\hat{V}}{d\xi} \frac{d\xi}{\sqrt{1-\xi}}}_{\text{Drag force associated with unsteady motion}} \quad (4.2)
 \end{aligned}$$

where the subscript p refers to the seeding particle and the subscript f refers to the fluid.

The equation (4.2) is valid under the following assumptions:

- the turbulence is homogeneous and time-invariant
- particles are smaller than the turbulence micro scale
- Stokes drag law applies (particles are spherical)
- particles are always surrounded by the same fluid molecules
- there is no interaction between particles.
- external forces, such as gravitational, centrifugal and electrostatic forces have been neglected.

The first term in this equation represents the force required to accelerate the particle whereas the second term describes the viscous drag as given by the Stokes law. Acceleration of the fluid produces a pressure gradient in the vicinity of the particle, and hence additional force on the particle as described by the third term. The fourth term is the resistance of an inviscid fluid to the acceleration of the sphere, and is predicted by the potential flow theory. The last term is the “Basset history integral” representing the drag force arising from derivation of the flow pattern from that occurring in steady flow. Note that when the first, the third and the fourth terms are combined, the accelerating force is equivalent to that of a sphere whose mass is increased by an additional “virtual mass” equal to half the mass of the displaced fluid.

The choice of seeding depends on a number of parameters. Primarily the seeding material should be chosen considering the flow that is to be measured, and the illumination system available. In general seeding particles should be chosen as large as possible in order to scatter the maximum light, but the particle size must be limited, since too large particles will not track the flow properly. In general, the maximum allowable particle size decreases with increasing flow velocity, turbulence and velocity gradients.

It should be noted that the camera images of seeding particles should have a diameter corresponding to at least 2 pixels, preferably 3 or more pixels in the digital image. This will allow the system to estimate the particle positions and displacements to sub-pixel accuracy, effectively increasing the resolution of the technique.

For the present experiments, hollow glass spheres coated with silver, SGH-10 [84] are chosen as seeding material. The specifications of the seeding material used during the present experiments are given in Table 4.1.

Table 4.1 Specifications of seeding particle

Mean particle size (μm)	10
Size distribution	2-20 μm
Particle shape	Spherical
Density (g/cm^3)	1.4
Melting point ($^{\circ}\text{C}$)	740
Refractive index	-
Material	Borosilicate glass

4.2.2 Illumination

There are three ways to produce a light sheet in PIV technique. The illumination system chosen for the experimental setup is a two pulsing beams combined from a double-cavity Q-switched Nd:YAG laser which is then formed into pulsing light-sheets using cylindrical lens and proper optics. For water applications, lower-energy Nd:YAG lasers are preferred. This type of laser has the following advantages:

- Q- switched pulses, which are of short duration, effectively freeze the motion of particles
- two cavities mean the widest possible range of time between pulses can be selected

- two cavities mean that the illumination energy budget does not vary with the time between pulses, as it would with a double-Q-switched single lasing cavity/shuttered/scanning illumination methods
- the output beam energy can be selected to suit the application e.g. 400 mJ lasers for airflows and 15 mJ lasers for water flows

But the optical components are more costly compared to argon-ion lasers and careful alignment of two lasing cavities is required.

Since the pulsing frequency of YAG lasers is such that it can be disorientating a filter is placed in front of the cameras as it is recommended in the manual to eliminate the background lighting so the application area can be well lit. Thus, the pulsing of the laser is less disturbing for the people working in the room.

Nd:YAG laser , which is the most commonly used pulsed laser, is a solid state laser. A flash lamp and a YAG crystal are placed at the two origins of a mirrored elliptical cavity to maximize the energy transfer from the flash lamp to the crystal. The flash lamp excites the cavity for a short time and the excess heat build-up is thermally dissipated by cooling water before the next pulse of the flash lamp. Today's standard lasers have a flash lamp, which excites the lasing cavity for around 250 μ s, and this is typically repeated at a frequency of 10 Hz.

Nd:YAG lasers has a typical pulse energy of 200 mJ, which is released during a period of around 10 ns. This gives an average power of 20 MW

distributed over a beam diameter of 4 - 6 mm. the beam is transported using a special light-guiding arm which comprises a sequence of flexible mirrored joints which deflect the incoming beam from one mirror to the next, irrespective of the orientation of the joint. These joints are connected by hollow tubes through which the beam passes. The pulsing beam is converted into a pulsing light sheet by the 80X20 optical assembly, which is screwed on to the end of the light guiding arm. The thickness of the light sheet can be adjusted and the divergence angle is typically 15° for a 6 mm input beam. Different divergence angles can be achieved using additional optical assemblies.

During the first visualization tests, dark regions due to the shadow of the airfoil were observed. In order to illuminate these dark regions, a mirror of dimensions 20 cm by 150 cm was placed at the rear end of the water tank. When the vector fields of the images taken with and without the mirror were compared, it was observed that there were no significant differences in the velocity fields observed. In order to avoid any reflections that can harm the CCD cameras, it was decided not to have a mirror in the experiments.

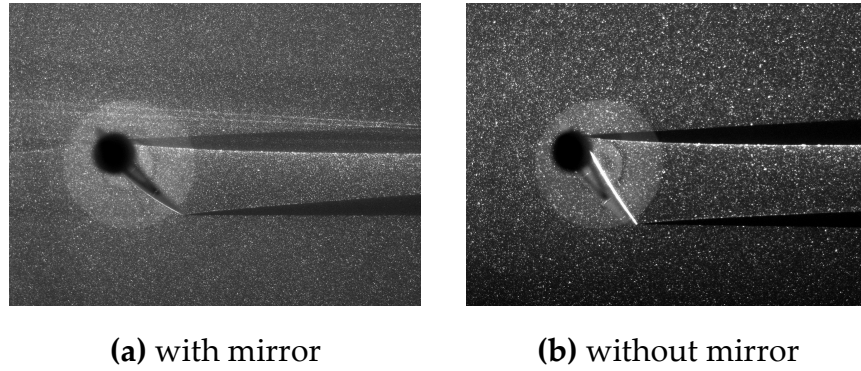


Figure 4.5 The experimental visualization with and without mirror in the water tank.

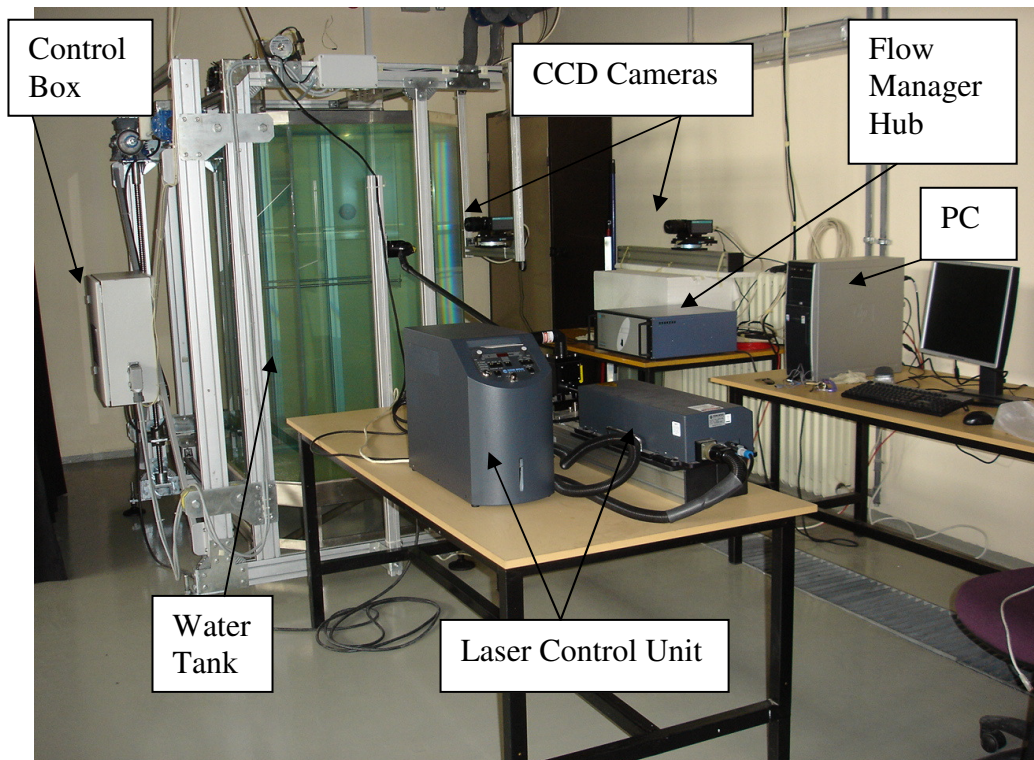


Figure 4.6 Water tank with the whole experimental setup.

4.2.3 Cameras

The purpose of the digital camera is to capture the initial and final positions of the seeding particles which will enable the calculations of the velocity vectors. The present setup has two CCD (Charged Coupled Device) cameras for taking the images with an objective of AF-MICRO-NIKOR of 60 mm to observe the entire flow domain of total 6 chord lengths. In the processor of the DANTEC system, FlowMap PIV system, CCD cameras are used since these provide an instantaneous digital signal of the image map of seeding particle positions. Historically, photographic film has been used. A CCD camera comprises an array of detectors called pixels. Each pixel is a MOS capacitor, being charged by converting the incident photons of light into electrons, like in a photodiode. The cells are isolated from each other by potential wells, created by the doping of the silicon chip and by applying voltages to a grid of transparent metallic electrodes deposited on the CCD surface. Light falling on a pixel is thus converted into an electronic charge. The charge falling on the individual pixels is transformed to a voltage during read-out of the CCD chip and the value of the voltage is seen as a grey scale distribution on the PIV image map. Ideally, images should have a high charge i.e. appear white and the background noise level of the CCD chip should be low i.e. appear dark.

In two-dimensional measurements, the camera is placed at right angles to the light sheet. Seeding particles scatter light from the first pulse of the light-sheet and this scattered light is detected by the camera ideally as a bright signal on a dark background. Thus, the camera image map has

sampled the initial positions of the seeding particles. This first image is moved to non-light sensitive storage area on the CCD. This process is called frame transfer. The light-sheet is switched off and the seeding particles are transported by the movement of the flow field and, in cross-correlation the camera frame is advanced. The second pulse of the light-sheet is fired and the seeding particles scatter light which is imaged onto the camera detector so the final positions of the seeding particles are sampled.

The cameras operate at double frame; i.e. at each time each take two images. They allow a broad control range of opening and exposure time. The time between two laser flashes is 80 000 μ s during which a particle can move approximately 3 mm. The exposure time is 500 ms and the F number is adjusted to 2.8. The cameras are placed approximately 120 cm away from the water tank perpendicular to the illumination plane for two-dimensional experiments.

It is not possible to present the results at every instant. Instead it makes sense to present the results at specified time intervals. In order to be consistent with both the experimental measurements and the numerical calculations, a non-dimensional time is used which is defined as follows as the ratio of the time to the period of flapping:

$$t^* = \frac{t}{T_{per}} \quad (4.3)$$

Images are taken at each non-dimensional time step of $\Delta t^*=0.01$. Note that $t^*=1$ corresponds to one full period. The experimental and numerical periods are compared in Table 4.2.

The experiments are carried out for different kinematic parameters and various angles of attack values. The increment for taking the images is set to $\Delta t^*=0.01$, which is input to the Flow Manager software of the DANTEC PIV system as 500 ms as the time between two successive images.

Table 4.2 Comparison of experimental and numerical periods for $Re=1000$.

	Experiment	Numerical	Experiment	Numerical
α	45	45	45	45
x_v	2c	2c	2.5c	2.5c
V [m/s]	0.01666	1.45388	0.01666	1.45388
T [sec]	51.65	0.0982	47.5	0.0904
V_P [m/s]	0.00697	0.611	0.00759	0.664

The control program can output the actual displacement, speed and the angle of attack measured at the center of rotation point at every 50 milliseconds. The start of the outputs is initiated with the triggering of the camera, i.e. the signal that the CCD cameras start to take images. Experiments are performed at least after 10-15 cycles has elapsed

following the start of the motion of the wing in order to achieve the steady state behavior and complete periodicity of the flow. For numerical simulations, the processing of results is performed after the 6th period. This period number is significantly larger for experiments.

4.2.4 Synchronization

The non-dimensional time used for the synchronization is the same as defined above. Both of the cameras take the first image of the particles scattering the first pulse of laser is recorded on frame 1 whereas the second image corresponding to the second pulse of the laser is recorded on the second frame 2. This procedure is known as double frame or double exposure. In the experiments the start of the events begins with the trigger signal coming from the control program and taking the image of subsequent events are done on fixed interval basis. At the beginning of a period, the trigger signal of 5V is sent to the FlowMap Hub which synchronizes the cameras and the two laser flashes. As stated previously, the time between two the laser flashes is set to 80 000 μ s.

No pre-processing was done to the PIV images since after first trials it was found that the shadow of the airfoil and the background do not influence much the velocity vectors and the quality of the pictures were relatively good.

4.2.5 Correlation

The camera image is subdivided into a number of so-called “interrogation areas”, and within each of these interrogation areas the first and the second camera frames are correlated to estimate an average displacement vector. This method does not require the tracking of individual particles, instead demands several particles within each interrogation region to produce reliable results.

Basically two different correlation techniques can be used: auto-correlation and cross correlation. In the vast majority of cases, cross-correlation is superior to autocorrelation. Although the computational cost for cross-correlation is much lower than adaptive correlation, it is used as testing the quality of images and adaptive correlation is used for the calculation of velocity vectors. The method is briefly outlined in the flow chart given in Figure 4.7.

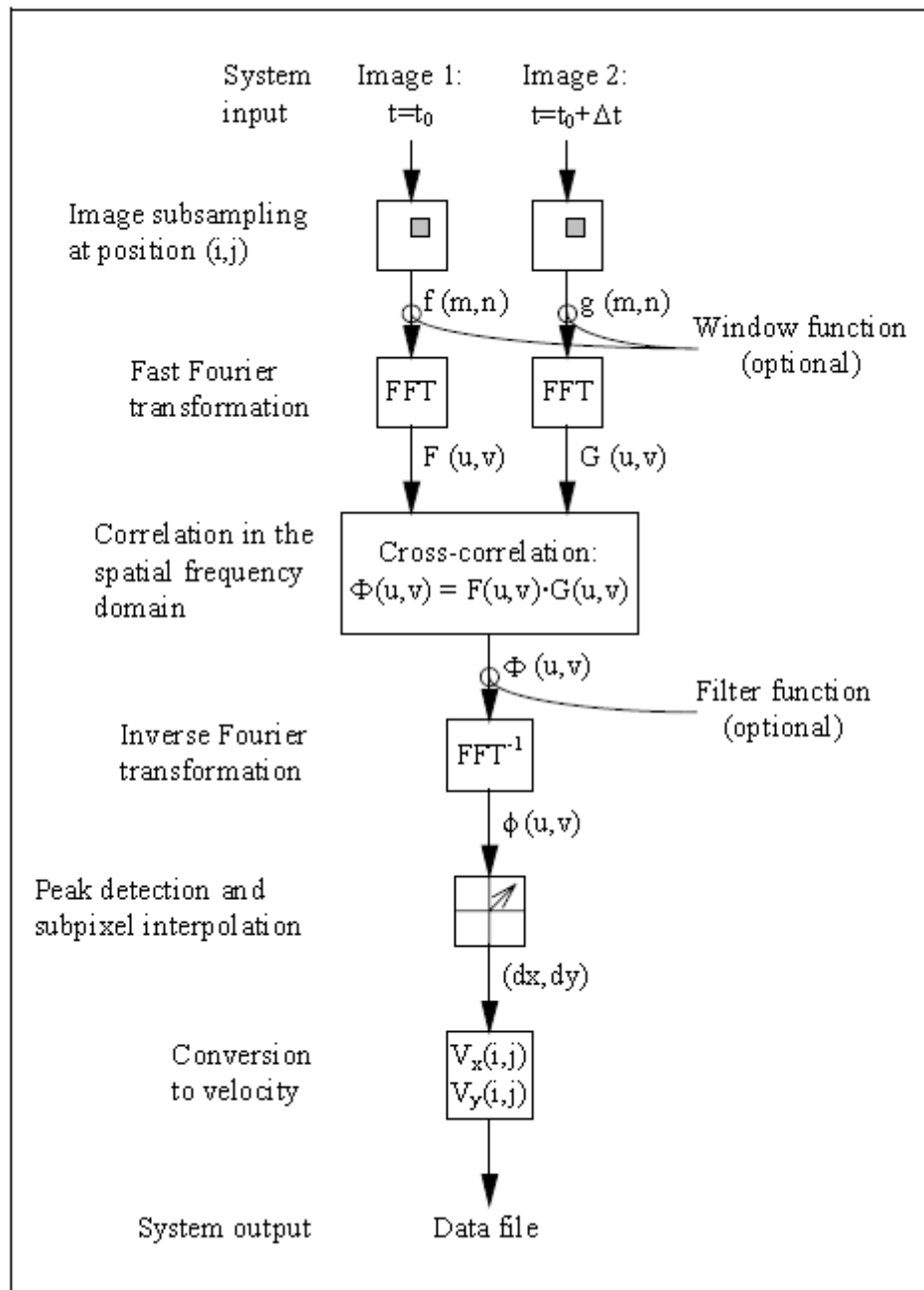


Figure 4.7 Numerical processing flowchart in Flow Manager Software

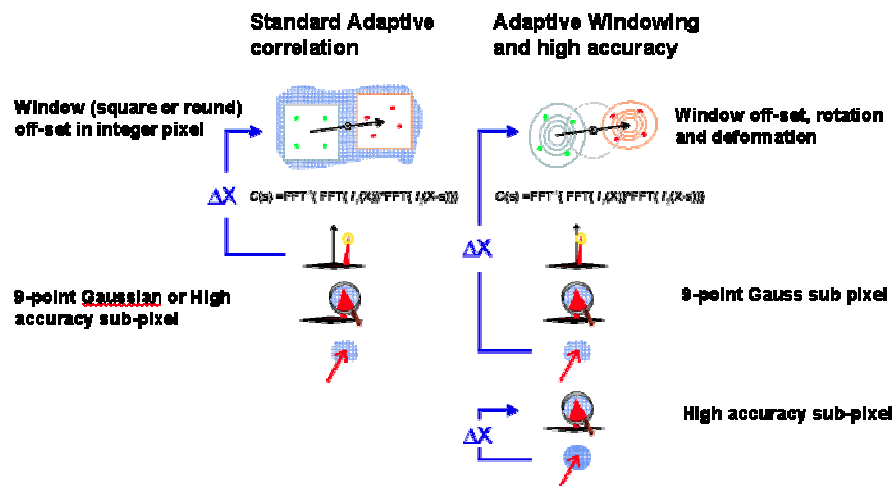


Figure 4.8 Flow diagram of adaptive processing in Flow Manager Software

In this study, the adaptive correlation method is used as indicated in the flow diagram given in Figure 4.8. The method calculates velocity vectors with an initial interrogation area (IA) of the size N time the size of the final IA and uses the intermediary results as information for the next IA of smaller size, until the final IA size is reached. In the calculation of vector fields, IA is taken as (128×128) and N is equal to 2 which leads to final interrogation area size of 32×32 pixels. The parameter "Overlap – Horizontal/Vertical" defines a relative overlap among neighboring interrogation areas, as illustrated in Figure 4.9 for (H-50%, V-50%). It can be set independently for the horizontal and vertical overlaps, offering total freedom to increase vector map resolution in any direction. Since double exposure is used, the overlap is taken as 50 % which is the usual recommended value.

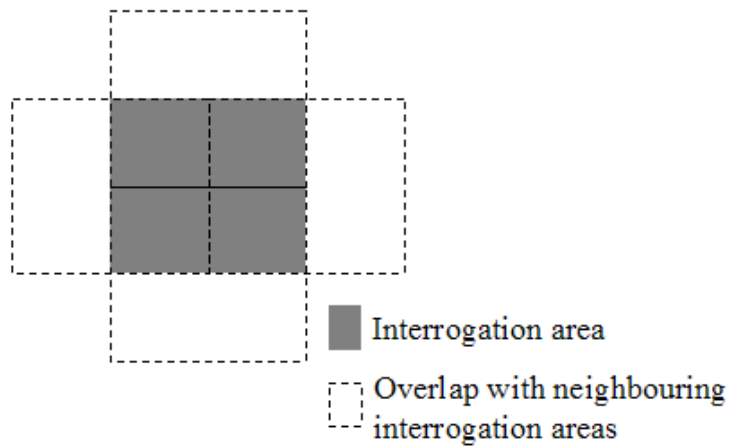


Figure 4.9 Overlapping of interrogation areas.

Adaptive and deforming windows

As in any signal analysis, windowing and zero-padding discrete data is required in order to avoid aliasing. In standard adaptive correlation the situation is like shown below:

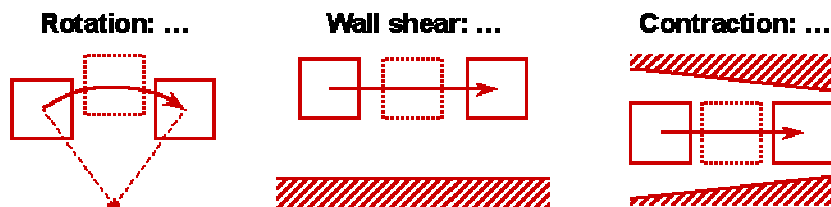


Figure 4.10 Deformation options in PIV.

A typical choice for PIV is a round Hanning window. However, the windowing does not take into account that there are velocity gradients in the flow. Hence, ideally cross correlation should be between windows, which follow the flow gradients. This can be adapted in an iterative loop, where interrogation area size and shape is chosen to suit the velocity gradients. This procedure gradually builds up the signal strength and results in successful reduction of the interrogation spot to an absolute minimum.

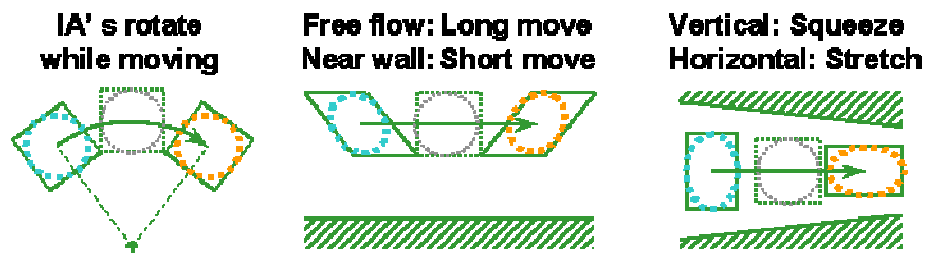


Figure 4.11 .Window options in adaptive correlation procedure in Flow Manager software.

When the adaptive deforming window is applied in non-integer steps, the iterative capture of the two interrogation spots further ensures that particle images on the border of the interrogation regions are equally weighted by the window function. This is particularly important when reducing the size of the interrogation spots to a minimum, because non-

equal weighted border particles, will slightly bias the measured displacement.

Second order difference:

Velocity vectors are estimated from mean particle displacement inside the interrogation areas (IA). Mathematically,

$$D(\vec{X}; t_0, t_{+1}) \approx \int_{t_0}^{t_{+1}} u(\vec{X}(t), t) dt \quad (4.4)$$

where 'D' is the displacement and 'u' is the velocity, in the main formula used to calculate the velocity vectors. This formula is transformed into an algebraic equation either using a Central Difference Scheme or a Forward Difference Scheme.

The Central Difference Scheme is equivalent to a three-point symmetric algorithm for the evaluation of $d(\vec{X})/dt$, with a reference 'point' created at the time $t_{+1/2}$. The Forward Difference Scheme, on the other hand, considers the temporal reference t_0 . Note that the Central Difference Scheme is mathematically the most accurate methodology and therefore shall be preferred with PIV measurements. When processing further advanced measurements such as PIV/LIF, the Forward Difference Scheme shall be used because the LIF-image will get the same temporal reference (t_0) as the velocity vector map, which will not be the case with the Central Difference Scheme.

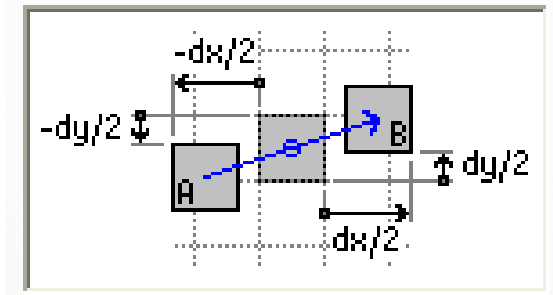


Figure 4.12 Velocity vector located at the center of the interrogation window (second order interpolation).

4.2.6 Validation and further analysis

Validation parameters for the adaptive correlation method are various and can also be used in combination to fine-tune the processing and, when needed, to remove spurious vectors.

In the "Peak validation" section, the user can set values for the minimum and the maximum peak widths as well as the minimum peak height (between 1st and 2nd peak) and thereby put more stringent conditions on peak identification for the subsequent determination of vectors. In the study, minimum peak height relative to peak 2 is set 1.4. The peak ratio factor Q is defined as:

$$Q = \frac{P1 - \min}{P2 - \min} > 1 \quad (4.5)$$

With "Local neighbourhood validation", individual vectors are compared to the local vectors in the neighbourhood vector area, of size (MxM) is set by the user. If a spurious vector is detected, it is removed and replaced by a vector, which is calculated by local interpolation of the vectors present in the (MxM) area. Interpolation is performed using median or moving average methodology (with n iterations). The M value is set to 3 and validation is performed for three iterations.

Spurious vectors are identified via the value given to the "Acceptance Factor". This factor effectively allows a given degree of freedom on velocity vector gradient inside the (MxM) area and if the calculated gradient is larger than set, the central vector is removed. The larger this factor is, the less the velocity vector map is spatially corrected. On the other hand, with low factor values, the vector map is smoothed at a level that removed all valid vectors as well as bad vectors.

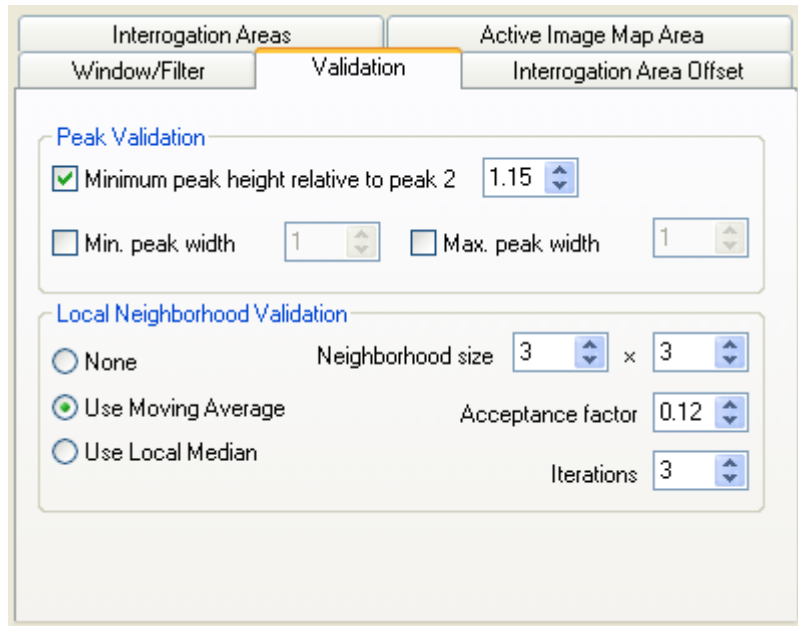
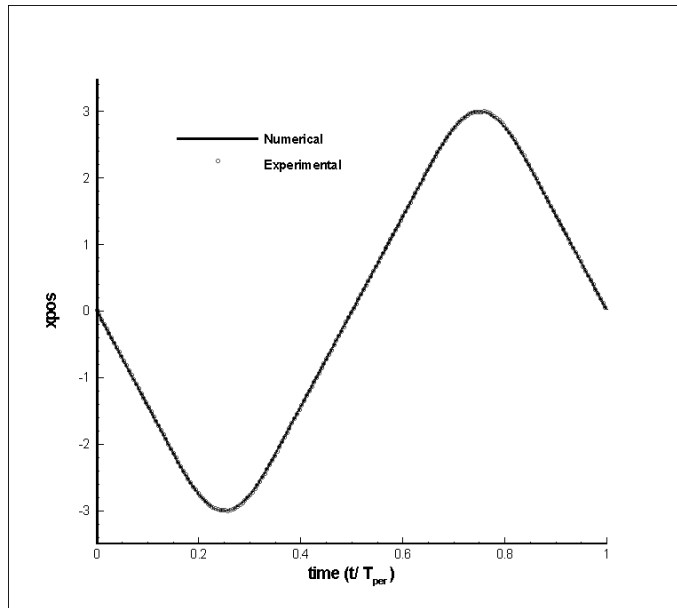
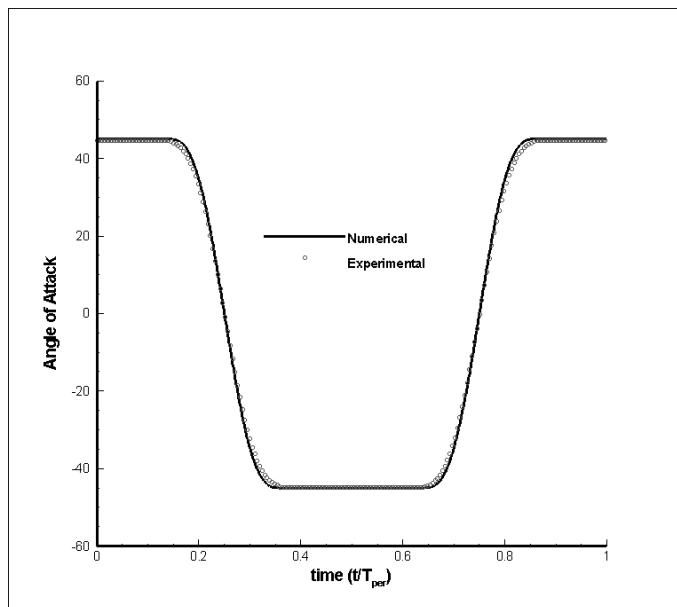


Figure 4.13 Example of validation settings for PIV analysis using adaptive correlation methodology.

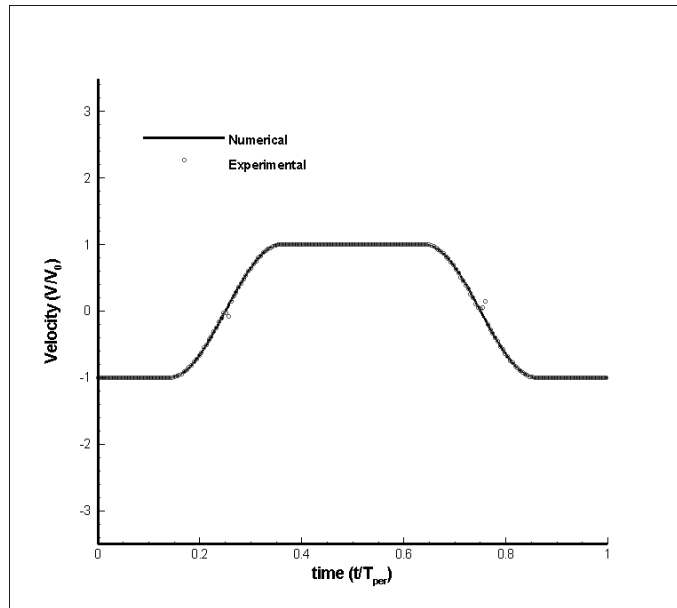
The desired motion of the airfoil is set up with the help of a control program. The output of the control program can also be extracted as a data file. Figure 4.14 compares the actual velocity and angle of attack variations over a period of motion to the desired input values.



(a) Comparison of non-dimensional desired input values for x-position to actually measured values within one period of motion.

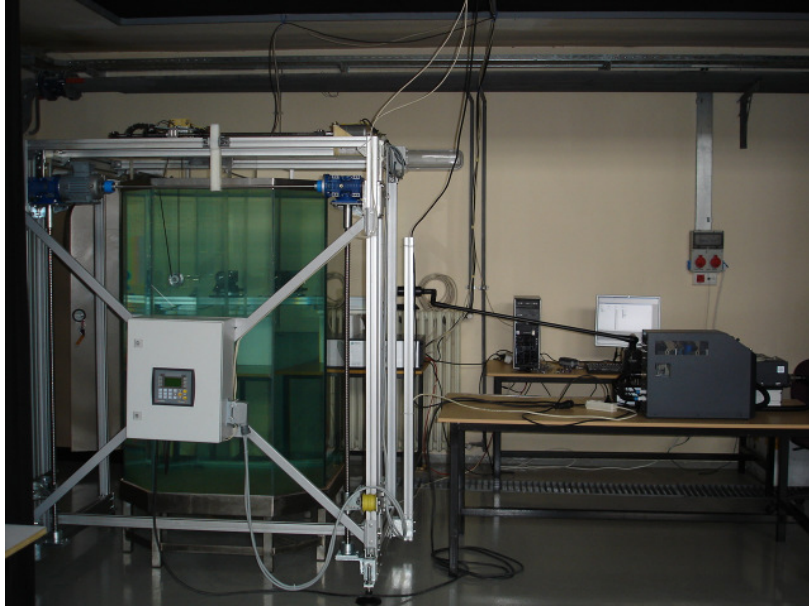


(b) Comparison of non-dimensional desired input values for angle of attack distribution to actually observed values within one period of motion.

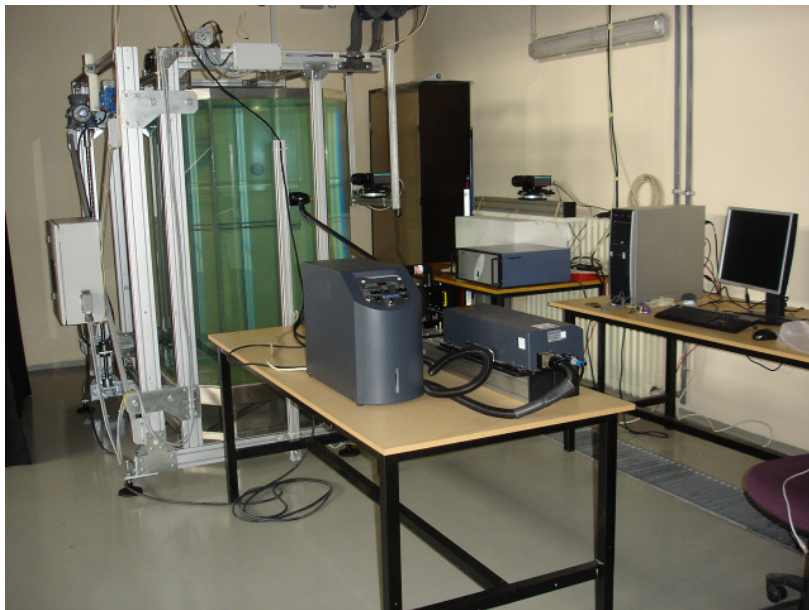


(c) Comparison of non-dimensional desired input velocity distribution to actually observed values

Figure 4.14 (a)- (c) Comparison of non-dimensional desired x-position, velocity and angle of attack distributions to actually observed values data at $\alpha=45^\circ$, $Re=1000$, $x_v= x_a=2c$.



(a)



(b)

Figure 4.15 Experimental setup (a) front view, (b) side view.

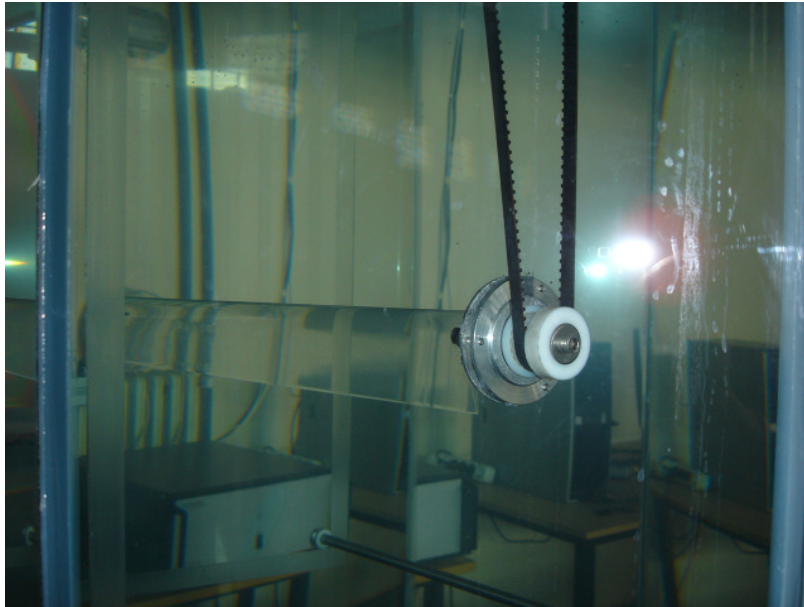


Figure 4.16 Airfoil made of transparent acrylic in the water tank.

4.3 Vortex Identification Techniques

The concept of a vortex exists in almost every branch of fluid dynamics but still there is no agreed definition of a vortex. There are mathematical definitions of “vorticity” and “helicity”, but the vortical flow is not completely characterized by these definitions. For instance, Banks et al. [85] state that there is no vortical motion in a shear flow even though it exhibits vorticity at every point. The difficulty to obtain a precise definition for a vortex arises from many reasons which will be outlined. Robinson [86] suggested the following definition for the identification of a vortex:

A vortex exists when instantaneous streamlines mapped onto a plane normal to the vortex core exhibit a roughly circular or spiral pattern, when viewed from a reference frame moving with the center of the vortex core.

Unfortunately, this definition requires a knowledge of the vortex core before one can determine whether something is a vortex.

According to Jeong and Hussain [87], vortex should at least possess the following properties:

- (i) a vortex core must have a net vorticity, consequently a net circulation. By this requirement, potential flow regions are excluded from vortex core and a potential vortex is vortex with zero cross-section.
- (ii) the geometrical characteristics of a vortex region should be Galilean invariant.

In spite of these prerequisites, Cucitore et al. [88] state that there is no single technique for the identification of vortices. The procedures are based on the search for regions of the flow field characterized by some property, intuitively related to a vortical motion.

4.3.1 Scalar methods

In the early times, scalar methods were used to identify the vortices. These scalar methods were also called intuitive definitions. For instance, several authors (see Spalart, 1998) used the magnitude of the vorticity vector, $|\omega|$, as an indicator of vortical structures.

It must be said, however, that the use of $|\omega|$ may be misleading: it may fail, for example, in wall-bounded flows, because it cannot distinguish between rotation due to pure shear and rotation due to an actual swirling motion. Consequently, problems arise when $|\omega|$ due to the background shear becomes comparable to that due to a swirling motion (the simple Couette flow is a clear example of high values of $|\omega|$ not corresponding in any way to vortical motion). Even in free shear flows, it has been showed how the vorticity magnitude is not an adequate criterion for the identification of vortices by Jeong and Hussain [87].

Cucitore et al. [88] describes another pressure as a frequently used scalar indicator of vortical motion. With a steady inviscid planar two-dimensional flow, in fact, in the case of rotating motion the pressure shows a minimum at the center of the circular pattern. This is simply a consequence of the balance of the forces acting on a fluid element in the radial direction; the centrifugal force must be balanced by the force due to a radial pressure gradient, which is responsible for the minimum on the axis of the rotation. However when the flow is unsteady, viscous, or three-dimensional, this is no longer true as shown by Jeong and Hussain [87]. In

the case of Karman's viscous pump, because of viscous effects the pressure has no minimum on the axis near the wall, while the motion is clearly vortical. An unsteady, inviscid flow, where because of unsteadiness the pressure has a well-defined minimum on the axis of a clearly non-rotating motion. Cucitore et al. [88] note that it is commonly accepted that vortical structures are basically characterized by a swirling motion, in a suitable reference frame, and in fact their presence has been widely associated with the presence of closed or spiral streamlines or pathlines. It is evident that these methods of identifying vortices do not prove to be Galilean invariant. Besides, as shown by Jeong and Hussain [87], there is the problem that a particle must complete a full revolution around the vortex center, in order to have a circular streamline or pathline, and this is not always the case in the presence of highly unsteady flows.

More recently, three additional definitions of a vortex have been proposed, by Chong et al. [90], Hunt et al. [91] and Jeong and Hussain [87]. All of them are based on the analysis of the velocity gradient tensor $\nabla u = u_{i,j}$ (the subscript $/,j$ denotes differentiation). These definitions are Galilean invariant, and are based on less intuitive physical considerations. The Galilean invariance makes the property independent of the coordinate system used. The issue of vortex identification is by no means trivial, and in fact several of the existing techniques can give good results in many situations, but all of them can be shown to fail (or, at least, to produce ambiguous answers) in particular conditions.

The main existing vortex definitions will be briefly reviewed in the next section, with emphasis on those based on the analysis of the velocity gradient tensor and with particular attention to their physical foundation.

4.3.2 Second invariant of velocity gradient, Q criterion

Hunt et al. [91] define vortices as regions where the second invariant Q of the tensor ∇u is positive, with the additional condition that the pressure is lower than the ambient value.

Any tensor can be decomposed in a symmetric and antisymmetric part. When this decomposition is applied to the velocity gradient tensor, the deformation and rotation tensors are the symmetric and antisymmetric parts respectively as explained by Repellin [92].

$$\nabla u = S + \Omega \tag{4.6}$$

where the symmetric and anti-symmetric parts of the velocity gradient tensor is defined as:

$$S = \frac{1}{2} \left(\frac{\partial u_i}{\partial x_j} + \frac{\partial u_j}{\partial x_i} \right) \tag{4.7}$$

$$\Omega = \frac{1}{2} \left(\frac{\partial u_i}{\partial x_j} - \frac{\partial u_j}{\partial x_i} \right) \tag{4.8}$$

For an incompressible flow the second invariant Q of the velocity gradient tensor can be rewritten as follows:

$$Q = \frac{1}{2} (\|\Omega\|^2 - \|S\|^2) \quad (4.9)$$

where

$$\|\Omega\| = [\text{tr}(\Omega\Omega^T)] \text{ and } \|S\| = [\text{tr}(SS^T)]$$

The Q criterion, proposed by Hunt et al. [91] identifies vortices as flow regions with positive second invariant of ∇u , i.e. $Q > 0$. Additionally, the pressure in the eddy region is required to be lower than the ambient pressure. This additional condition makes the criterion independent of the sign of Q .

$$\nabla^2 p = 2\rho Q \quad (4.10)$$

There is no explicit connection between a region with $Q \geq 0$ and a region containing a pressure minimum.

In an incompressible flow, Q is a local measure of the excess rotation rate relative to the strain rate. It should be noted that $Q > 0$ does not guarantee the existence of a pressure minimum inside the region identified by it [88]. The use of Q criterion without the additional pressure condition is also done in literature and acceptable [94].

The relation (4.9) shows the quantity Q represents a local balance between the rotation and deformation rates of a fluid element. This is the same definition of a vortex that has been formulated by Chong [90] : a vortex is a connected region where the antisymmetric component of ∇u predominates over the symmetric one.

The maximum principle applied to this equation states that pressure maxima can occur only on the boundary if $Q \Rightarrow 0$ and the pressure minima can occur only on the boundary if $Q > 0$. However, $Q \geq 0$ does not necessarily imply that pressure minima occur within the region. Thus there is no explicit connection between a region with $Q \geq 0$ and a region containing a pressure minimum [88].

4.3.3 Two Negative Eigenvalues of $(S^2 + \Omega^2)$, λ_2 Criterion

As defined by Jeong and Hussain [87], for a constant property fluid, in a vortex core $(S^2 + \Omega^2)$ has two negative eigenvalues. Jeong and Hussain tried to improve the performance of the criterion based on the search for pressure minima by overcoming the causes of its failure like unsteady straining and viscous effects. The gradient of Navier-Stokes equations can be written as:

$$\frac{\partial a_i}{\partial x_j} = -\frac{1}{\rho} \frac{\partial^2 p}{\partial x_i \partial x_j} + \nu \frac{\partial^3 u_i}{\partial x_j \partial x_k \partial x_k} \quad (4.11)$$

The term on the left hand side is the acceleration gradient and the first term on the right hand side is the Hessian of pressure which contains the information about the local pressure extrema. The acceleration gradient can also be decomposed into symmetric and antisymmetric part:

$$\frac{\partial a_i}{\partial x_j} = \left[\frac{DS_{ij}}{Dt} + \Omega_{ik}\Omega_{kj} + S_{ik}S_{kj} \right] + \left[\frac{D\Omega_{ij}}{Dt} + \Omega_{ik}S_{kj} + S_{ik}\Omega_{kj} \right] \quad (4.12)$$

where the symmetric part of the acceleration gradient is

$$\frac{DS_{ij}}{Dt} - v \frac{\partial^2 S_{ij}}{\partial x_k \partial x_k} - \Omega_{ik}\Omega_{kj} + S_{ik}S_{kj} = -\frac{1}{\rho} \frac{\partial^2 p}{\partial x_i \partial x_j} \quad (4.13)$$

If the term on the right hand side related to pressure has two positive eigenvalues, there is a local pressure minimum on the plane of the two eigenvectors associated with these eigenvalues.

The first term of Equation (4.12) represents the unsteady irrotational straining and the second term represents the viscous effects. Therefore the tensor $(S^2 + \Omega^2)$ allows determining the existence of a local pressure minimum due to a vortical motion. If these unsteady and viscous effects are neglected, the symmetric part of the gradient of the incompressible Navier-Stokes equation can be written as:

$$S^2 + \Omega^2 = -\frac{1}{\rho} \nabla(\nabla p) \quad (4.14)$$

where p is the pressure and equation (4.14) is a representation of the pressure Hessian $(\nabla(\nabla p))_{ij} = \frac{\partial^2 p}{\partial x_i \partial x_j}$. Since $(S^2 + \Omega^2)$ is symmetric then the eigenvalues of this tensor are real. For two-dimensional flow, if the eigenvalues of the symmetric tensor $(S^2 + \Omega^2)$ are ordered as $\lambda_1 \geq \lambda_2$, then the second largest eigenvalue should be negative which is equivalent to saying that $\lambda_2 < 0$ at every point inside the vortex core. Thus this method is also referred as λ_2 criterions.

This method to obtain the Hessian of the pressure is also applicable to compressible flows as well but it should be noted that the equivalence of the methods based on the analysis of the velocity gradient tensor for two dimensional flows is no longer valid due the additional terms which come from non-zero velocity gradients and the non-zero trace of velocity gradient tensor as noted by Cucitore et al. [88].

The λ_2 criterion removes the main causes of inaccuracy, i.e. unsteady effects and viscous effects. Jeong and Hussain [87] defined the vortex core as a connected region with two positive eigenvalues of the pressure Hessian to capture the region of local pressure minimum in a plane.

Moreover these eigenvalues are related to Q by

$$Q = -\frac{1}{2}(S^2 + \Omega^2) = -\frac{1}{2}(\lambda_1 + \lambda_2) \quad (4.15)$$

From Jeong and Hussain [87], it can be shown that while Q criterion measures the excess of rotation rate over the strain magnitude in all directions, the λ_2 criterion looks for this excess only on a specific plane.

The study of Chakraborty et al. [93] states that the point of local pressure minimum in a plane requires two eigenvalues of the local pressure Hessian to be positive and the local pressure gradient component on the plane to be zero. The region in which the two eigenvalues of the pressure Hessian are positive is thus less restrictive and may not include the point of planar pressure minimum in its interior (if there does not exist a point of vanishing pressure gradient on the plane). Furthermore, the relationship between the actual and the modified pressure distribution that neglects the unsteady and viscous terms is not clear. Also, Cucitore et al. [88] note that the pressure Hessian concept defined above is not applicable for the case of compressible flows because of non-vanishing density gradient and divergence of velocity.

The condition $\Delta > 0$ implies that ∇u has complex eigenvalues. But the $Q > 0$ criterion is more restrictive than $\Delta > 0$ criterion as noted by Chakraborty et al [93].

Identification of vortices is generally accomplished by identifying isolated regions of significant vorticity (vortex core) and calculation of its statistics (i.e. size, strength, etc.). In complex flow fields, vortices are normally overshadowed by regions of significant shear, making it nearly impossible to obtain a reliable vortex statistics and to find contribution to the overall flow. Hussain et al. [94] used Q and λ_2 criteria to educe coherent vortices

from the flow field. Higher positive values of Q signifying dominance of rotation over strain are representative of coherent structures.

As stated by Dubief et al. [95] the choice of the Q criterion as a vortex identification method is strongly supported by:

- i) its relation to pressure low
- ii) the very definition of Q
- iii) as the balance between the local rotation rate and strain rate.

The λ_2 approach proposed by Jeong and Hussain [87] has proven to be an effective technique for locating vortex cores in many real-world applications. However, Kenwright et al. [98] point out that the problems such as the appearance of discontinuous line segments and the influence of a curling flow require that the underlying theory be revisited.

CHAPTER V

TWO-DIMENSIONAL NUMERICAL ANALYSIS OF FLAPPING MOTION

5.1 Definition of Geometry and Flapping Motion in Numerical Analysis

The wing stroke of an insect is typically divided into four kinematic phases: two translational phases (upstroke and downstroke), when the wings sweep through air with a high angle of attack, and two rotational phases (pronation and supination), when the wings rapidly rotate and reverse the direction of motion.

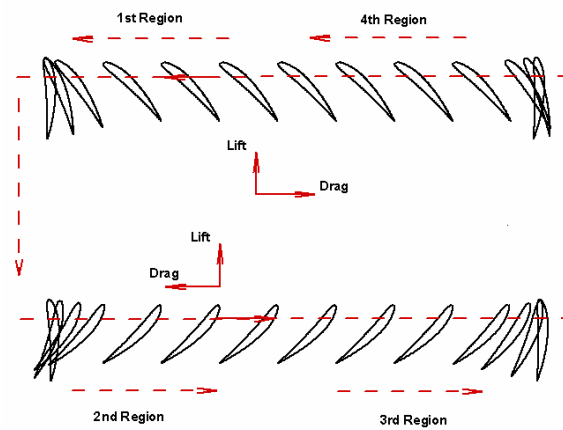


Figure 5.1 Kinematics of flapping motion

The flapping motion is divided into 4 regions. The first region corresponds to half of the downstroke where the leading edge is pointing in positive direction and the second one corresponds to the half of the upstroke (Figure 5.2). The third and the fourth regions are the mirror images of the first two regions and correspond to the second half of upstroke and downstroke respectively. Each region is composed of a translational phase and a rotational phase. In the translational phase, the airfoil translates with a constant velocity until a predefined position, where a rotational motion around a point along the chord line is superposed at the end of the translational motion. Each half cycle starts from rest and comes to a stop. The rotation is such that the leading edge stays always as leading edge during all phases of the motion.

For numerical analysis of the flapping motion different airfoil sections have been selected and the effects of parameters such as the thickness and the camber of the airfoil sections are investigated.

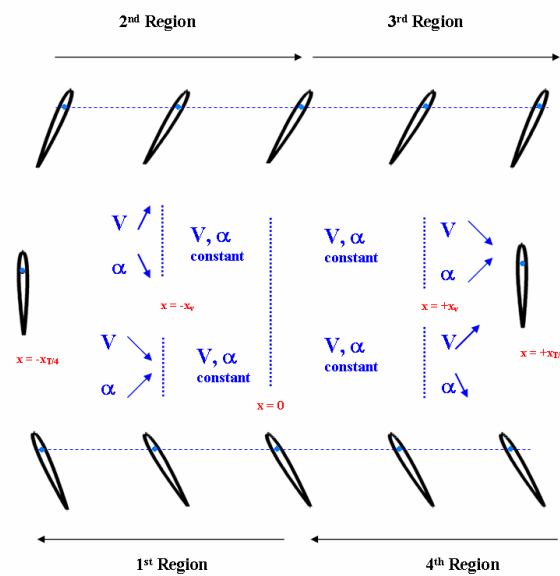


Figure 5.2 Definition of flapping motion

The numerical analysis followed is similar to the analysis adopted by Kurtuluş [4] and the details for the formulation of the motion are given by her in reference. The pre-described regions are completed in one period of simulation, T . During the time interval $[t_v, T/4]$, the airfoil decelerates and it reaches $V_o=0$ at $t=T/4$. By the same time it starts to rotate around its center of rotation reaching 90° angle of attack at the end of the quarter period.

5.2 Solver Description, STAR-CD

Numerical calculations are carried out by using a commercially available finite-volume Direct Numerical Simulation (DNS) tool, STAR-CD. Unsteady, incompressible, laminar and two-dimensional Navier-Stokes equations are solved in a moving domain.

The equations for the conservation of mass and momentum for general incompressible or compressible fluid flows and in a moving coordinate frame in Cartesian tensor notation are given by:

$$\frac{1}{\sqrt{g}} \frac{\partial}{\partial t} (\sqrt{g} \rho) + \frac{\partial}{\partial x_j} (\rho \tilde{u}_j) = s_m \quad (5.1)$$

$$\frac{1}{\sqrt{g}} \frac{\partial}{\partial t} (\sqrt{g} \rho u_i) + \frac{\partial}{\partial x_j} (\rho \tilde{u}_j u_i - \tau_{ij}) = -\frac{\partial p}{\partial x_i} + s_i \quad (5.2)$$

where for Newtonian fluid, the constitutive relation for the stress tensor is:

$$\tau_{ij} = 2\mu s_{ij} - \frac{2}{3}\mu \frac{\partial u_k}{\partial x_k} \delta_{ij} \quad (5.3)$$

with

$$s_{ij} = \frac{1}{2} \left(\frac{\partial u_i}{\partial x_j} + \frac{\partial u_j}{\partial x_i} \right) \quad (5.4)$$

The computation of unsteady viscous flow fields is performed on a HP 4000 workstation. The pre-processing such as defining the geometry, mesh generation, setting up the boundary and initial conditions, defining the fluid and solid material properties and assigning the analysis control parameters and the pro-processing of data files such as reading and manipulating the data files, data plotting and animation of calculated results are all done using the interface, PROSTAR of Star CD software.

General mesh motion and internal sliding mesh for unsteady flow solutions are handled by STAR-CD by means of user-defined functions. Although STAR-CD has three solution procedure alternatives, which are SIMPLE, SIMPLEC and PISO, it is compulsory to use PISO scheme for unsteady calculations. Scalar solver type and implicit temporal discretization is used during these calculations with an Upward Difference (UD) scheme. The program uses implicit methods to solve the algebraic finite-volume equations. Each run during this study lasted approximately 10 hours. The equations are solved either by using the Conjugate gradient (CG) type solvers or the algebraic multigrid (AMG) approach [100].

5.3.2 Computational Domain

For two-dimensional analyses O-type grids are used. The motion is implemented by user defined subroutines by moving the whole computational domain. The grid is a single block hyperbolic grid which is generated by the commercially available mesh generator software,

GRIDGEN. The mesh is fine around the airfoil (i.e. $y^+ = 1$) and gets coarser at the far field. Although, y^+ value is an important issue for turbulent flow simulations, this value is still kept small (around the values appropriate for Large Eddy Simulations or Detached Eddy Simulations) in order to be able to resolve properly the regions dominated by viscous forces at low Reynolds numbers. The mesh size for different airfoil profiles are given in Table 5.1.

Table 5.1 Two-dimensional solution domain details for different airfoil profiles

Profile	Number of cells	Number of vertices	Radius of disc
NACA 0010	16830	34057	~15c
NACA 0012	17226	34849	~15c
NACA 0015	16830	34057	~15c
NACA 6412	14388	29212	~15c

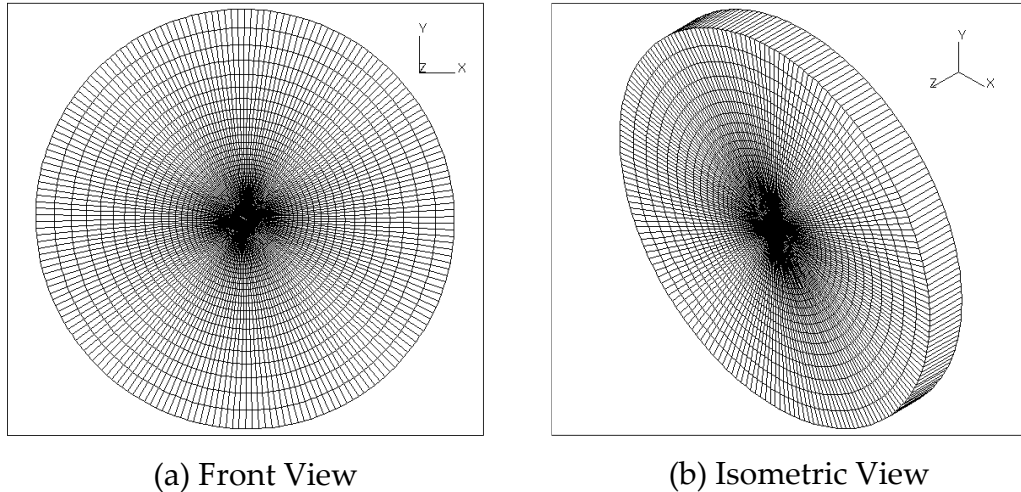


Figure 5.3 (a)-(b) Two-dimensional grid domain for NACA 0012.

Boundary Conditions

The free stream velocity is zero for hovering flapping motion. On the airfoil surface, no-slip boundary condition is applied. The local velocity of the profile which is prescribed by the user defined subroutines calculates the translational and the rotational motion of the model which is also the instantaneous flow velocity. At the far field, the pressure boundary conditions are applied. The far field pressure is assumed to be the standard air pressure. The velocities at the corresponding cell faces are linked to the local pressure gradients by special momentum equations, whose coefficients are equated to those at the cell centers. These equations, together with the continuity constraint, effectively allow the correct calculations of magnitude and directions of the local flow (which may be inwards or outwards) velocities. For 2-D calculations, the front and back

side of the grid domain are defined as symmetry boundary conditions (see Figure 5.4).

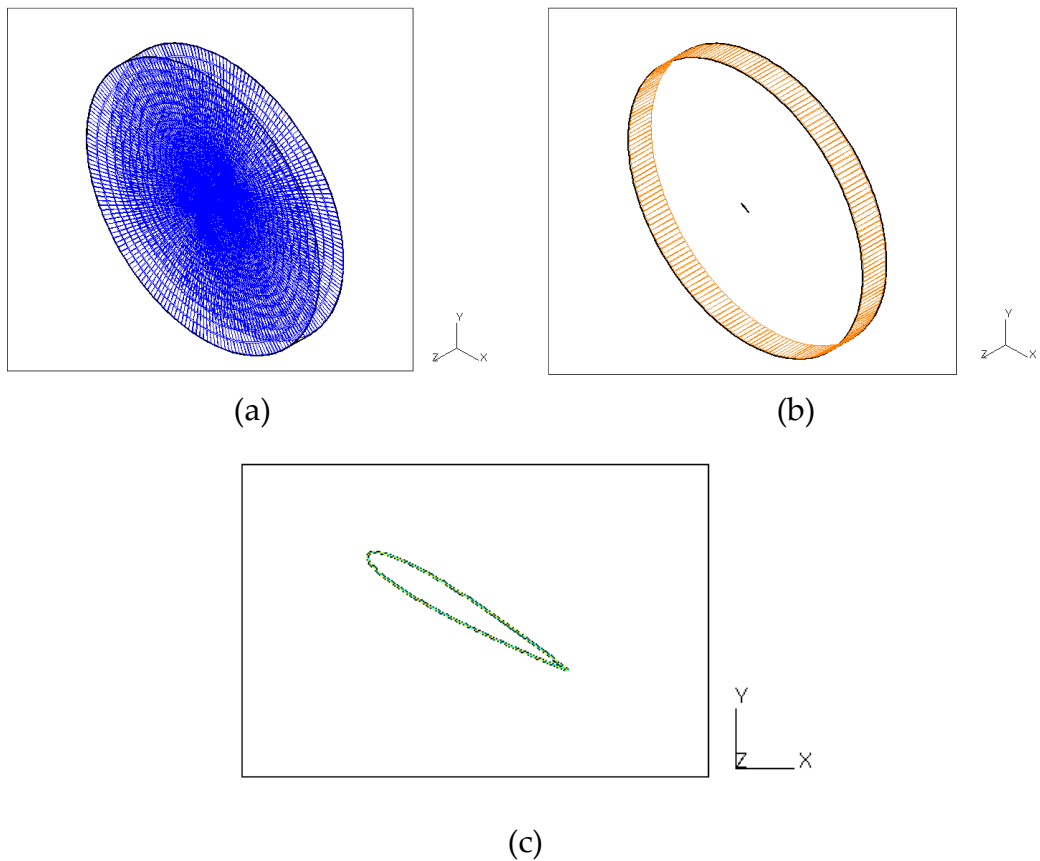


Figure 5.4 Boundary Conditions. (a) Symmetry planes for both sides of the discs, (b) Pressure Boundary for the far field, (c) Wall boundary

In order to determine the far field location and test the solution for grid independency, a grid dependency study was also performed for NACA 6412 profile at a Reynolds number 1000 for an angle of attack $\alpha=45^\circ$. The

total solution domain is chosen such that the upstream is set at least 6 chords length and the downstream is set at 7 chords away from the model, resulting in a total computational domain of 13 chords radius. The solver is tested for two different grid domains and the results are shown below. The 15c and 20c solutions differ only at the positive peak location by a small amount. The solution obtained from the 15 chords radius overestimates the positive peak values when compared to the solution obtained from 20 chords radius. For saving computer time and memory 15 chords radius domain is used during all of the STAR-CD computations.

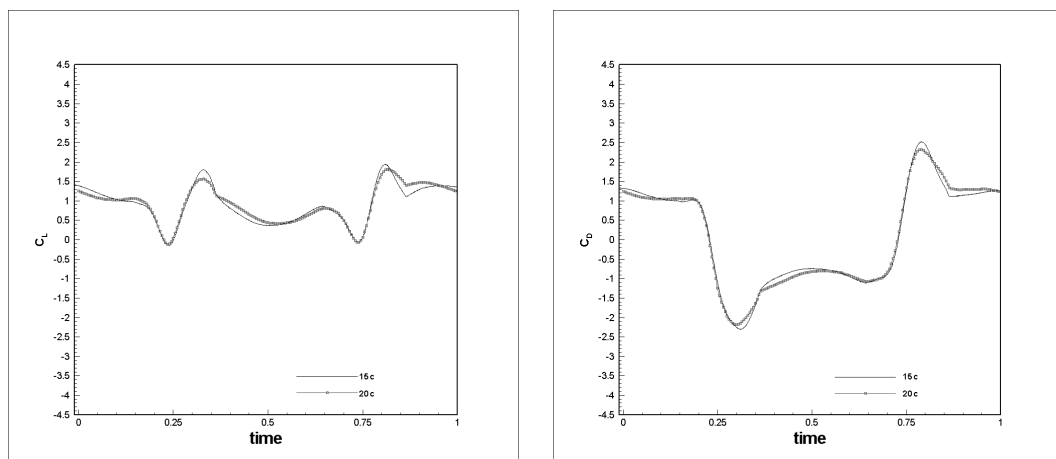


Figure 5.5 Grid dependence study for two dimensional flapping motion analyses

5.3.3 Numerical Parametric Study

Two dimensional flapping wing motion analyses is carried out on a rectangular wing. Although in reality, the wings of insects and birds are fully 3 dimensional having different cross sections at different span wise locations, in this preliminary analysis stage everything is kept simple and only two dimensional analyses is performed to investigate the effects of different parameters, such as the thickness and the camber distributions of the profile on the flapping motion.

5.3.3.1 Effect of Thickness on Flapping Motion

To investigate the effect of profile thickness on the flapping motion, three different symmetrical airfoils, namely NACA 0010, NACA 0012 and NACA 0015, having different thicknesses are solved for the same angle of attack of 30 degrees. The lift and drag coefficients values for these airfoils are compared.

As stated previously, all of the numerical solutions are done using the STAR-CD software. In Figure 5.6, the computational domain for each symmetrical airfoil is shown.

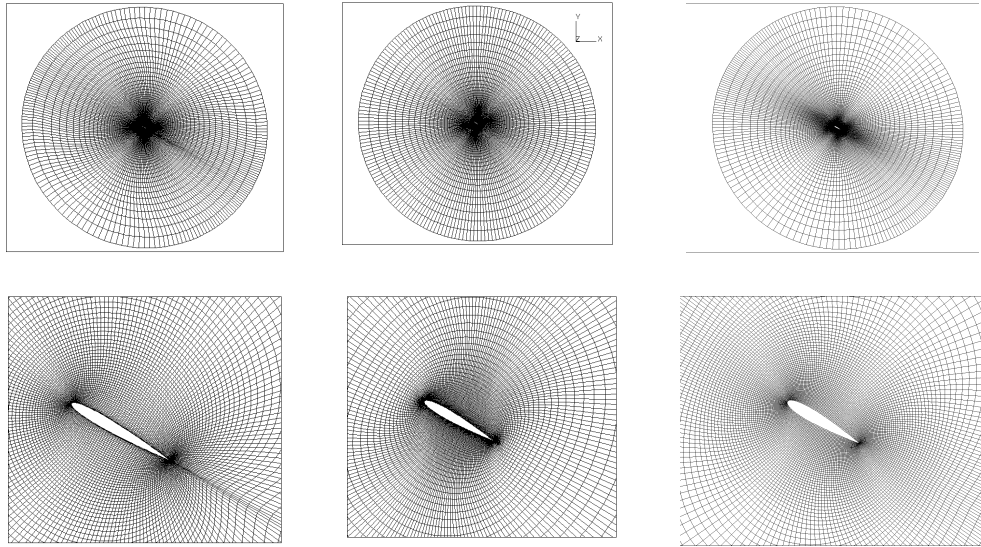


Figure 5.6 Computational mesh for NACA 0010 (1st column), NACA 0012 (2nd column) and NACA 0015 (3rd column) (a) full mesh, (b) closer view around the profile.

The effect of thickness variation in two-dimensional flapping motion is analyzed for three different airfoil profiles having different thicknesses and for three different angles of attack. The variation of aerodynamic force coefficients are compared over two non-dimensionalized periods. There exists two positive and two negative peaks in one period of simulation. The first positive peak occurs at the end of the first half downstroke, namely during the pronation phase and the second one occurs at the end of the second downstroke phase, namely in the supination phase.

At $\alpha = 30^\circ$ for which the variation of aerodynamic force coefficients are presented, the maximum lift coefficient is observed for the profile having the maximum thickness. It should be noted that the NACA 0010 and

NACA 0012 have similar behavior in lift coefficient variations with time. The negative peaks corresponding to the minimum lift coefficient values; the profile which has the minimum thickness has the minimum lift coefficient value. For drag coefficient variation with time, two peaks are observed: one is a negative peak and the other one is a positive peak. The effect of thickness at angle of attack $\alpha = 30^\circ$ can be seen more clearly in drag coefficient variation with time. As seen in this plot, NACA 0015, the thickest profile, has the lowest drag coefficient at the positive peak whereas it has the highest drag value at the negative peak. In flapping motion, the force coefficient in the flow direction can be either a drag or thrust (which is equal to a negative drag for forward flapping flight, i.e. when the forward velocity is not equal to zero). In hovering flight, i.e. when the forward flight velocity is zero, the mean drag coefficient should sum up to zero for one period. The drag variation curves also shows the thrust characteristics of the profiles when they are used in forward flapping flight.

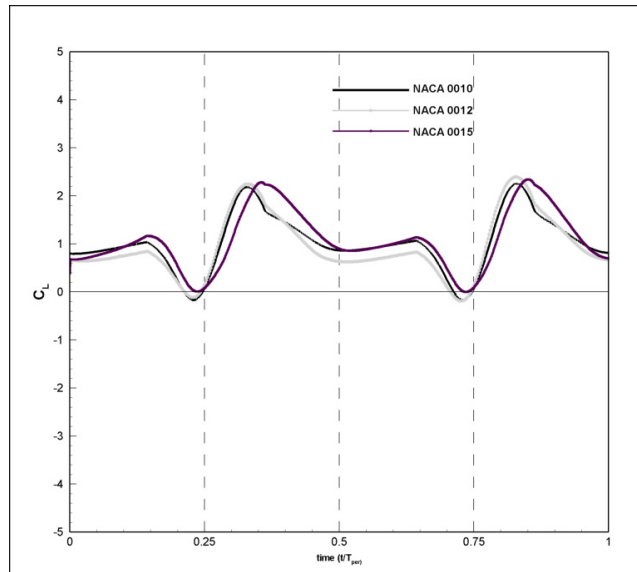


Figure 5.7 Lift coefficient distribution with respect to time for $\alpha=30^\circ$, $x_v=2c$, $Re=1000$ with rotation axis at $1/4c$ for one period.

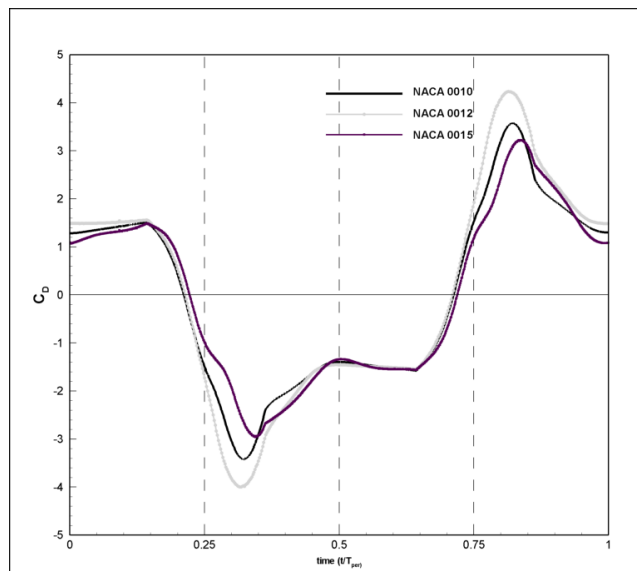


Figure 5.8 Drag coefficient distribution with respect to time for $\alpha=30^\circ$, $x_v=2c$, $Re=1000$ with rotation axis at $1/4c$ for one period.

Effect of thickness is analyzed at different angles of attack by Sarigöl et al [102]-[103]. The increase in angle of attack causes a decrease in drag coefficient values for all profiles. The lift coefficient distributions are strongly dependent on the starting angle of attack regardless of the profile thickness.

The results of numerical simulations are also analyzed using the vortex identification techniques as described in Chapter 3. Non-dimensional vorticity contours are drawn for visualizing the vortices generated during flapping motion. The identification of vertical flow regions are done mostly via non-dimensional Q and λ_2 contours technique. Figures 5.9- 5.11 present the vortex regions for a quarter period during both the translational and rotational motions.

During the first half downstroke, a vortex at the leading edge is created. This leading edge vortex is the primary cause for the generation of lift during the translational motion. Then the airfoil starts to rotate and the previously formed leading and trailing edge vortices start to separate from the profile while new vortices are created at the leading and trailing edges during this rotational phase which is called "pronation". Since the direction of the motion is changing following this rotation the newly forming vortices rotate in the opposite direction, i.e. leading edge vortex is in cold color while translating during the first half downstroke but it is presented in warm colors when the airfoil changes its direction. For simplicity and ease of comparison all of the results are presented in terms of non-dimensional time steps defined as:

$$t^* = \frac{t}{T_{per}} \quad (5.5)$$

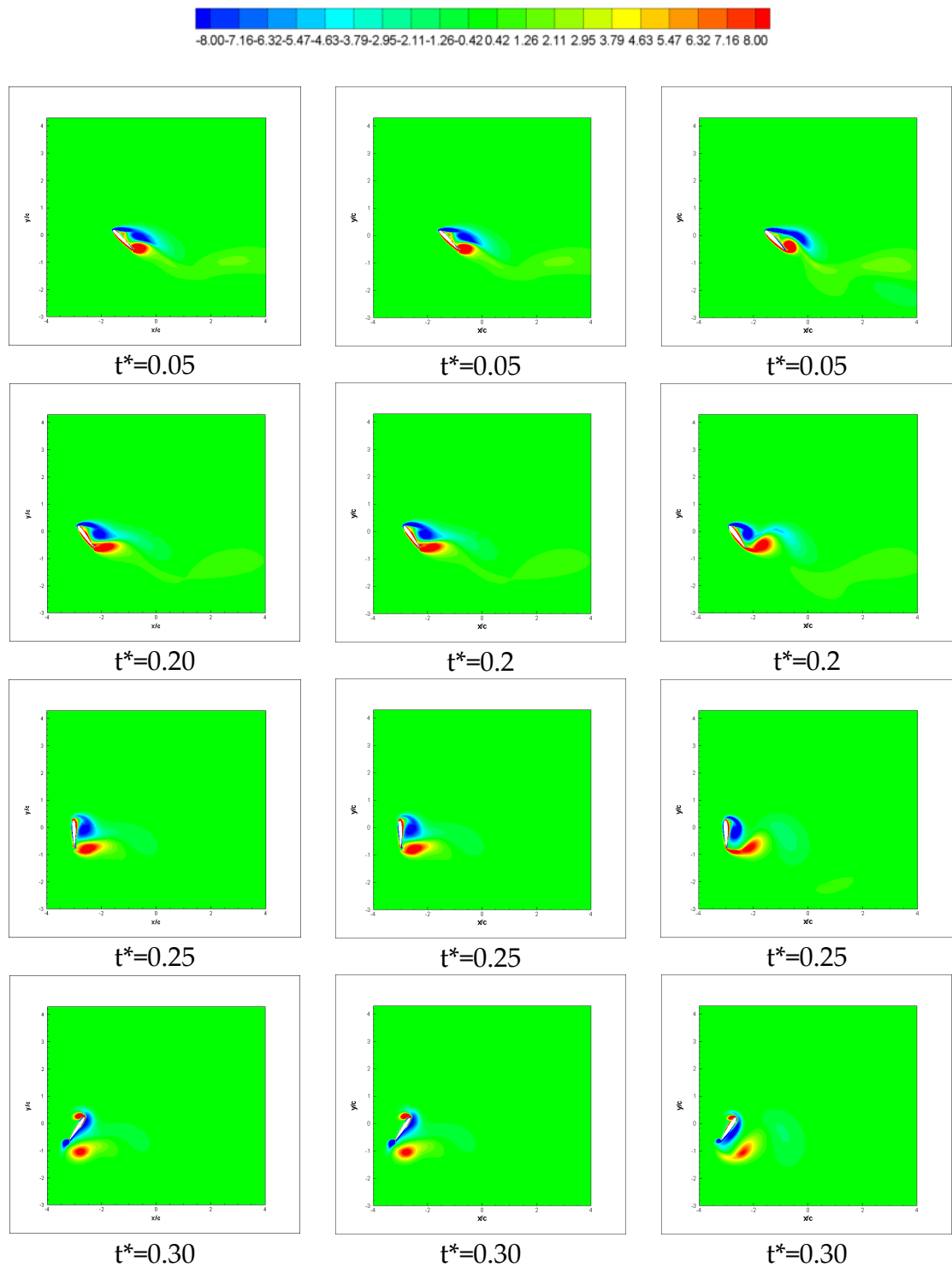


Figure 5.9 Non-dimensional vorticity contours of NACA 0010 (1st column), NACA 0012 (2nd column) and NACA 0015 (3rd column) during the first half downstroke for $\alpha=45^\circ$, $x_v=2c$, $Re=1000$.

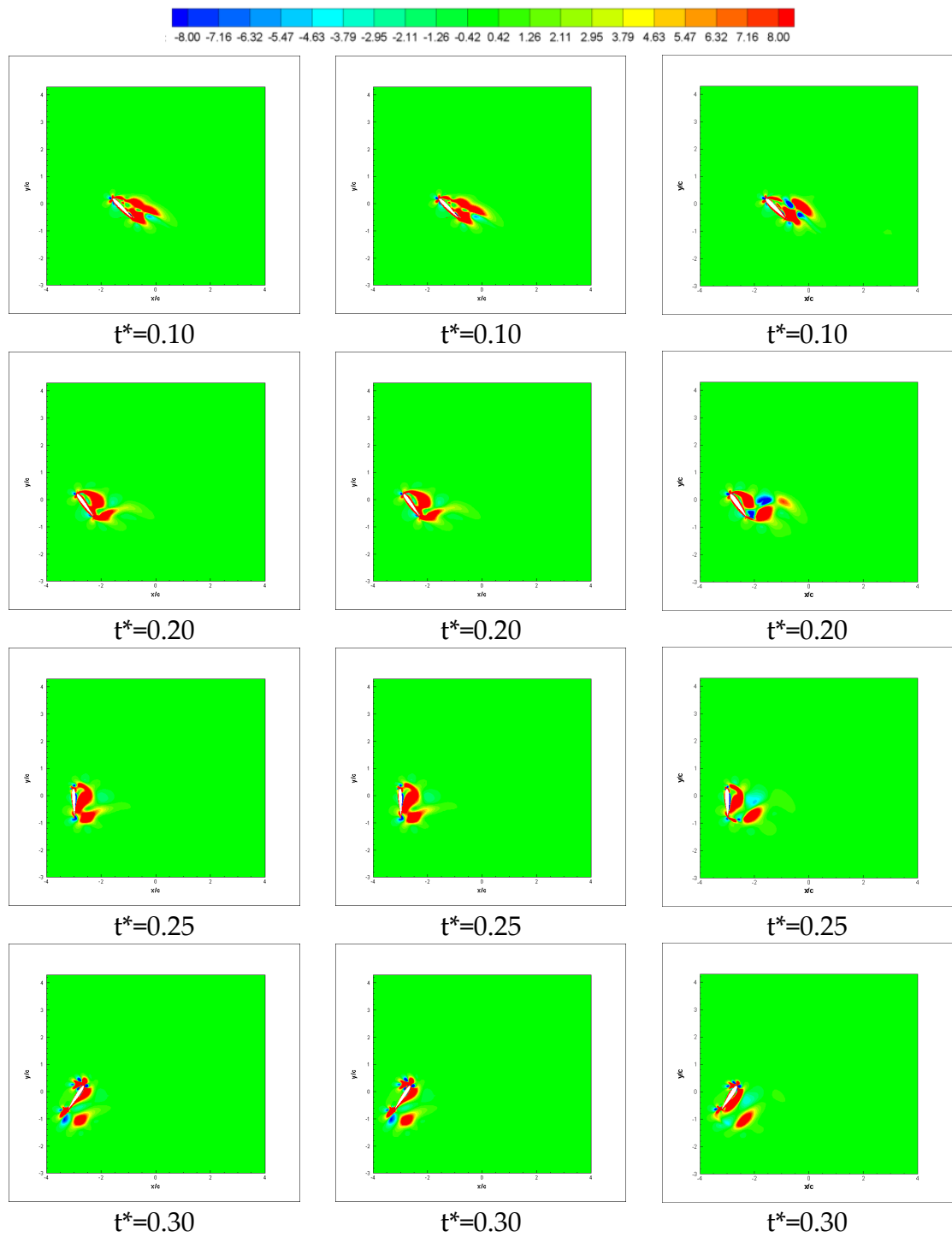


Figure 5.10 Non-dimensional Q (second invariant of velocity gradient) contours of NACA 0010 (1st column), NACA 0012 (2nd column) and NACA 0015 (3rd column) during the first half downstroke for $\alpha=45^\circ$, $x_v=2c$, $Re=1000$.

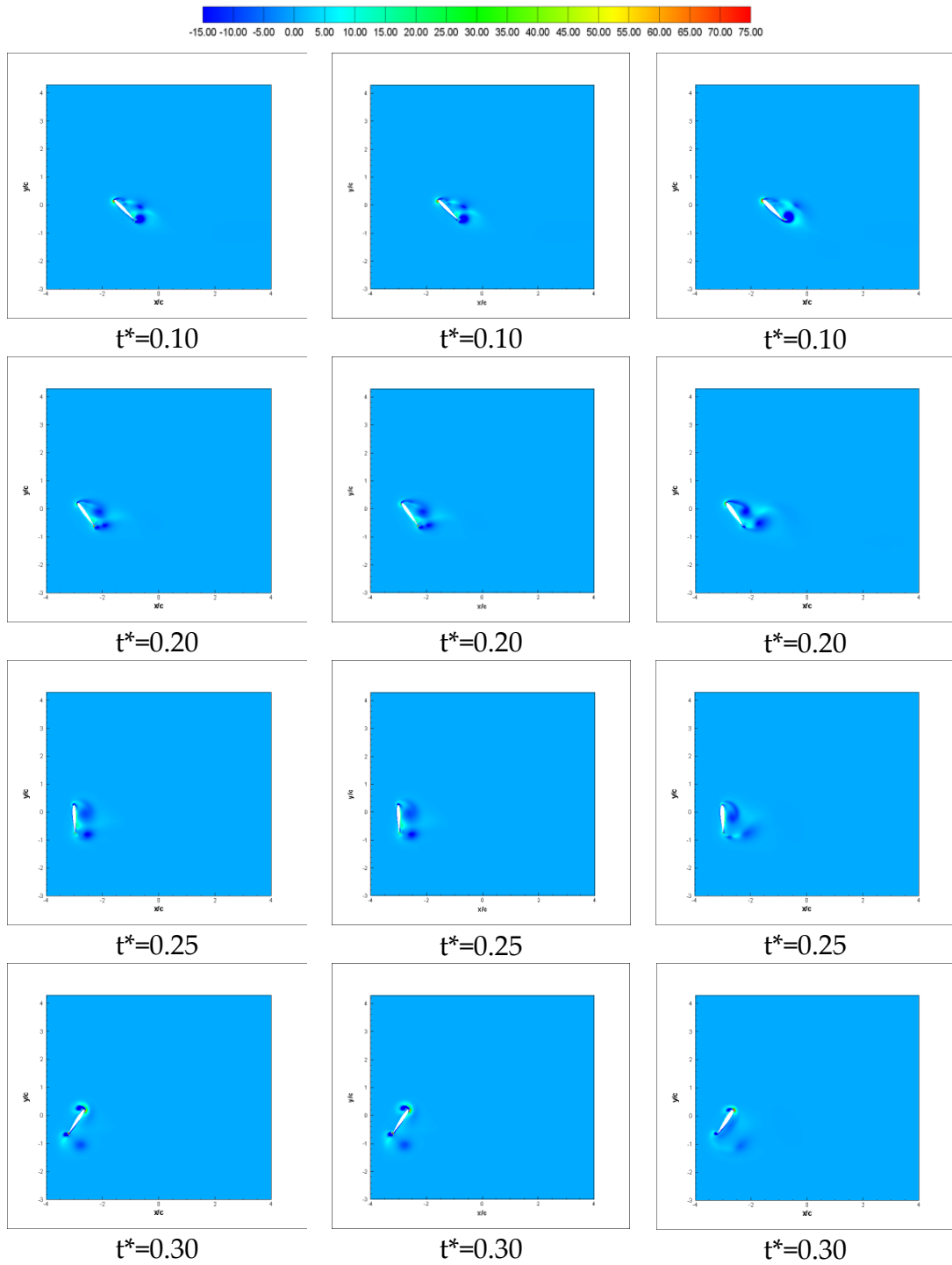


Figure 5.11 Non-dimensional λ_2 (second negative eigenvalue of $(S^2 + \Omega^2)$) contours NACA 0010 (1st column), NACA 0012 (2nd column) and NACA 0015 (3rd column) during the first half downstroke for $\alpha=45^\circ$, $x_v=2c$, $Re=1000$.

The effect of starting angles of attack on aerodynamic performances of the symmetric profiles is also investigated. The aerodynamic force coefficient variations with respect to time have been drastically affected with the angle of attack change. The thinnest profile, NACA 0010, achieved the maximum lift coefficient values for $\alpha=60^\circ$ whereas the absolute drag coefficient peak values showed a decrease when the angle of attack is $\alpha=60^\circ$. On the other hand, NACA 0012 obtained maximum absolute peak values at $\alpha=30^\circ$. In a similar fashion, NACA 0015 having the maximum thickness showed a similar behavior. The aerodynamic force coefficients were higher for 30° and 45° angles of attack. [102]- [103].

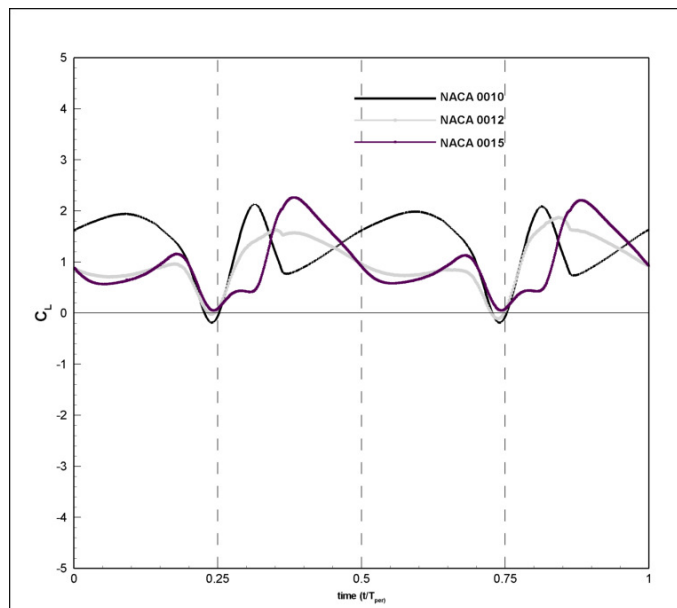


Figure 5.12 Lift coefficient variations with respect to time for $\alpha=45^\circ$, $x_v=2c$, $Re=1000$ with rotation axis at $\frac{1}{4}c$ for one period.

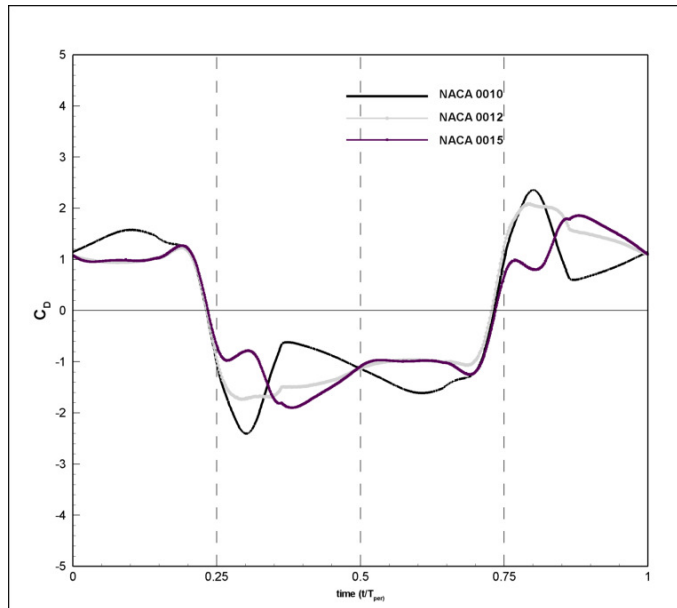


Figure 5.13 Drag coefficient variations with respect to time for $\alpha=45^\circ$, $x_v=2c$, $Re=1000$ with rotation axis at $\frac{1}{4}c$ for one period.

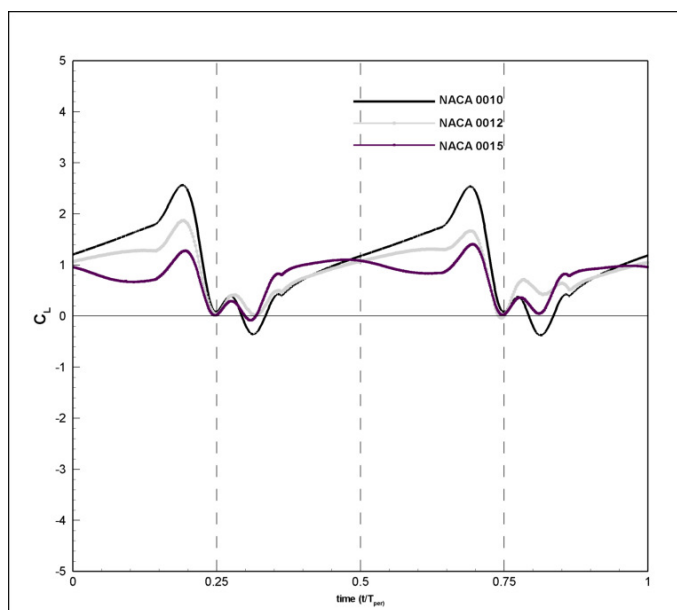


Figure 5.14 Lift coefficient variations with respect to time for $\alpha=60^\circ$, $x_v=2c$, $Re=1000$ with rotation axis at $\frac{1}{4}c$ for one period.

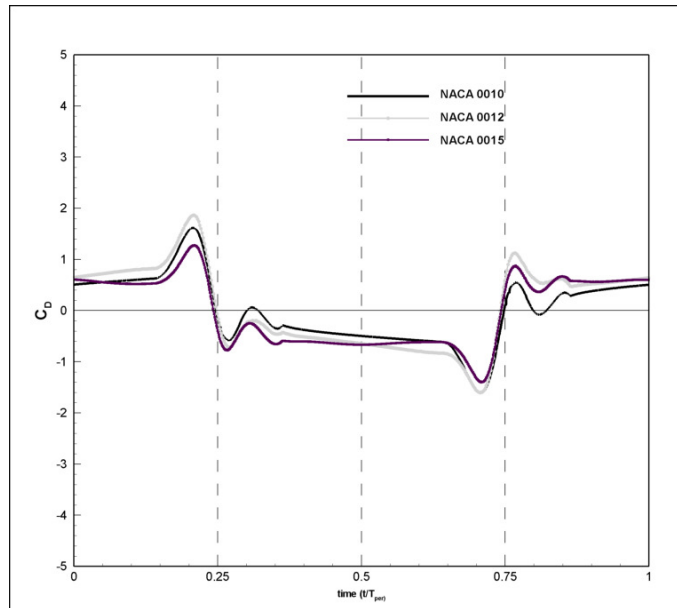


Figure 5.15 Drag coefficient variations with respect to time for $\alpha=60^\circ$, $x_v=2c$, $Re=1000$ with rotation axis at $1/4c$ for one period.

Lift-to-drag ratio is the amount of lift generated by a wing compared to the drag it creates while moving through the air. In steady state aerodynamics, a higher L/D ratio is preferred since the lift needed for a particular air vehicle does not change but achieving this lift with lower drag leads to better aerodynamic performance and economy. In Figure 5.16, lift to drag ratio variation of symmetric profiles are compared at $\alpha=30^\circ$. During the rotational phases, the drag drops to very small values and may even become zero. Therefore this leads to very high lift-to-drag ratio values. One of these extremely high peak values is positive and the other is negative. Keeping in mind that the direction of drag force changes when the profile changes its direction of motion, it would be wiser to consider the absolute value of this ratio. Excluding these peak values, the

absolute value of the lift-to-drag ratio is nearly constant during the translational phases of the period.

At $\alpha=45^\circ$, higher peak values for lift and drag coefficients are observed during the rotational phases when compared to the ones observed at $\alpha=30^\circ$ (Figure 5.17). At this angle of attack, excluding the peak values, the constant tendency of the lift-to-drag ratio is lost but there is almost a linear variation. These linear variations of lift-to-drag ratios are observed during the translational phases, i.e. when the speed or the angle of attack does not change.

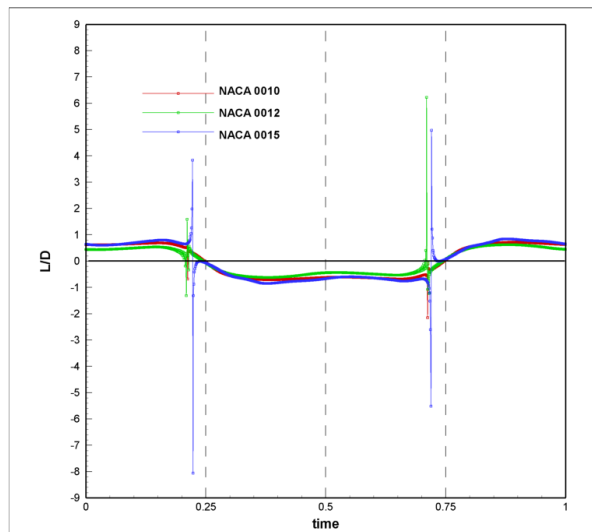


Figure 5.16 Lift to drag ratio variation over one period at $\alpha=30^\circ$, $x_v=2c$, $Re=1000$

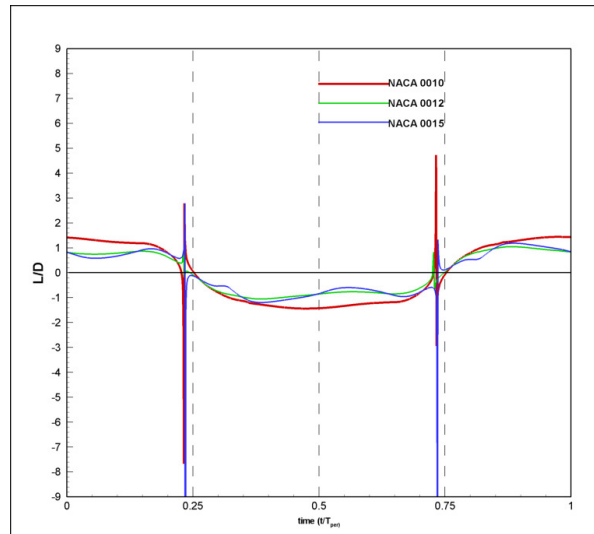


Figure 5.17 Lift to drag ratio variation over one period at $\alpha=45^\circ$, $x_v=2c$, $Re=1000$

At $\alpha=60^\circ$, the peak values of the L/D ratios for thinnest profile is very large and becomes out of the range considered for the small set angles of attack (Figure 5.18). For NACA 0012 and NACA 0015, the absolute values of these peaks are nearly of the same order of magnitude to the ones obtained at smaller angles of attack. The constancy of lift-to-drag ratio is clearly lost at higher angles of attack and there is clearly a linear variation with respect to the position of the profile during the translational phases of the motion.

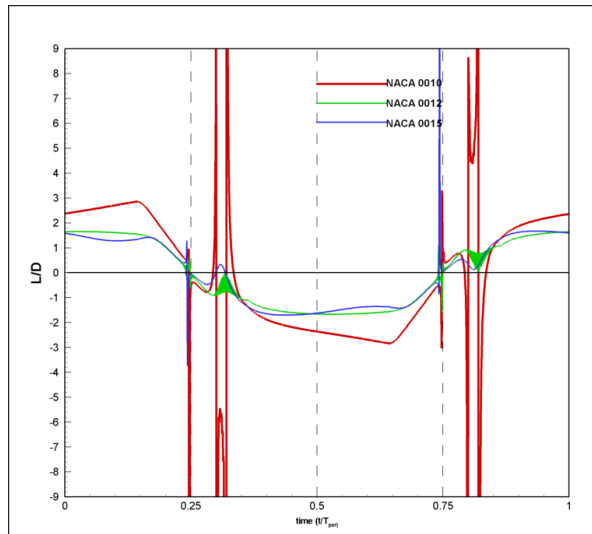


Figure 5.18 Lift to drag ratio variation over one period at $\alpha=60^\circ$, $x_v=2c$, $Re=1000$

The pressure contours of symmetric airfoils are presented in Figure 5.19 in order to see if the minimum pressure regions coincide with the vortex regions identified by the non-dimensional Q (second invariant of velocity gradient) or λ_2 (second negative eigenvalue of $S^2+\Omega^2$) contours. Q values are the laplacian of pressure (Eqn. 4.10). The minimum pressure regions will be at the vortex cores which will correspond to center of pressure suction peaks although there is no explicit connection between a region with $Q \geq 0$ and a region containing a pressure minimum. When the vortex regions identified by the non-dimensional Q (second invariant of velocity gradient) or λ_2 (second negative eigenvalue of $S^2+\Omega^2$) contours are compared to pressure minimum regions, it is seen that the vortex cores of leading and trailing edge vortices do coincide.

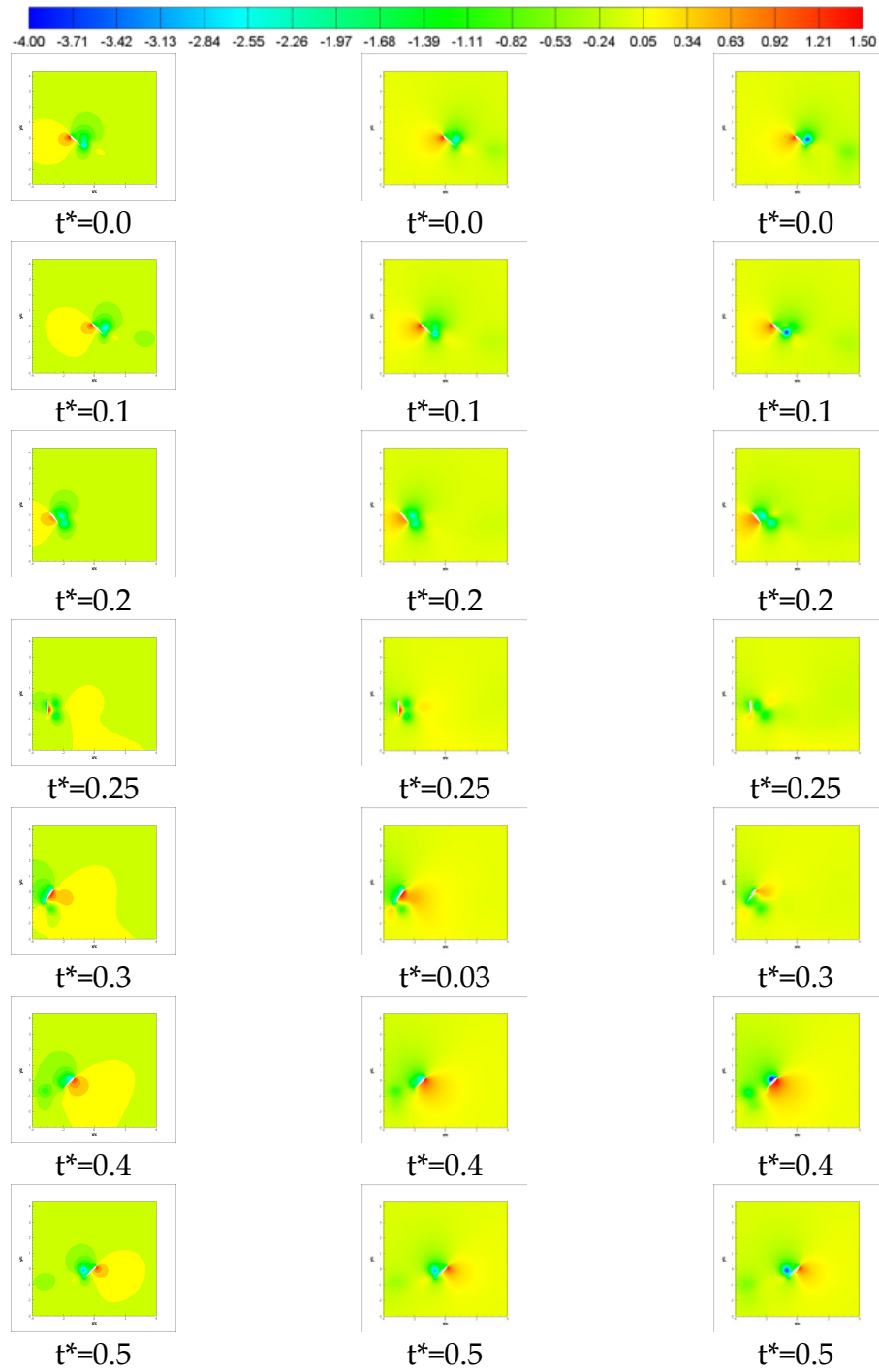


Figure 5.19 Pressure contours of NACA 0010 (1st column), NACA 0012 (2nd column) and NACA 0015 (3rd column) for $\alpha=45^\circ$, $x_v=2c$, $Re=1000$.

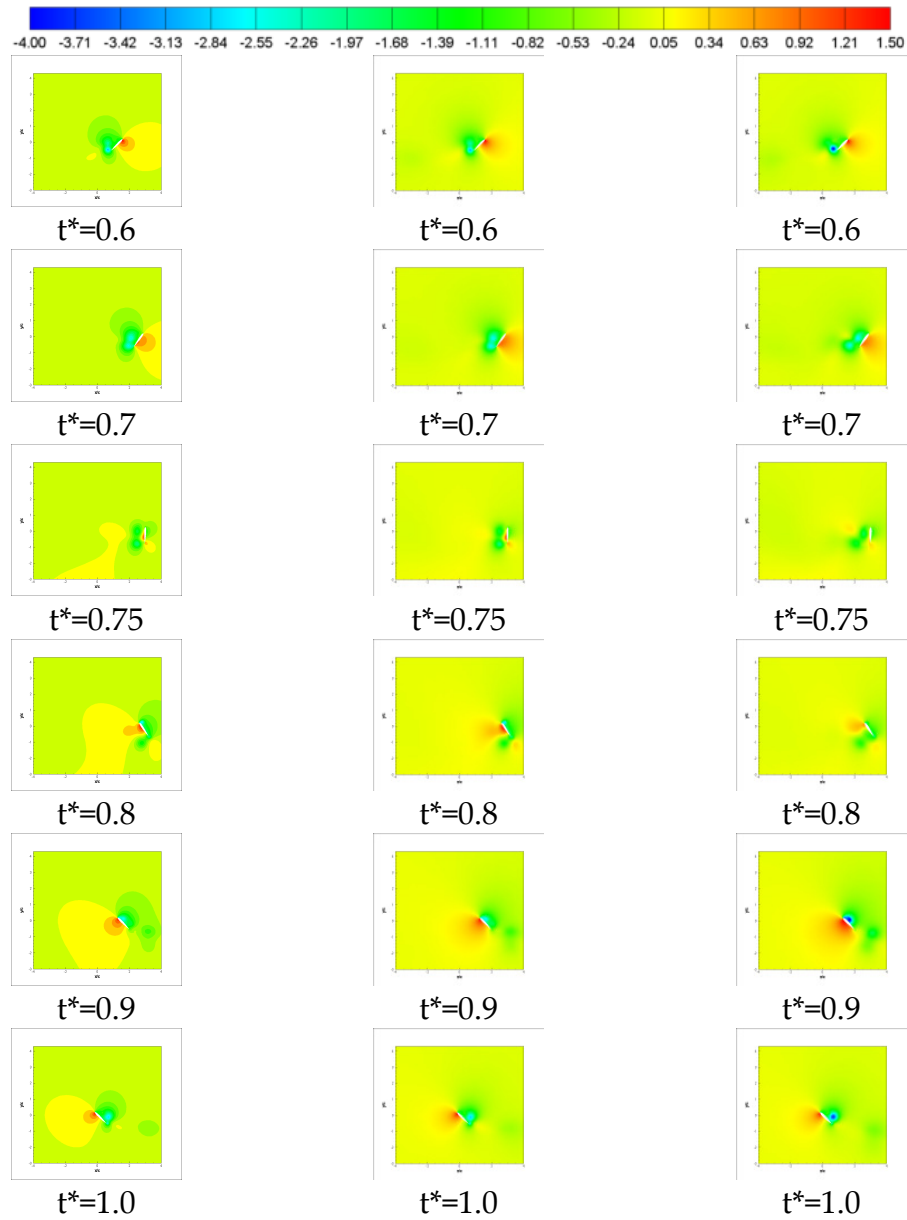


Figure 5.19 (Continued) Pressure contours of NACA 0010 (1st column), NACA 0012 (2nd column) and NACA 0015 (3rd column) for $\alpha=45^\circ$, $x_v=2c$, $Re=1000$.

5.3.3.2 Effect of Camber on Flapping Motion

The aim in this investigation was to see the effect of the camber on the lift and drag generated during the two-dimensional flapping motion. The lift and drag values calculated for a cambered airfoil profile are compared to the values calculated for a symmetrical airfoil such as NACA0012. The chosen cambered profile is NACA 6412. The thickness value is chosen same as in the symmetric case so that it would be possible to make a comparison in terms of lift and drag coefficients. The computational domain is kept nearly the same as for the symmetrical airfoils for comparison purposes. For comparison only the last two periods have been chosen in order to avoid all the impulsive starting effects on the calculated results. As in the previous analysis for the thickness effect, the numerical simulation of flapping motion for the cambered profile has been performed for three different angles of attack and for two different Reynolds numbers.

As shown in Figure 5.19, NACA 6412 is a four digit, subsonic airfoil which combines a 12% thickness with a two-digit 64 camber line. A “64 camber line” has 6% maximum camber at 40% chord location.

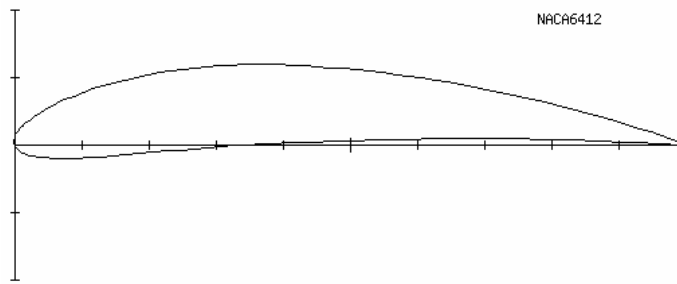


Figure 5.20 NACA 6412 airfoil profile

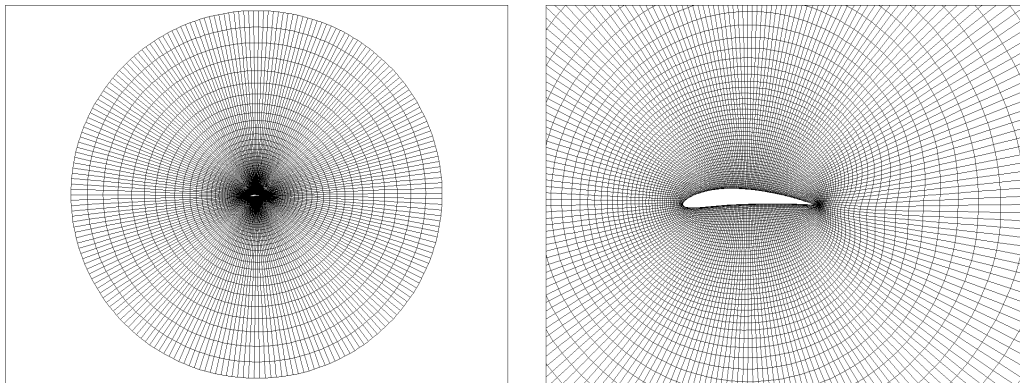


Figure 5.21 Computational mesh for NACA 6412

In Figures 5.22-5.27, the effect of camber is compared to symmetrical airfoil, NACA0012, in terms of aerodynamic force coefficient variations at each angle of attack. For $\alpha = 30^\circ$ angle of attack, the positive peak values of the coefficients are higher for the cambered profile whereas the negative peak values do not differ much from that of the symmetrical airfoil case especially in lift coefficient variation. It is also seen that the lift coefficient distribution is smoother and the peak values are slightly higher than that

of the NACA 0012, the symmetric profile, for $\alpha=30^\circ$. Again for this angle of attack, the drag coefficient curve has higher peak values and smoother distribution than that of NACA 0012.

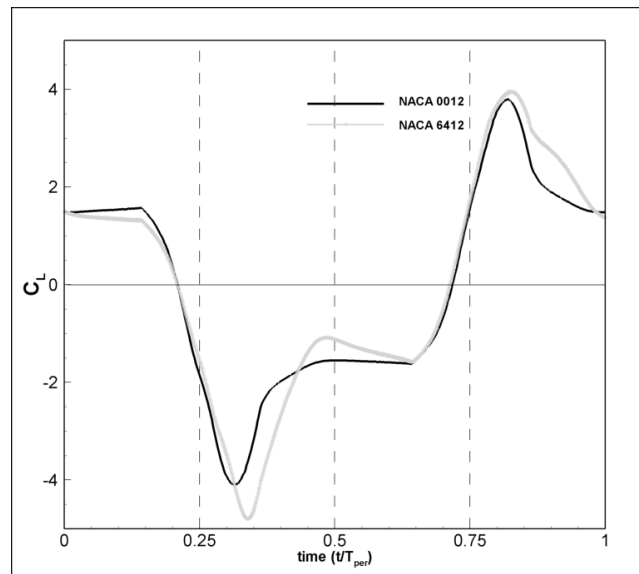


Figure 5.22 Comparison of drag coefficients of NACA 6412 and NACA 0012 for $Re = 1000$ at $\alpha = 30^\circ$

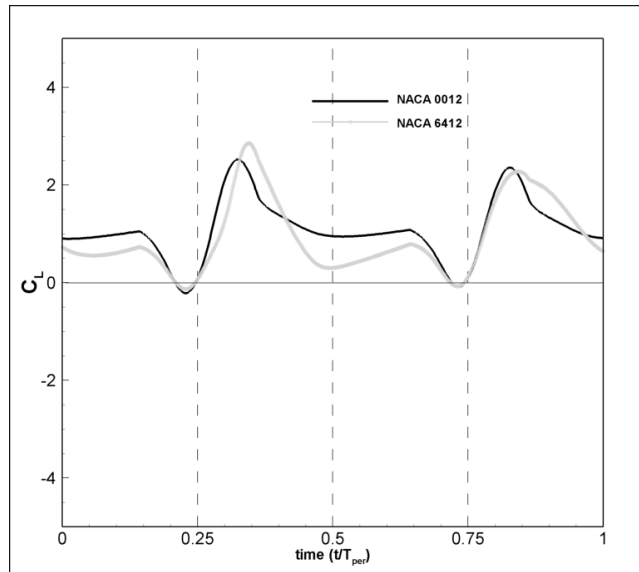


Figure 5.23 Comparison of lift coefficients of NACA 6412 and NACA 0012 for $Re = 1000$ at $\alpha = 30^\circ$

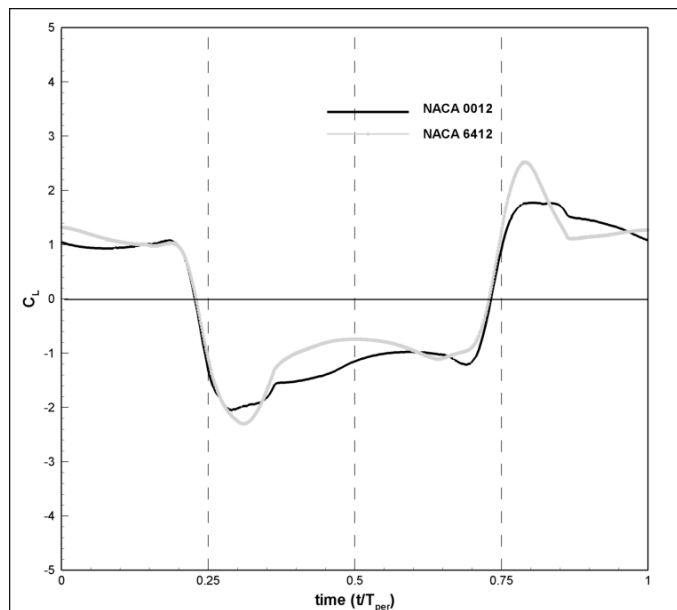


Figure 5.24 Comparison of drag coefficients of NACA 6412 and NACA 0012 for $Re = 1000$ at $\alpha = 45^\circ$

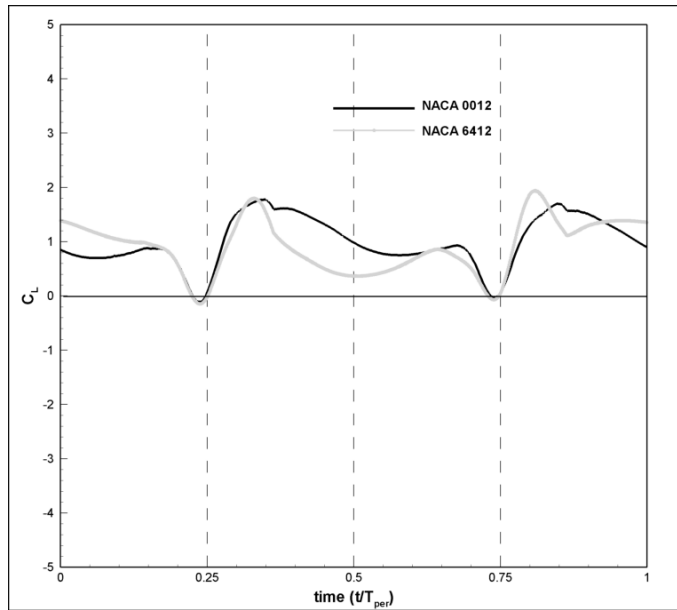


Figure 5.25 Comparison of lift coefficients of NACA 6412 and NACA 0012 for $Re = 1000$ at $\alpha = 45^\circ$

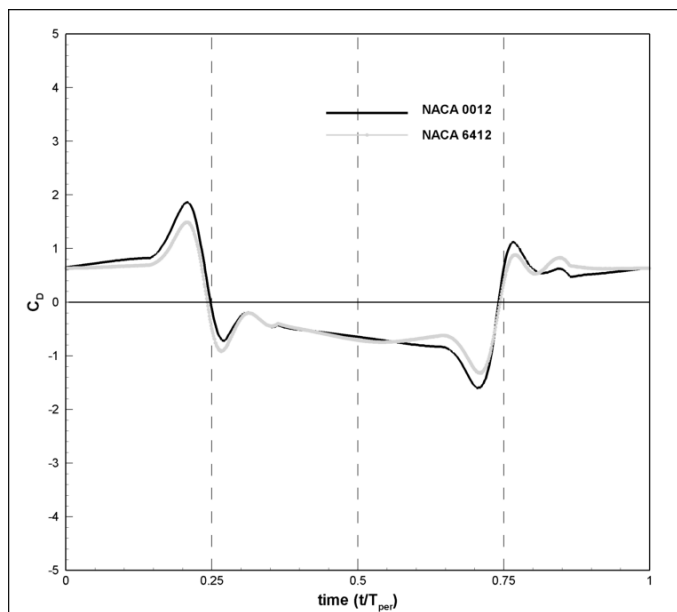


Figure 5.26 Comparison of drag coefficients of NACA 6412 and NACA 0012 for $Re = 1000$ at $\alpha = 60^\circ$

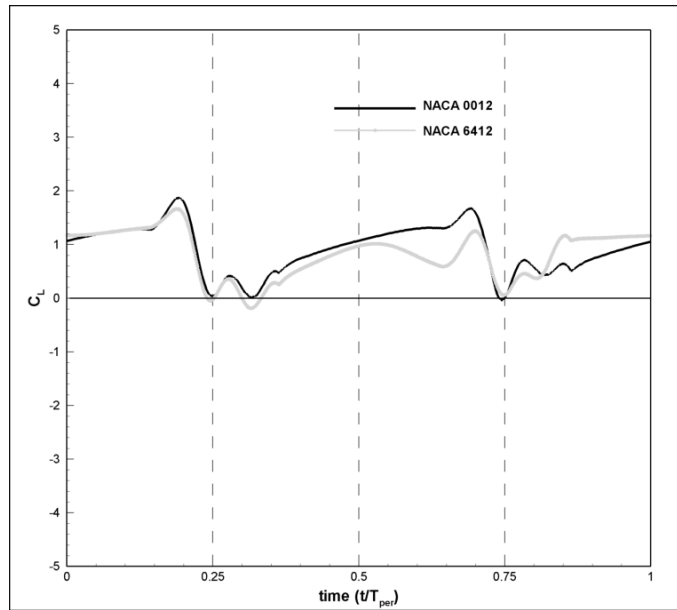


Figure 5.27 Comparison of lift coefficients of NACA 6412 and NACA 0012 for $Re = 1000$ at $\alpha = 60^\circ$

As the angle of attack increases the shape of the drag coefficient variation curves change. For $\alpha=45^\circ$, the lift and drag coefficients are higher than the symmetric case as well as the peak values. For $\alpha=60^\circ$, symmetric airfoil gives better results than the cambered one.

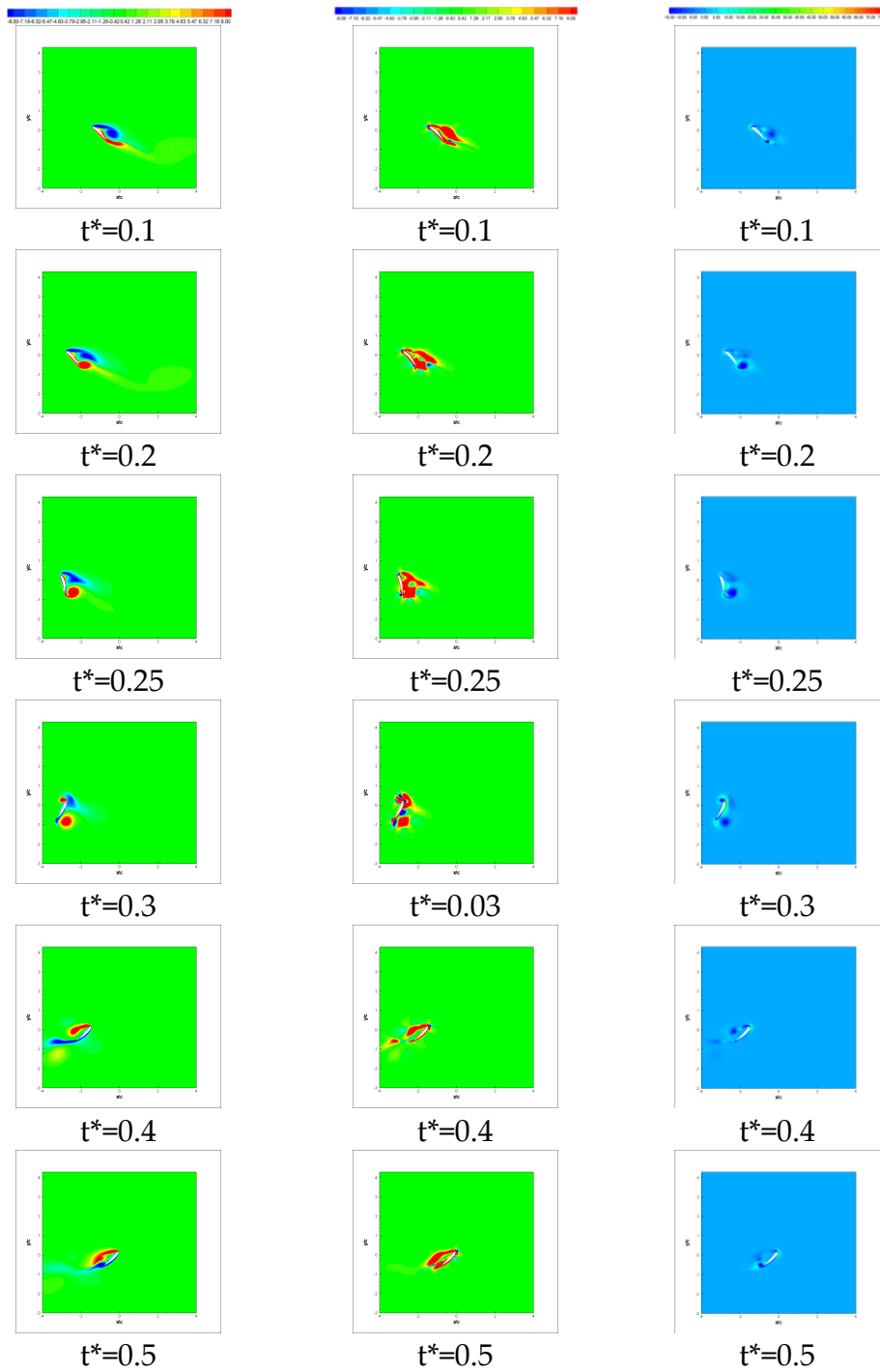


Figure 5.28 Identification of vortex regions of NACA 6412 by non-dimensional vorticity (1st column), second invariant of velocity gradient, Q criteria (2nd column) and, λ_2 contours, second negative eigenvalue of $(S^2 + \Omega^2)$ (3rd column) during the first half period for $\alpha=45^\circ$, $x_v=2c$, $Re=1000$.

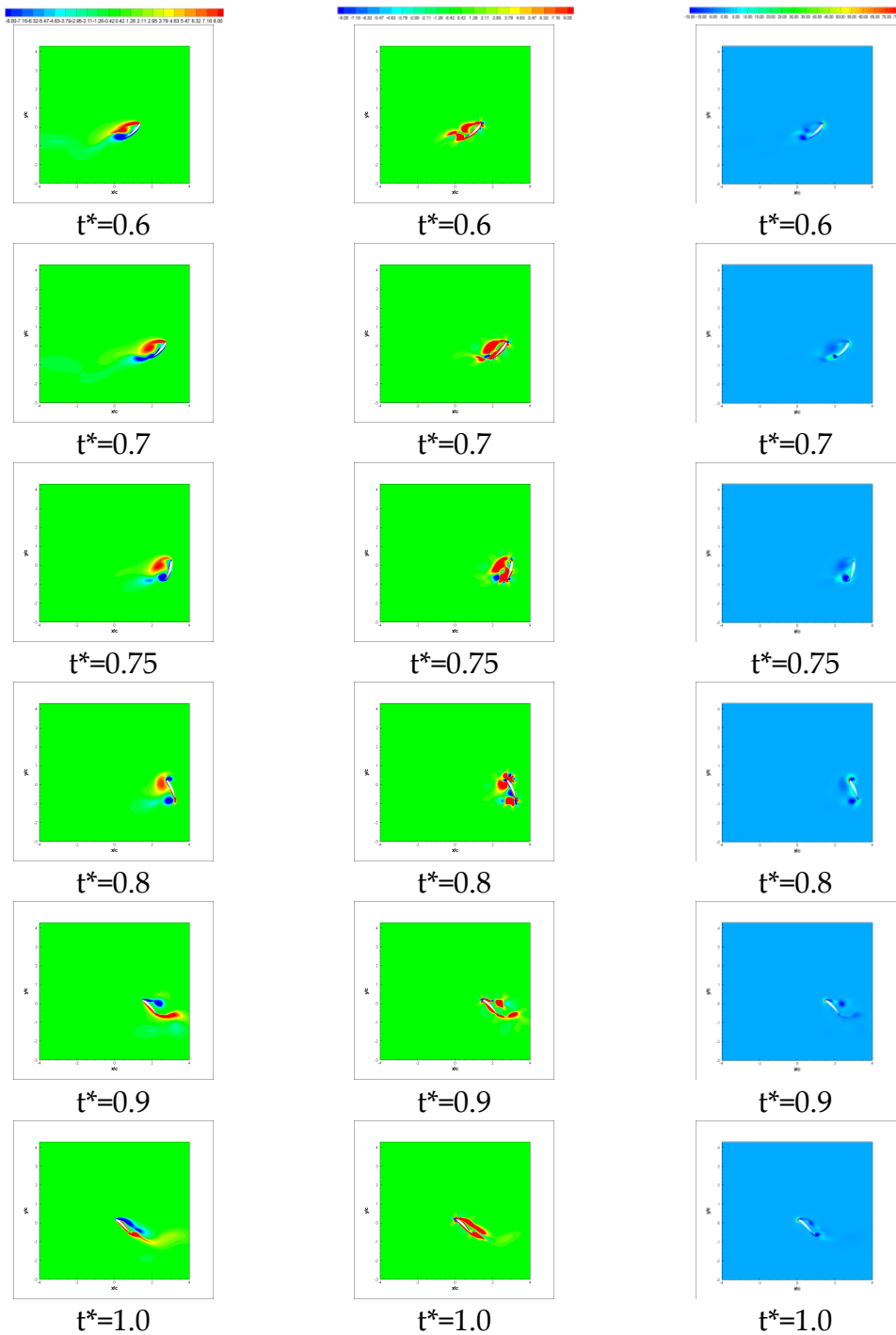


Figure 5.28 (continued) Identification of vortex regions of NACA 6412 by non-dimensional vorticity (1st column), second invariant of velocity gradient, Q criteria (2nd column) and, λ_2 contours, second negative eigenvalue of $(S^2 + \Omega^2)$ (3rd column) during the second half period for $\alpha=45^\circ$, $x_v=2c$, $Re=1000$.

When the drag coefficients calculated at a Reynolds number of 1000 are examined, the effect of starting angle of attack is clearly evidenced. As the angle of attack decreases the drag coefficient decreases. The lift coefficient is much higher for $\alpha=30^\circ$ angle of attack and there is a decrease as the angle of attack increases. The timing for peak positions is similar for $\alpha=30^\circ$ and $\alpha=45^\circ$ but there is a significant difference for $\alpha=60^\circ$ which may be due to separation of the flow.

The effect of camber can most easily be seen when the airfoil is in the rotational phase of the motion (during the pronation or supination phases). In Figure 5.29, the vortex regions are identified using the techniques described in Chapter 3. As it can be seen the major change is the shape of leading edge vortex, which is more attached to the profile when it is symmetric and more prone to detach when it is cambered. Moreover, the trailing edge vortex is slightly larger for the cambered profile.

The effect of angle of attack together with the camber effect is identified at the pronation phase. For angles of attack less than 30° , the shape of the profile is immaterial. It does not matter whether it is symmetric or cambered. But when the angle of attack is increased beyond 30° , the leading and trailing edge vortices evolve readily and newly forming vortices can easily and clearly be identified. For $\alpha=30^\circ$ angle of attack, the trailing edge vortex has already separated from NACA 0012 but for NACA 6412 it is still attached which is a desired condition for getting more lift and thrust. For $\alpha=45^\circ$ angle of attack, similar behavior is observed for both profiles but the regions enclosed by trailing and leading

edge vortices are much bigger when compared to NACA 0012. For $\alpha=60^\circ$ angle of attack, the trailing edge vortex is much closer and seems more attached in NACA 6412.

NACA 6412 profile was also tested at two different Reynolds numbers in order to see the Reynolds number effect. Following figures show the effect of Reynolds number at each starting angle of attack. For all angles of attack it is clear that there is a time wise shift in the peak occurrence as well as magnitude wise. For small angles of attack as the Reynolds number increases the lift and drag coefficients are also increased. For $\alpha=45^\circ$ and for $\alpha=60^\circ$, the magnitude of the lift and the drag coefficients have not been affected significantly from the Reynolds number but there is a time wise shift in the peak occurrence: i.e. peaks do occur earlier than before. Due to this reason power density spectrum analyses were also carried out to see the differences of the results.

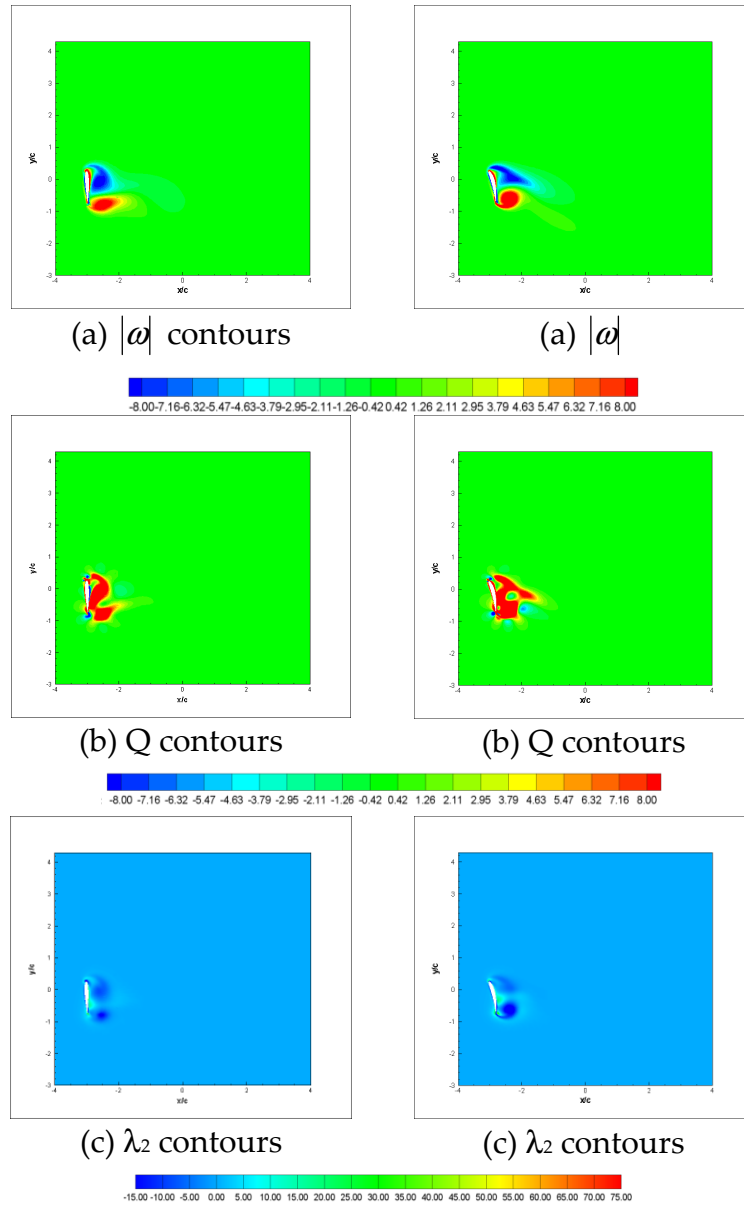


Figure 5.29 Comparison of vortex regions of NACA 0012 (left) and NACA 6412 (right) by non-dimensional vorticity contours, second invariant of velocity gradient tensor, Q contours and second negative eigenvalue of $(S^2 + \Omega^2)$, λ_2 contours at the end of the first half downstroke ($t^* = 0.25$) for $\alpha = 45^\circ$, $x_v = 2c$, $Re = 1000$.

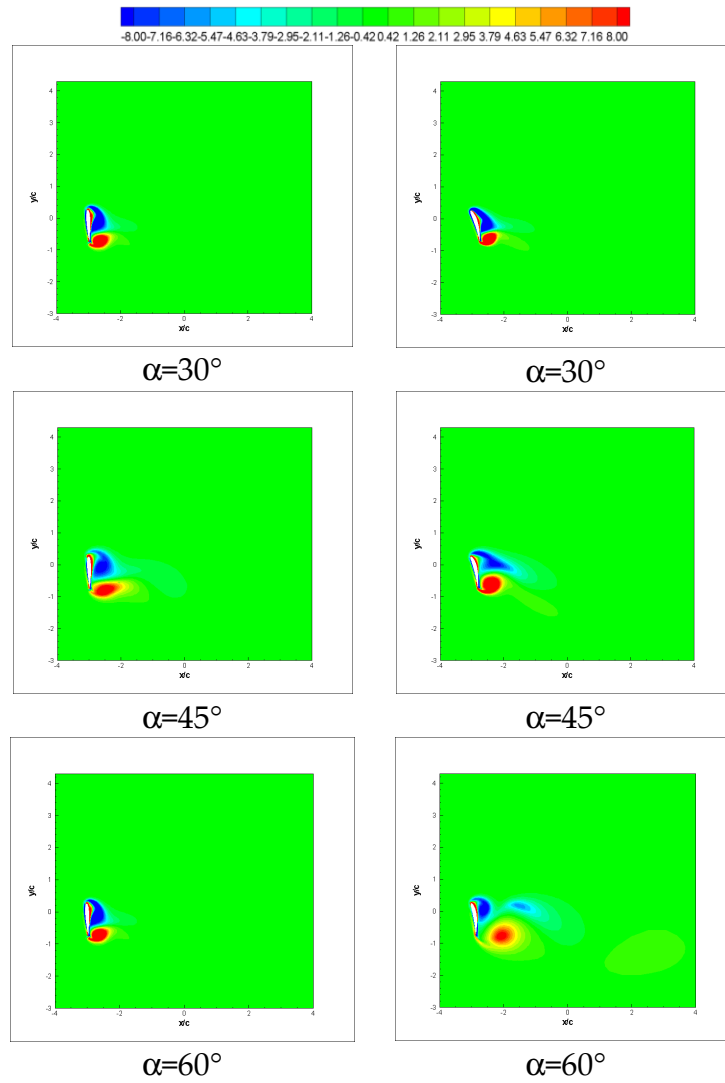


Figure 5.30 Comparison of vortex regions of NACA 0012 (left) and NACA 6412 (right) by non-dimensional vorticity contours at different angles of attack at the end of the first half downstroke ($t^*=0.25$).

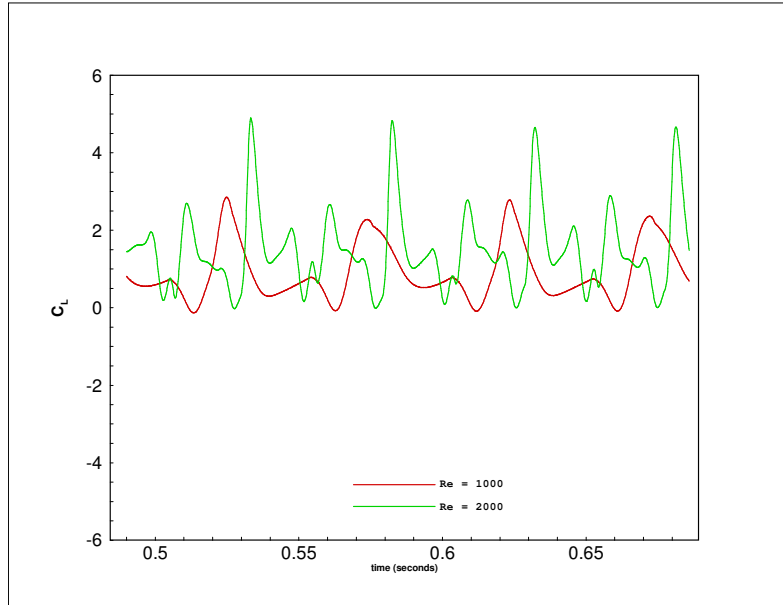


Figure 5.31 Lift coefficient variation versus Reynolds number comparison for NACA 6412 at $\alpha=30^\circ$.

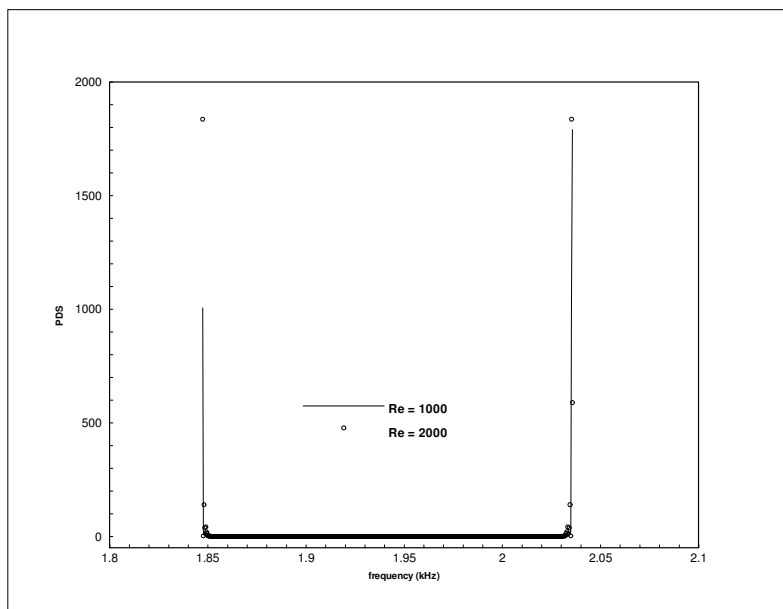


Figure 5.32 Power density spectrum analysis for Reynolds number at $\alpha=30^\circ$

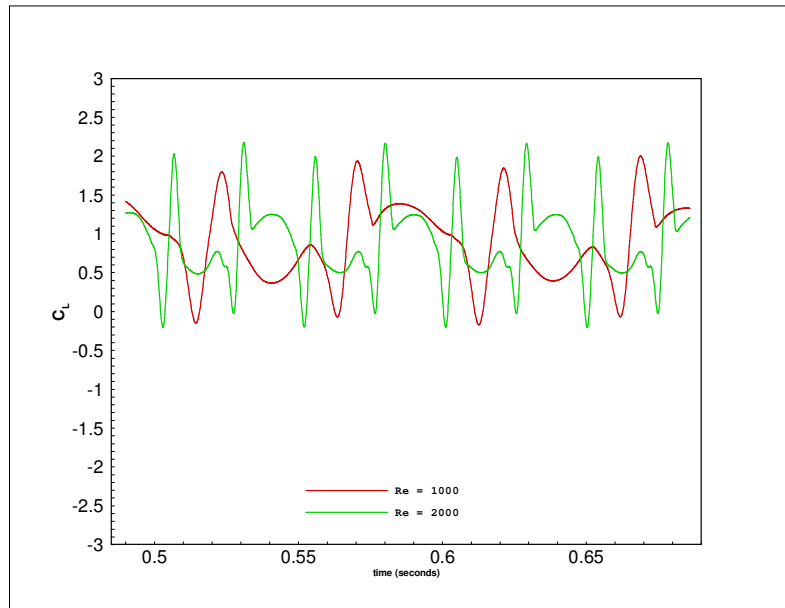


Figure 5.33 Lift coefficient variation versus Reynolds number comparison for NACA 6412 at $\alpha=45^\circ$.

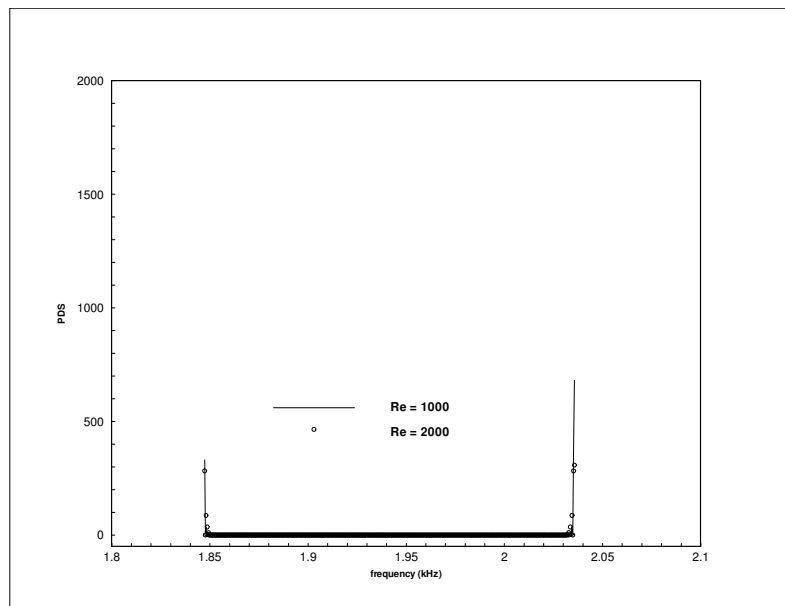


Figure 5.34 Power density spectrum analysis for Reynolds number at $\alpha=45^\circ$

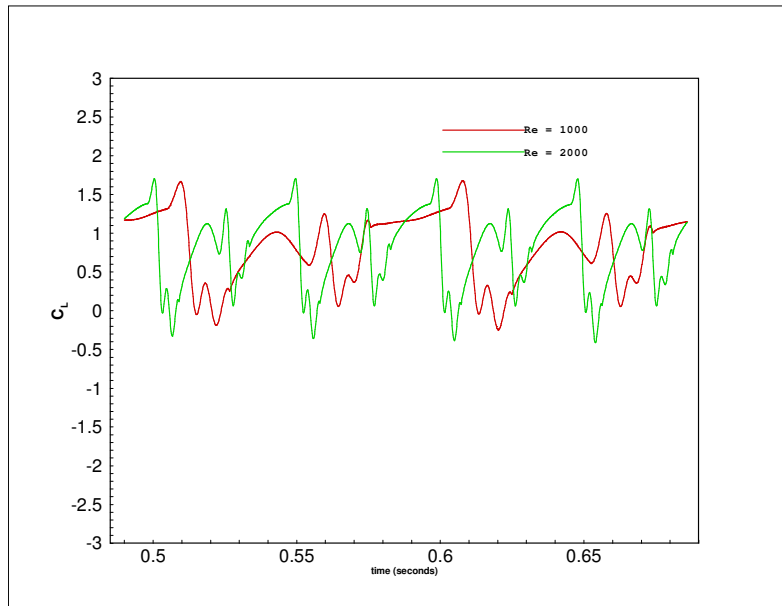


Figure 5.35 Lift coefficient variation versus Reynolds number comparison for NACA 6412 at $\alpha=60^\circ$.

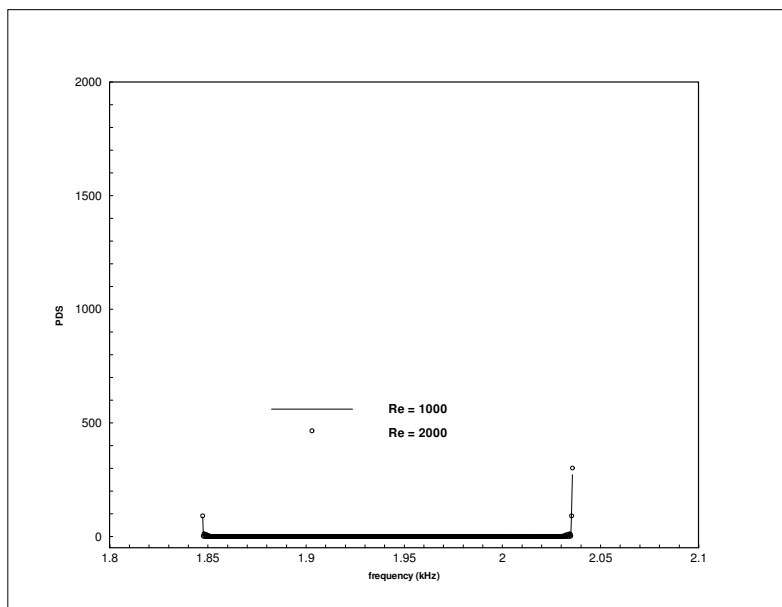


Figure 5.36 Power density spectrum analysis for Reynolds number at $\alpha=60^\circ$.

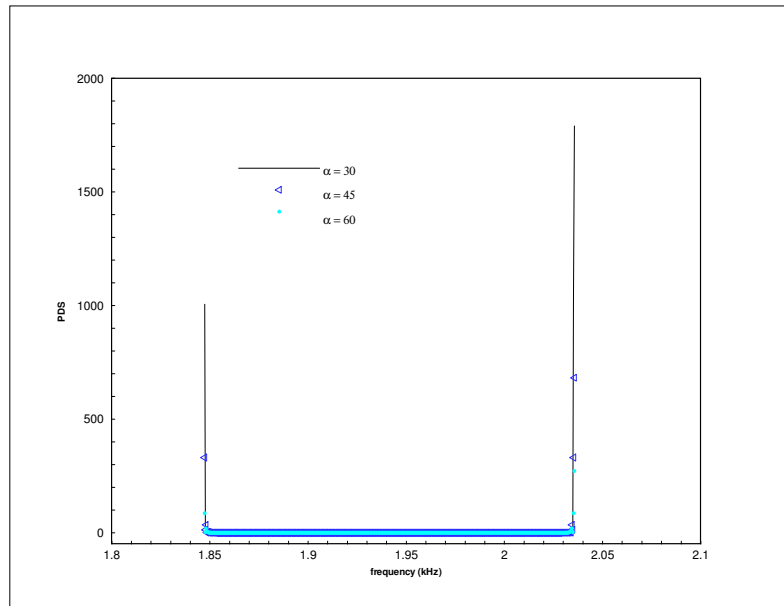


Figure 5.37 Power density spectrum analysis for angle of attack at $Re=1000$.

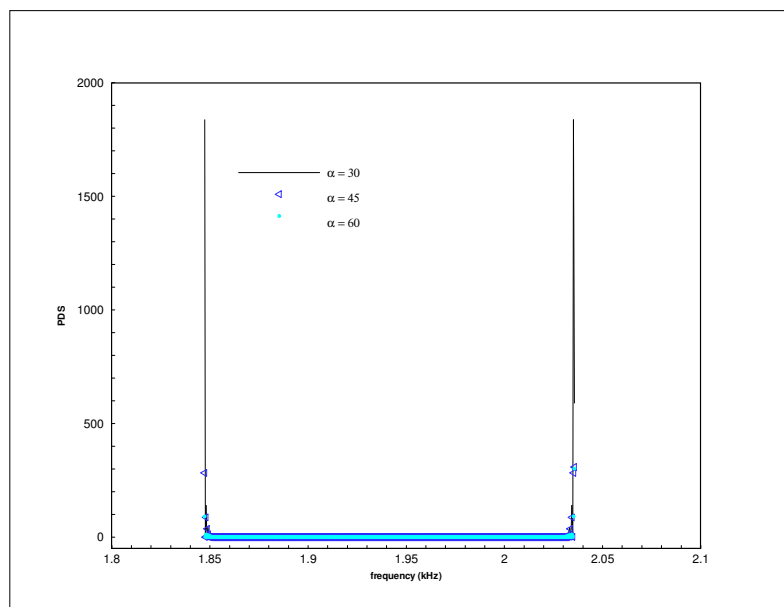


Figure 5.38 Power density spectrum analysis for angle of attack at $Re=2000$.

For the power density spectrum analysis, the lift coefficient variation with time is compared at the positive peak locations corresponding to frequencies $f=1.85$ Hz and $f=2.035$ Hz. At a set angle of attack $\alpha=30^\circ$, the positive peak values of lift coefficient increases as Reynolds number increase (Figure 5.31). The power density spectrum value also increases for increasing Reynolds number at this set angle of attack (Figure 5.32). The increasing trend of positive peak values of lift coefficient with increasing Reynolds number is also seen for the set angle of attack $\alpha=45^\circ$ (Figure 5.33). However, the power density spectrum value decreases as Reynolds number increases as seen in Figure 5.34. For the set angle of attack $\alpha=60^\circ$, positive peak values of lift coefficients are very close and the power density spectrum values are also nearly same (Figure 5.35-5.36). For a given Reynolds number, the power density spectrum value decreases as the set angle of attack value increases (Figure 5.37-5.38). There is a big difference in power density spectrum value for changing Reynolds number at $\alpha=30^\circ$, but the difference is not so significant for $\alpha=45^\circ$ and $\alpha=60^\circ$.

Table 5.2 Average lift and drag coefficients over [5T 6T]

	$\alpha=30^\circ$	$\alpha=45^\circ$	$\alpha=60^\circ$
NACA 6412	$\overline{C}_L = 0.9283$ $\overline{C}_D = 1.7954$	$\overline{C}_L = 0.8863$ $\overline{C}_D = 1.1261$	$\overline{C}_L = 0.8099$ $\overline{C}_D = 0.66915$
NACA 0012	$\overline{C}_L = 0.9386$ $\overline{C}_D = 1.7891$	$\overline{C}_L = 0.9853$ $\overline{C}_D = 1.1782$	$\overline{C}_L = 0.9004$ $\overline{C}_D = 0.7161$
$\Delta \overline{C}_L =$ $\overline{C}_{L_{cambered}} - \overline{C}_{L_{symm}}$	-0.0103	-0.0990	-0.0906
$\Delta \overline{C}_D =$ $\overline{C}_{D_{cambered}} - \overline{C}_{D_{symm}}$	0.0062	-0.0521	-0.0470

5.3.3.3 Analysis of Different Cambered Profiles

A parametric study is also performed for different cambered profiles, and the calculated aerodynamic force coefficients are compared to that of NACA 0012. For this purpose, Eppler E471 and Gottingen GOE122 profiles are used and their results are compared to NACA 6412 as well as to NACA 0012 profiles. The selected cambered profiles are chosen such that they can represent the cross-section of a real flier's wing.

The aerodynamic characteristics of cambered profiles are compared in terms of their calculated aerodynamic lift and drag force coefficients during a period of flapping motion. At $\alpha = 30^\circ$, the maximum positive peak values in drag coefficient are achieved by NACA 6412 and the other two cambered profiles show similar behavior but lower peak values for drag coefficient (Figure 5.39). For lift coefficient distributions, cambered airfoil sections show higher values during both the pronation and supination phases whereas the symmetrical airfoil exhibits higher lift coefficients during the translational phase.

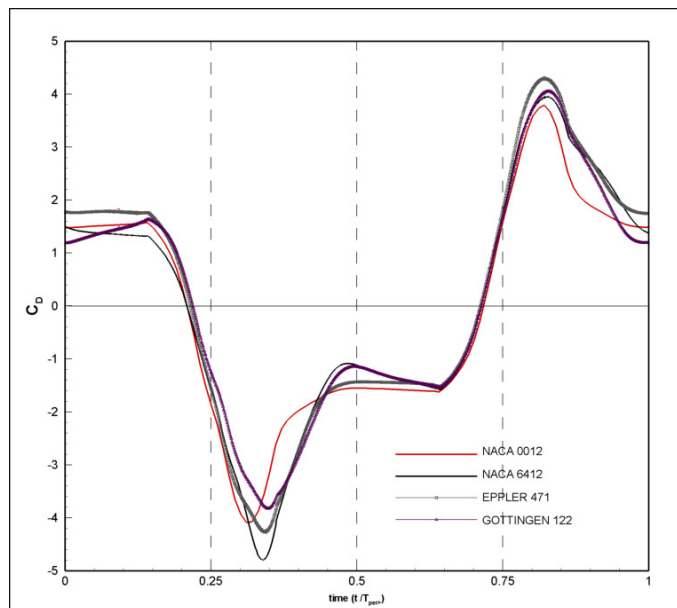


Figure 5.39 Comparison of drag coefficient distributions of different airfoil sections at $Re = 1000$, $\alpha = 30^\circ$.

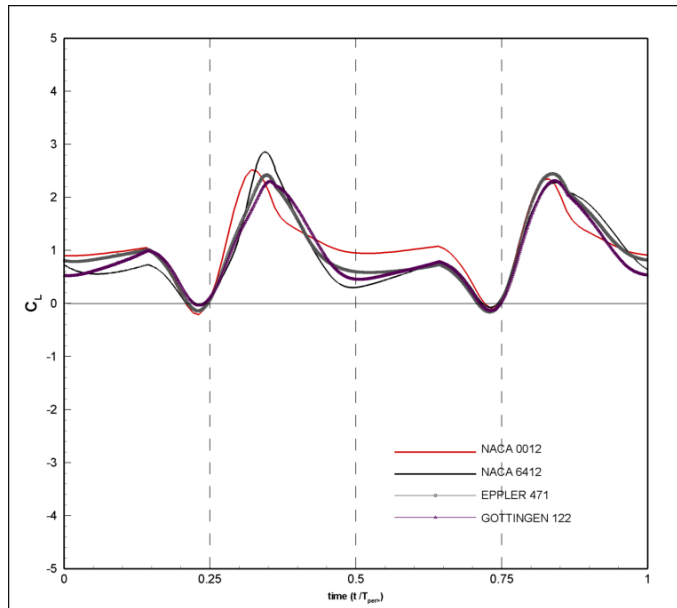


Figure 5.40 Comparison of lift coefficient distributions of different airfoil sections at $Re = 1000$, $\alpha = 30^\circ$.

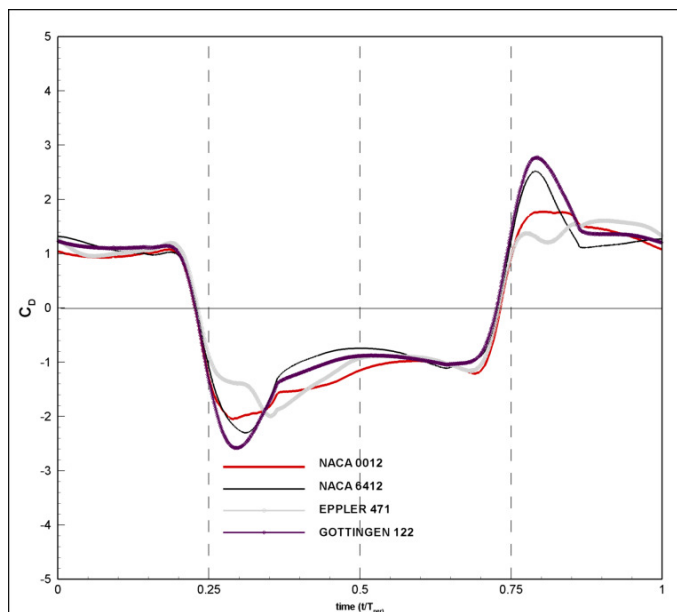


Figure 5.41 Comparison of drag coefficient distributions of different airfoil sections at $Re = 1000$, $\alpha = 45^\circ$.

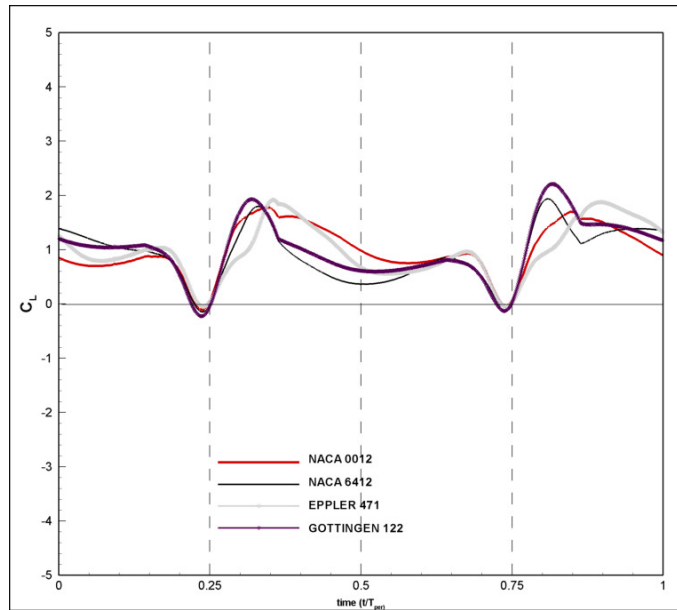


Figure 5.42 Comparison of lift coefficient distributions of different airfoil sections at $Re = 1000$, $\alpha = 45^\circ$.

As seen in Figure 5.41 and Figure 5.42, the camber effect becomes more pronounced in the drag coefficient variations with increasing angle of attack. At $\alpha = 45^\circ$, Göttingen airfoil has the maximum positive peak values in lift coefficient. NACA 6412 profile's lift behavior is also very similar to that of Göttingen airfoil. When $\alpha = 60^\circ$, the performances of Eppler and Göttingen airfoils are very similar to each other and better than the other two profiles.

It was observed that the forces calculated during the downstroke and upstroke periods are not symmetrical. Warrick et al. [64] also stated this phenomenon in their study on hovering hummingbirds. They stated that this asymmetry is probably due to the inversion of their cambered wings

during upstroke. The wake of hummingbird wings also reveals the evidence of leading-edge vortices created during the downstroke, indicating that they may operate at Reynolds numbers sufficiently low to exploit a key mechanism typical to insect hovering.

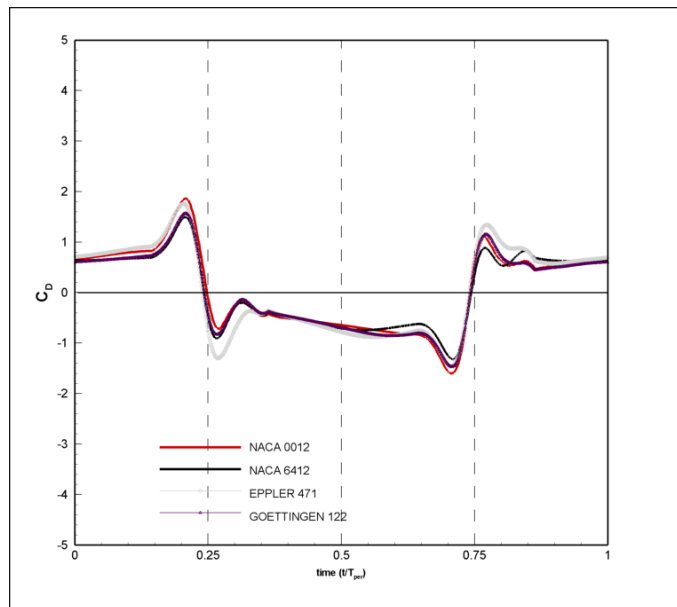


Figure 5.43 Comparison of drag coefficient distributions of different airfoil sections at $Re = 1000$, $\alpha = 60^\circ$.

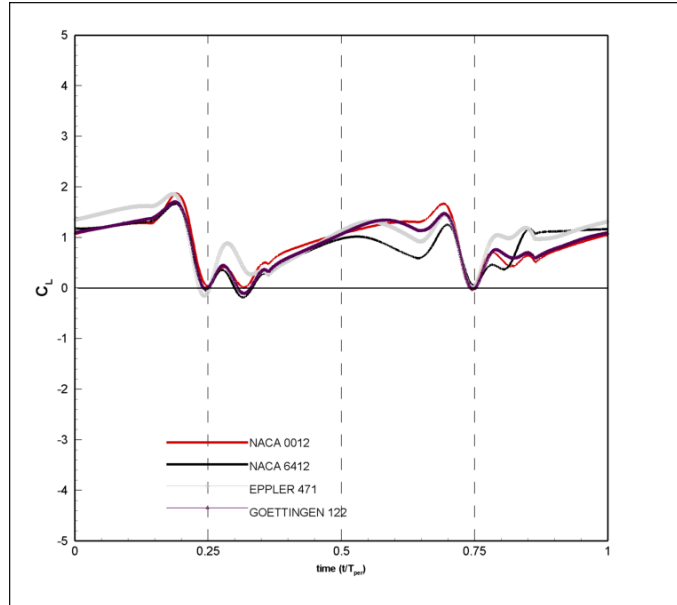


Figure 5.44 Comparison of lift coefficient distributions of different airfoil sections at $Re = 1000$, $\alpha = 60^\circ$.

The lift-to-drag ratio distributions of cambered profiles are given in Figures 5.45-5.47. As the angle of attack increases, the negative peak values at the end of the first quarter period decreases and the positive peak values during the pronation and supination phases increase. If these peak values are excluded from the analysis, we will observe that the absolute value of the lift-to-drag ratio is nearly constant during the translational phases at $\alpha = 30^\circ$. The same behavior is also observed for $\alpha = 45^\circ$ when the peak values are excluded. For $\alpha = 60^\circ$, the ratio is no longer constant during the upstroke phase of the motion whereas it is nearly constant during the downstroke phase for all of the profiles considered.

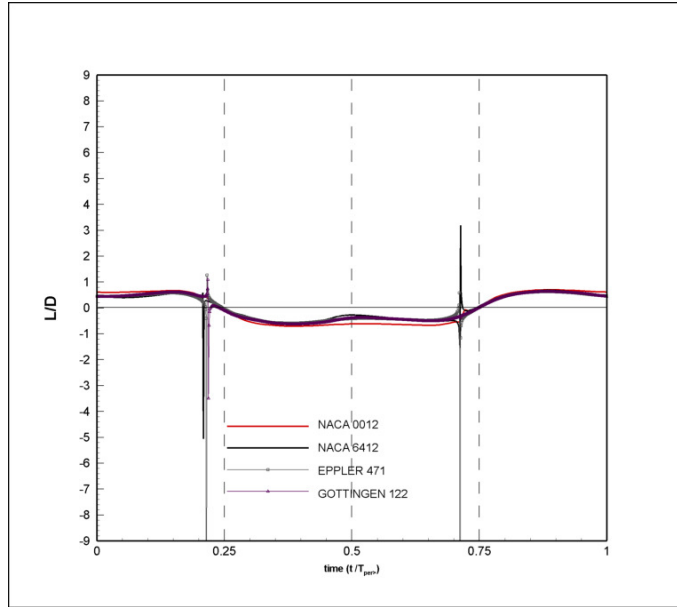


Figure 5.45 Comparison of lift-to-drag ratio variations of different airfoil sections at $Re = 1000$, $\alpha = 30^\circ$ in one period.

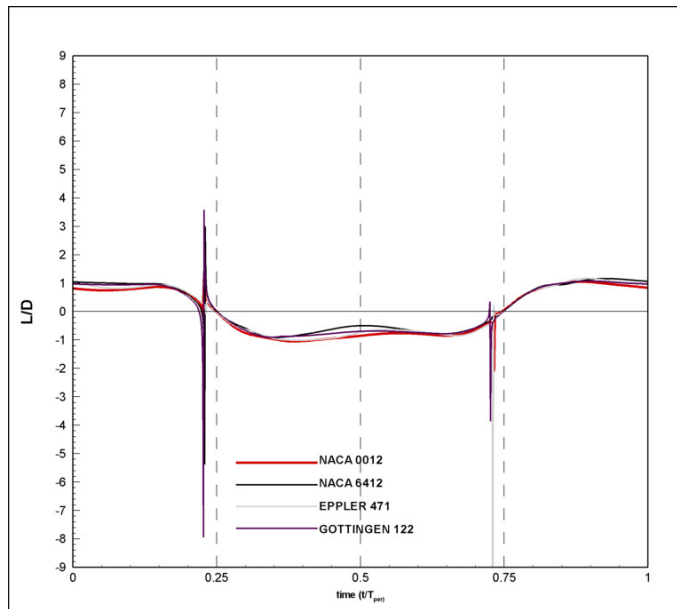


Figure 5.46 Comparison of lift-to-drag ratio variations of different airfoil sections at $Re = 1000$, $\alpha = 45^\circ$ in one period.

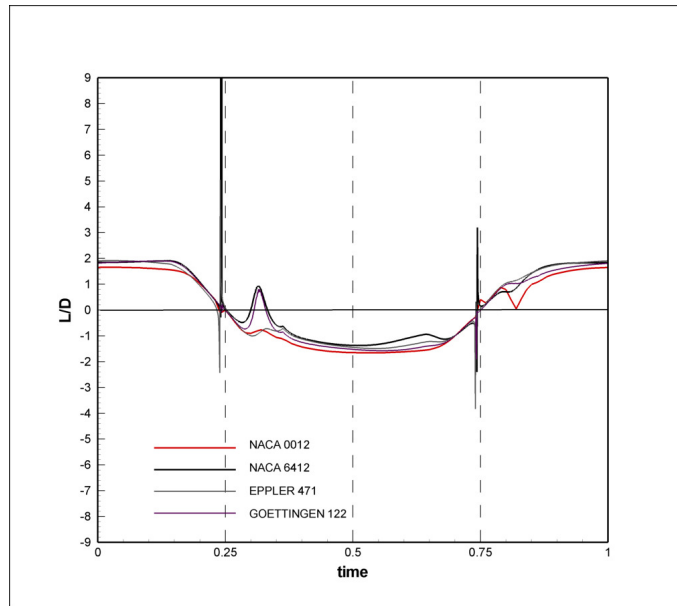


Figure 5.47 Comparison of lift-to-drag ratio variations of different airfoil sections at $Re = 1000$, $\alpha = 60^\circ$ in one period.

5.3.3.4 Effect of Leading Edge Radius on Flapping Motion

Since most of the lift generated during flapping motion is due to leading edge vortex created during the downstroke phase, leading edge radius is another significant parameter that should be investigated. For this reason, airfoils having different leading edge radii are investigated and their aerodynamic force coefficients are compared to each other. The airfoils and their leading edge radii used in this investigation are listed in Table 5.3.

Table 5.3 Leading edge radii values of different airfoil profiles

Profile	Leading Edge Radius (%c)
Eppler E471	3.24
Göttingen GOE122	0.33
NACA 6412	1.580
NACA 63-218	2.120
NACA 63-215	1.570
NACA 64(2)015	1.594

When the lift coefficient variations over a period of motion are considered, all profiles achieve nearly the same minimum peak values towards the end of the first quarter and the third quarter periods. The trends of lift coefficient variations in the translational phase of the upstroke are nearly the same for all profiles except for NACA 6412. There is a small difference in the lift coefficients achieved by the profiles excluding NACA 6412. Similar behavior is also observed for the drag coefficient changes during one period of motion. Again, with the exception of NACA 6412 profile, all of the profiles have similar behaviors in the translational phases of the motion and the peak values are nearly the same.

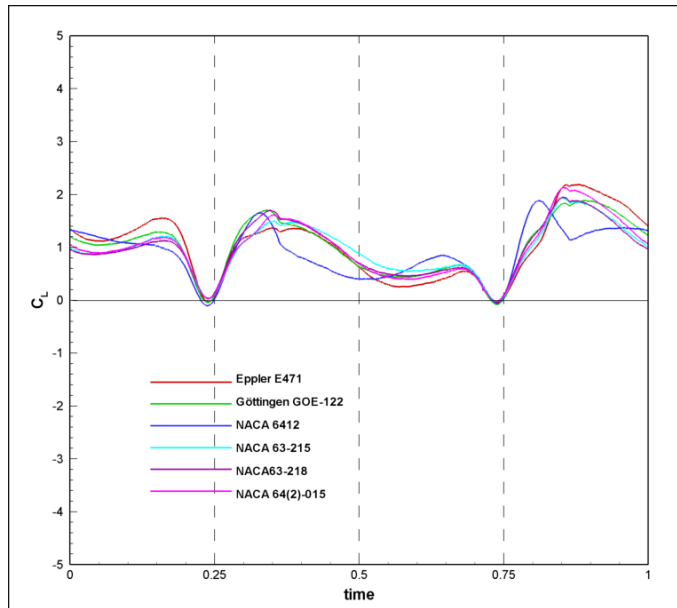


Figure 5.48 Comparison of lift coefficient variations in one period for different airfoil profiles at $Re = 1000$, $\alpha = 45^\circ$

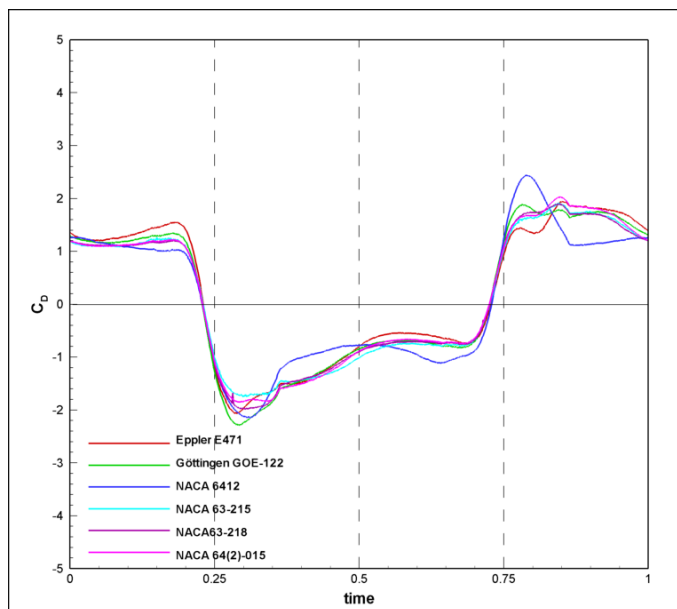


Figure 5.49 Comparison of drag coefficient variations in one period for different airfoil profiles at $Re = 1000$, $\alpha = 45^\circ$

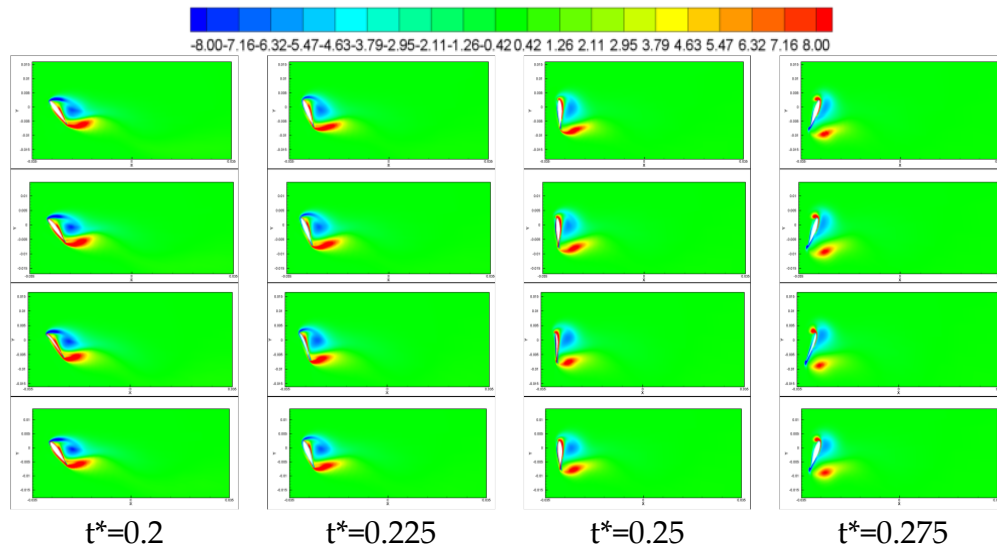


Figure 5.50 Comparison of vortex regions by non-dimensional vorticity contours during the first rotational phase at $Re = 1000$, $\alpha = 45^\circ$ (NACA 63-215 airfoil at the 1st row, NACA 64(2)015 airfoil at the 2nd row, Göttingen GOE 122 airfoil at the 3rd row and NACA 63218 airfoil at the 4th row).

The effect of leading edge radius on the dynamic stall of pitching airfoils is investigated by Grohsmeyer et al. [104] and Jones and Platzer [105]. In all these references the flow was assumed to be turbulent and the Reynolds number was relatively high compared to one used in the present study. Grohsmeyer et al. [104] found that a larger leading edge radius, thicker contouring of the forward part of the airfoil, or increasing the pitch rate resulted in delaying the flow separation and formation of the dynamic stall vortex to a higher angle of attack, yielding a higher peak lift coefficient. The results of Jones and Platzer [104] demonstrated that the delay in dynamic stall onset is directly related to the dynamic pressure lag, that may be obtained at the point of separation using a purely inviscid

analysis. It should be noted that in these studies the velocities were also higher than the present study as well as the Reynolds number ($Re \sim O(10^6)$).

5.3 Solver Description, Fluent

The numerical simulation of flapping motion is also performed using another commercially available flow solver, Fluent V.2.22. Two-dimensional time-dependent Navier-Stokes equations are solved using the finite-volume method for an incompressible flow. The governing equations are described by [106]:

$$\nabla \cdot \vec{V} = 0 \tag{5.5}$$

$$\frac{\partial}{\partial t} (\vec{V}) + (\vec{V} \cdot \nabla) \vec{V} = -\frac{1}{\rho} \nabla p + \nu \nabla^2 \vec{V} \tag{5.6}$$

where \vec{V} is the flow velocity vector, ρ is constant density, ν is the kinematic viscosity and p is the static pressure.

The space discretization scheme used is the first order upwind as well as the time discretization which is the only way to use the dynamic mesh module implemented in Fluent V2.22. The pressure-velocity coupling in incompressible flow simulations was obtained using the iterative pressure implicit with splitting operators (PISO) scheme with under-relaxation coefficients for pressure, momentum and body forces equal to 0.3, 0.7 and 1.0 respectively. The accuracy was set to double-precision. The

convergence criterion for the iterative method was satisfied with mass and momentum residues dropping to an order of magnitude of $O(10^{-3})$.

5.3.1 Parallel Implementation

Parallel algorithm used in the solutions splits up the grid and data into multiple partitions, then assigns each grid partition to a different compute process (or node). The compute-node processes can be executed on a massively-parallel computer, a multiple-CPU workstation, or a network of workstations using the same or different operating systems. FLUENT uses a host process that does not contain any grid data. Instead, the host process only interprets commands from FLUENT's graphics-related interface, cortex. The host distributes those commands to the other compute nodes via a socket communicator to a single designated compute node called compute-node-0. This specialized compute node distributes the host commands to the other compute nodes. Each compute node simultaneously executes the same program on its own data set. Communication from the compute nodes to the host is possible only through compute node-0 and only when all compute nodes have synchronized with each other. A FLUENT communicator is a message-passing library which could be a vendor implementation of the Message Passing Interface (MPI) standard [106]. Computations are performed on a 64-bit HP workstation having two dual core processors, total four cores, on Linux operating system. Each core has a CPU speed of 3.0 GHz.

5.3.2 Speedup and Efficiency

In parallel computing, speedup is the measure how much a parallel algorithm is faster than a corresponding sequential algorithm. It is defined by:

$$S_p = \frac{T_1}{T_p} \quad (5.7)$$

where the subscript p is the number of processors, T_1 is the execution time of the sequential algorithm and T_2 is the execution time of the parallel algorithm with p processors.

Linear speed-up or ideal speed-up is obtained when $S_p = p$. When running an algorithm with linear speed-up, doubling the number of processors doubles the speed. As it is ideal, it is considered very good scalability.

Efficiency is a performance metric defined as:

$$E_p = \frac{S_p}{p} \quad (5.8)$$

The value of efficiency typically varies between zero and 1, estimating how well the processors are utilized in solving the problem, compared to how much effort is wasted in communication and synchronization. Algorithms with linear speed-up and algorithms running on a single

processor have an efficiency of 1, while many difficult-to-parallelize algorithms have an efficiency such as $\frac{1}{\log p}$ that approaches zero as the number of processors increases [107].

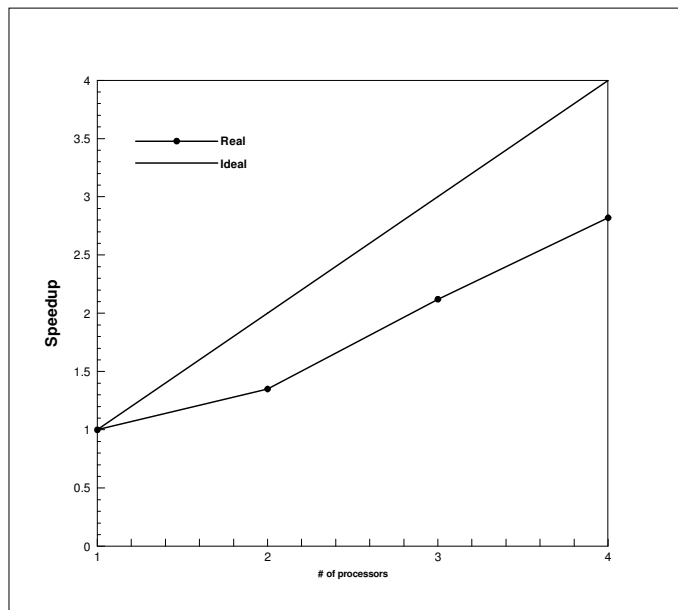


Figure 5.51 Speedup plot for two-dimensional results

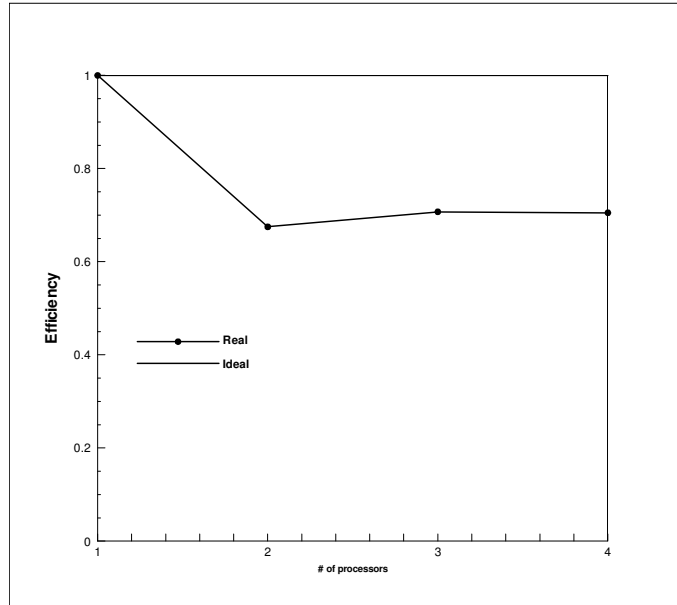


Figure 5.52 Efficiency plot of two-dimensional results

5.3.3 Computational Domain

In this section numerical simulations performed by using the flow solver FLUENT will be presented. As stated previously FLUENT is also a finite volume flow solver as STAR-CD. So far all the computational results presented in this chapter were obtained by using the STAR-CD software. Since the FLUENT software was licensed to the Aerospace Engineering Department of METU, in its parallel version it was extremely beneficial to use this software in its parallel version to speed up the computations in particular the 3D computations which will be detailed in Chapter 7. Similar to the simulations performed by STAR-CD, no-slip wall boundary conditions are implied at the airfoil surface. The far field is described as

the pressure outlet which is the only way to implement the pressure boundary condition for incompressible flows. The computational domain consists of approximately 30 000 elements on a single block. The grid used is structured hyperbolic grid, generated with a normal distance giving $y^+=1$ at the wall surface [108]-[109].

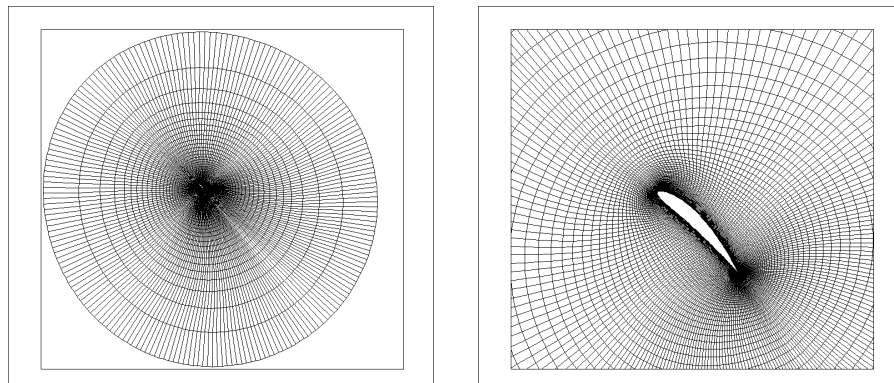


Figure 5.53 Computational domain in Fluent simulations.

5.3.4 Comparison of Results of STAR-CD and FLUENT

In order to compare the results of the two solvers, the solution is obtained by using the same computational mesh which was used for STAR-CD calculations. The results obtained from these solvers are compared for the

lift and the drag coefficient distributions over one period of flapping (Figure 5.54).

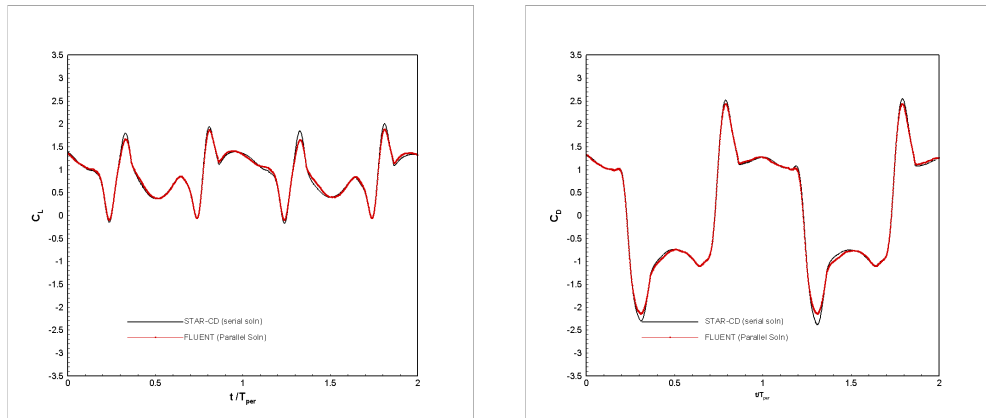


Figure 5.54 Comparison of lift (left) and drag (right) coefficient distributions calculated by Fluent and STAR-CD at $\alpha=45^\circ$, $x_v=2c$, $Re=1000$ with rotation axis at $\frac{1}{4}c$ for 6th and 7th period.

Solutions obtained for NACA 6412 at $\alpha=45^\circ$ angle of attack by the two solvers are compared. The two flow field solutions are compared using the previously defined vortex identification techniques for the first quarter period including both translational and rotational motions. As seen from Figures (5.55-5.57), the two solutions are very similar to each other. The shapes of the identified vortex regions show very little differences in non-dimensional Q contours whereas their shapes are very much similar in non-dimensional λ_2 contours.

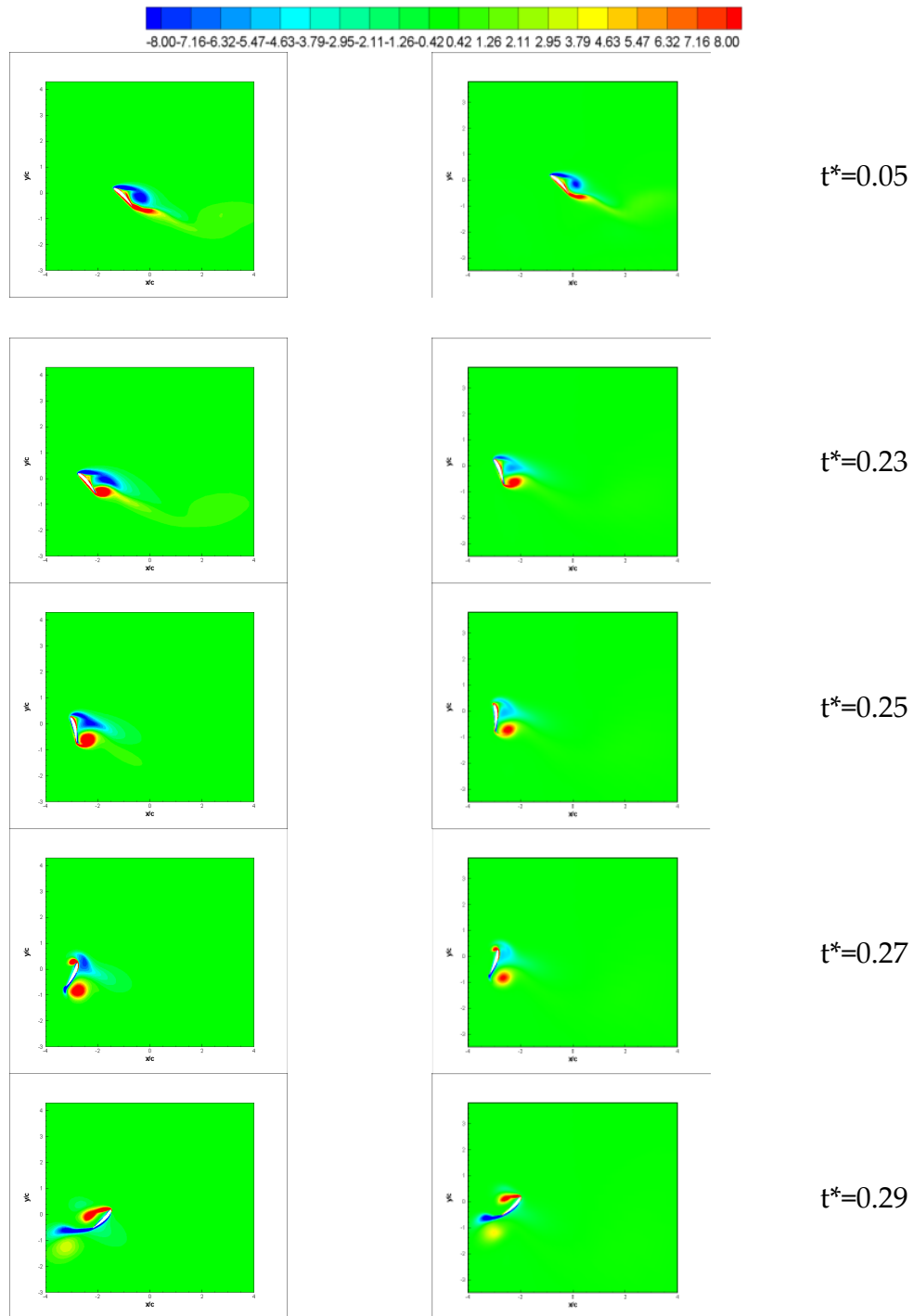


Figure 5.55 Comparison of STAR-CD (left) and Fluent (right) solutions in terms of non-dimensional vorticity contours at $Re = 1000$ and $\alpha = 45^\circ$ during the first half period.

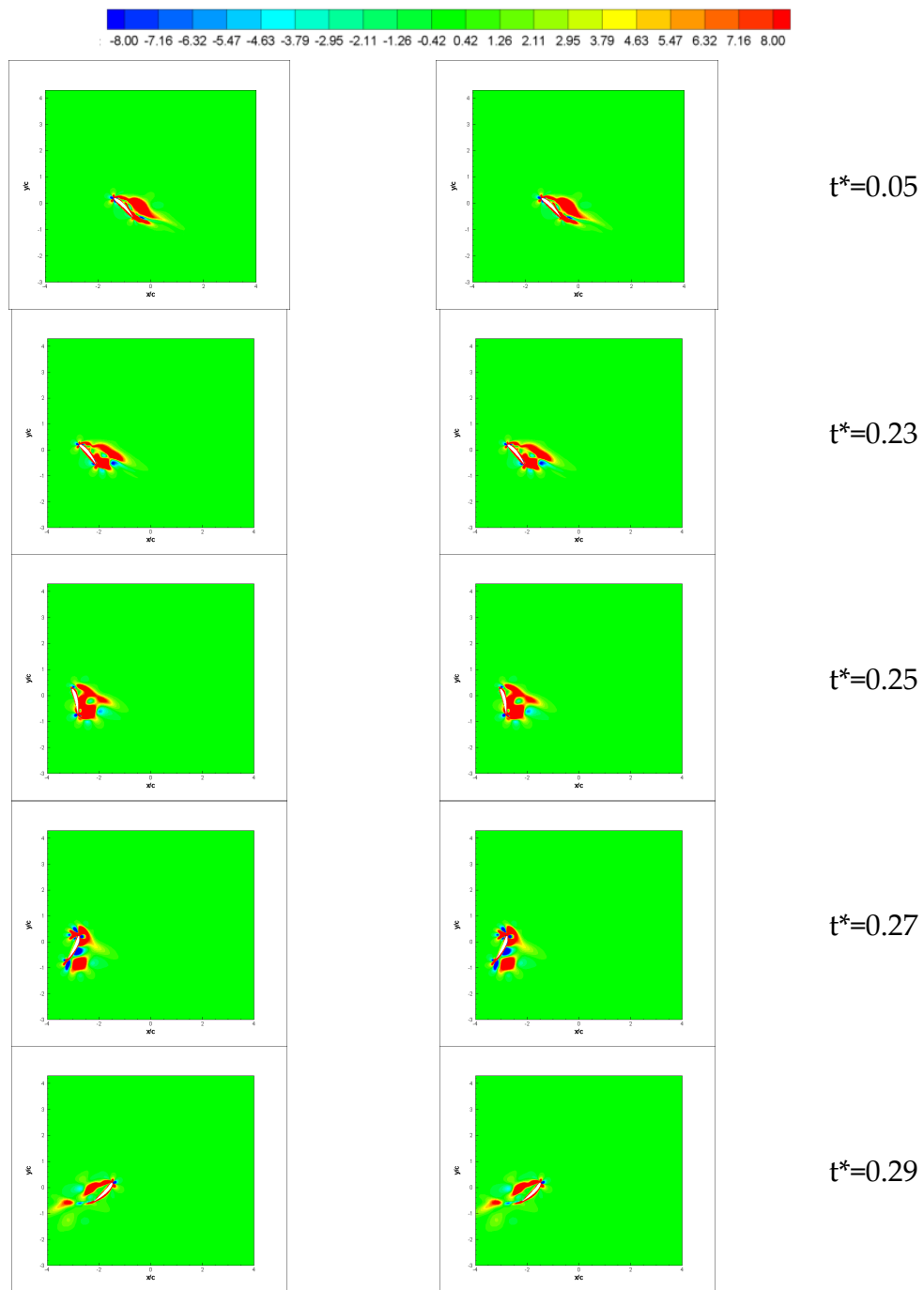


Figure 5.56 Comparison of STAR-CD (left) and Fluent (right) solutions in terms of non-dimensional second invariant of velocity gradient, Q contours at $Re = 1000$ and $\alpha = 45^\circ$ during the first half period.

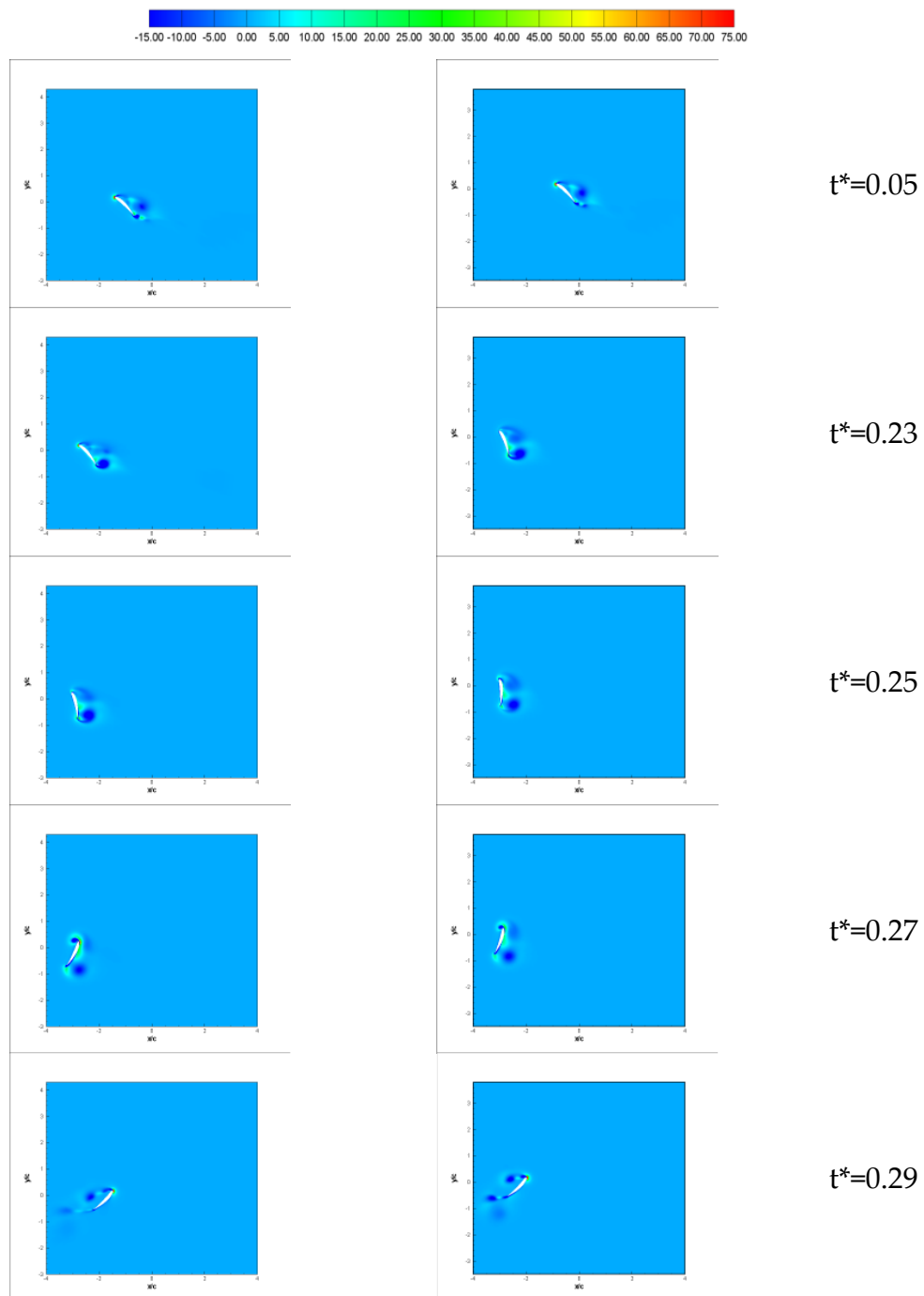


Figure 5.57 Comparison of STAR-CD (left) and Fluent (right) solutions in terms of non-dimensional λ_2 contours, second negative eigenvalue of $(S^2 + \Omega^2)$ at $Re = 1000$ and $\alpha = 45^\circ$ during the first half period.

CHAPTER VI

TWO-DIMENSIONAL EXPERIMENTAL ANALYSIS OF FLAPPING MOTION

Two dimensional experiments are carried out for the cambered airfoil NACA 6412. The velocity fields are obtained for different angles of attack and are compared to numerical solutions given for one period of simulation at $\alpha = 45^\circ$ $x_v = x_a = 2c$ at $Re=1000$ via the vortex identification techniques described in Chapter 4.

6.1 Experimental Results

Two CCD cameras give two velocity vector fields from the images obtained with an overlap region. A rectangular domain covering a region of both cameras with an airfoil at the desired angle of attack and location is created with the same mesh quality as the PIV outputs. The result of the PIV measurements is then interpolated to the rectangular domain by kriging technique which is a built-in interpolation function in Tecplot (a commercial plotting and post processing software). Kriging is a more complex interpolation technique and it requires more computer memory and time. The technique uses the current frame's coordinates for interpolation. The range beyond which the source points become insignificant for the kriging is an important parameter. Moreover, the semi-variance which is the certainty of the value at a data point should be specified at each source data point on a normalized scale from one to zero. The points selected to be non-collinear is specified by setting the 'Drift' option to linear, quadratic or none to eliminate the coincident points. The last option is the point specification for the source data to be interpolated. According to the choice, the computational time and memory requirements can increase rapidly as the number of selected source data points increases.

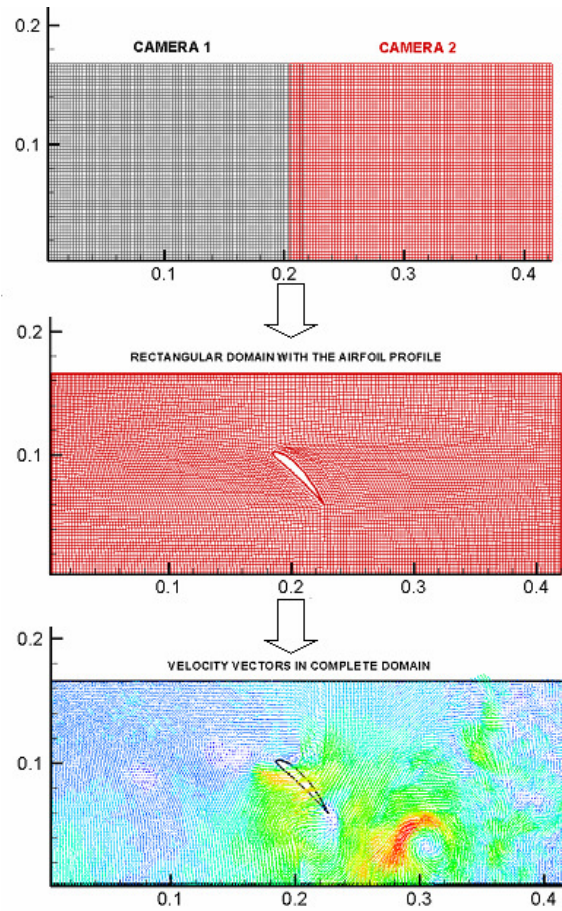


Figure 6.1 Procedure for obtaining the velocity vectors from PIV measurements.

Two-dimensional experimental measurements are carried out using two CCD cameras. The whole domain is covered when view domain of each camera is joined so the middle of the measurement domain can not be seen by any cameras separately but there is an overlapping region. Moreover the velocity vectors calculated at the boundaries may be erroneous, which is also stated in the user's manual of the PIV software. When the domain of one camera is joined with the other domain, (see

Figure 6.1) the calculated variables may lead to spurious results which are mostly seen in the visualization of non-dimensional contours of second invariant of velocity gradient, Q criteria.

Another approach to eliminate the spurious results is to merge the whole domain before calculating the velocities of the particles in the flow. For this reason, the separate images are merged taking into account the overlapping region. The merging of the images is done using a MATLAB script. After merging, the velocity field is calculated using an adaptive cross-correlation technique. The calculated velocity field is then krigged onto the rectangular domain with airfoil. The procedure is summarized in Figure 6.3.

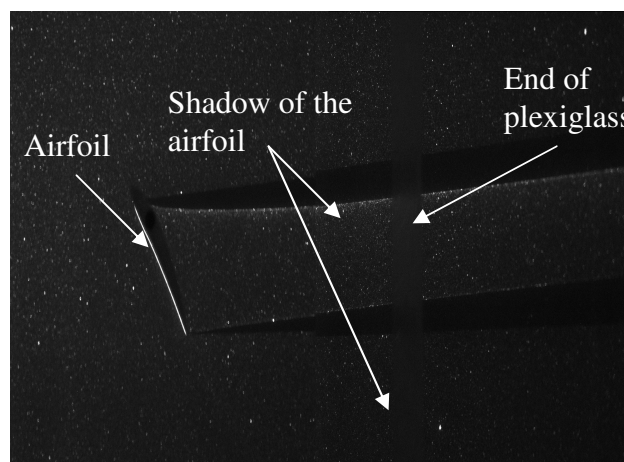


Figure 6.2 PIV image of the airfoil obtained by merging the images of the cameras.

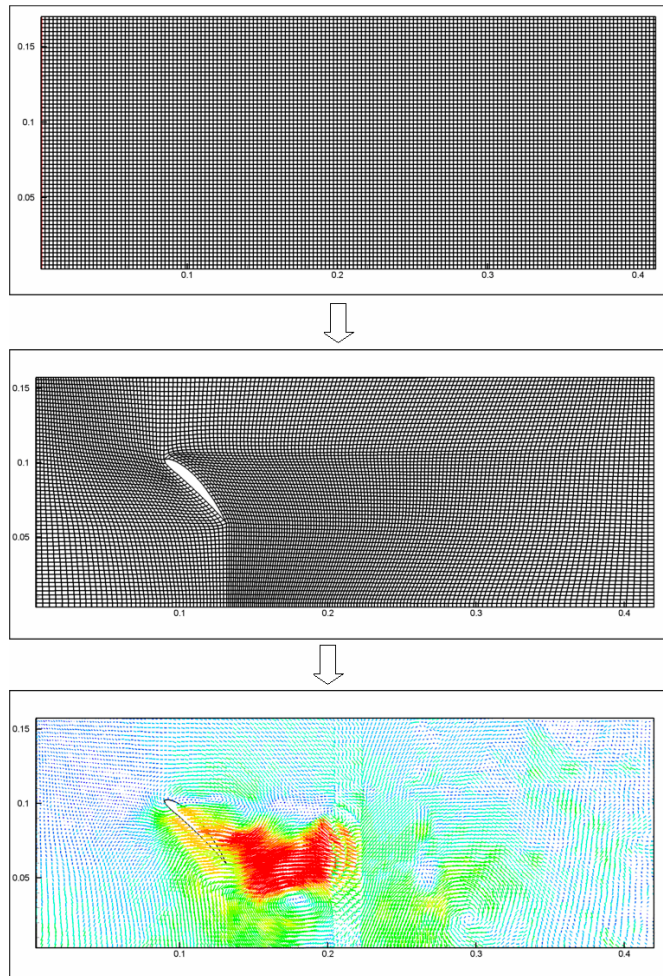


Figure 6.3 Procedure for obtaining the velocity vectors from merged images.

When these two procedures are compared, it is seen that there are less erroneous vectors at the overlapping region if the images are merged before processing to obtain the velocity field.

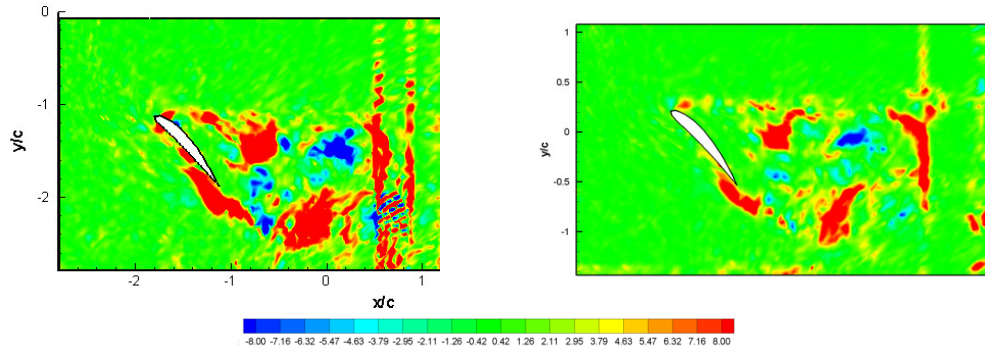


Figure 6.4 Comparison of second invariant of velocity gradient, Q contours at $t^*=0.20$ at the overlapping region.

Flapping motion has three main aerodynamic mechanisms that are responsible for the generation of aerodynamic forces: delayed stall, rotational lift and wake capture. These three mechanisms are directly related to the three main types of vortices generated during the motion; leading edge vortex which is formed at the leading edge, translational vortex which is formed at the trailing edge and rotational stopping vortex which is formed at the trailing edge of the airfoil at the end of the rotation phase and detaches from the profile just after the rotation process ends. There are different forms of leading and translational vortices during the motion. These vortices may be seen before the translation phase, just after the translational motion begins, during pure translation, at the beginning and at the end of the rotational phase. On the contrary, the rotational stopping vortex is observed only at the end of the rotation phase (Figure 6.5). The numbering of these vortices depends on the initial analysis time and the kinematic parameters such as the constant velocity, angle of attack and the total distance of the flapping motion.

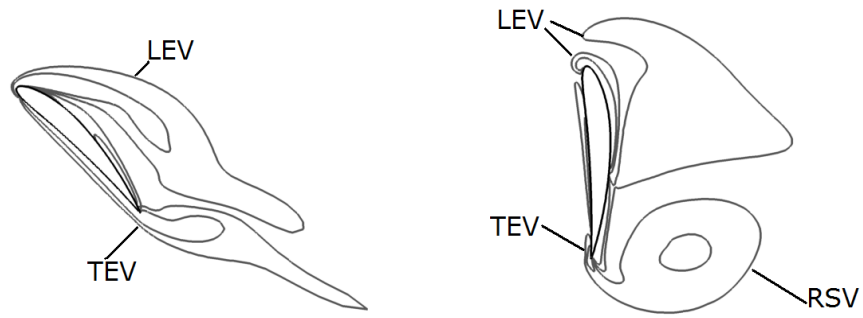
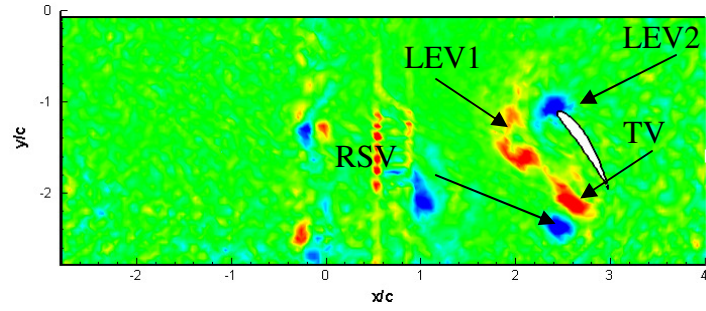
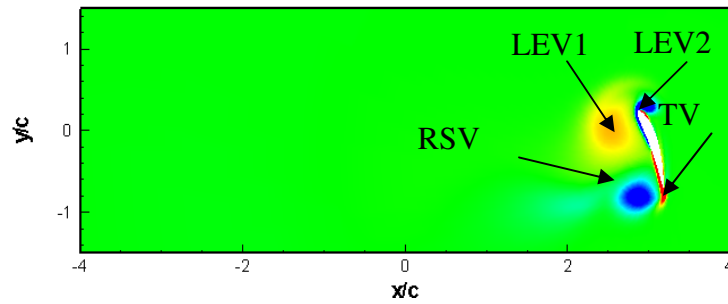


Figure 6.5 Schematic representations of vortex regions shown with the airfoil.

The vortices are identified in Figure 6.6. The leading edge vortex from previous time step (LEV1) and the newly forming leading edge vortex (LEV2) are seen. At the trailing edge the translational vortex (TV) is seen and the rotational stopping vortex (RSV) is seen warm color detached from the model at the trailing edge.



(a) Experimental



(b) Numerical

Figure 6.6 Identification of vortices according to their locations on both experimental and numerical non-dimensional vorticity contours at the beginning of the second downstroke phase ($t^*=0.77$)

During the first quarter of the period, the leading edge vortex regions are very similar in shape and location both in experiments and numerical results. On the other hand, the vortex regions at the trailing edge are slightly separated in the experiments when compared to numerical solutions. At $t^*=0.10$, during the beginning of the translational phase, the first leading edge vortex and the translational vortex at the trailing edge are clearly identified.

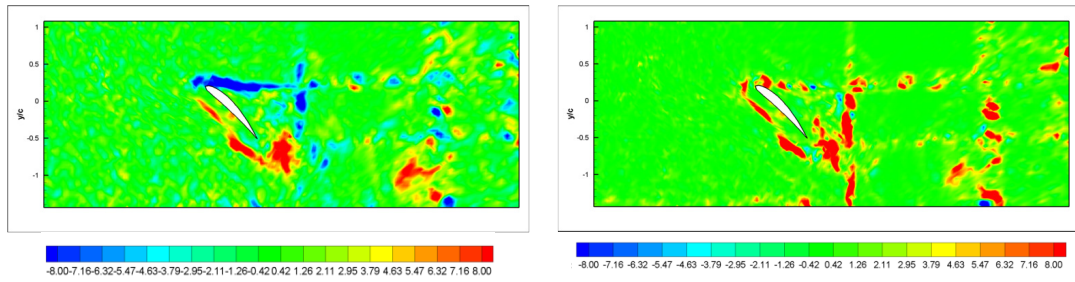


Figure 6.7 Identification of vortex regions by non-dimensional vorticity, $|\omega|$ and second invariant of velocity gradient, Q contours at $t^*=0.10$ (first half of downstroke)

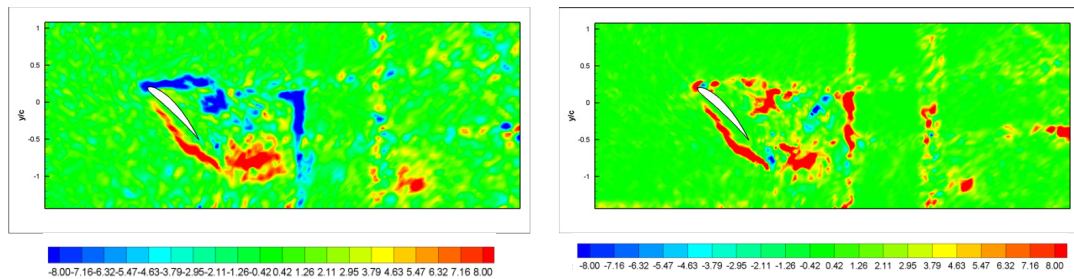


Figure 6.8 Identification of vortex regions by non-dimensional vorticity, $|\omega|$ and second invariant of velocity gradient, Q contours at $t^*=0.15$ (first half of downstroke)

During pure translation, at $t^*=0.15$, the shedding of leading edge vortex is observed with the newly forming vortex at the leading edge. The translational vortex from previous time step is detaching from the profile and the second translational vortex is formed at the trailing edge (see Figure 6.8). At $t^*=0.20$, the first leading edge and translational vortices are detached from the profile and the shedding of secondary vortices are progressing.

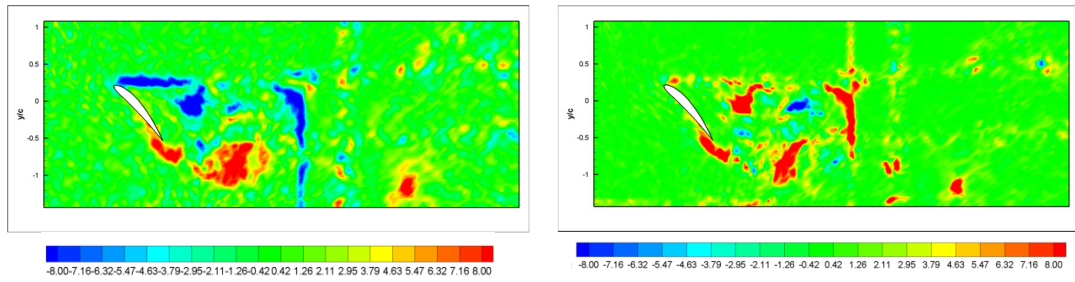


Figure 6.9 Identification of vortex regions by non-dimensional vorticity, $|\omega|$ and second invariant of velocity gradient, Q contours at $t^*=0.20$ (first half of downstroke)

When the rotation starts, the leading edge vortex is about to separate from the profile whereas the translational vortex is still attached to the profile at $t^*=0.23$ (Figure 6.10).

At the end of the first quarter period, $t^*=0.25$, all vortices are detached from the airfoil and the rotational stopping vortex is seen at the trailing edge of the profile separated from the airfoil (Figure 6.11).

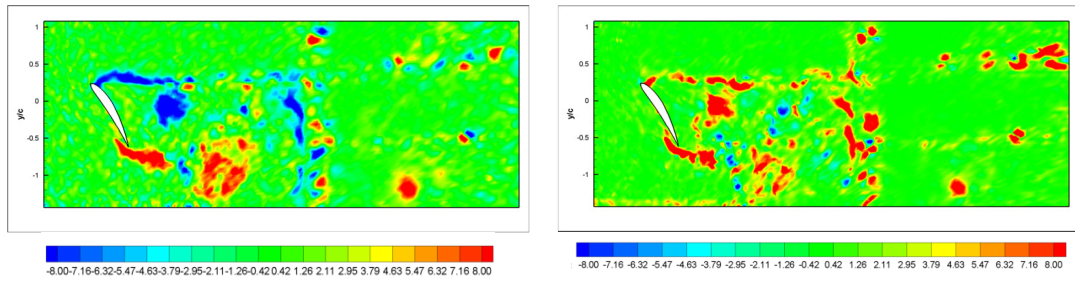


Figure 6.10 Identification of vortex regions by non-dimensional vorticity, $|\omega|$ and second invariant of velocity gradient, Q contours at $t^*=0.23$ (first half of downstroke)

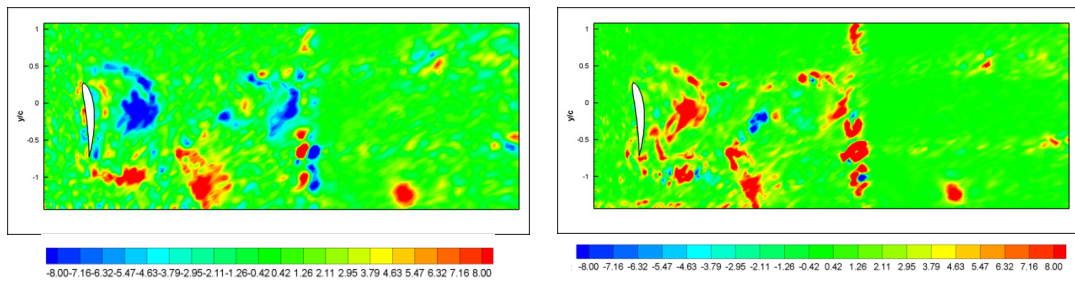


Figure 6.11 Identification of vortex regions by non-dimensional vorticity, $|\omega|$ and second invariant of velocity gradient, Q contours at $t^*=0.25$ (end of first half of downstroke)

6.2 Comparison of Experimental and Numerical Results

The comparison of experimental and numerical simulations are presented for the cambered airfoil NACA 6412 at $Re = 1000$ and at an angle of attack of $\alpha = 45^\circ$ for one period. The qualitative comparisons of vortex regions are better distinguished via non-dimensional Q, second invariant of velocity

gradient and λ_2 contours, second negative eigenvalue of $(S^2 + \Omega^2)$. However, non-dimensional vorticity contours make easier to visualize these regions.

During the first quarter of the period, the leading edge vortex regions are very similar in shape and location both in experiments and numerical results. On the other hand, the vortex regions at the trailing edge are slightly separated in the experiments when compared to numerical solutions.

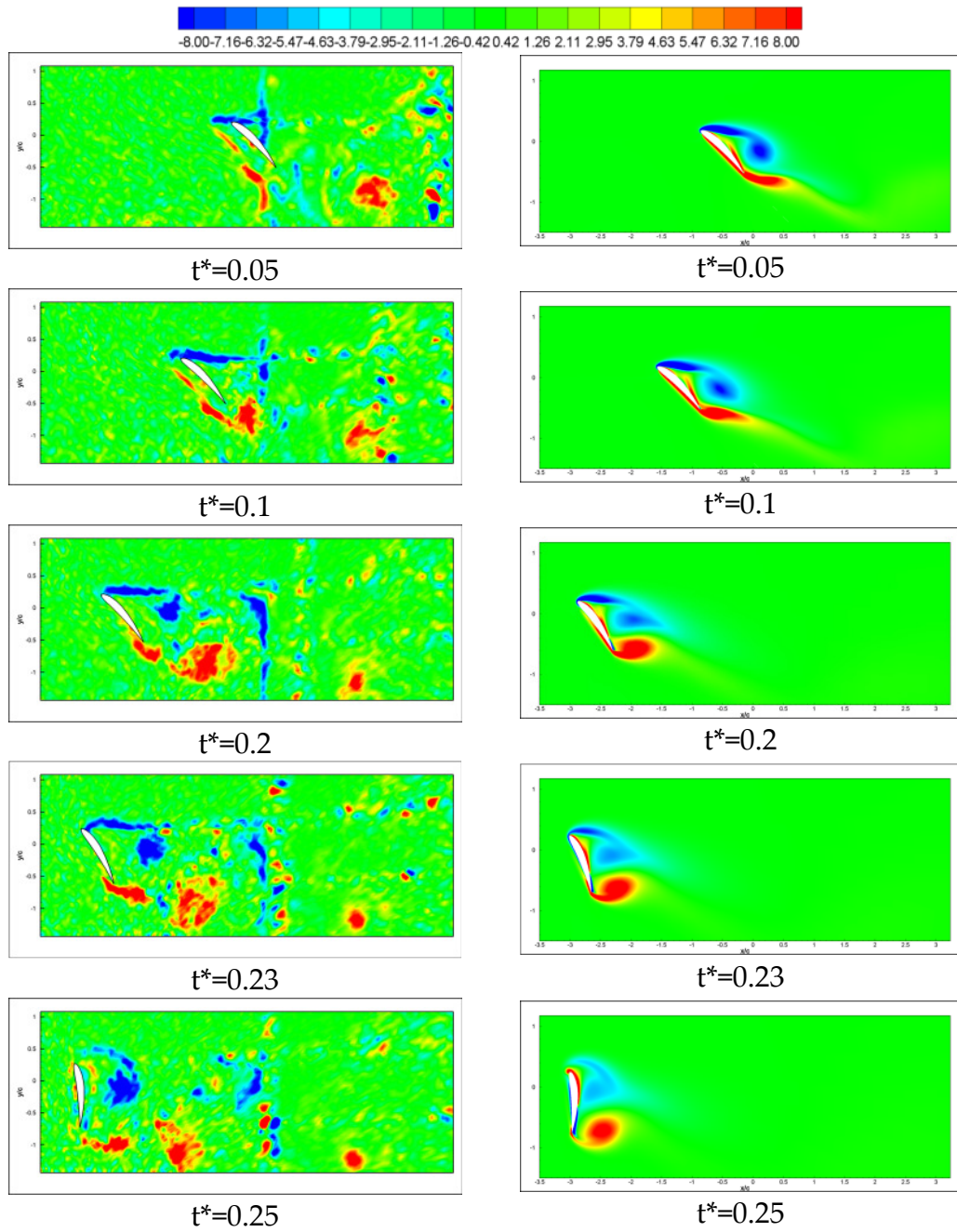


Figure 6.12 Comparison of experimental (left) and numerical (right) non-dimensional vorticity contours at the first quarter period at $\alpha=45^\circ$, $Re = 1000$.

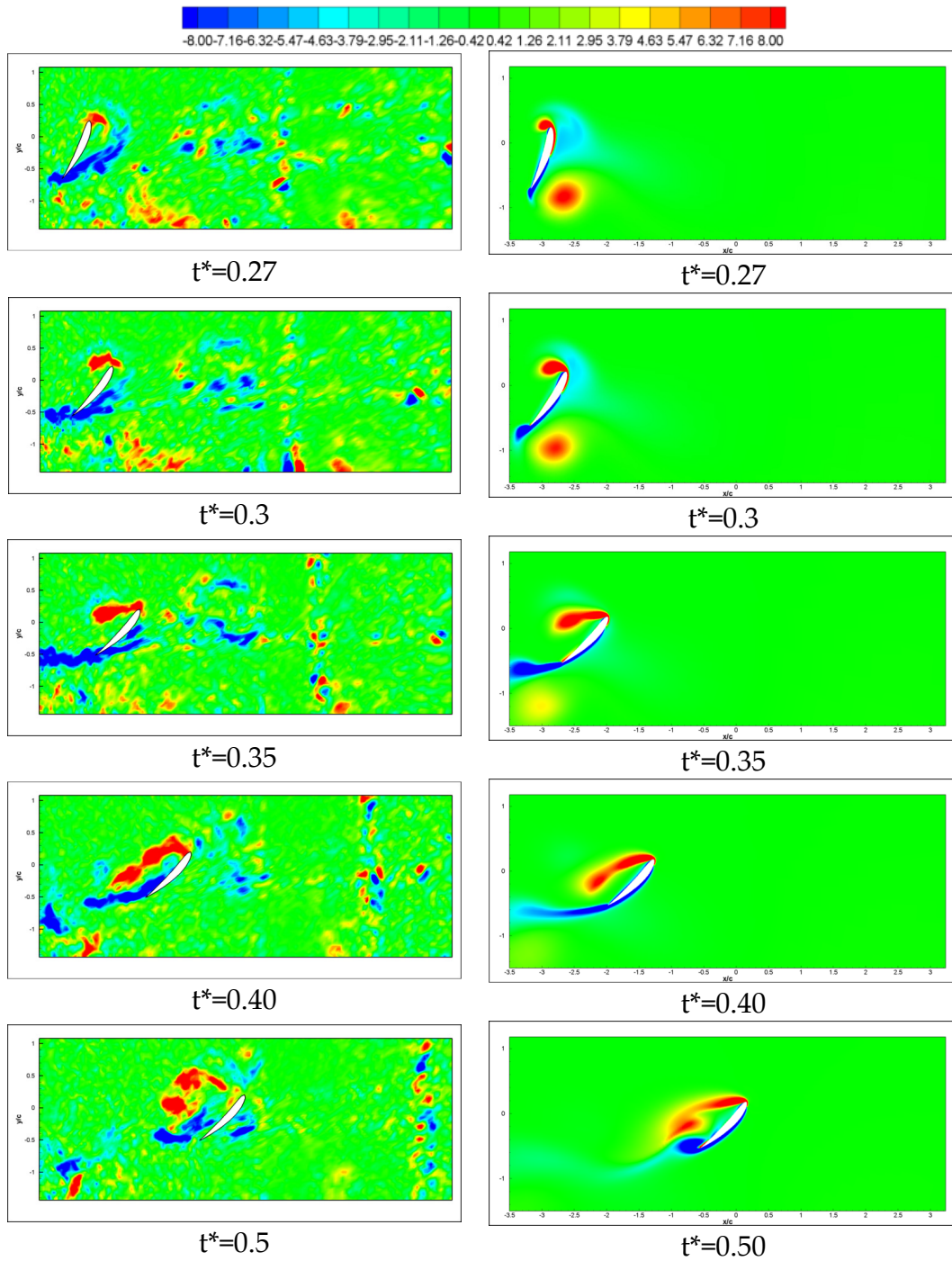


Figure 6.12 (continued) Comparison of experimental (left) and numerical (right) non-dimensional vorticity contours at the second quarter period at $\alpha=45^\circ$, $Re = 1000$.

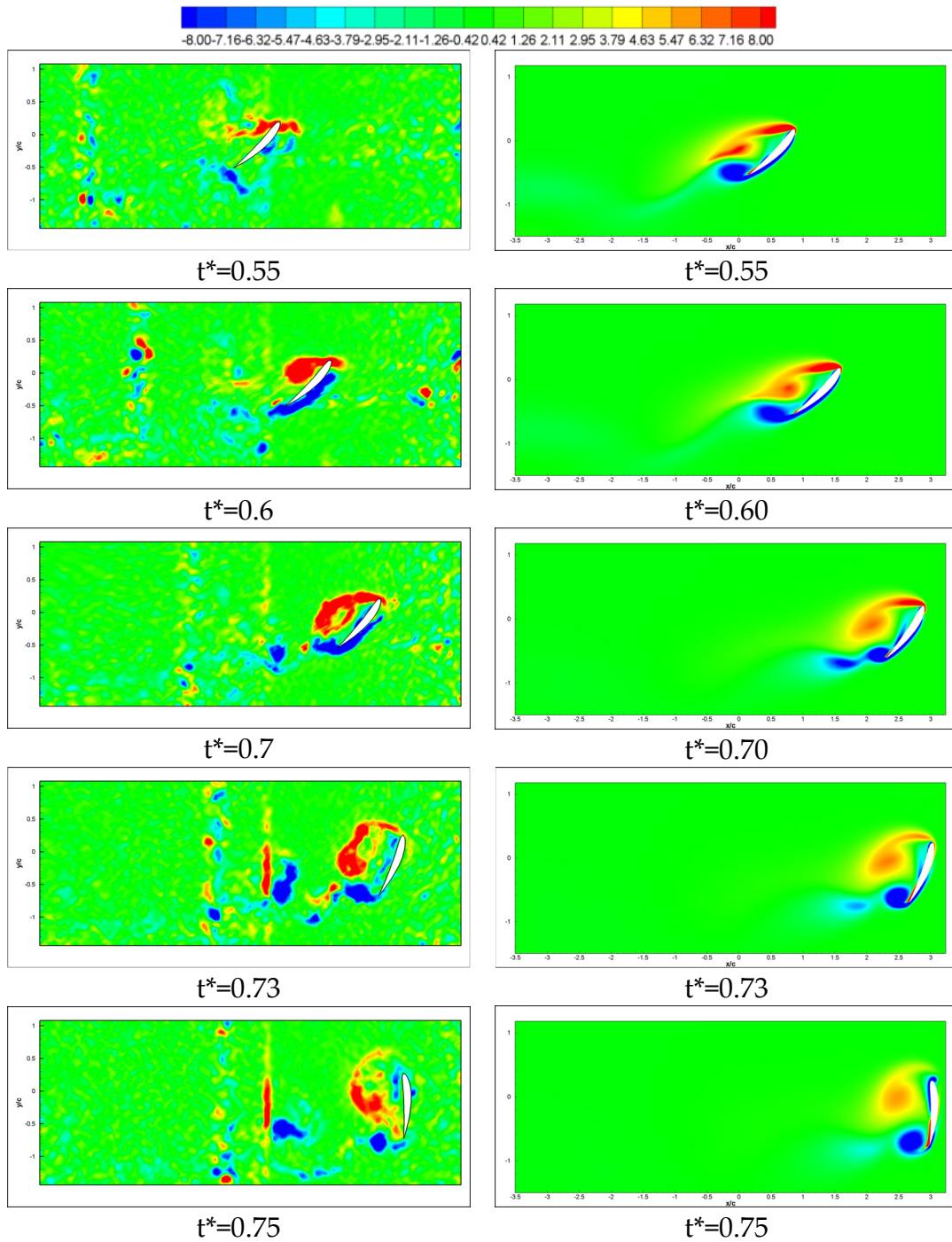


Figure 6.12 (continued) Comparison of experimental (left) and numerical (right) non-dimensional vorticity contours at the third quarter period at $\alpha=45^\circ$, $Re = 1000$.

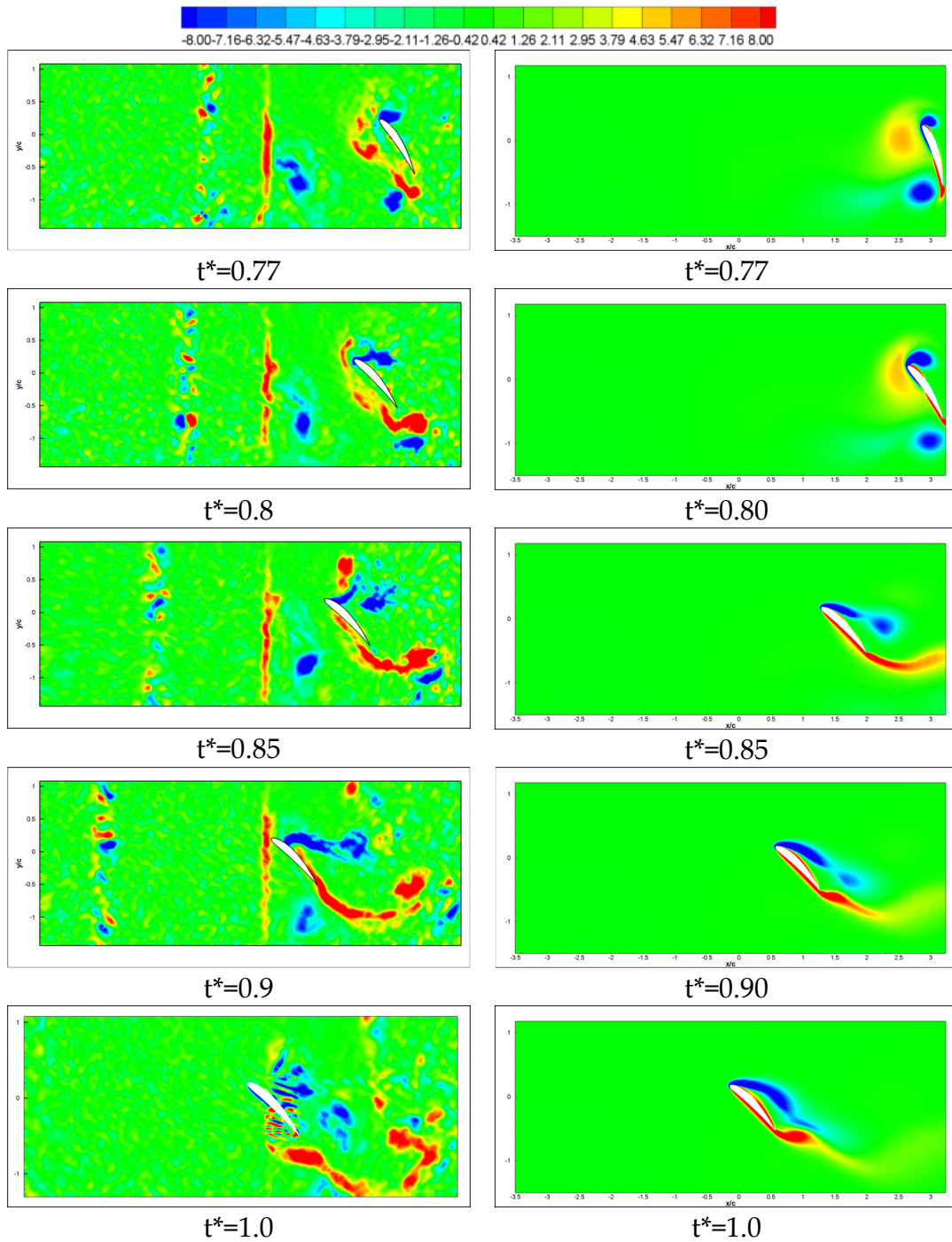


Figure 6.12 (continued) Comparison of experimental (left) and numerical (right) non-dimensional vorticity contours at the fourth quarter period at $\alpha=45^\circ$, $Re = 1000$.

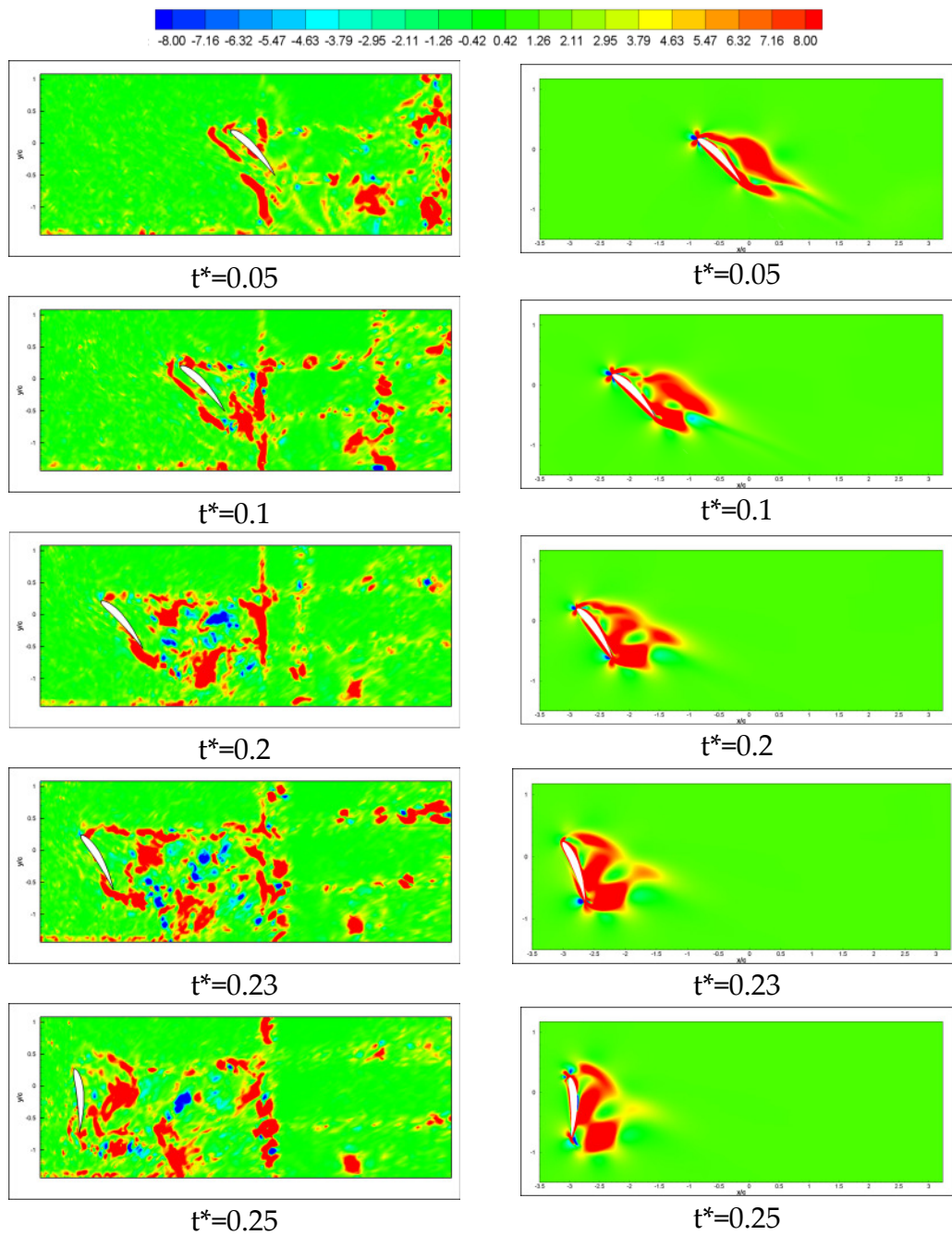


Figure 6.13 Comparison of experimental (left) and numerical (right) non-dimensional Q contours, second invariant of velocity gradient tensor, at the first quarter period at $\alpha=45^\circ$ $Re = 1000$.

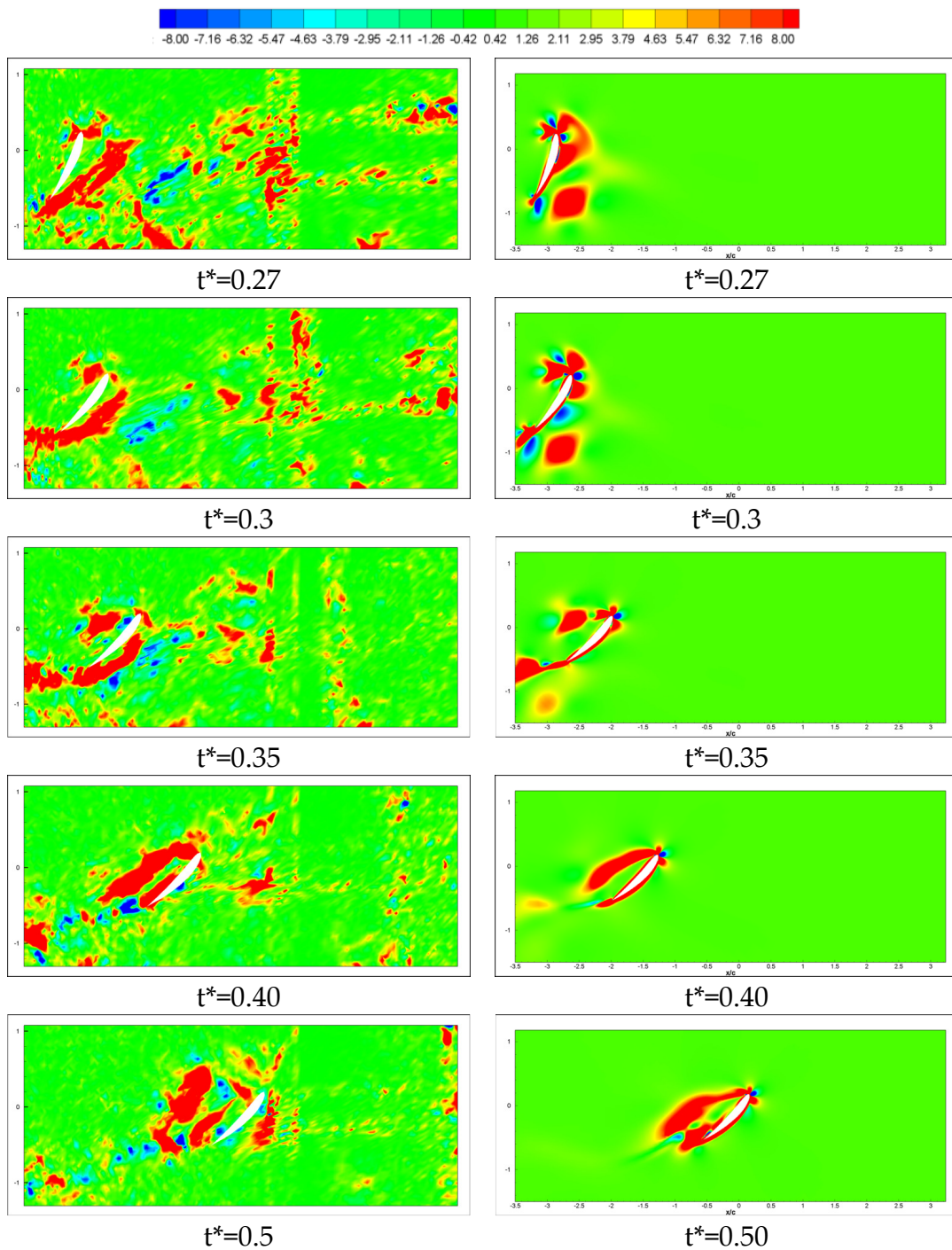


Figure 6.13 (continued) Comparison of experimental (left) and numerical (right) non-dimensional Q contours, second invariant of velocity gradient tensor, at the second quarter period at $\alpha=45^\circ$, $Re = 1000$.

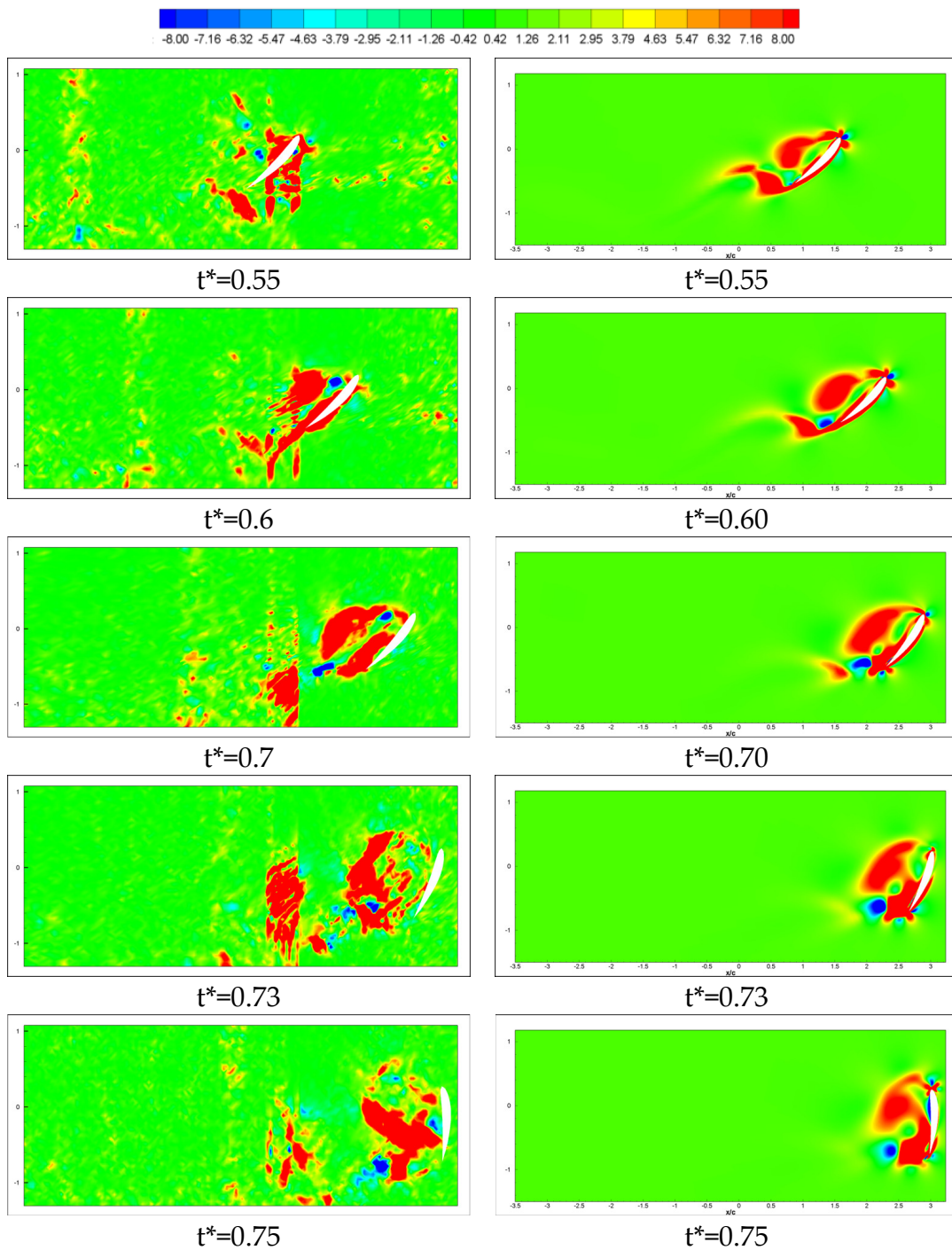


Figure 6.13 (continued) Comparison of experimental (left) and numerical (right) non-dimensional Q contours, second invariant of velocity gradient tensor, at the third quarter period at $\alpha=45^\circ$, $Re = 1000$.

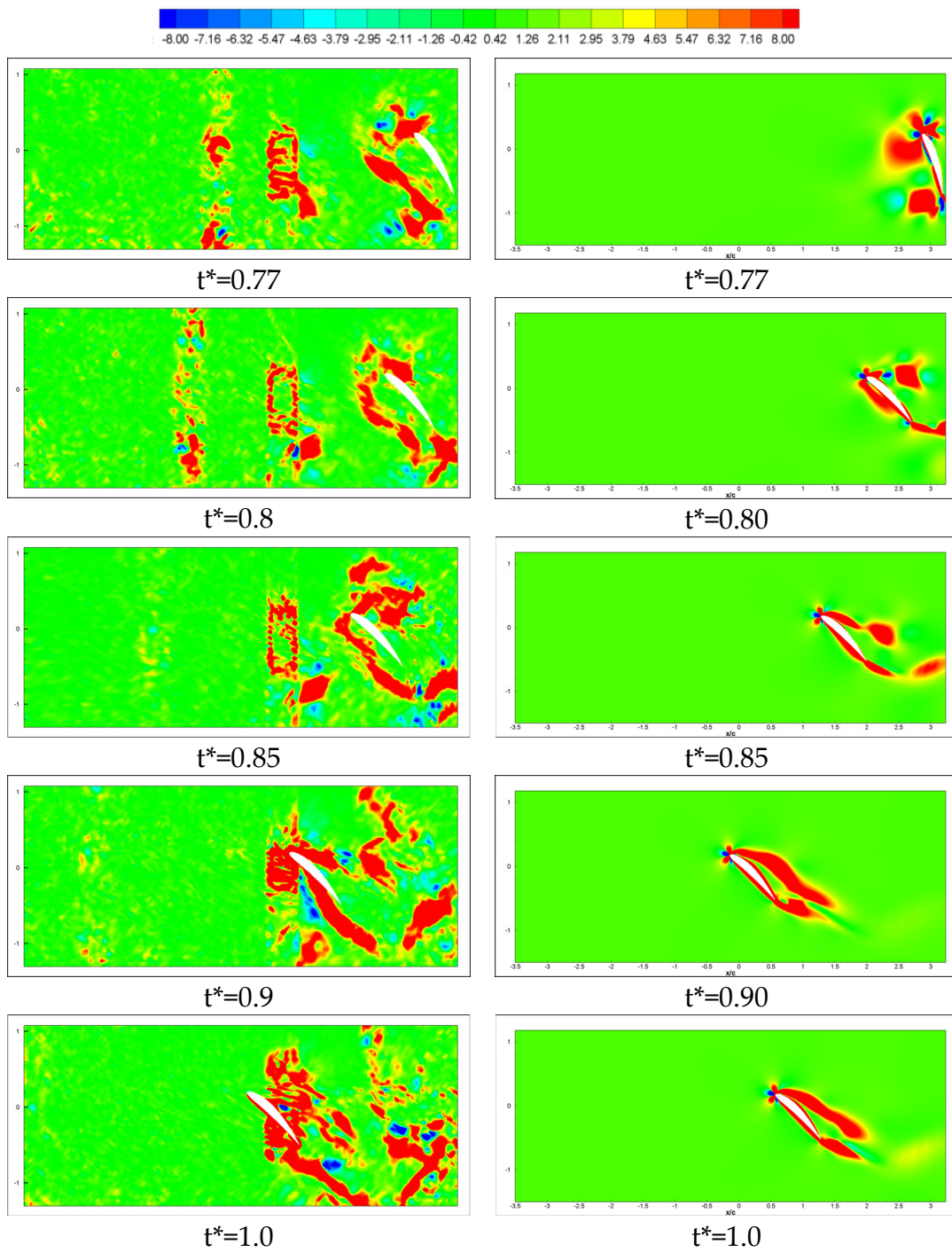


Figure 6.13 (continued) Comparison of experimental (left) and numerical (right) non-dimensional Q contours, second invariant of velocity gradient tensor, at the fourth quarter period at $\alpha=45^\circ$, $Re = 1000$.

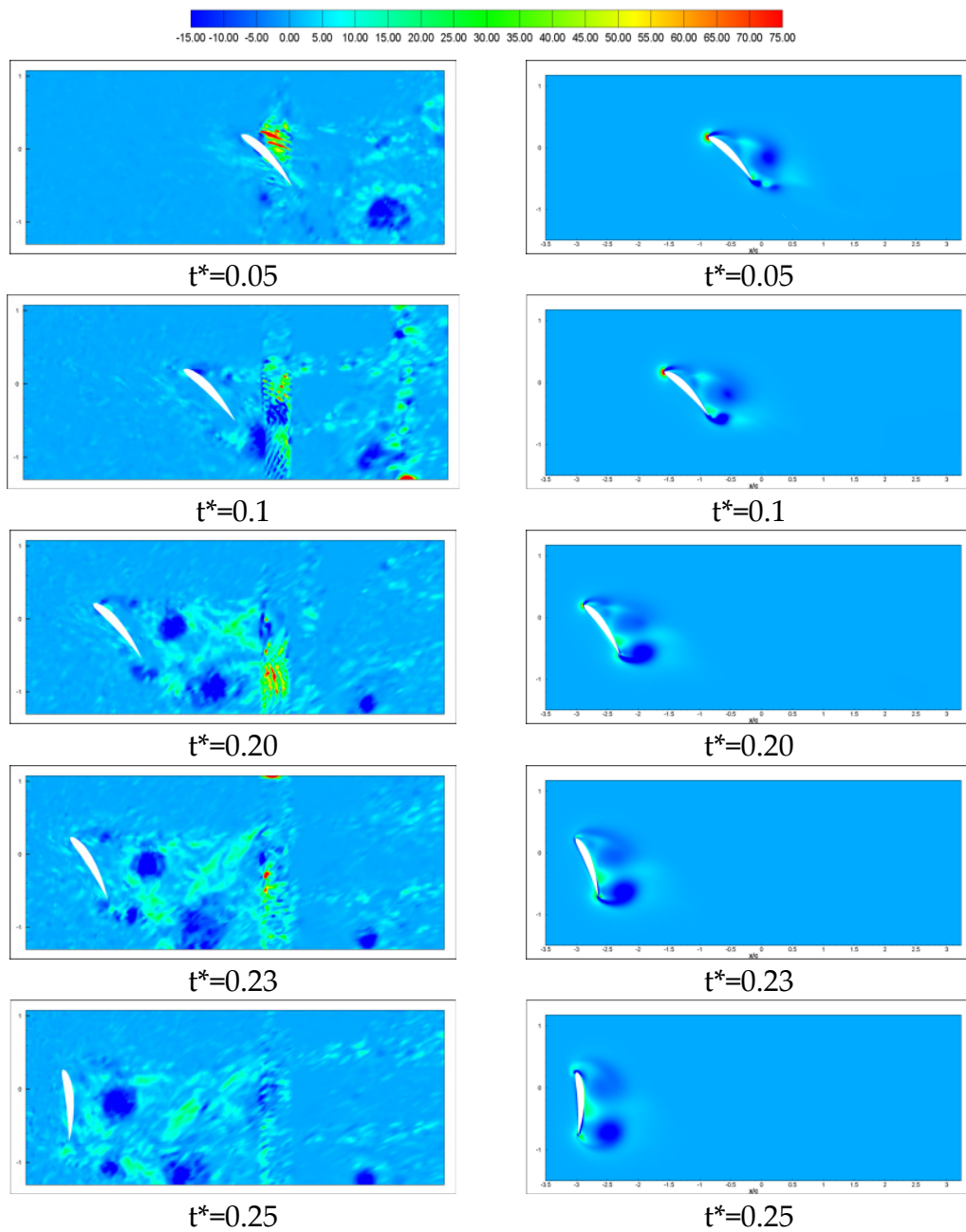


Figure 6.14 Comparison of experimental (left) and numerical (right) non-dimensional λ_2 contours, second negative eigenvalue of $(S^2 + \Omega^2)$, at the first quarter period at $\alpha=45^\circ$, $\text{Re} = 1000$.

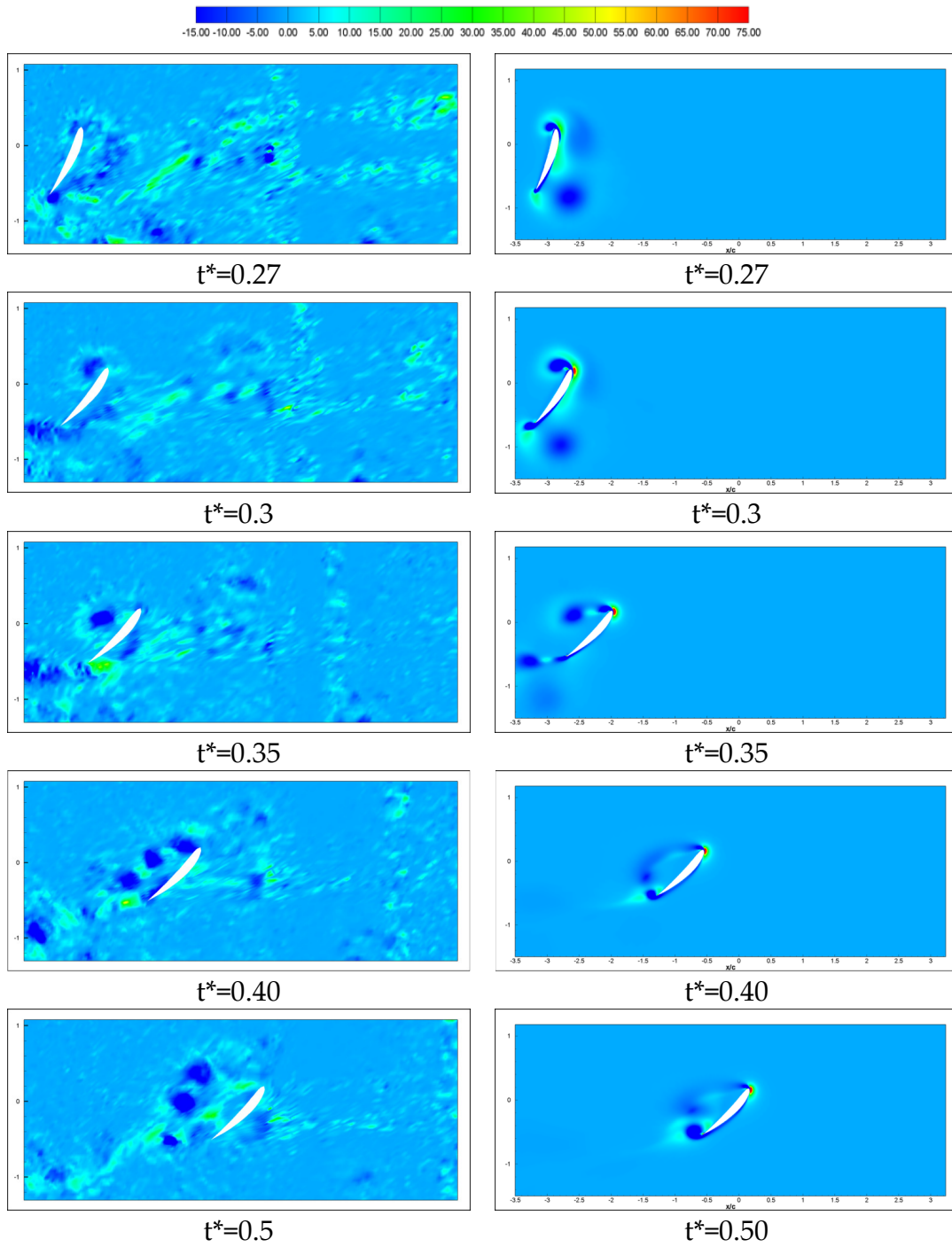


Figure 6.14 (continued) Comparison of experimental (left) and numerical (right) non-dimensional λ_2 contours, second negative eigenvalue of $(S^2 + \Omega^2)$, at the second quarter period at $\alpha = 45^\circ$, $\text{Re} = 1000$.

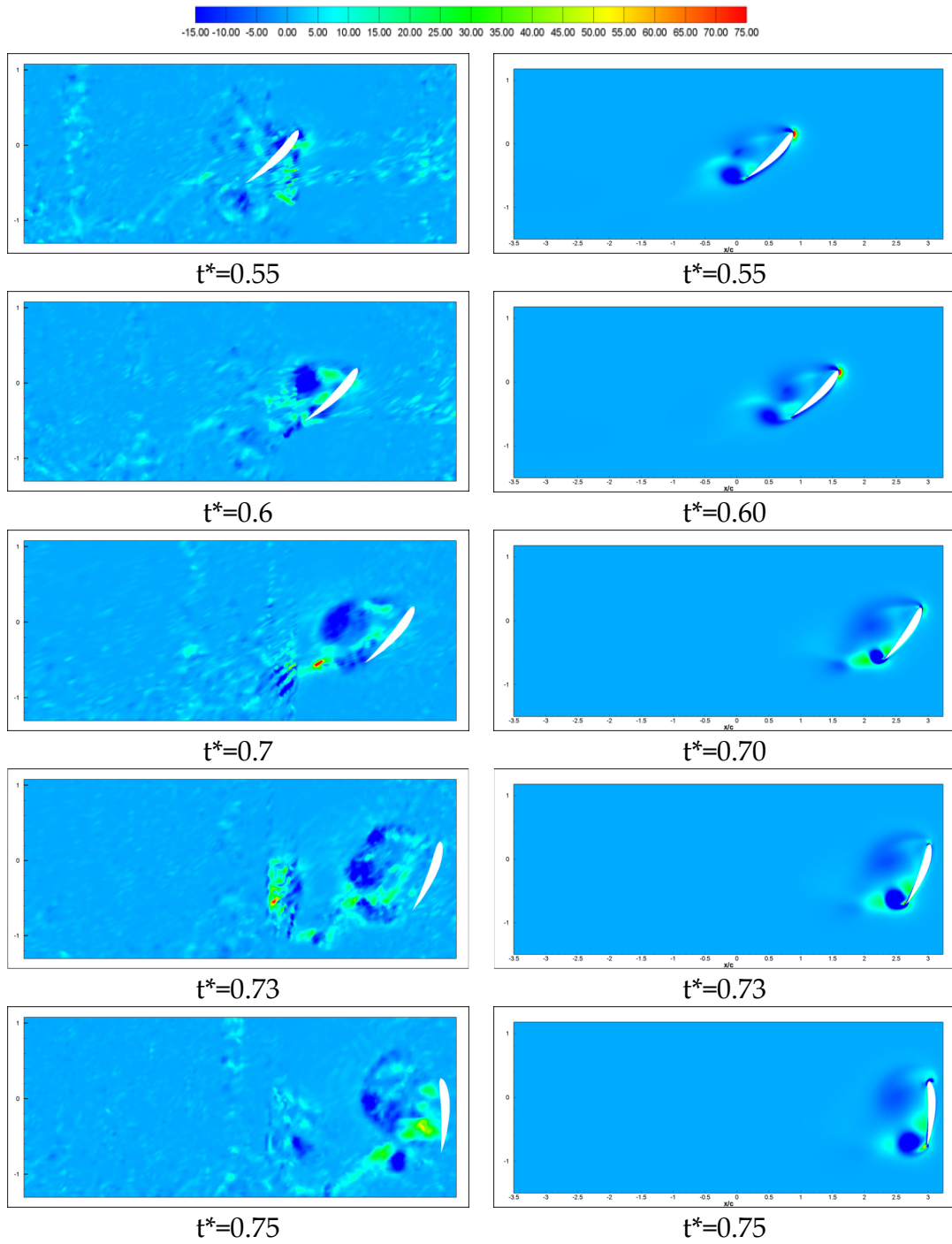


Figure 6.14 (continued) Comparison of experimental (left) and numerical (right) non-dimensional λ_2 contours, second negative eigenvalue of $(S^2 + \Omega^2)$, at the third quarter period at $\alpha=45^\circ$, $Re = 1000$.

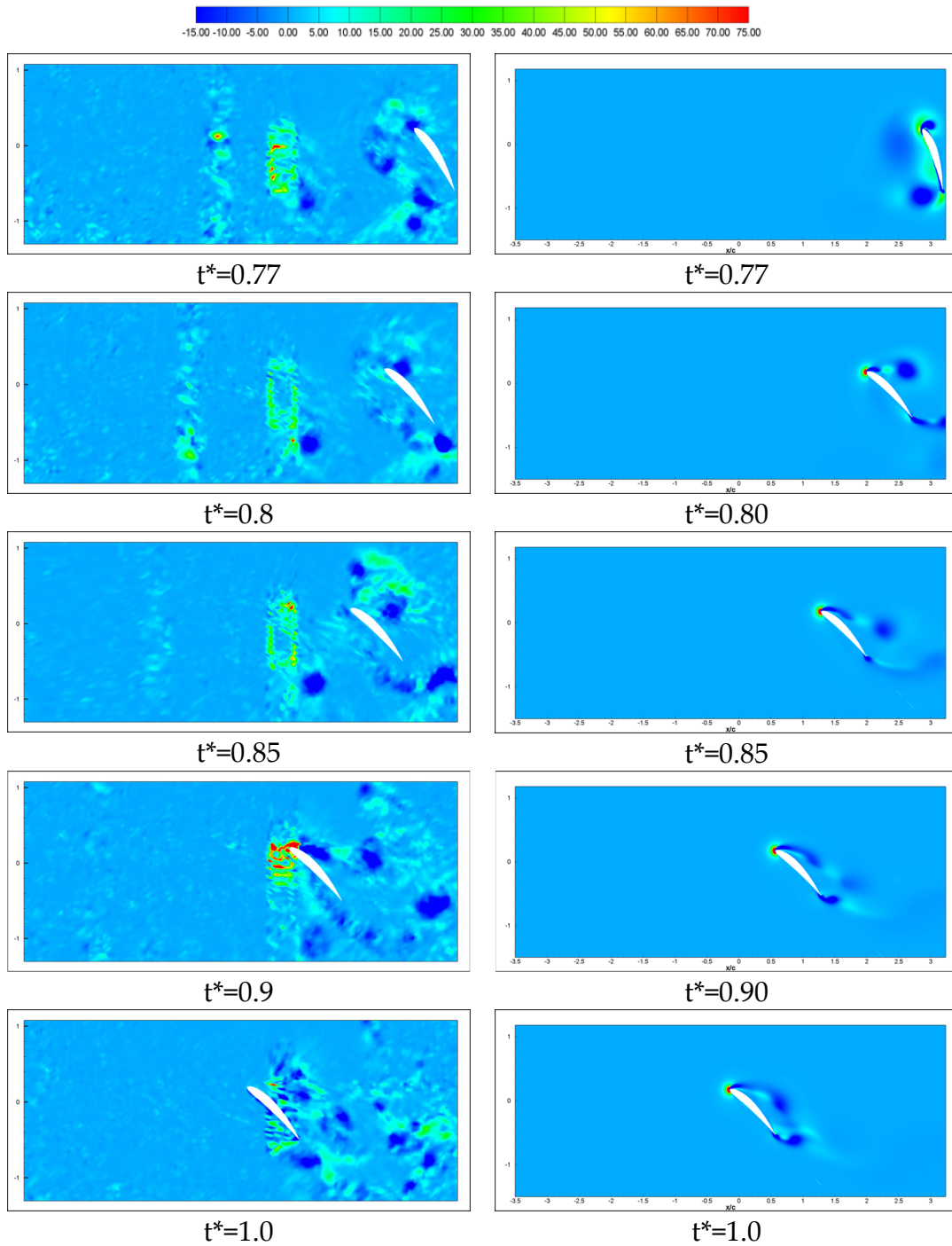


Figure 6.14 (continued) Comparison of experimental (left) and numerical (right) non-dimensional λ_2 contours, second negative eigenvalue of $(S^2 + \Omega^2)$, at the fourth quarter period at $\alpha=45^\circ$, $Re = 1000$.

CHAPTER VII

THREE-DIMENSIONAL NUMERICAL ANALYSIS OF FLAPPING MOTION

7.1 Numerical Analysis

The flapping motion in three-dimensional space has the same kinematic parameters as in two-dimensional motion. The effect of spanwise flow on the vortex creation has been investigated. Three-dimensional analysis is carried out on the cambered airfoil NACA 6412 having 6 cm chord length and 30 cm span corresponding to an aspect ratio of 5. Small birds and insects that are capable of hovering usually have an aspect ratio varying from 3 to 11. A typical dragonfly's wings have an aspect ratio of 11 which gives the aspect ratio around 5 for half wing. Moreover, studies concerning on robotic models of insect wings usually have similar aspect ratio values. Dickinson et al [66] and Usherwood et al. [59] state that the effect of aspect ratio is relatively minor especially below 50° angle of

attack. In three-dimensional simulations, the experimental model is mounted on a plexiglas end-plate from one side which acts like a symmetry plane. In order to have consistency between the experimental and numerical studies, the wing root is also attached to the symmetry plane in the numerical studies.

For three dimensional numerical analysis of flapping motion, the commercially available flow solver, Fluent^R is employed. The details of FLUENT solver were given in Chapter 4. The parallel solution of the problem is obtained with a computational mesh having approximately 1.6M elements. The computational mesh is generated using the GAMBIT and the TGRID, mesh generators of Fluent. Unstructured grids are employed with 12 boundary layer prism caps on the wall having a value of $y^+ = 1$ at the surface. No-slip wall boundary condition is implemented with a prescribed motion given by user defined functions. At the tip of the wing, a wingtip is created based on the mean camber line of the airfoil. The finite wing, whose cross-section is NACA 6412, has an aspect ratio of 5 and the wing is placed in a half sphere having a radius of approximately 16 chords. The outer surface of the half sphere is specified as pressure outlet boundary condition. The computational domain and the boundary conditions are given in Figures 7.1- 7.2.

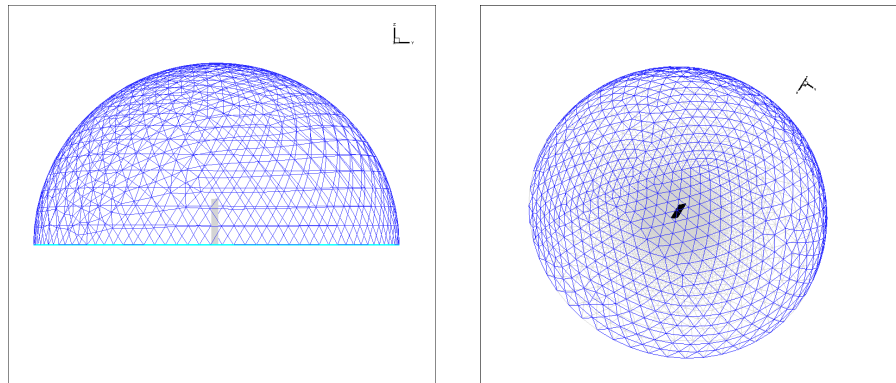


Figure 7.1 Three-dimensional computational mesh.

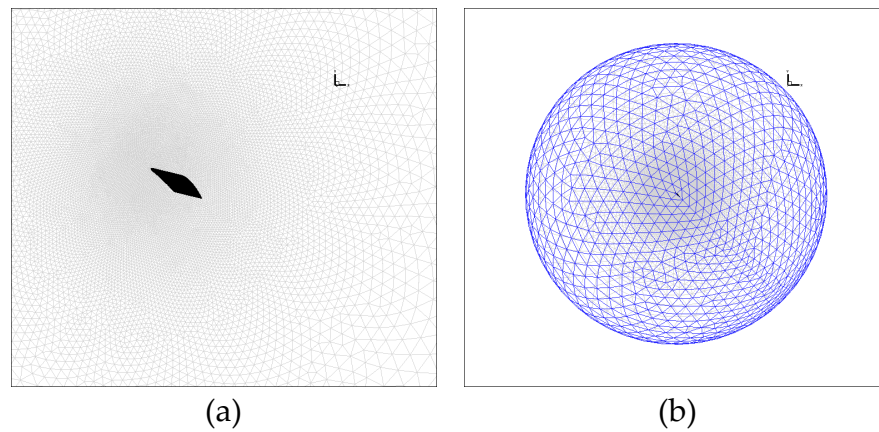


Figure 7.2 Boundary conditions: (a) symmetry plane and the wing, (b) pressure outlet at the far field.

To accelerate the full 3D computations are carried out using the FLUENT solver in parallel. The parallel speedup is compared for one period time (Figure 7.3) and the efficiency gained is shown in Figure 7.4.

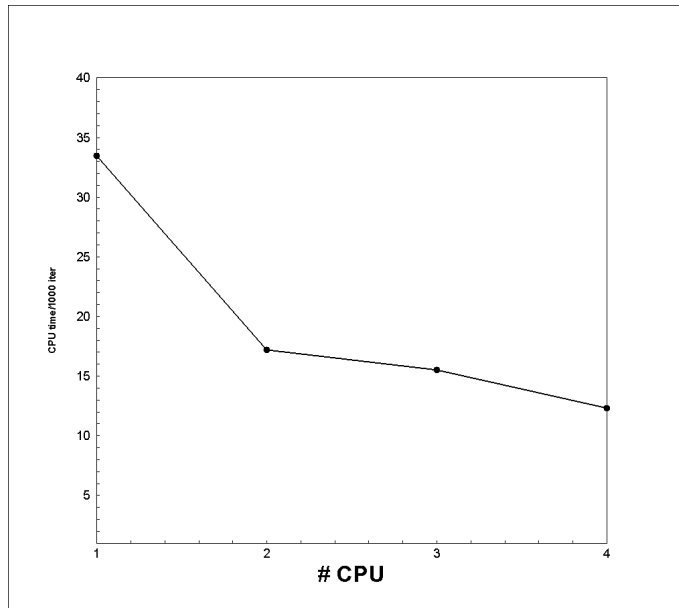


Figure 7.3 CPU time comparisons for three-dimensional solutions

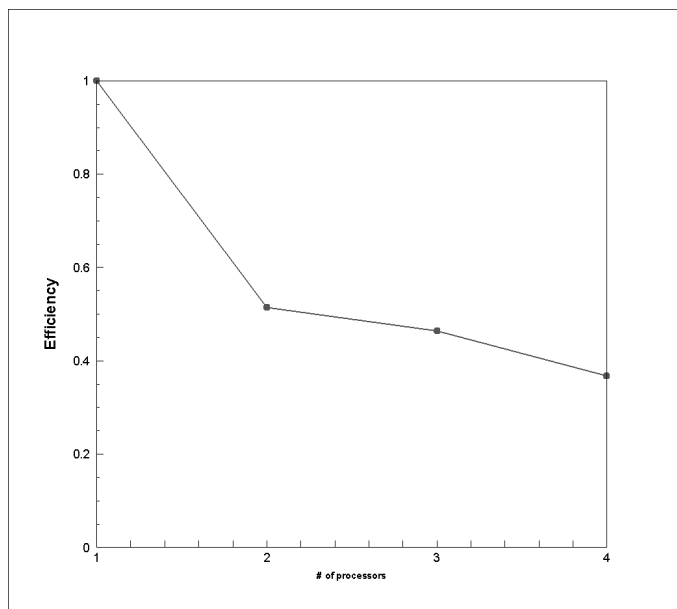


Figure 7.4 Efficiency plot for three-dimensional solutions.

In three-dimensional analysis, the identification of vortex regions is not possible using scalar quantities, such as the magnitude of vorticity or pressure. Therefore, the identified vortex regions will be presented in terms of non-dimensional Q contours only. As stated previously, positive Q regions will define vortex regions and for Q=8 iso-contours at $\alpha=45^\circ$, $Re = 1000$ will be presented for a full period of motion. As shown in Figure 7.5, the formation of the leading edge vortex and the translational vortex at the trailing edge can easily be seen. The shedding of vortices after rotational motion is also observed in the plots. The time sequence of plots shown in these figures are all three dimensional, but viewed along the spanwise direction, in the z axis. It should be noticed that these plots do not belong to a single plane along the z axis but covers the total full depth of the z axis as one observes flow from the wing tip. Therefore, these images reflect the integration of all the vortex distributions along the spanwise direction.

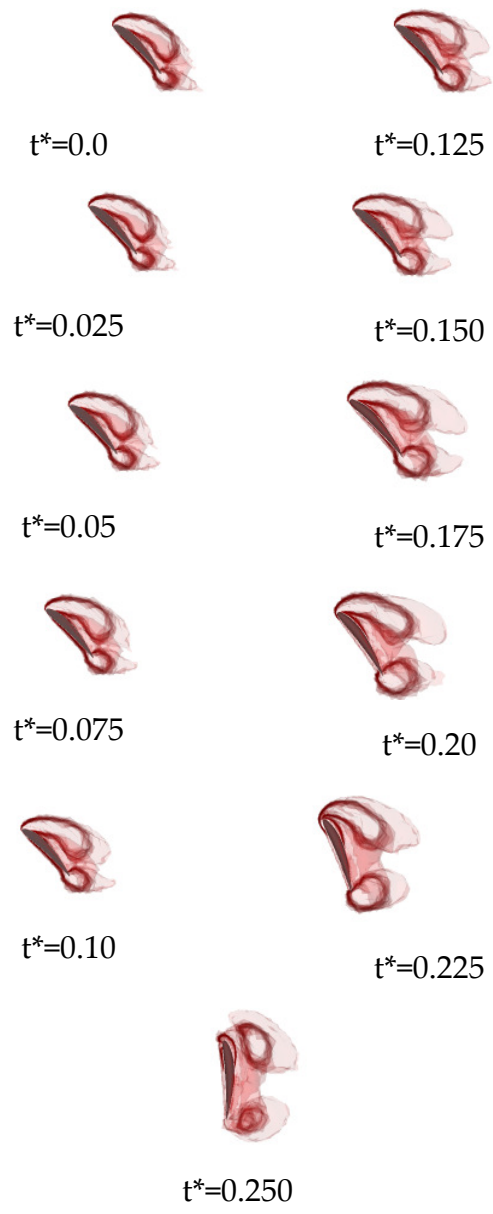


Figure 7.5 Iso-contours, $Q=8$ at $\alpha=45^\circ$, $Re = 1000$ during the first half downstroke.

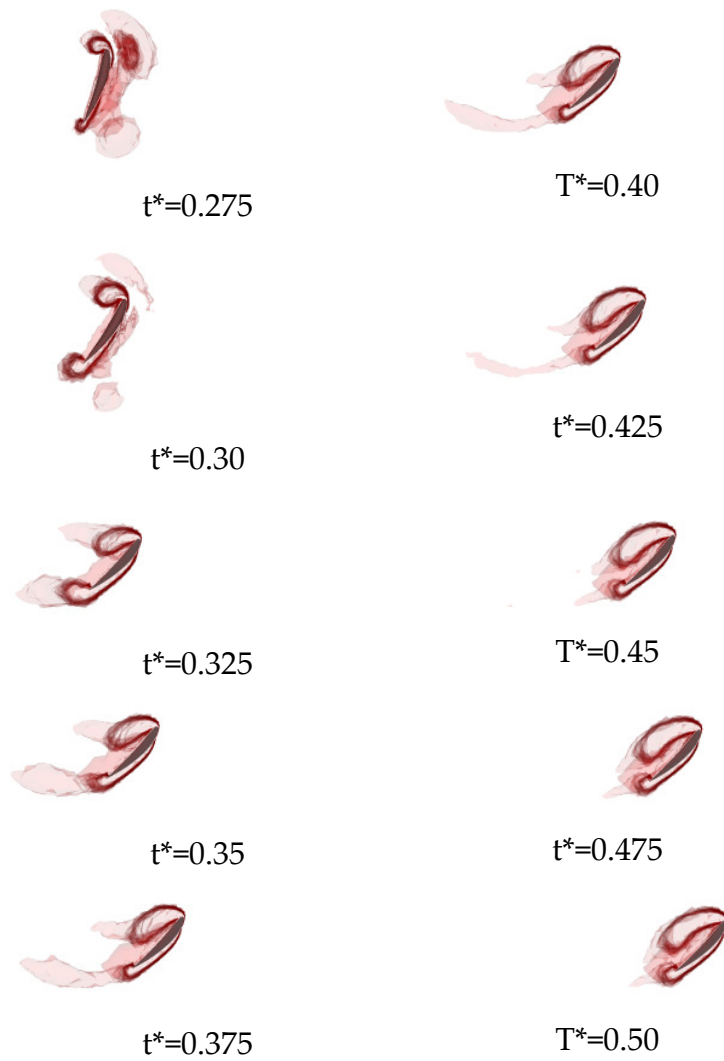


Figure 7.5 (continued) Iso-contours, $Q=8$ at $\alpha=45^\circ$, $Re = 1000$ during the first half upstroke.



Figure 7.5 (continued) Iso-contours, $Q=8$ at $\alpha=45^\circ$, $Re = 1000$ during the second half upstroke.

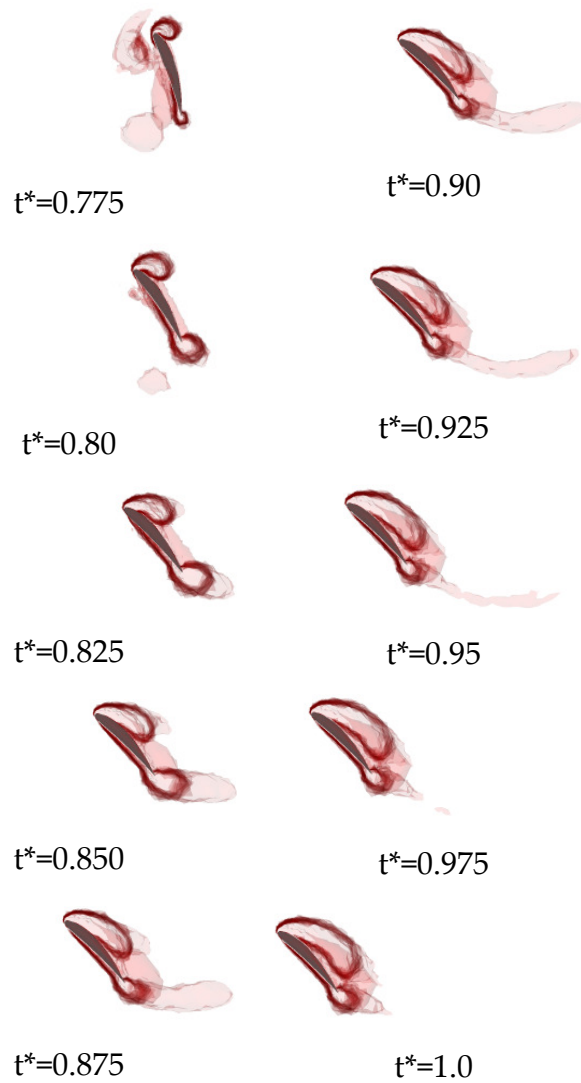


Figure 7.5 (continued) Iso-contours, $Q=8$ at $\alpha=45^\circ$, $Re = 1000$ during the second half downstroke.

On the three-dimensional wing it is seen that the leading edge vortex is also three dimensional and the core of this three dimensional vortex form a line which is nearly parallel to the spanwise direction. At the instant considered, the distance from the leading edge of the wing to the vortex

core does not change significantly until the tip of the wing. Although the wing is set at a considerably high angle of attack there is no catastrophic stall. Instead there is a stable and lift enhancing leading edge vortex extending the along the spanwise direction. As noted by Knowles et al. [111], sweeping motion of 3D wing leads to conical leading edge vortex which then leads to spanwise flow extracting vorticity from the leading edge core and stabilizing the leading edge vortex. 3D leading edge vortex is stable and lift-enhancing despite the occurrence of Kelvin-Helmholtz instability [111]. The vortex core line for the leading edge vortex is drawn on the wing's leading edge surface and it is observed that the vortex core is aligned along the spanwise direction. The stream ribbons are also plotted colored by the second invariant of velocity gradient value, Q criteria. At the tip of the wing, the flow separates from the wing and has a helical shape.

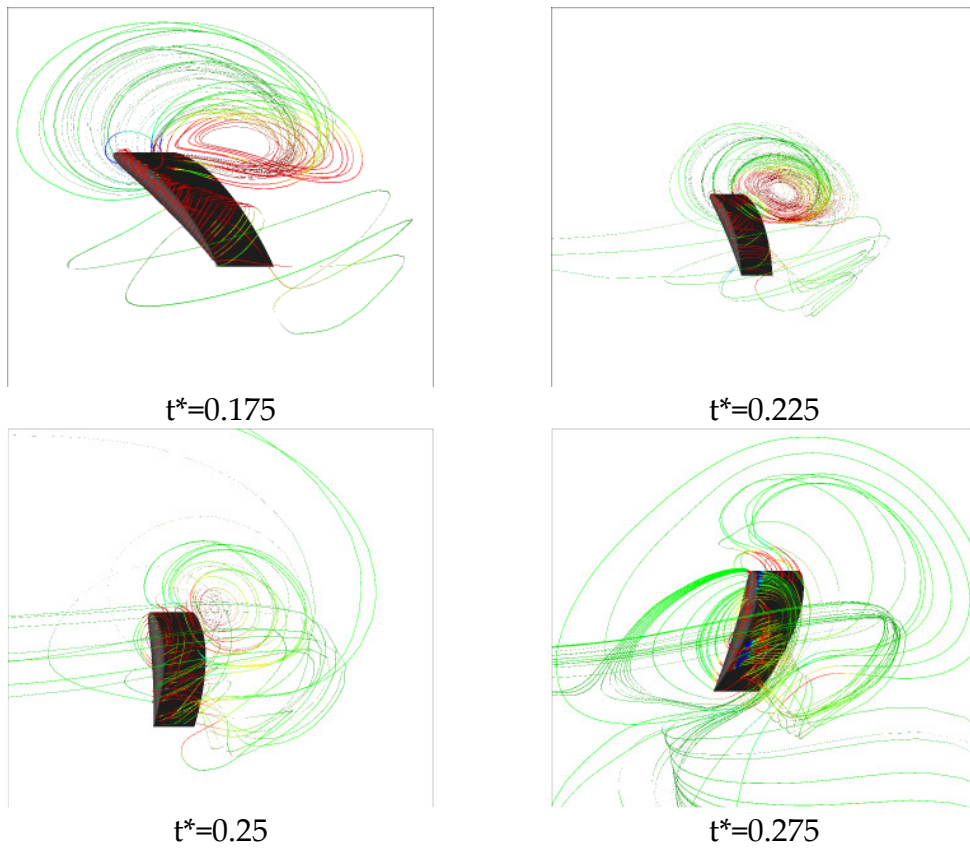


Figure 7.6 Stream ribbons during the first quarter period (first downstroke) at $\alpha=45^\circ$, $Re = 1000$.

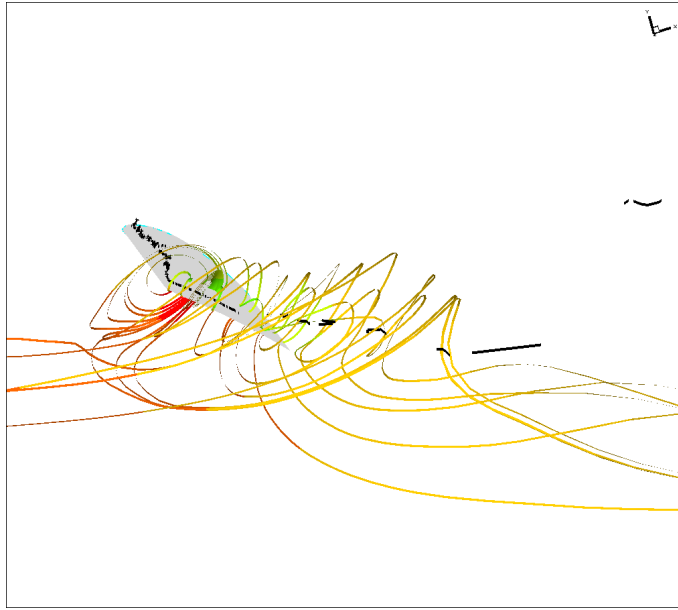


Figure 7.7 Stream ribbons at the tip of the wing when $t^*=0.1$ (during first downstroke) at $\alpha=45^\circ$, $Re = 1000$

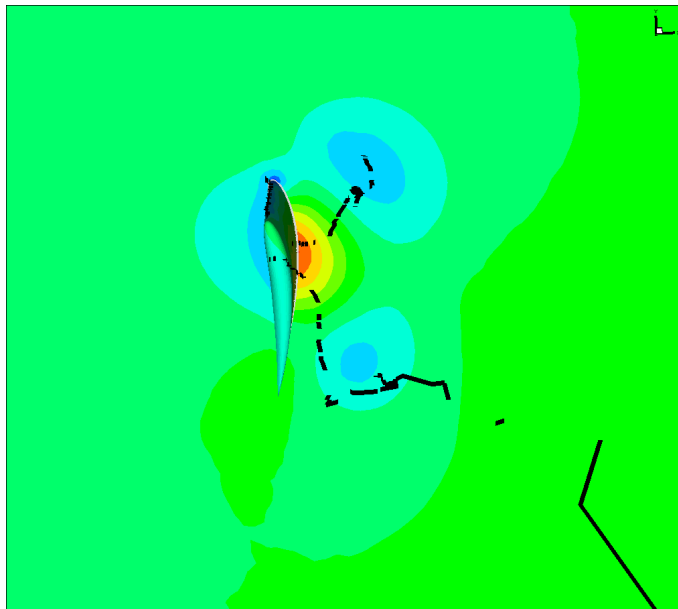


Figure 7.8 Pressure coefficient contours with vortex core lines at the end of the first quarter period ($t^*=0.25$).

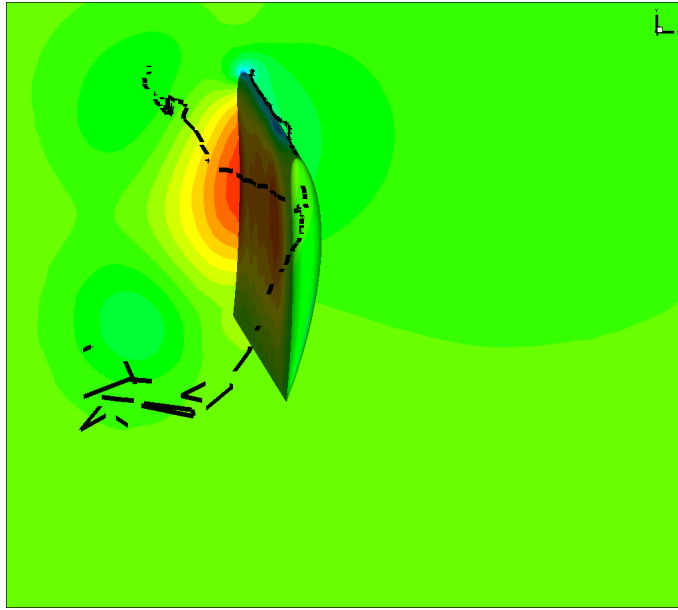


Figure 7.9 Pressure coefficient contours with vortex core lines at the end of the third quarter period ($t^*=0.75$).

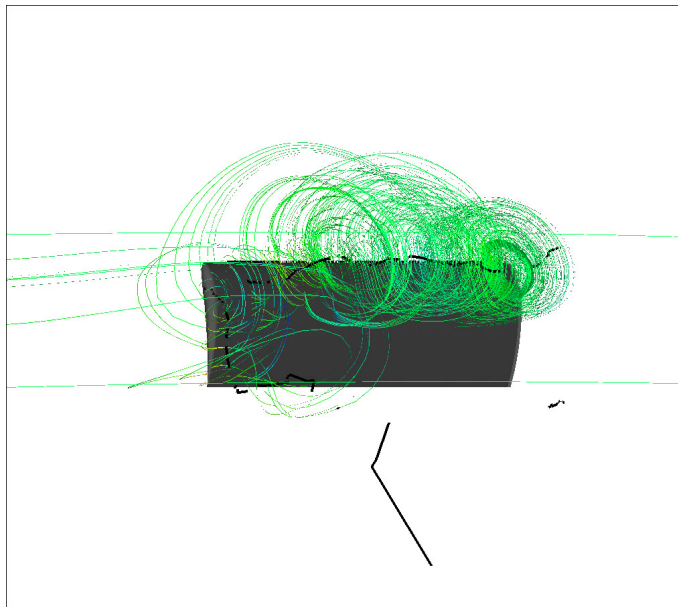


Figure 7.10 Stream ribbons (colored) and vortex core lines (black) at the end of the first half downstroke ($t^*=0.25$) for $\alpha=45^\circ$, $Re = 1000$.

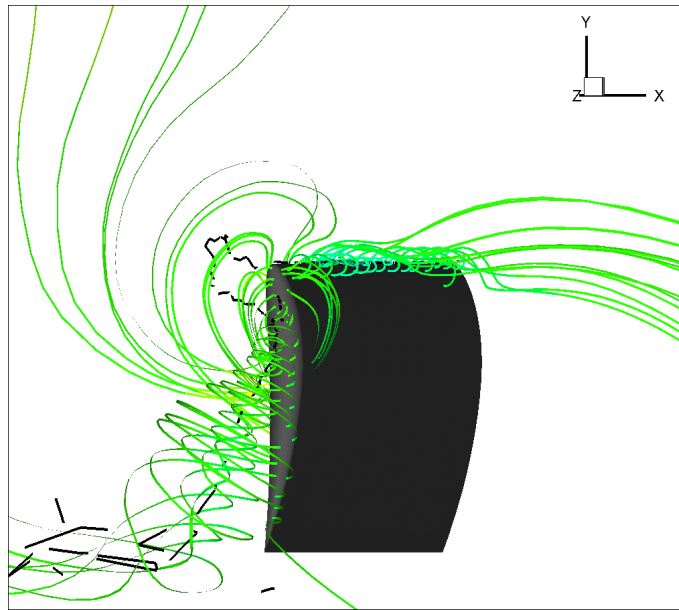


Figure 7.11 Stream ribbons (colored) and vortex core lines (black) at the end of the second half upstroke ($t^*=0.75$).for $\alpha=45^\circ$, $Re = 1000$ (left view).

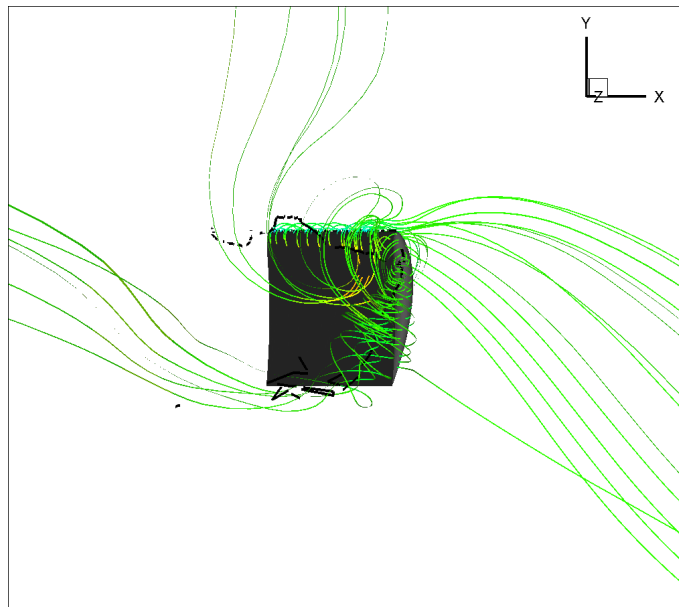


Figure 7.12 Stream ribbons (colored) and vortex core lines (black) at the end of the second half upstroke ($t^*=0.75$).for $\alpha=45^\circ$, $Re = 1000$ (right view).

The flow traces showed that the spanwise flow has a stabilizing effect on the leading edge structure for 3D flow whereas in 2D cases the leading edge flow detaches readily. At the tip of the wing, the flow separates from the wing and leaves the wing tip in a helical shape, forming the well known wing tip vortices as observed in Figure 7.7 and Figure 7.11. Van Den Berg and Ellington [70],[71] showed that the leading-edge vortex has a strong axial flow velocity component along the spanwise direction which stabilizes the vortex and reduces its diameter. In their research, they found out that the leading-edge vortex separated from the wing at approximately at 75% of the wing span and fed vorticity into a large, tangled tip vortex. Birch and Dickinson [69] states that the flow structure largely responsible for the good performance of insect wings is identified as the leading-edge vortex. But because such vortices become detached from a wing in two-dimensional flow, an unknown mechanism must keep them attached in three-dimensional flapping wings. The current explanation, analogous to a mechanism observed on delta-wings, is that spanwise flow through a spiral vortex drains energy from the vortex core. They also reported that, at those Reynolds numbers matching the flow regimes for most insects, flapping wings do not generate a spiral vortex akin to that produced by delta-wing aircraft and that limiting spanwise flow with fences and edge baffles does not cause detachment of the leading edge vortex. The data support an alternative hypothesis that downward flow induced by the tip vortices limits the growth of the leading-edge vortex.

In three-dimensional analysis, the vorticity contours can no longer be used for the identification of vortices. Instead, non-dimensional contours of the second invariant of the velocity gradient, Q criteria is used for this purpose. In Figure 7.13, the spanwise evolution of vortex regions on the finite wing is explored at specified non-dimensional time steps. At the instant considered, the vortex regions occupy a larger space at the root location and this region shrinks a little bit just after moving from the root location along the span of the wing and stays nearly constant along the wing span. The leading and trailing edge vortices are clearly identified. At the tip of the wing, the leading and trailing edge vortex regions start to merge and detach from the wing after the tip. The stream ribbon plots shows how the fluid detaches from the wing and the complexity of the flow.

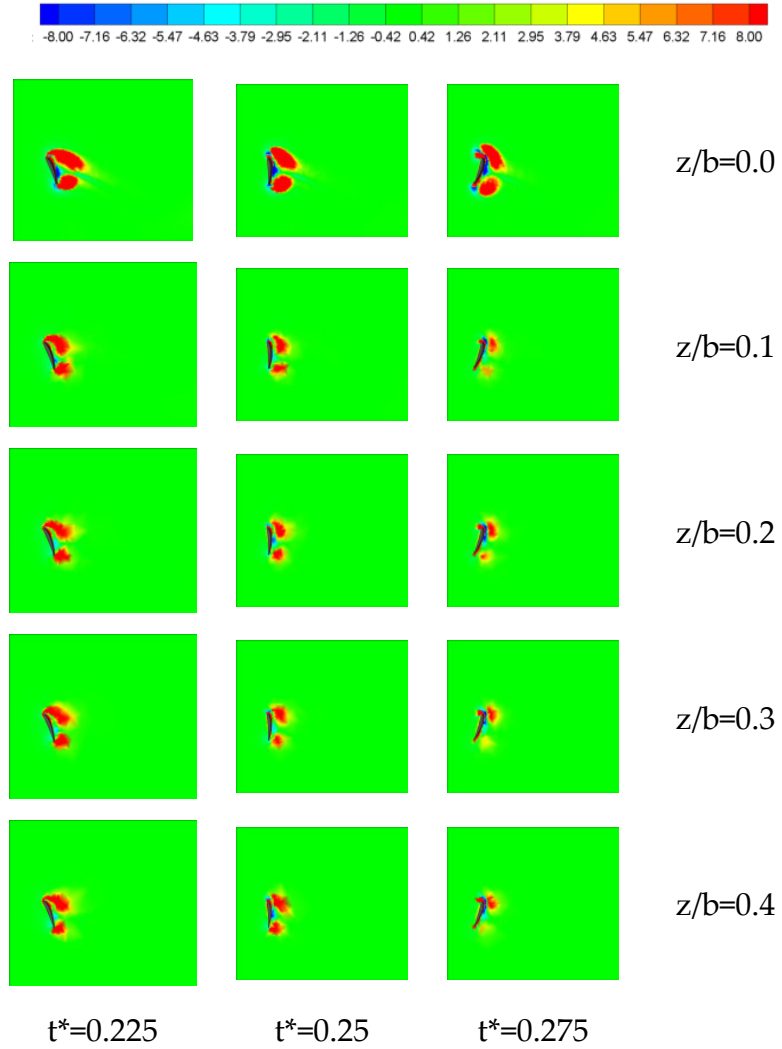


Figure 7.13 Spanwise evolution of vortex regions during the first rotational phase for $\alpha=45^\circ$, $Re = 1000$.

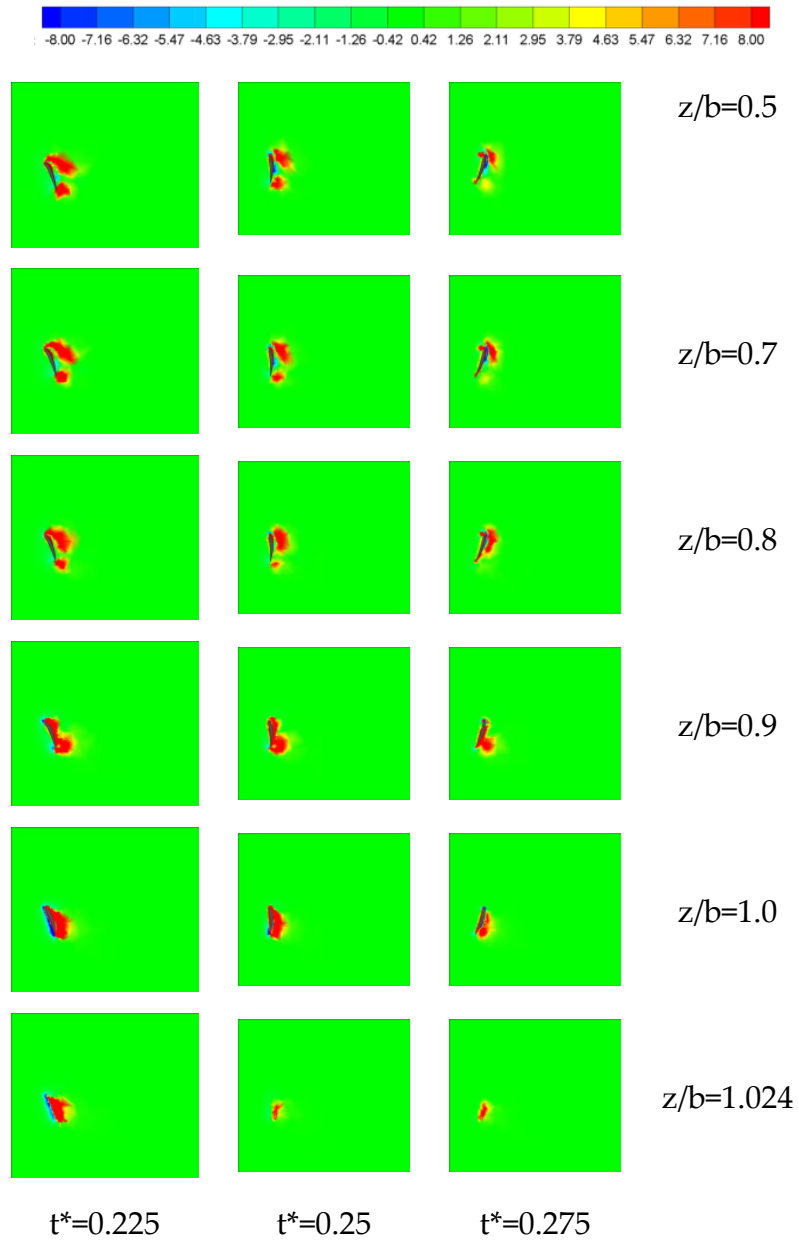


Figure 7.13 (Continued) Spanwise evolution of vortex regions during the first rotational phase for $\alpha=45^\circ$, $Re = 1000$.

7.2 Comparison of Two-Dimensional and Three-Dimensional Numerical Solutions

Two and three dimensional numerical solutions are compared in terms of the aerodynamic force coefficients generated and the vortex regions identified using the second invariant of the velocity gradient tensor, the so called "Q criteria". In the following figures, Figures 7.14 - 7.16, the effect of three dimensionality is evidenced. The absolute values corresponding to the peaks for the three dimensional cases are smaller than the two-dimensional results. Oscillations observed in the three dimensional force coefficients during the translational motion (i.e. constant velocity and angle of attack) are probably due to the mesh quality. As noted in literature, two-dimensional solutions over predict the three-dimensional force coefficients.

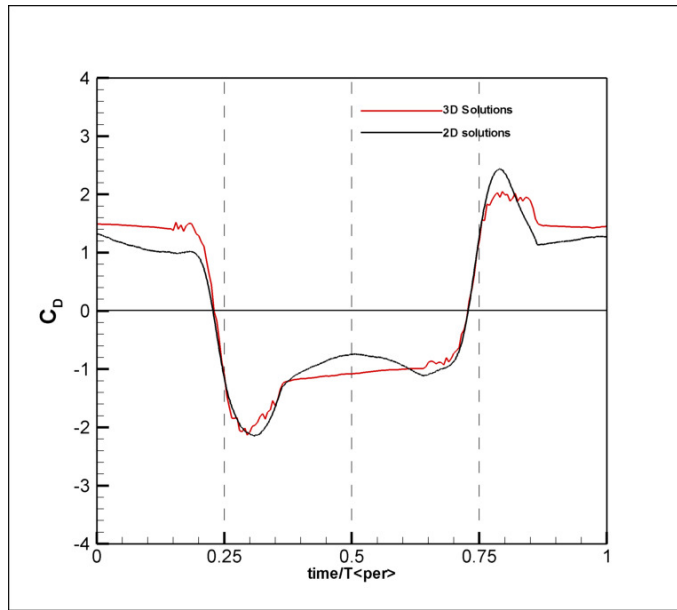


Figure 7.14 Comparison of drag coefficient distribution for two and three-dimensional numerical solutions.

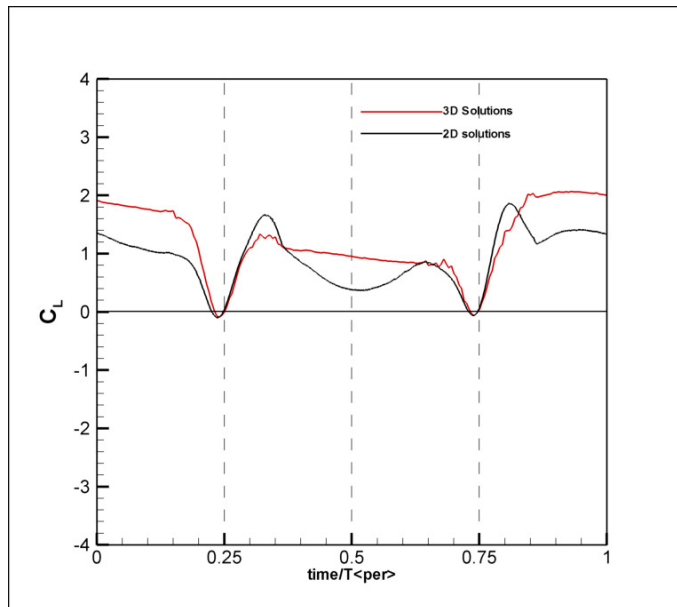


Figure 7.15 Comparison of lift coefficient distribution for two and three-dimensional numerical solutions.

Detailed flow field solutions obtained for the three-dimensional wing at its mid span are compared to the two-dimensional solutions in Figure 7.16, as sequence of images during the first half cycle of the downstroke of the complete period. As seen from these sequence of images, the Q contours observed in the 3D case exhibit a more isolated behavior for the leading and the trailing edge vortices (they are more distinguished) where as for the 2D case these contours show a more mixed and merged behavior .

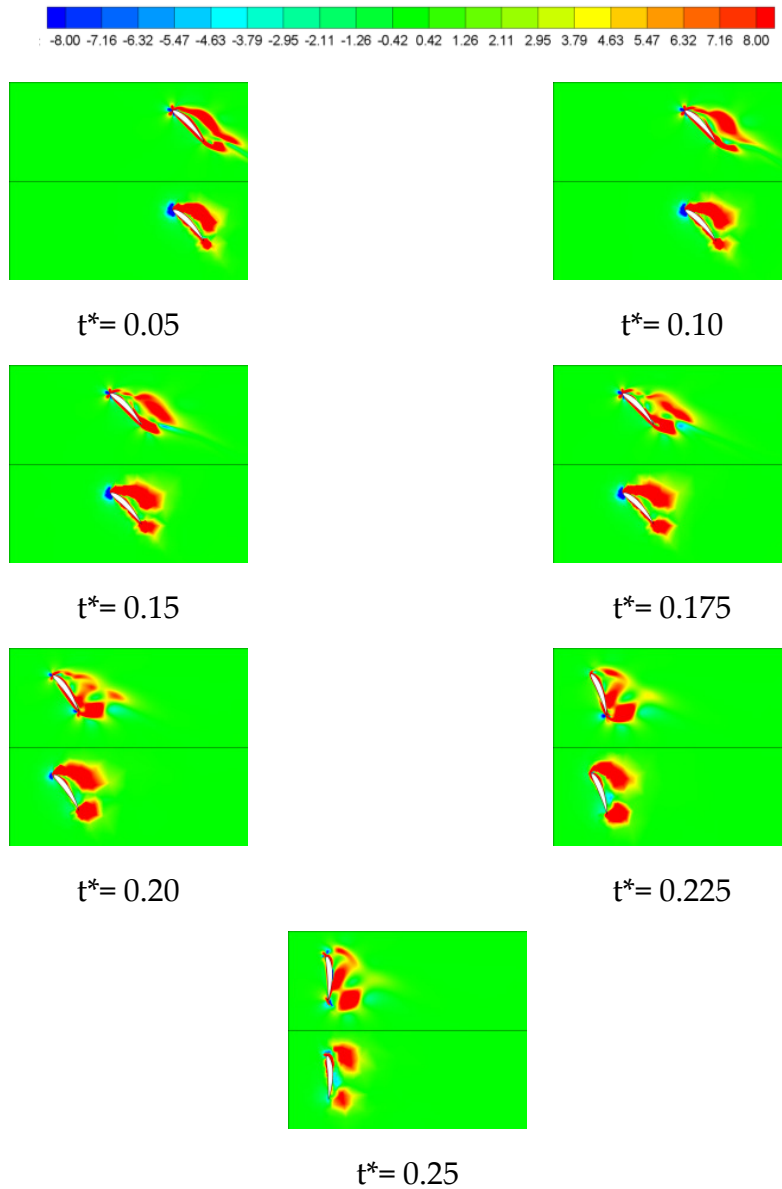


Figure 7.16 Comparison of vortex structures for two-dimensional (top) and three-dimensional solutions (bottom) at the midspan in terms of non-dimensional Q criteria, for $\alpha=45^\circ$, $Re = 1000$ during the first quarter period.

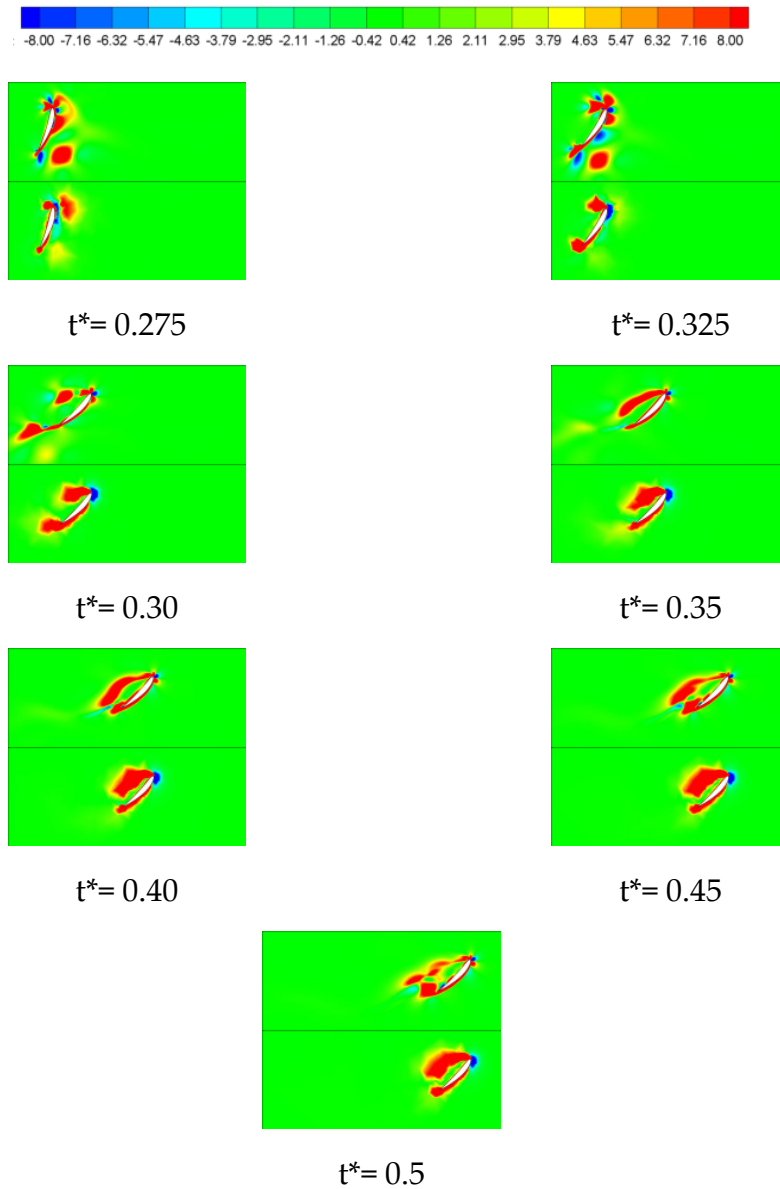


Figure 7.16 (Continued) Comparison of vortex structures for two-dimensional (top) and three-dimensional solutions (bottom) at the midspan in terms of non-dimensional Q criteria, for $\alpha=45^\circ$, $Re = 1000$ during the second quarter period.

CHAPTER VIII

THREE-DIMENSIONAL EXPERIMENTAL ANALYSIS OF FLAPPING MOTION

8.1 Experimental Analysis

Same PIV technique as used in the 2D flow field measurements is used for three-dimensional velocity fields' measurements for the flapping motion simulations over a finite wing configuration. The same experimental set up is used with slight modifications. One of the end plates is removed from the 2D wing attachment configuration and the 3D wing model is attached to one of the existing end plates. In this way the three dimensional behavior of flow is observed since one of the trailing edges of the wing is set free in the flow field. The 3D wing model has the same chord length of 6 cm and a span of 30 cm yielding an aspect ratio of 5.

Three dimensional PIV measurements are carried out at different spanwise planes. As specified previously the PIV system used is a stereo system operating with dual cameras. With the help of the dual cameras (dual view system) it is possible to resolve the third component of the velocity perpendicular to the laser illuminated plane.

The measurements are carried out at four different spanwise locations three of which are shown on the wing for the first half period (Figure 8.1). Three dimensional flow field measurements using the PIV technique requires stereoscopic analysis. However the system must be calibrated before being used for stereoscopic measurements.

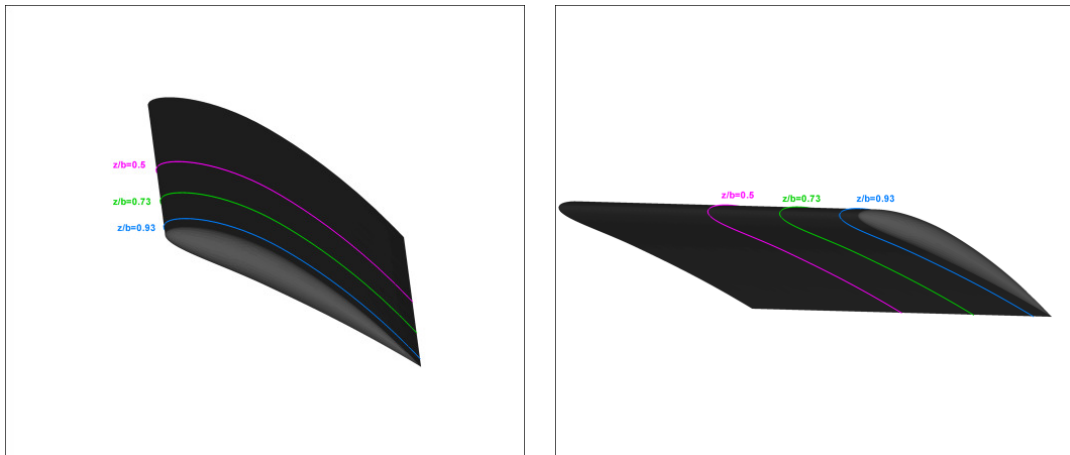


Figure 8.1 Spanwise locations for 3D measurements.

The system uses its own calibration system although the software allows the use of any valid calibration technique as long as it fulfills the measurement specifications.

The simultaneous calibration images taken from the two cameras are given in Figure 8.2. The PIV images of the cameras are shown in Figure 8.3.

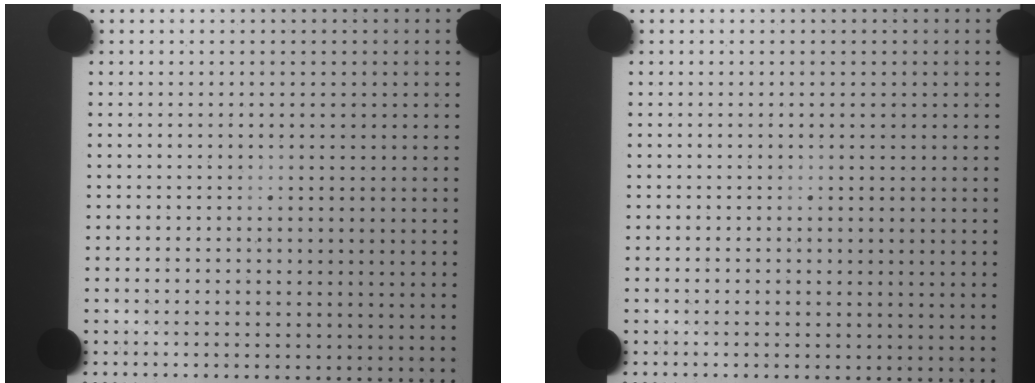


Figure 8.2 Calibration images of Camera 1 (left) and Camera 2 (right) for 3D visualizations.

In three-dimensional PIV measurements, each camera sees the same illuminated plane at different angles. At each spanwise location, the viewing angle of the camera changes. In contrast to 2D measurement principles, the laser sheet should be thicker such that the thickness encloses a volume of width approximately 11 mm. The three-dimensional velocity

fields are then obtained by combining the two-dimensional velocity fields measured by each of the cameras using their respective calibration images.

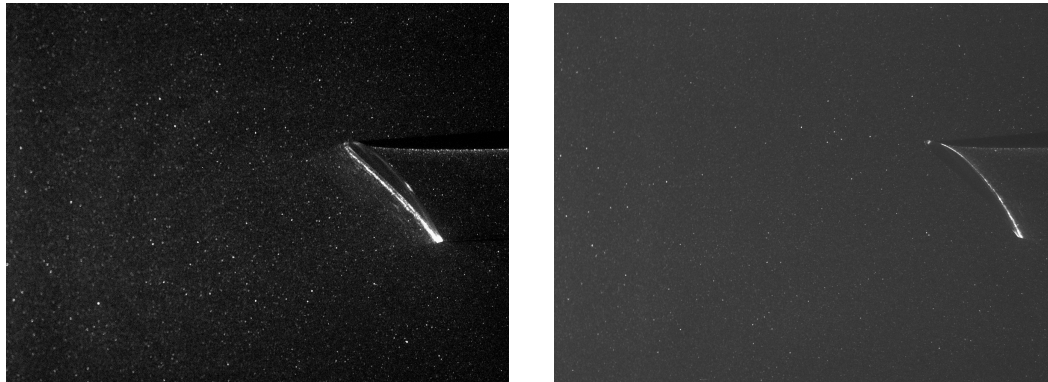


Figure 8.3 Sample PIV images of Camera 1 (left) and Camera 2 (right) for 3D measurements.

The velocity fields obtained are represented by two-dimensional velocity vectors on the plane where the measurements are effected and the third component of the velocity vector is given as a contour plot at the specified z-coordinate. The results can then be processed by using a moving average filter. Figures 8.4 and 8.5 show the raw velocity vectors and the moving averaged velocity vectors respectively. The raw velocity vectors obtained from the images are of good quality (blue vectors) and the vector fields are checked if the substituted vectors (green vectors) disturb the original vector fields. As it can be observed from these figures the substituted vectors align very well with the original vector field.

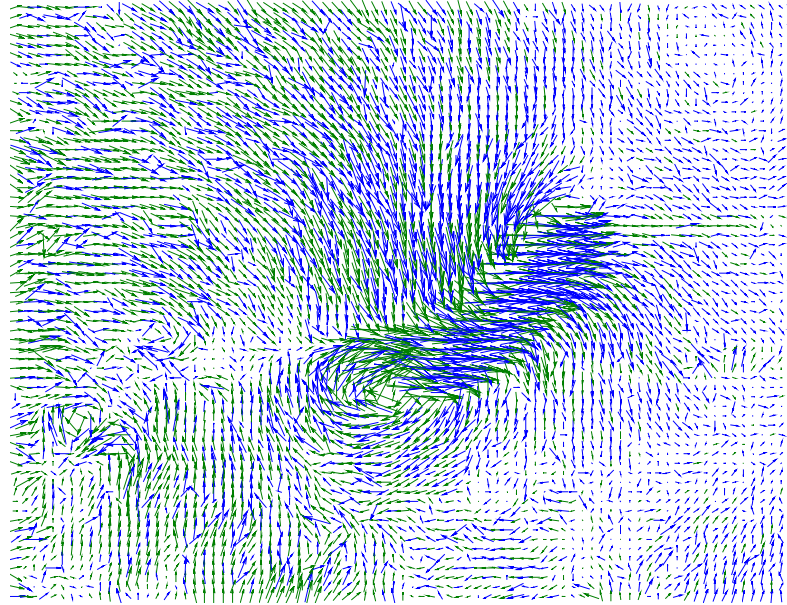


Figure 8.4 Velocity vectors obtained via adaptive correlation.

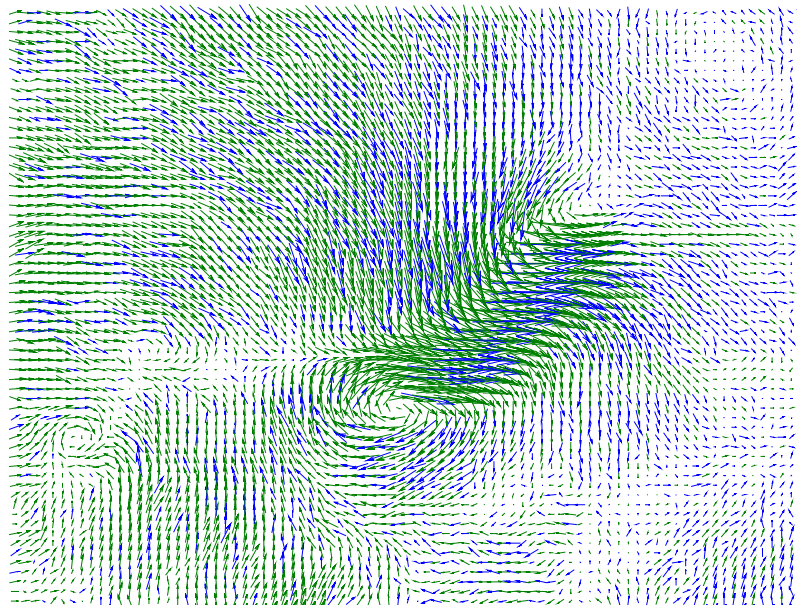


Figure 8.5 3D velocity vectors after applying moving average filter.

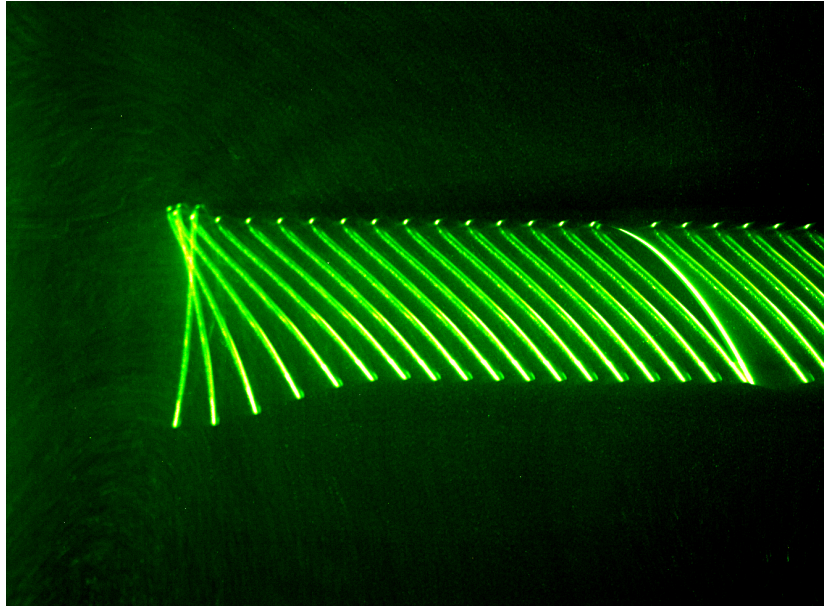


Figure 8.6 Laser sheet visualization of hovering motion during the first quarter period at $\alpha=45^\circ$, $Re = 1000$.

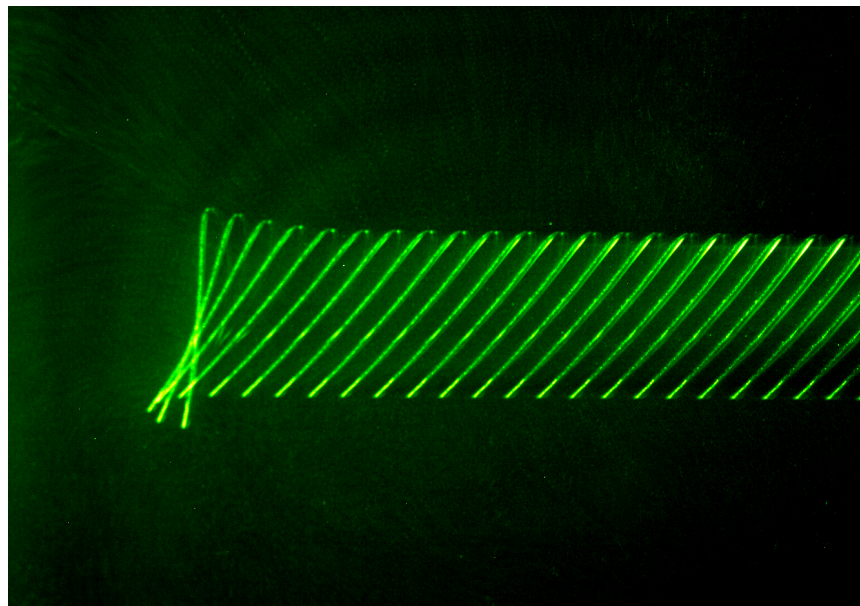


Figure 8.7 Laser sheet visualization of hovering motion during the second quarter period at $\alpha=45^\circ$, $Re = 1000$.

8.2 Three-dimensional Experimental Results

Velocity fields around a finite wing having the cross-section of NACA 6412 airfoil are obtained using the stereoscopic Particle Image Velocimetry technique at four different spanwise locations. The 3D vortex regions around the wing are identified using the method of second invariant of velocity and the second negative Eigen value of the velocity gradient tensor. Scalar methods such as the magnitude of the vorticity and the pressure are no longer valid in 3D measurements since these methods fail in three-dimensional analyses. The presented results are from measurements that are done for the first half period of flapping simulation at an angle of attack of $\alpha=45^\circ$ and $Re=1000$.

The present measurements have put into evidence the behavior of the three dimensional leading edge and the translational vortices. The evolution of these vortices along the spanwise direction of the wing is also investigated. These measurements are discussed within the light of the previous investigations available in the literature, and compared to the 3D numerical studies presented in the previous chapter.

As expected, the 3D vortices separate from the wing at its tip and leave the wing in a helical pattern. As it can be seen from Figure 8.8, the vortex regions are getting smaller along the spanwise direction while approaching the wing tip. The vortices disappear completely after the wing tip in the free stream flow.

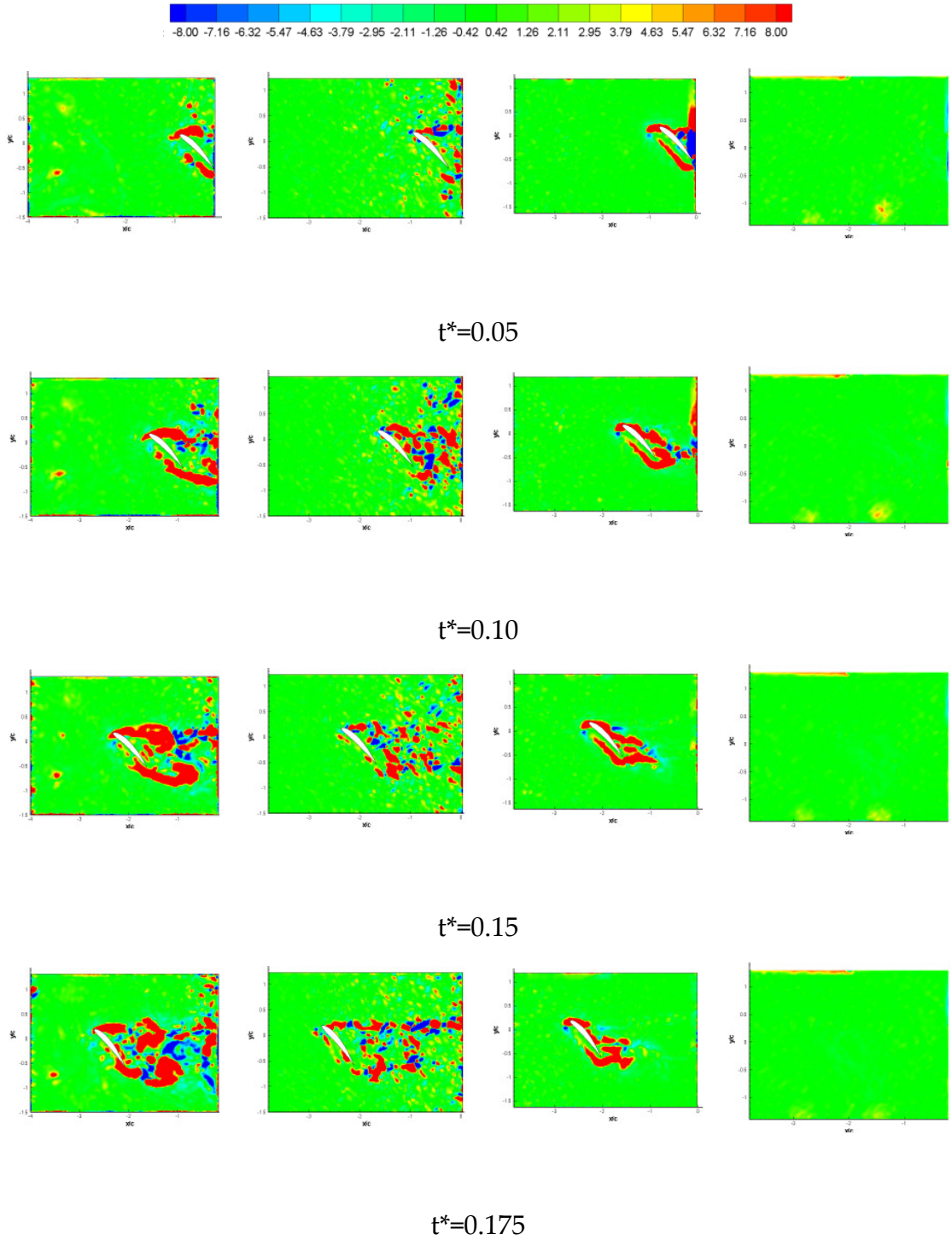


Figure 8.8 Vortex regions identified by Q criteria during the first downstroke at different spanwise locations: $z/b=0.5$ (first column), $z/b=0.73$ (2nd column), $z/b=0.93$ (third column) and $z/b=1.03$ (fourth column).

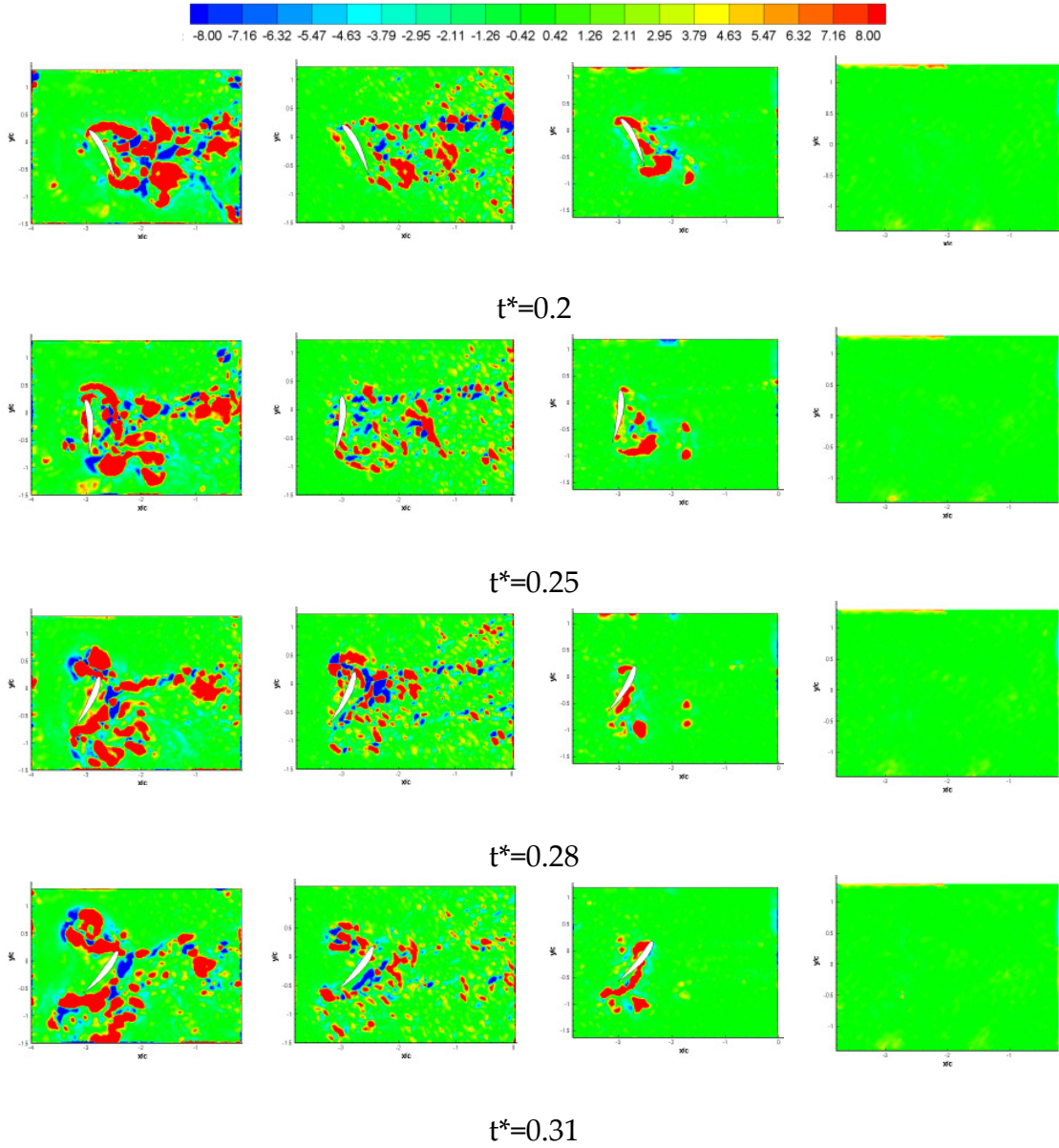


Figure 8.8 (continued) Vortex regions identified by Q criteria during first downstroke and upstroke at different spanwise locations: $z/b=0.5$ (first column), $z/b=0.73$ (2nd column), $z/b=0.93$ (third column) and $z/b=1.03$ (fourth column).

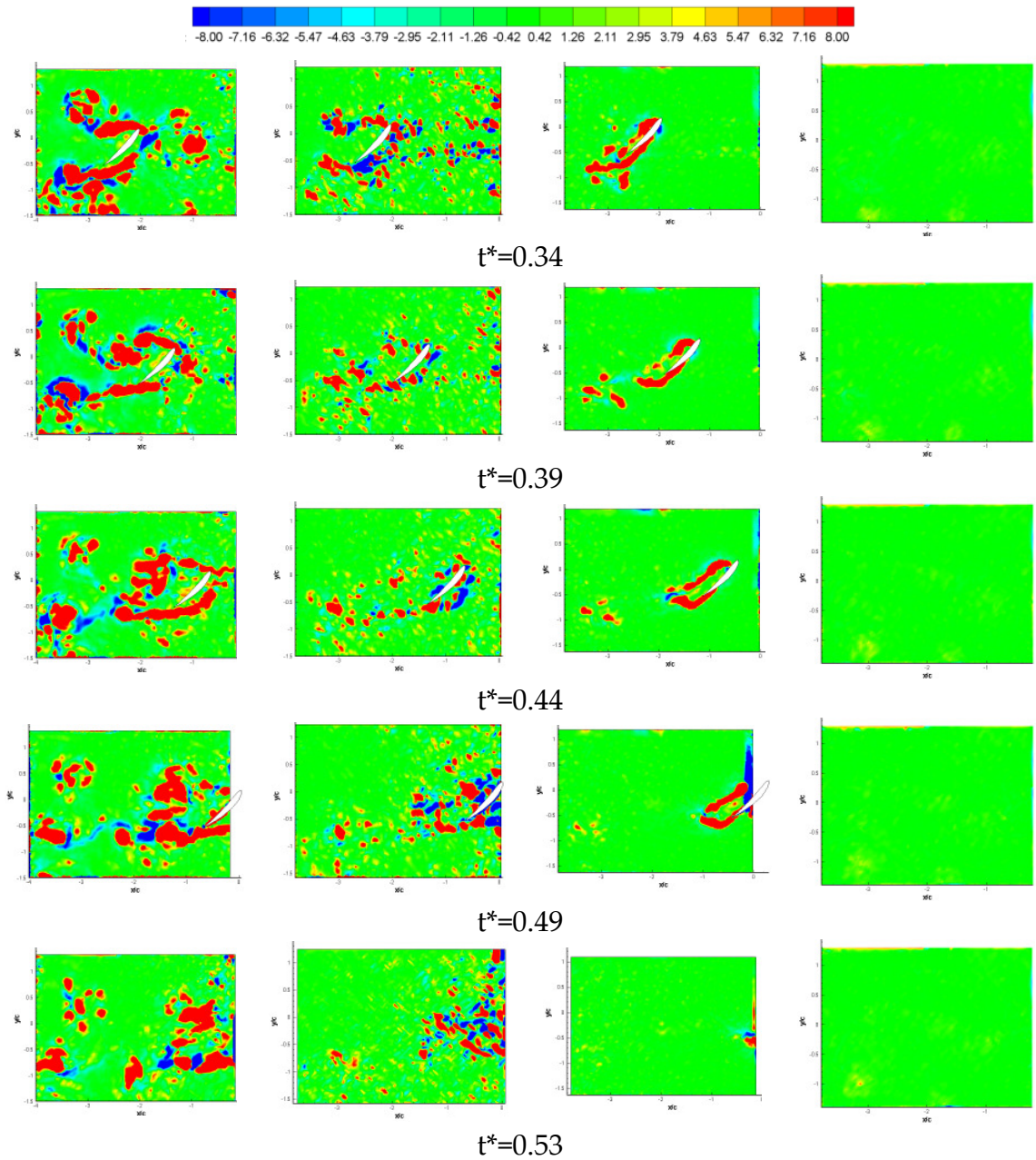


Figure 8.8 (continued) Vortex regions identified by Q criteria during first upstroke at different spanwise locations: $z/b = 0.5$ (first column), $z/b = 0.73$ (2nd column), $z/b = 0.93$ (third column) and $z/b = 1.03$ (fourth column).

8.3 Comparison of Experimental Results to Numerical Computations

Experimental results are compared to numerical solutions at the specified spanwise locations using the second invariant of the velocity gradient, Q criteria for the first half period of the motion. These comparisons are done at the midspan location and are presented in Figure 8.9 as time sequence of images.

As mentioned before, the viewing areas of the cameras cover both the translational and rotational phases of the motion but not the whole translational phase during the first half period, meaning that the measurements can not be done at the beginning of the motion, i.e. $t^*=0.0$. The wing enters the viewing area completely after it has translated for a while. This is also seen in Figure 8.9 as well for $t^*=0.05$ and $t^*=0.49$. The vortex cores are still identified at correct locations for these non-dimensional time steps but the shapes of the vortices are smaller compared to that of numerical solutions. The leading and leading edge vortices are clearly identified both in experimental and numerical results after $t^*=0.10$. The shapes of the vortex regions are similar at the compared time steps. Again, the effect of free stream turbulence and unreal vortex regions at the boundaries are seen in the experimental results. The leading edge vortex is captured both in shape and location in experimental and numerical simulations but the shape of the trailing edge vortex in experimental results is bigger than that of numerical results.

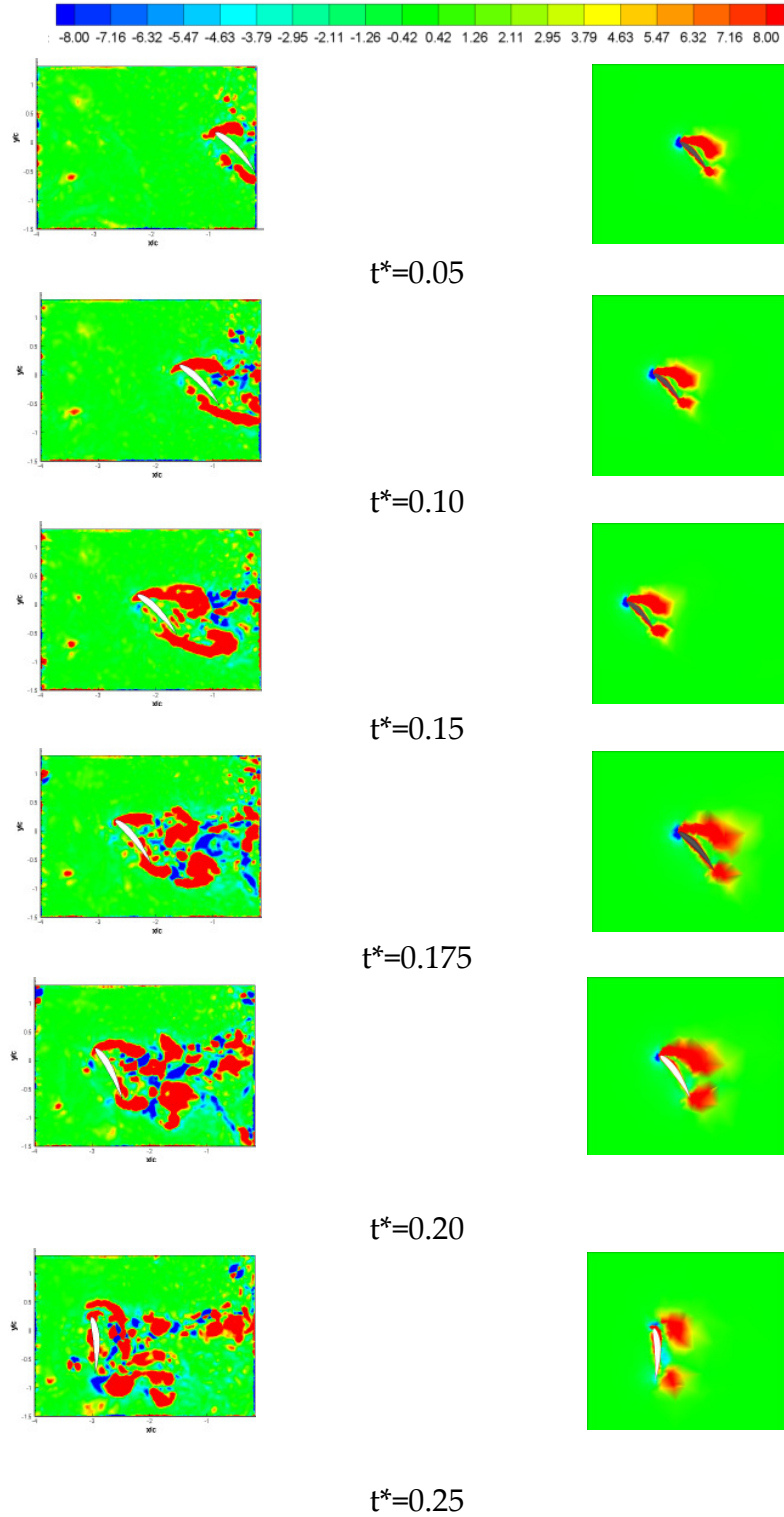


Figure 8.9 Comparison of experimental (left) and numerical (right) results for the first quarter period at $z/b=0.5$ spanwise location.

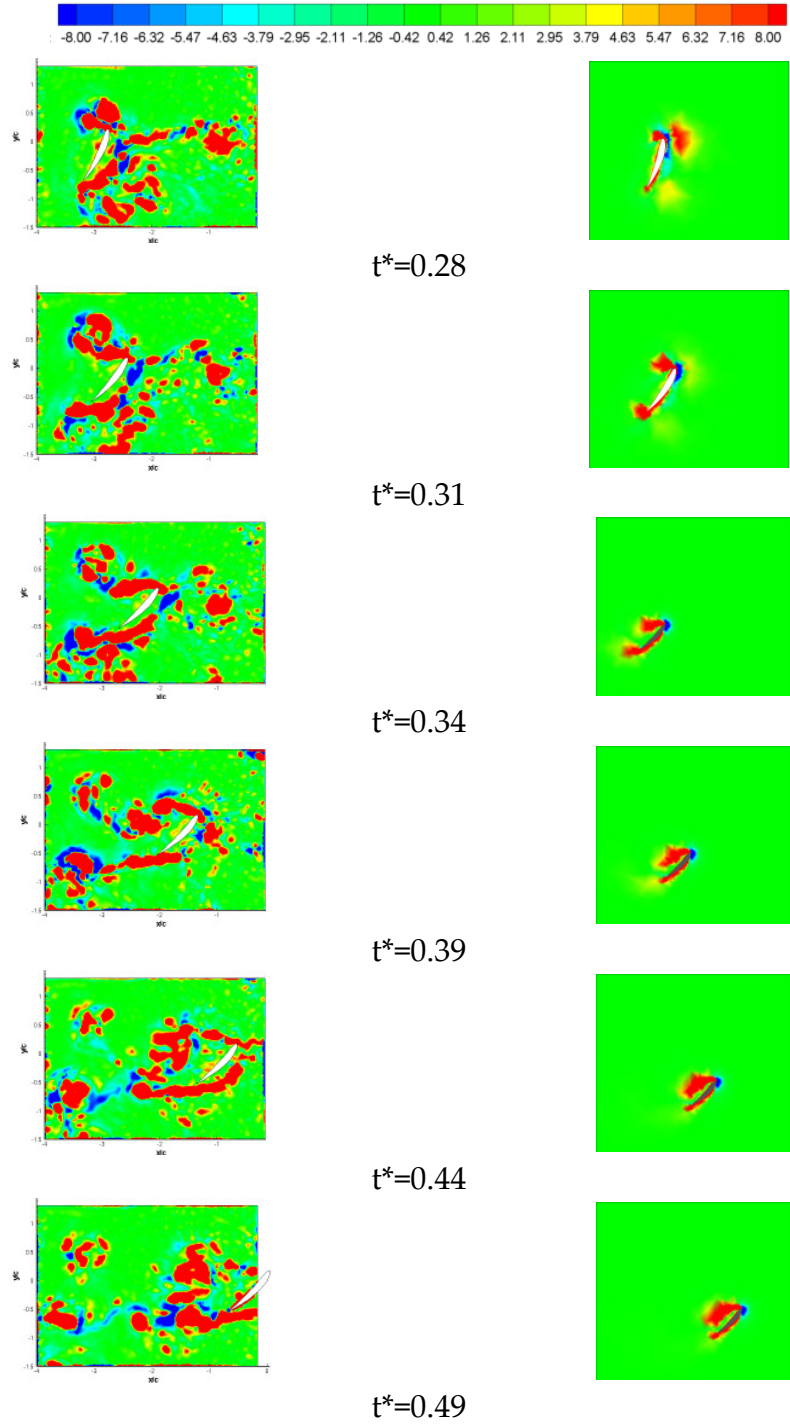


Figure 8.9 (continued) Comparison of experimental (left) and numerical (right) results for the second quarter period at $z/b= 0.5$ spanwise location.

Although the unrealistic vortex regions together with leading and trailing edge vortices are more during the second quarter period of the motion in the experiments, this does not affect the identification of vortex regions. In the second quarter period the newly forming leading and trailing edge vortices are seen in both simulations. The leading edge vortex sheds more in the experiments when compared to numerical results. At $t^*=0.49$, the leading edge part of the wing can not be seen by the cameras but the rest of the wing is still in sight. Therefore, the mesh for processing the vectors includes the complete airfoil for visual purposes.

As it can be observed from these images, the leading and translational vortices are clearly identified by both techniques and the agreement between the experimental results and the numerical solutions are very good.

In Figure 8.10, the comparison of experimental and numerical studies of flapping motion is given at a spanwise location near the tip of the wing, $z/b=0.93$. At this spanwise location, both predictions of the numerical simulations and the measurements performed by the experiments are also in very good agreement as far as the locations and the evolution of the vortex regions are concerned. The formation and shedding mechanisms of both the leading edge and the trailing edge vortices are clearly identified by both methods and it is observed that they are in very good agreement. However, it is observed that in numerical simulations the vortices are more attached and closer to the wing when compared to the experiments. The same observation was true for the comparison of the 2D calculations and measurements.

The unrealistic vortex regions are less seen in the experiments at the spanwise location, $z/b=0.93$ (Figure 8.10). Only the right most boundary region contains unrealistic vortices which correspond to the timing of the wing entering and the leaving of the viewing area. Note that the leading and trailing edge vortex regions shrink when compared to those at the midspan location for both experimental measurements and numerical simulations. In Chapter 7, three-dimensional numerical simulations supported by the previous studies in literature yielded that the leading-edge vortex has a strong axial flow velocity component along the spanwise direction which stabilizes the vortex and reduces its diameter. This fact is also confirmed by the experimental results.

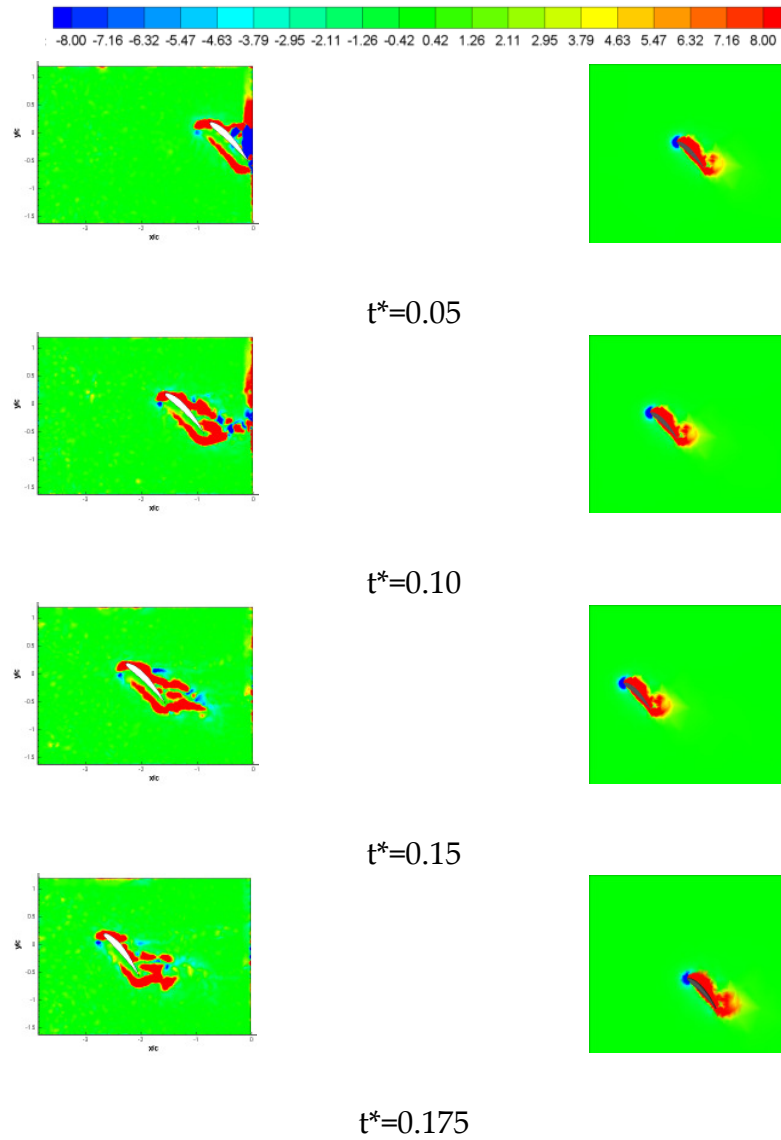


Figure 8.10 Comparison of experimental (left) and numerical (right) results for the first half period at $z/b= 0.93$ spanwise location.

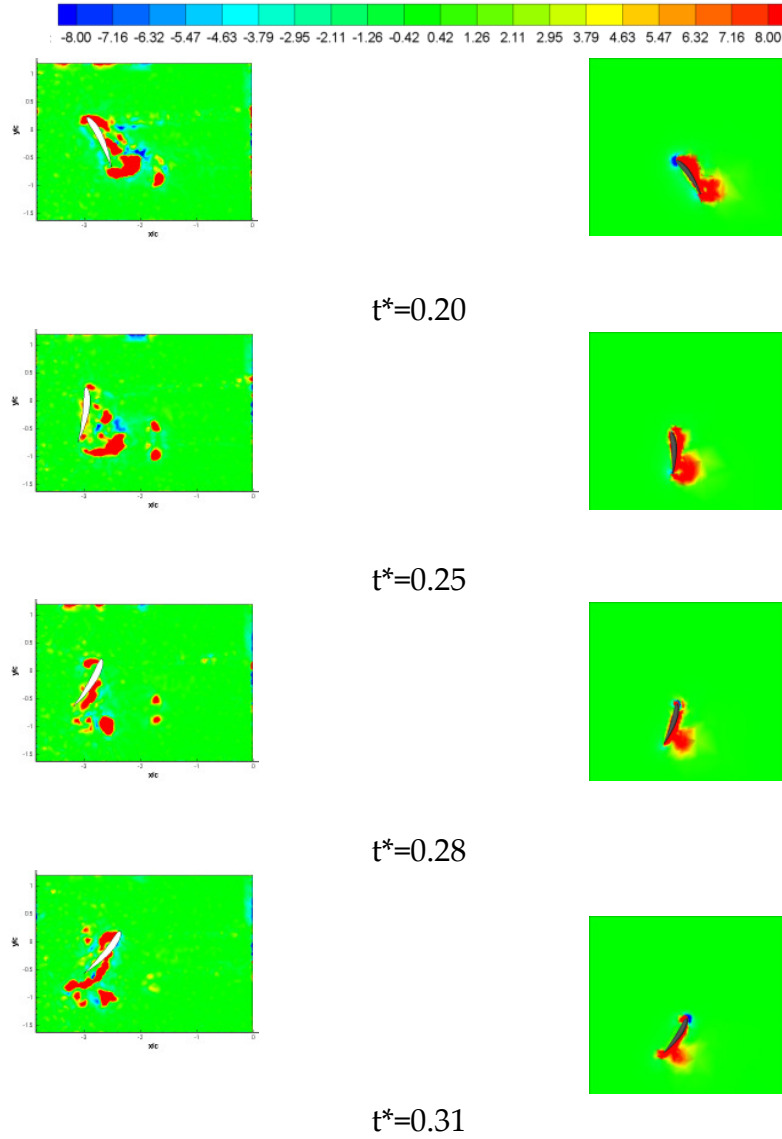


Figure 8.10 (continued) Comparison of experimental (left) and numerical (right) results using the second invariant of velocity gradient tensor, Q criteria for the first half period at $z/b = 0.93$ spanwise location.

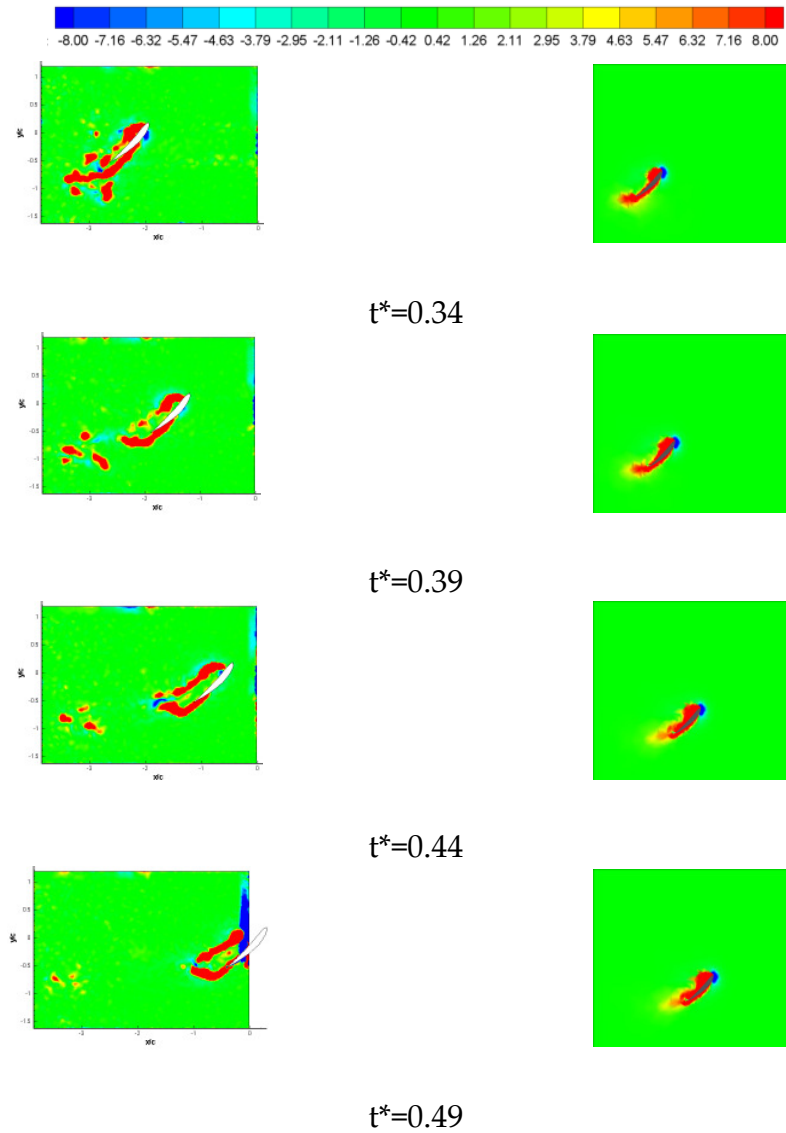


Figure 8.10 (continued) Comparison of experimental (left) and numerical (right) results for the first half period at $z/b= 0.93$ spanwise location.

CHAPTER IX

CONCLUSION

In this study, two- and three-dimensional analyses of flapping wing motion in hover are carried out both numerically and experimentally. The flapping wing motion is analyzed with a simplified motion definition so that it can be applied to flying vehicles. One has to understand the underlying aerodynamic mechanisms for the generation of lift and drag during the flapping motion of a wing before it can be implemented to micro/mini robotic vehicles. In spite of the complexity of the problem, the analysis is extended from symmetrical airfoils to cambered ones, from two-dimensional to three-dimensional cases.

The objective of the present study is to describe the physics of the flapping motion and to understand the aerodynamic mechanism for the generation of lift and drag forces during the flapping wing motion by increasing the complexity of the problem.

The tools used for these investigations are two folds: the numerical solution techniques using CFD and the experimental measurements using the PIV techniques. The numerical simulations are performed using the DNS techniques that are obtained by using two different flow solvers with moving grid capability. The experimental investigations are performed using the stereoscopic 3D Particle Image Velocimetry (PIV) technique.

9.1 General Conclusions

At first numerical tests are carried out on the symmetrical NACA 0012 airfoil for different angles of attack. Based on the literature survey and the previous work done by Kurtuluş [4], the numerical parametric studies are devoted to the physical parameters such as the effect of profile thickness rather than the kinematics of the motion. For this reason, the flapping motion in hover is analyzed on two other symmetrical airfoils having different thickness values, NACA 0010 and NACA 0015. The effect of airfoil profile thickness on the aerodynamic forces generated during the motion is investigated for different angles of attack. The effect of angle of attack on the lift and drag coefficient variations is also studied. Having seen that the negative lift values are avoided for angles of attack higher than 30° , the results presented for the investigation of vortex dynamics are for 45° angle of attack. Throughout the study, the center of rotation point for the airfoils is kept always at the same location in order to be consistent with the experimental studies.

The parametric study on the effect of the profile thickness showed that the absolute peak values of drag coefficients are decreasing as the angle of attack is increased for any given profile. The lift coefficient is strongly dependent on the angle of attack regardless of the profile thickness. Higher lift coefficient peak values are observed for thinner profiles and for increasing angles of attack. It is also observed that the vortex pattern is also changing for different profile thickness values. The shedding of leading edge vortex and the detachment of vortices from the profile occurred earlier as the thickness increased. Leading and trailing edge vortices are more attached to the profile for NACA 0015. Again, for the thickest profile, shedding of leading edge vortex is better observed. For NACA 0010 and NACA 0012 formation of new leading and trailing edge vortices are better observed. Similar rotational stopping vortex patterns are observed for NACA 0010 and NACA 0012, and they are completely separated from the profiles. But for NACA0015 airfoil the vortices are more attached to the profile and consequently their shedding is not very clear. Moreover, bigger vortex regions are observed on the lower surface of NACA 0015 profile after the rotational phases. The shedding of leading edge vortex and the detachment of vortices from the profile occurred earlier as the thickness of the profile is increased. Moreover, the rotational stopping vortex is bigger for thicker profiles.

In two-dimensional parametric studies, the second parameter investigated is the camber effect. As cambered airfoil NACA 6412 is selected and its aerodynamic performance is compared with that of a symmetrical airfoil, NACA 0012 during flapping motion. The selected airfoil profile had the same thickness value as the NACA 0012 and had a camber of 6%, a rather

high value to see the camber effect. At low angles of attack, below 45° , the variations of force coefficients are similar for both cambered and symmetrical profiles but the peak values of lift and drag coefficients of cambered profile are higher than that of the symmetrical one. For $\alpha=45^\circ$, the cambered airfoil achieved higher lift and drag coefficients than the symmetrical one. However, at $\alpha=60^\circ$, symmetric airfoil gives better results than the cambered one. The camber effect is observed to be more significant during the pronation and supination phases. The major change is the shape of the leading edge vortex, which is more attached to the profile when it is symmetric and more prone to detach when it is cambered. Moreover, the translational vortex and the rotational stopping vortex at the trailing edge are larger for flow around the cambered profile. The presence of camber makes the airfoil more sensitive to angle of attack effect. The leading edge vortex separates from the profile earlier and the rotational stopping vortex is getting bigger during pronation phase as the angle of attack is increased from 30° to 60° . Vortex regions characteristics are different for NACA 6412 and NACA 0012 profiles. The shape of LEV of NACA 6412 is different than that of NACA 0012. Leading edge vortex is more attached for the symmetrical profile whereas it is shedding more rapidly for NACA 6412 airfoil. Larger trailing edge and rotational stopping vortex regions are observed for the cambered profile, NACA 6412.

The two-dimensional parametrical numerical studies are then extended to even more cambered profiles which mimic more realistically the wing profiles of small birds and insects. Thus, Eppler 471 and Gottingen 122 airfoils are chosen to analyze the flapping motion in hover and the results

are compared to those of NACA 6412 and NACA 0012. Camber effect is noticeable for angles of attack higher than 30° for all of the profiles considered and cambered airfoils achieved higher absolute peak values at high angles of attack compared to the symmetrical airfoil, NACA 0012. Eppler and Göttingen airfoils are more cambered than NACA 6412 profile and the camber effect is mainly felt on the drag coefficient variations. Negative lift coefficients can be observed even at $\alpha=45^\circ$ for all profiles. Variation of lift coefficients is not as linear for Eppler profile as the other profiles during the first upstroke phase. All cambered profiles achieved nearly the same lift coefficient values at the end of the first and third quarter periods. During one complete period of simulation, the first peak values are nearly the same for all the profiles studied however the absolute value of the peak are higher for Göttingen and NACA 6412 profiles. Again for the variation of the lift coefficient with time, cambered airfoils had higher values during the rotational phases (pronation and supination) of the motion. For symmetrical airfoils higher lift coefficient values were observed during the translational phase of the motion. Drag coefficients are almost constant during the first downstroke phase whereas higher values are obtained during the upstroke phase in particular for NACA 6412 airfoil. Minimum absolute peak values of drag coefficient are achieved by the Eppler profile.

Effect of leading edge radius on the lift and drag coefficients is also investigated. The literature survey on this topic showed that the effect of leading edge radius was studied for turbulent flows and higher velocities. It was observed that the effect of the leading edge radius on the delayed stall was the same for hovering flapping motion..

The most promising feature of flapping motion is the ability to achieve very high unsteady aerodynamic force coefficients. Numerical solutions revealed that the unsteady aerodynamic force coefficients achieved during flapping are higher than the corresponding steady values of the same profiles without flapping.

For three-dimensional numerical simulations, the computational mesh and the complexity of the problem required more computer resources and therefore they are solved using a parallel computational environment. Because of the availability of a parallel user licence, another flow solver, FLUENT V2.22, is used and tested for the two dimensional solution of NACA 6412 airfoil while keeping similar solution schemes and boundary conditions as in STAR CD solver. The two-dimensional results obtained with FLUENT are then compared to those obtained from STAR-CD simulations. It was observed that the lift and drag coefficient variations were in very good agreement. The results were also compared in terms of vortex dynamics of the flow field and it is seen that both of the solutions were in perfect agreement.

Three-dimensional numerical solutions are carried out for a rectangular finite wing having the cross-section of NACA 6412 with a chord of 6 cm. The span of the wing is taken as 30 cm corresponding to an aspect ratio value of 5. Due to mesh quality problems, a wing tip is added to the profile and unstructured mesh is used for the same reason. The three-dimensional solutions are presented again for 45° angle of attack. During these analyses main focus was on the structure of the leading edge vortex created during the motion. Iso-contours of second invariant of the velocity

gradient, Q criteria, showed the formation, evolution and shedding of these vortices. Three-dimensional solutions at the midspan location are then compared to the two-dimensional ones in terms of the aerodynamic force coefficients and vortex dynamics. Two-dimensional solutions of Wang et al. [77] over predicted the three-dimensional quasi-steady experimental values. This was not the case observed for the present study. Over predicting occurred only at the peak locations and the differences were relatively small. Three-dimensional numerical analysis of finite wing configuration showed that the spanwise flow stabilized the location of the leading edge vortex and the vortex itself. These results were also verified by other researchers. The vortex breakdown was observed at the tip of the wing, leaving the wing tip in a well known helical shape as in trailing edge vortex. At any instant of the motion, leading edge vortex region was larger at the wing root and got smaller just after the root section and kept its shape almost constant along the span. As time evolved LEV regions got bigger at all spanwise locations. The leading and trailing edge vortices merged at the wing tip and completely disappeared after leaving the wing tip.

The vortex regions of three-dimensional solutions at the midspan location were compared to two-dimensional results via Q criteria and it was observed that the Q contours in the 3D case exhibited a more isolated behavior for the leading and the trailing edge vortices (they were more distinguished) where as for the 2D case these contours showed a more mixed and merged behavior. Larger vortex regions were observed both at the leading and trailing edges for 3D wing when compared to 2D numerical studies

The results of the present numerical simulations were presented and published in various conferences [102], [103], [108]- [110].

The experimental investigations of flapping motion were performed using the stereoscopic Particle Image Velocimetry (PIV) technique in two steps. In the first step a two-dimensional cambered airfoil motion was studied. In the second step a three dimensional cambered wing motion was investigated. Two-dimensional experimental measurements were conducted on the midspan of the model and then compared to the numerical computations obtained by two different flow solvers using both scalar and Galilean invariant methods. In two-dimensional experiments, the formation and evolution of vortices are clearly identified. Experimental results were in good agreement with two-dimensional numerical solutions. Leading and trailing edge vortex shapes were observed to be similar both in numerical and experimental results but vortices were found to be more attached in numerical simulations compared to experimental measurements.

Stereoscopic PIV measurements were performed to put into evidence the three dimensional behavior (spanwise behavior) of the vortices that were shed from the leading and the trailing edges of the wing. Flow field measurements were done at four different spanwise locations for the same time intervals, during the first half period of the flapping motion. These flow field measurements are then compared to the numerical solutions in order to understand and to relate the aerodynamic force generation mechanisms to vertical flow structure. A number of vortex identification methods, such as magnitude of vorticity, second invariant of velocity

gradient tensor and the second eigenvalue of the velocity gradient tensor, were used for the comparison of experimental and numerical results. The shapes and locations of vortex regions were very similar for both three-dimensional experiments and numerical studies. In this respect both numerical simulations and experimental techniques used during this investigation were complimentary to each other. One technique was used to validate the results of the other technique.

9.2 Future Work

During the present study, only one type of hovering motion, hovering motion in one plane, is considered and analyzed by both numerical and experimental techniques. Other types of hovering motions, such as asymmetric hovering motion, can also be studied in the future using the same experimental set-up since the current experimental setup can be reprogrammed to generate any appropriate combinations of motions both in the vertical and the horizontal planes. Three-dimensional investigation for the present study is limited to only one profile and one aspect ratio wing. In the future this investigation can be extended to different wing profiles having different aspect ratios as well as different wing planforms, elliptical, tapered etc. At present there is no capability for measuring forces acting on the wing during the flapping motion. In the future force measuring capability can be added to the experimental setup and with this capability it will be possible to compare more quantitatively the experiments with the numerical simulations.

REFERENCES

- [1] Ames, Richard Gene, *"On The Flowfield and Forces Generated by a Rectangular Wing Undergoing Moderate Reduced Frequency Flapping at Low Reynolds Number"*, PhD Dissertation, Georgia Institute of Technology Department of Aerospace Engineering, April 2001
- [2] McMichael, J. M., Francis, M. S., *"Micro Air Vehicles - Toward a New Dimension in Flight"* http://www.darpa.mil/tto/mav/mav_auvsi.html, 1997. (Last Accessed:)
- [3] Shyy, W., Berg, M. And Ljungqvist, *"Flapping and flexible wings for biological and micro air vehicles"*, Progress in Aerospace Sciences, Vol. 35, pp.455-505, 1999. Kurtulus, D.F., *"Experimental and Numerical Analysis of flapping motion in hover. Application to micro air vehicles"*, PhD. Dissertation, METU Aerospace Engineering Department, 2005. Sane, S.P., *"Review The aerodynamic of insect flight"*, The Journal of Experimental Biology 206, pp. 4191-4208, 2003.
- [6] Walker, P.B., *"Experiments on the growth of circulation about a wing"*, ARC Tech. Rep. No. 1402, 1931

- [7] Schenato, L., *"Analysis and Control of Flapping Flight: from Biological to Robotic Insects"*, Ph.D. Dissertation, Electrical Engineering and Computer Sciences Department, University California at Berkeley, Fall 2003
- [8] Hall, A., *"Fly like a fly"*, <http://www.sciam.com/article.cfm?articleID=000DF125-5545-1C75-9B81809EC588EF21> (Last Accessed: 20.05.2006)
- [9] Ellington, C.P., *"The Aerodynamics of Hovering Insect Flight I. The Quasi-Steady Analysis"*, Phil. Trans. R.Soc. Lond. B Vol.305, pp.1-15, 1984.
- [10] Maxworthy, T., *"The Fluid Dynamics of Insect Flight"*, Ann. Rev. Fluid.Mech., 198, 13, 329-50, 1981.
- [11] Aono, H. and Liu, H., *"Vortical Structures and Aerodynamics of Hawkmoth Hovering"*, Journal of Biomechanical Science and Engineering, Vol. 1, No.1, pp.234-245, 2006
- [12] Ellington, C.P., *"The Novel Aerodynamics of Insect Flight: Applications to Micro-Air Vehicles"*, The Journal of Experimental Biology 202, pp. 3439-3448, 1999.
- [13] Wang, Z. J., *"Dissecting Insect Flight"*, Annu. Rev. Fluid Mech. Vol.137, pp. 183-210, 2005.
- [14] Wang, Z. J., *"Two Dimensional Mechanism for Insect Hovering"*, Physical Review Letters, Vol. 85, No. 10, September 2000.
- [15] Wang, Z.J., *"Computation of insect hovering"*, Math. Meth. Appl. Sci. 2001; 24:1515–1521, 2001.
- [16] Wang, Z.J., *"Vortex shedding and frequency selection in flapping flight"*, J. Fluid Mech. , Vol.410, pp. 323-341, 2000.

- [17] Streitlien, K. and Triantafyllou, G.S., "*On thrust estimates for flapping foils*", *Journal of Fluids and Structures*, Vol. 12, pp.47-55, 1998.
- [18] Taylor, G.K. and Thomas, A.L.R., "*Animal flight dynamics II:longitudinal stability in flapping flight*", *J. Thoeru. Biol.*, Vol. 214, pp.351-370, 2002
- [19] Read, D.A., Hover, F.S. and Triantafyllou, M.S., "*Forces on oscillating foils for propulsion and maneuvering*", *Journal of Fluids and Structures*, Vol. 17, pp.163-183, 2003.
- [20] Watts, P., Mitchell, E.J. and Swartz, S.M., "*A computational model for estimating the mechanics of horizontal flapping flight in bats: model description and validation*", *J. Exp. Biol.*, 204,pp.2873-2898, 2001.
- [21] Wang, J.K. and Sun, M., "*A computational study of the aerodynamics and forewing-hindwing interaction of a model dragonfly in forward flight*", *J. Exp. Biol.*, 208, pp.3785-3804, 2005.
- [22] Zuo, D., Peng, S., Chen, W. and Zhang, W., "*Numerical simulation of flapping-wing insect hovering flight at unsteady flow*", *Int. J. Numer. Meth. Fluids*, 2006.
- [23] Sun, M. and Tang, J., "*Unsteady aerodynamic force generation by a model fruit fly wing in flapping motion*", *J. Exp. Biol.*, 205, pp.55-70, 2002.
- [24] Miller, L.A. and Peskin, C.S., "*A computational fluid dynamics of 'clap and fling' in the smallest insects*", *J. Exp. Biol.*, 208, pp.195-212, 2005.
- [25] Miller, L.A. and Peskin, C.S., "*When vortices stick: an aerodynamic transition in tiny insect flight*", *J. Exp. Biol.*, 207, pp.3073-3088, 2004.

- [26] Lewin, G.C. and Haj-Hari, H., "*Modelling thrust generation of a two-dimensional heaving airfoil in a viscous flow*", J. Fluid Mech., vol. 492, pp.339-362, 2003.
- [27] Smith, M.J.C., Wilkin, P.J. and Williams, M.M., "*The advantages of an unsteady panel method in modeling the aerodynamic forces on rigid flapping wings*", J. Exp.Biol., 199, pp.1073-1083, 1996.
- [28] Ramamurti, R. and Sandberg, W.C., "*A three-dimensional computational study of the aerodynamic mechanisms of insect flight*", J. Exp. Biol., 205, pp.1507-1518, 2002.
- [29] Ramamurti, R. and Sandberg, W.C., "*Computational study of 3-D flapping foil flows*", Proc. of 39th AIAA Aerospace Sciences Meeting & Exhibit, 8-11 January 2001, Reno, NV.
- [30] Ramamurti, R. and Sandberg, W.C., "*Simulation of flow about flapping airfoils using finite element incompressible flow solver*", AIAA Journal, Vol.39, No.2, pp. 253-260, 2001
- [31] Sun, M. and Tang, J., "*Lift and power requirements of hovering flight in Drosophila virilis*", J. Exp. Biol., 205, pp.2413-2427, 2002
- [32] Sun, M. and Wu, J.H., "*Aerodynamic force generation and power requirements in forward flight in a fruit fly with modeled wing motions*", J. Exp. Biol., 206, pp.3065-3083, 2003
- [33] Bozkurttaş, M., Dong, H., Seshadri, V., Mittal, R. and Najjar,F., "*Towards numerical simulation of flapping foils on fixed cartesian grids*", 43rd AIAA Aerospace Sciences Meeting and Exhibit, January 10*13, Reno, Nevada, 2005

- [34] Wu, J.H. and Sun, M., "*Unsteady aerodynamic forces of a flapping wing*", J. Exp. Biol., 207, pp.1137-1150, 2004
- [35] Eldredge, J.D., "*Efficient tools for the simulation of flapping wing flows*", 43rd AIAA Aerospace Sciences Meeting and Exhibit, 10*13 January Reno, Nevada, 2005.
- [36] Sun, M. and Yu, X., "*Aerodynamic force generation in hovering flight in a tiny insect*", AIAA Journal, Vol. 44, No.7, pp.1532-1540, 2006.
- [37] Bos, F.M., Lentink, D., van Oudheusden, B.W: and baji, H., "*Numerical study of kinematic wing models of hovering insect flight*", 45th AIAA Aerospace Sciences Meeting and Exhibit, 8-11 January 2007, Reno-Nevada.
- [38] Kaya, M., "*Computation of viscous flows over flapping airfoils and parallel optimization of flapping parameters*", M.S. Thesis, METU Aerospace Engineering Department, July 2003.
- [39] Kaya, M. and Tuncer, İ.H., "*Path optimization of flapping airfoils for maximum thrust based on unsteady viscous flow solutions*", 3rd Ankara International Conference, August 22-25, 2005.
- [40] Kaya, M. and Tuncer, İ.H., "*Path optimization of flapping airfoils based on NURBS*", Proceedings of Parallel CFD 2006 Conference, Busan, South Korea, May15-18, 2006.
- [41] Ellington, C.P., "*The Aerodynamics of Hovering Insect Flight II. Morphological Parameters*", Phil. Trans. R.Soc. Lond. B Vol.305, No. 1122, pp.17-40, 1984.
- [42] Ellington, C.P., "*The Aerodynamics of Hovering Insect Flight III Kinematics*", Phil. Trans. R. Soc. Lond. B Vol.305, No. 1122, pp.41-78, 1984.

- [43] Ellington, C.P., *"The Aerodynamics of Hovering Insect Flight IV Aerodynamic Mechanisms"*, Phil. Trans. R. Soc. Lond. B Vol.305, No. 1122, pp.79-113, 1984.
- [44] Ellington, C.P., *"The Aerodynamics of Hovering Insect Flight V A Vortex Theory"*, Phil. Trans. R. Soc. Lond. B Vol.305, No. 1122, pp.115-144, 1984.
- [45] Ellington, C.P., *"The Aerodynamics of Hovering Insect Flight VI Lift and Power Requirements"*, Phil. Trans. R.Soc. Lond. B Vol.305, No. 1122, pp.145-181, 1984.
- [46] Dickinson, M.H., Lehmann, F.O. and Sane, S.P., *"Wing rotation and the aerodynamic basis of insect flight"*, Science, Vol. 284, pp.1954-1960.
- [47] Lehmann, F.O., Sane, S.P. and Dickinson, M., *"The aerodynamic effects of wing-wing interaction in flapping insect wings"*, The Jour. Of Exp. Biol., 208, pp.3075-3092, 2005.
- [48] http://flybase.bio.indiana.edu/anatomy/Drosophilidae/Drosophila_melanogaster_m/index.html (Last Accessed: 13.07.2007)
- [49] Fry, S. N., Sayaman, R. and Dickinson, M. H., *"The aerodynamics of hovering flight in Drosophila"*, The Journal of Experimental Biology 208, 2303-2318, 2005
- [50] Dickson , W.B. and Dickinson , M.H., *"The effect of advance ratio on the aerodynamics of revolving wings"*, The Journal of Experimental Biology 207, 4269-4281, 2004
- [51] Bomphrey ,R. J., Lawson, N. J., Harding, N.J. ,Taylor, G.K., and Thomas, A.L.R., *"The aerodynamics of Manduca sexta: digital particle image*

- velocimetry analysis of the leading-edge vortex*", The Journal of Experimental Biology 208, pp.1079-1094, 2005
- [52] <http://waynesword.palomar.edu/manduca2.htm> (Last Accessed: 13.07.2007)
- [53] Birch, J.M. and Dickinson, M.H., "*The influence of wing-wake interactions on the production of aerodynamic forces in flapping flight*", The Journal of Experimental Biology 206, pp.2257-2272, 2003
- [54] Hedrick, T.L., Usherwood, J.R. and Biewener, A.A., "*Wing inertia and whole-body acceleration: an analysis of instantaneous aerodynamic force production in cockatiels (Nymphicus hollandicus) flying across a range of speeds*", The Journal of Experimental Biology 207, pp.1689-1702, 2004.
- [55] Usherwood, J.R., Hedrick, T.L., McGowan, C.P., and Biewener, A.A., "*Dynamic Pressure Maps for Wings and tails of pigeons in slow, flapping flight, and their energetic implications*", Journal of Experimental Biology 208, pp. 355-369, 2005
- [56] http://en.wikipedia.org/wiki/Rock_Pigeon (Last Accessed: 13.07.2007)
- [57] Hover, F.S., Haugsdal, Ø and Triantafyllou, M.S., "*Effect of angle of attack profiles in flapping foil propulsion*", Journal of Fluids and Structures, Vol. 19, pp.37-47, 2004
- [58] Dickinson, M.H. and Götz, K., "*Unsteady Aerodynamic Performance of Model Wings at Low Reynolds Numbers*", J. Exp. Biol., 174, pp.45-64, 1993
- [59] Usherwood, J.R. and Ellington, C.P., "*The Aerodynamics of revolving wings: I Model Hawkmoth wings*", J. Exp. Biol., 205, pp.1547-1564, 2002.

- [60] Usherwood, J.R. and Ellington, C.P., "*The Aerodynamics of revolving wings: II Propeller force coefficients from mayfly to quail*", J. Exp. Biol., 205, pp.1565-1576, 2002.
- [61] Willmott, A.P. and Ellington, C.P., "*The Mechanics of Flight in the Hawkmoth *Manduca sexta* I. Kinematics of Hovering and Forward Flight*", J. Exp. Biol., 200, pp.2705-2722, 1997.
- [62] Willmott, A.P. and Ellington, C.P., "*The Mechanics of Flight in the Hawkmoth *Manduca sexta* II. Aerodynamic Consequences of Kinematic and Morphological Variation*", J. Exp. Biol., 200, pp.2723-2745, 1997.
- [63] <http://www.flickr.com/photos/65429206@N00/215385572/> (Last Accessed: 13.07.2007)
- [64] Warrick, D.R., Tobalske, B.W. and Powers, D.R., "*Aerodynamics of the hovering hummingbird*", Nature, Vol. 435,23, pp. 1094-1097, 2005.
- [65] <http://www.hummingbirds.net/rufous.html> (Last Accessed: 13.07.2007)
- [66] Dickinson, M.H., Lehmann, F.O. and Götz, K.G., "*The active control of wing rotation by *Drosophila**", J. Exp. Biol. 182, pp.173-189, 1993.
- [67] Birch, J.M., Dickson, W.B. and Dickinson, M.H., "*Force production and flow structure of the leading edge vortex on flapping wings at high and low Reynolds numbers*", J. Exp. Biol., 207, pp.1063-1072, 2004.
- [68] Sane, S.P. and Dickinson, M.H., "*The aerodynamic effects of wing rotation and a revised quasi-steady model of flapping flight*", J. Exp. Biol., 205, pp.1087-1096, 2002
- [69] Birch, J.M. and Dickinson, M.H., "*Spanwise flow and the attachment of the leading-edge vortex on insect wings*", Nature, Vol.142, pp.729-733, 2001.

- [70] Van Den Berg, C. and Ellington, C.P., "*The three-dimensional leading-edge vortex of a 'hovering' model hawkmoth*", *Phil. Trans. R. Soc. Lond. B* 352, pp.329-340, 1997
- [71] Van Den Berg, C. and Ellington, C.P., "*The vortex wake of a 'hovering' model hawkmoth*", *Phil. Trans. R. Soc. Lond. B* 352, pp.317-328, 1997
- [72] Combes, S.A. and Daniel, T.L., "*Into thin air: contributions of aerodynamic and inertial-elastic forces to wing bending in the hawkmoth *Manduca sexta**", *The Journal of Experimental Biology*, 206, pp. 2999-3006, 2003
- [73] Lu, Y., Shen, G.X. and Su, W.H., "*Flow visualization of dragonfly hovering via electromechanical model*", *AIAA Journal*, Vol.45, No.3, pp. 615-623, 2007.
- [74] Liu, H., "*Computational Biological Fluid Dynamics: Digitizing and Visualizing Animal Swimming and Flying*", *Integr. Comp. Biol.*, 42:1050–1059, 2002.
- [75] Sane, J.P., "*Induced airflow in flying insects I. A theoretical model of the induced flow*", *J. Exp. Biol.*, 209, pp.32-42, 2006.
- [76] Sane, J.P. and Jacobson, N.P., "*Induced airflow in flying insects II. Measurement of induced flow*", *J. Exp. Biol.*, 209, pp.43-56, 2006.
- [77] Wang, Z.J., Birch, J.M. and Dickinson, M.H., "*Unsteady forces and flows in low Reynolds number hovering flight: two-dimensional computations vs robotic wing experiments*", *J. Exp. Biol.*, 207, pp.449-460, 2004.
- [78] Flow Manager Manual, 2007.
- [79] F. Durst, A. Melling & J. H. Whitelaw: "*Principles and practice of laser-Doppler anemometry*", second edition, *Academic Press*, 1981.

- [80] H.C. van de Hulst: *"Light Scattering by Small Particles"*, Dover publications, 1981
- [81] Basset, A.B., *"Treatise on Hydrodynamics Vol. II"*, London Deighton Bell & Co., 1988.
- [82] Hinze, J.O., *"Turbulence"*, McGraw-Hill Press, New York, 1959.
- [83] http://www.dantecdynamics.com/Download/pdf_files/pi270003.pdf
(Last Accessed: 26.10.2006)
- [84] [http://www.dantecdynamics.com/PE/seeding/Index.html#Polyamide%20seeding%20particles%20\(PSP\)](http://www.dantecdynamics.com/PE/seeding/Index.html#Polyamide%20seeding%20particles%20(PSP)) (Last Accessed: 26.10.2006)
- [85] Banks, D. C and Singer, B. A., *"Vortex Tubes in Turbulent Flows: Identification, Representation, Reconstruction"*, IEEE, pp. 132-, 1994
- [86] Robinson , S. K., *"Coherent motions in the turbulent boundary layer"*
Annu. Rev. Fluid Mech. 23, 601, 1991
- [87] Jeong and Hussain, *"On the identification of a vortex"*, J. Fluid Mech. Vol.285, pp.69-94, 1995
- [88] Cucitore, R., Quadrio, M. and Baron, A., *"On the effectiveness and limitations of local criteria for the identification of a vortex"*, Eur. J. Mech. B/Fluids, 18, No 2, pp. 261-282, 1999.
- [89] Kline, S.J. and Robinson, S.K., *"Turbulent Boundary Layer Structure: Progress, Status and Challenges"* Structure of Turbulence and Drag Reduction, ed. A.Gyr, Springer., 1990
- [90] Chong M.S., Perry A.E. and Cantwell B.J., *"A general classification of three-dimensional flows"*, Phys. Fluids A 2, 765, 1990.

- [91] Hunt J.C.R., Wray A.A. and Moin P., "*Eddies, stream and convergence zones in turbulent flows*", Center for Turbulence Research Report CTR-S88, 193, 1998
- [92] Repellin O., "*Experimental characterization of vortical structures with aeroacoustic effects*", VKI Project Report 1999-28, June 1999.
- [93] Chakraborty P., Balachandar S. And Adrian R.J., "*On the relationships between local vortex identification schemes*", J. Fluid Mech., Vol. 535, pp.189-214, 2005
- [94] Hussain A., Baig M.F. and Varshney H., "*Investigation of coherent structures in rotating Rayleigh-Benard convection*", Phys. Fluids 18, 2006.
- [95] Dubief, Y. and Delcayre, F., "*On coherent-vortex identification in turbulence*", Journal of Turbulence, Vol.1, 2000.
- [96] Jespersen ,T. S., Thomassen, J.Q., Andersen, A. and Bohr, T., "*Vortex dynamics around a solid ripple in an oscillatory flow*", Eur. Phys. J. B 38, pp. 127–138 (2004)
- [97] Jeon, D. And Gharib, M., "*On the relationship between the vortex formation process and cylinder wake vortex patterns*", J. Fluid Mech., vol. 519, pp. 161–181, 2004
- [98] Kenwright, D. and Haines, R., "*Vortex identification - applications in aerodynamics: a case study*", Proceedings of the 8th IEEE Visualization '97 Conference, 1997
- [99] Graftieaux, L., Michard, M. and Grosjean, N., "*Combining PIV, POD and vortex identification algorithms for the study of unsteady turbulent swirling flows*", Meas. Sci. Technol. 12, pp. 1422–1429.

- [100] STAR-CD Users Guide
- [101] Gridgen Manual
- [102] Sarıgöl, E., Kurtuluş, D.F. and Alemdaroğlu, N., "*Çırpan kanat probleminde kanat profile kalınlığının sayısal incelenmesi*", Uluslararası Katılımlı Kayseri VI. Havacılık Sempozyumu, Kayseri, Türkiye, 12-14 Mayıs 2006 (in Turkish).
- [103] Sarıgöl, E. and Alemdaroğlu, N., "*A parametric study on two dimensional flapping motion*", Proc. 2nd European Micro-air Vehicles Conference EMAV 2006, Braunschweig, Germany, 2006.
- [104] Grohsmeier, S.P., Ekaterinaris, J.A. and Platzer, M.F., "*Numerical investigation of the effect of leading edge geometry on dynamic stall of airfoils*" AIAA-91-1798-CP.
- [105] Jones, K.D. and Platzer, M.F., "*On the prediction of dynamic stall onset on airfoils in low speed flow*", Proceedings of the 8th International Symposium on Unsteady Aerodynamics and Aeroelasticity of Turbomachines, Ed. T. H. Fransson, Kluwer Academic Publications, Dordrecht, The Netherlands, 1998, pp. 797-812.
- [106] Fluent v.6.3 Users Guide, 2006
- [107] <http://en.wikipedia.org/wiki/Speedup> (LastAccessed: 13.07.2007)
- [108] Sarıgöl, E. and Alemdaroğlu, N., "*Computation of unsteady hovering flapping motion in parallel environment*", International Conference on Parallel Computational Fluid Dynamics PARCFD 2007, Antalya, Turkey, 21-24 May 2007.

- [109] Sarıgöl, E., Alemdaroğlu, N. and Özgen, S., *“Investigation of camber effect in flapping motion during hover”*, Ankara International Aerospace Conference AIAC 07, Ankara, Turkey, 10-12 September 2007 (accepted)
- [110] Sarıgöl, E. and Alemdaroğlu, N., *“Flapping motion in 2D: Experimental and numerical analysis”*, 2nd European Conference on Aerospace Sciences, Brussels, Belgium, 1-6 July 2007.
- [111] Knowles, K., Ansar, S.A., Wilkins, P.C. and Zbikowski, R.W., *“Recent progress towards developing an insect-inspired flapping wing micro air vehicle”*, Proc. of AVT-146 Symposium on “Platform Innovations and System Integration for Unmanned Air, Land and Sea Vehicles”, 14-17 May 2007, Italy.

CURRICULUM VITAE

PERSONAL INFORMATION

Surname, Name: Sarıgöl, Ebru

Nationality: Turkish (TC)

Date and Place of Birth: 6 October 1977 , Ankara

Marital Status: Single

Address: Mesa 2. Batı Sitesi Özlemkent 11/10 Yeni batı Mah. 06370

Batıkent

ANKARA

Phone: +90 312 255 20 51

email: esarigol@ae.metu.edu.tr

EDUCATION

- | | |
|---------------------|--------------------------------------------------------------------------------------------------------|
| 2002 – Today | METU Department of Aerospace Engineering
<i>Ph.D. Graduate Program (3.50 / 4.00)</i> |
| 1999 – 2002 | METU Department of Aeronautical Engineering
<i>Master of Science Graduate Program (3.21 / 4.00)</i> |
| 1995 – 1999 | METU Department of Aeronautical Engineering
<i>Bachelor of Science (2.86 / Major)</i> |
| 1988 – 1995 | Atatürk Anatolian High School |

EXPERIENCE

June 2007-Today	STM Savunma Teknolojileri Mühendislik ve Ticaret A.Ş. Ankara, TÜRKİYE <i>Systems Engineer</i>
May 2007	<i>Local Comitee Member</i> of International Conference on Parallel Computational Fluid Dynamics PARCFD 2007, 21-24 May 2007, Antalya
November 2006	<i>Local Comitee Member</i> of NATO RTO Lecture Series on Mission Systems Engineering, 14-15 November 2006
September 2006	<i>Local Comitee Member</i> of 1. Ulusal Havacılık ve Uzay Konferansı UHUK 2006, 21-23 September 2006, Ankara
August 2005	<i>Local Comitee Member</i> of 3 rd Ankara International Aerospace Conference AIAC 2005, 22-25 August 2005, Ankara
September 2006- June 2007	PhD Fellow of TÜBİTAK
December 1999 – September 2006	METU Aerospace Engineering Department, Ankara, TÜRKİYE <i>Research Assistant</i>
7.1998 – 8. 1998	TURKISH AIRLINES, ESENBOĞA AIRPORT, Ankara, TÜRKİYE <i>Summer Practice</i>
7.1997 – 8.1997	TAI (TUSAS AEROSPACE INDUSTRIES), Ankara, TÜRKİYE <i>Summer Practice</i>

FOREIGN LANGUAGES

English	Fluent
German	Little

COMPUTER SKILLS

Programming Languages	FORTRAN, C
Software Applications	TECPLOT, MATLAB, MATHCAD, STAR-CD, FLUENT, GAMBIT, TGRID, GridGEN, Rhinoceros, MS OFFICE, FlowManager (PIV Measurement Software – DANTEC)
Operating systems	WINDOWS NT/98/2000/XP (Administrative Level),LINUX / UNIX (User Level)

PUBLICATIONS

- Numerical (ENO) Solution of a Travelling Vortex-Shock Interaction, Uluslararası Katılımlı Kayseri IV. Havacılık Sempozyumu, 13-15 Mayıs, 2002
- Weighted Essentially Non-Oscillatory (WENO) Euler Solution of Two-Dimensional High-Speed Flows, September 2002, M.Sc. Thesis, METU Aeronautical Engineering Department
- Isı Transferinin Sınır Tabaka Kararlılığı ve Geçiş Üzerindeki Etkisi, Uluslararası Katılımlı Kayseri V. Havacılık Sempozyumu, 11-13 Mayıs, 2004
- Effect of Heat Transfer on Boundary Layer Stability and Transition, 2004 WSEAS/IASME International Conference on FLUID MECHANICS and on HEAT and MASS TRANSFER, Corfu Island, Greece, 16-19 August, 2004
- İnsansız Hava Araçları Tasarım ve Teknolojileri, Havacılıkta İleri Teknolojiler ve Uygulamaları Sempozyumu (HİTEK), İstanbul, 9-10 Aralık, 2004
- Çırpan Kanat Probleminde Kanat Profili Kalınlığının Sayısal İncelenmesi, Uluslararası Katılımlı Kayseri VI. Havacılık Sempozyumu, 12-14 Mayıs, 2006
- A Parametric Study on Two dimensional Flapping Motion, Proceeding of European Micro Air Vehicle Conference and Flight Competition, Braunschweig Germany, 25-26 July 2006
- Computation of unsteady hovering flapping motion in parallel environment, International Conference on Parallel Computational Fluid Dynamics, Antalya, Turkey, 21-24 May 2007.

- Flapping Motion in 2D: Experimental and Numerical Anaysis, 2nd European Conference for Aero-Space Sciences, Brussels, Belgium 1-6 July, 2007
- Investigation of camber effect in flapping motion during hover, Ankara International Aerospace Conference, METU Ankara, Turkey, September 10-12, 2007 (accepted)